*République Algérienne Démocratique et Populaire*

*Ministère de L'Enseignement Supérieur et de la Recherche Scientifique*

*Université Mohamed El Bachir El Ibrahimi de Bordj Bou Arréridj*

*Faculté des Sciences et de la Technologie*

*Thèse présentée pour l'obtention du diplôme de DOCTORAT 3ème cycle L.M.D.*

*En : Electrotechnique*

*Spécialité : Commandes électriques*

Thème

# *Commandes Avancées Des Systèmes Photovoltaïques Dédiées A L'amélioration De La Qualité De L'énergie Dans Les Réseaux Electriques*

*Présentée par*

MOHAMED CHERIF DAIA EDDINE OUSSAMA

*Soutenue le :* 08 juillét 2025

Devant le jury composé de:

| | | | |
|---|---|---|---|
| HAMIMID Mourad | Prof. | Université de BBA | Président |
| CHEBABHI Ali | Prof. | Université de M'sila | Rapporteur |
| KESSAL Abdelhalim | Prof. | Université de BBA | Co-Rapporteur |
| TALHAOUI Hicham | Prof. | Université de BBA | Examinateur |
| AISSA Oualid | MCA | Université de BBA | Examinateur |
| BERRABAH Fouad | Prof. | Université de M'sila | Examinateur |
| DEFDAF Mabrouk | MCA | Université de M'sila | Examinateur |

*The People's Democratic Republic of Algeria*

*Ministry of Higher Education and Scientific Research*

*Mohamed El Bachir El Ibrahimi University, Bordj Bou Arreridj*

*Faculty of Science and Technology*

*Thesis submitted for the award of the 3rd cycle DOCTORATE L.M.D.*

*Field: Electrotechnics*

*Specialty: Electrical control*

*Entitled*

# *Advanced Controls for Photovoltaic Systems Dedicated to Improve the Power Quality in Electrical Grids*

*Presented by*

MOHAMED CHERIF DAIA EDDINE OUSSAMA

*defended on:* July 8, 2025

In front of the committee composed of:

| | | | |
|---|---|---|---|
| HAMIMID Mourad | Prof. | University of BBA | President |
| CHEBABHI Ali | Prof. | Université de M'sila | Supervisor |
| KESSAL Abdelhalim | Prof. | University of BBA | Co-Supervisor |
| TALHAOUI Hicham | Prof. | University of BBA | Examiner |
| AISSA Oualid | MCA | University of BBA | Examiner |
| BERRABAH Fouad | Prof. | University of M'sila | Examiner |
| DEFDAF Mabrouk | MCA | University of M'sila | Examiner |

# *Acknowledgement*

*In the name of Allah, the Most Gracious, the Most Merciful. I begin by expressing my deepest gratitude to Allah, the source of all knowledge and wisdom, for granting me the strength, patience, and guidance to complete this thesis. Without His blessings, this achievement would not have been possible.*

*I extend my heartfelt gratitude and sincere thanks to my supervisor,* ***Prof. CHEBABHI Ali****, for his invaluable guidance, unwavering support, and patience throughout this journey. His expertise, encouragement, and kindness have been a constant source of motivation for me. I am equally grateful to my co-supervisor,* ***Prof. KESSAL Abdelhalim****, for his insightful supervision, constructive feedback, and invaluable assistance, which have greatly enriched my work.*

*I would like to express my sincere appreciation to the members of my thesis committee, Prof.* ***HAMIMID Mourad****, Prof.* ***TALHAOUI Hicham****, Dr.* ***AISSA Oualid****, Prof.* ***BERRABAH Fouad****, and Dr.* ***DEFDAF Mabrouk,*** *for their time, thoughtful discussions, and constructive suggestions, which have significantly contributed to the improvement of this thesis.*

*I am deeply thankful to* ***all my colleagues*** *and* ***professors*** *at Mohamed El Bachir El Ibrahimi University, Bordj Bou Arreridj, for their support and encouragement throughout my academic journey. Special thanks go to the director of the* ***LPMRN laboratory*** *at Mohamed El Bachir El Ibrahimi University for their invaluable assistance and resources.*

*I lack the words to adequately express my profound gratitude to* ***my mother****, my greatest source of inspiration. Her prayers, sacrifices, and unwavering belief in me have been the foundation of my success. I am equally thankful to* ***my father*** *for his endless moral support and encouragement despite the distance between us. His faith in me has been a driving force throughout my academic career.*

*A special thanks to my brother,* ***Akrem****, my strong shoulder and constant support in this life. Your presence has been a source of strength and motivation for me. I would also like to express my heartfelt gratitude to* ***my fiancee*** *for her patience, understanding, and unwavering support during this challenging journey.*

*Finally, I am deeply grateful to all* ***my family*** *members and* ***friends*** *for their steadfast encouragement and support. Your love and belief in me have been a constant source of strength.*

***Thank you all for being part of this incredible journey.***

***MOHAMED CHERIF Daia Eddine Oussama***

# *Abstract*

This thesis investigates advanced control strategies for photovoltaic (PV) systems, focusing on power quality improvement and efficient energy injection into the grid. The limitations of conventional boost converters (CBC) are addressed by employing a four-leg interleaved boost converter (FLIBC), which offers reduced ripple, enhanced efficiency, and suitability for high-power applications.

Fuzzy logic and incremental conductance maximum power point tracking (MPPT) algorithms are compared, with fuzzy logic demonstrating superior performance in terms of convergence speed and reduced voltage ripple. Nonlinear control strategies, including backstepping (BS), sliding mode control (SMC), and super-twisting sliding mode control (STSMC), are implemented and compared with traditional proportional-integral (PI) controllers for the FLIBC. STSMC exhibits the best performance by eliminating chattering and achieving fast response.

For grid integration, a classical direct power control (DPC) strategy utilizing a switching table is initially explored for the FLIBC-based Multifunctional Grid-Connected PV (MGCPV) system. The FLIBC-based MGCPV system demonstrates superior performance compared to the CBC-based MGCPV system, particularly in terms of reduced power ripple, lower overshoot, and diminished harmonic distortion. These improvements highlight the enhanced efficiency and reliability of the FLIBC-based system in grid-connected photovoltaic applications.

Then, an enhanced DPC strategy combined with space vector modulation (SVM) and a grey wolf optimizer (GWO)-tuned BS controller is proposed. Simulation results validate the effectiveness of the proposed control schemes in achieving precise power regulation, minimizing harmonic distortion, reducing power ripple, and enhancing grid stability under various operating conditions, including changes in solar irradiance and load variations. The GWO-optimized BS controller demonstrates superior performance compared to PI controllers in the DPC-SVM strategy.

This research contributes to the development of robust and efficient control solutions for integrating PV systems into modern power grids, paving the way for enhanced power quality and a more sustainable energy future.

***Keywords:*** Photovoltaic, Grid connected PV system, Backstepping, Sliding mode control, Interleaved boost converter, Direct power control, Grey wolf optimizer

# *Résumé*

Cette thèse explore des stratégies de contrôle avancées pour les systèmes photovoltaïques (PV), en mettant l'accent sur l'amélioration de la qualité de l'énergie et l'injection efficace de l'énergie dans le réseau. Les limites des convertisseurs boost conventionnels (CBC) sont abordées en utilisant un convertisseur boost entrelacé à quatre branches (CBEQB), qui offre une réduction des ondulations, une efficacité améliorée et une adaptabilité aux applications de haute puissance.

Les algorithmes de suivi du point de puissance maximale (SPPM) basés sur la logique floue et la méthode de conductance incrémentale sont comparés, la logique floue démontrant des performances supérieures en termes de vitesse de convergence et de réduction des ondulations de tension. Des stratégies de contrôle non linéaires, notamment le backstepping (BS), le contrôle par mode glissant (CMG) et le contrôle par mode glissant super-twisting (CMGST), sont mises en œuvre et comparées aux contrôleurs traditionnels proportionnels-intégraux (PI) pour le FLIBC. Le CMGST présente les meilleures performances en éliminant le phénomène de chattering et en offrant une réponse rapide.

Pour l'intégration au réseau, une stratégie classique de contrôle direct de la puissance (CDP) utilisant une table de commutation est initialement explorée pour le système photovoltaïque multifonctionnel connecté au réseau (PMCR) basé sur le CBEQB. Ce système montre des performances supérieures par rapport au système PMCR basé sur le CBC, en particulier en termes de réduction des ondulations de puissance, de diminution des dépassements et de réduction de la distorsion harmonique. Ces améliorations mettent en évidence l'efficacité accrue et la fiabilité du système basé sur le CBEQB dans les applications photovoltaïques connectées au réseau.

Ensuite, une stratégie CDP améliorée, combinée à une modulation vectorielle (MV) et à un contrôleur BS optimisé par l'algorithme du loup gris (ALG), est proposée. Les résultats de simulation valident l'efficacité des schémas de contrôle proposés pour atteindre une régulation précise de la puissance, minimiser la distorsion harmonique, réduire les ondulations de puissance et améliorer la stabilité du réseau dans diverses conditions d'exploitation, notamment les variations de l'irradiation solaire et des charges. Le contrôleur BS optimisé par ALG démontre des performances supérieures par rapport aux contrôleurs PI dans la stratégie CDP-MV.

Cette recherche contribue au développement de solutions de contrôle robustes et efficaces pour l'intégration des systèmes PV dans les réseaux électriques modernes, ouvrant la voie à une meilleure qualité de l'énergie et à un avenir énergétique plus durable.

***Mots-clés:*** Photovoltaïque, système PV connecté au réseau, Backstepping, commande à mode glissant, convertisseur boost entrelacé, commande directe de puissance, optimiseur à loup gris.

# ملخص

تتناول هذه الأطروحة استراتيجيات التحكم المتقدمة لأنظمة الطاقة الكهروضوئية، مع التركيز على تحسين جودة الطاقة وفعالية حقن الطاقة في الشبكة. يتم معالجة قيود المحولات التعزيزية التقليدية من خلال استخدام محول تعزيز متداخل رباعي الأطراف ، الذي يوفر تموجًا أقل، وكفاءة محسّنة، وملاءمة للتطبيقات ذات الطاقة العالية.

تمت مقارنة خوارزميات المنطق الضبابي والتوصيل التزايدي لتعقب نقطة القدرة القصوى ، حيث أظهر المنطق الضبابي أداءً متفوقًا من حيث سرعة التقارب وتقليل التموج في الجهد. تم تنفيذ استراتيجيات التحكم غير الخطية، بما في ذلك التحكم المتراجع ، والتحكم بالانزلاق، والتحكم الفائق الالتواء بالانزلاق، ومقارنتها بالمتحكمات التقليدية ذات النسبية-التكاملية للمحول محول تعزيز متداخل رباعي الأطراف أظهر التحكم الفائق الالتواء بالانزلاق الأداء الأفضل من خلال القضاء على الاهتزاز وتحقيق استجابة سريعة.

بالنسبة لتكامل الشبكة، تم استكشاف استراتيجية التحكم المباشر في الطاقة التقليدية باستخدام جدول تبديل لأنظمة الطاقة الكهروضوئية المتعددة الوظائف المتصلة بالشبكة المعتمدة على محول تعزيز متداخل رباعي الأطراف. أظهرت الأنظمة المعتمدة على محول تعزيز متداخل رباعي الأطراف أداءً متفوقًا مقارنة بالأنظمة المعتمدة على محول التعزيز التقليدي، لا سيما من حيث تقليل تموج الطاقة، وخفض التجاوز، وتقليل التشوه التوافقي. تسلط هذه التحسينات الضوء على الكفاءة والموثوقية المعززة للنظام المعتمد على محول تعزيز متداخل رباعي الأطراف في تطبيقات الطاقة الكهروضوئية المتصلة بالشبكة.

لاحقًا، تم اقتراح استراتيجية التحكم المباشر في الطاقة محسّنة مدمجة مع تعديل متجه الفضاء ومتحكم المتراجع محسن باستخدام خوارزمية الذئب الرمادي. أكدت نتائج المحاكاة فعالية مخططات التحكم المقترحة في تحقيق تنظيم دقيق للطاقة، وتقليل التشوه التوافقي، وتقليل تموج الطاقة، وتعزيز استقرار الشبكة تحت ظروف تشغيلية مختلفة، بما في ذلك تغيرات الإشعاع الشمسي وتغيرات الأحمال. أظهر المتحكم المتراجع المحسّن بخوارزمية الذئب الرمادي أداءً متفوقًا مقارنة بالمتحكمات النسبية-التكاملية في استراتيجية التحكم المباشر في الطاقة القائمة على تعديل متجه الفضاء.

تسهم هذه الدراسة في تطوير حلول تحكم قوية وفعالة لدمج أنظمة الطاقة الكهروضوئية في شبكات الطاقة الحديثة، مما يمهد الطريق لتحسين جودة الطاقة ومستقبل أكثر استدامة للطاقة.

**الكلمات المفتاحية:** الخلايا الكهروضوئية، النظام الكهروضوئي المتصل بالشبكة، التقويم المتراجع، التحكم في الوضع المنزلق، محول التعزيز المتشابك، التحكم المباشر في الطاقة، خوارزمية الذئب الرمادي

# *List of Publications*

## *International Publications:*

D. E. O Mohamed Cherif, A. Chebabhi, A. Kessal, 'An Integral-Backstepping Controller for Interleaved Boost Converter based on Photovoltaic Systems', Electrotehnica, Electronica, Automatica (EEA), 71 (1), pp.13-21. Doi: 10.46904/eea.23.71.1.1108002

D. E. O Mohamed Cherif, A. Chebabhi, A. Kessal, 'Backstepping Based Grey Wolf and DPC for Power Quality Improvement and Active Power Injection in PV Grid-connected System Based on Interleaved Boost Converter', Periodica Polytechnica Electrical Engineering and Computer Science, 67 (3), pp. 268–280, 2023. Doi: 10.3311/PPee.21852

D. E. O Mohamed Cherif, A. Chebabhi, A. Kessal, 'GWO-super-twisting integral sliding mode control of 60 KW PV system based on interleaved boost converter', Engineering Review, 43 (2), 2023, pp. 68-79. Doi: 10.30765/er.2167

## *International Communications:*

D. E. O Mohamed Cherif, A. Chebabhi, A. Kessal, 'Four leg Interleaved DC/DC boost Converter based PV system using PSO Algorithm based PI controller', 19th International Multi-Conference on Systems, Signals & Devices (SSD), 06-10 May 2022, Setif, Algeria. Doi: 10.1109/SSD54932.2022.9955647

D. E. O Mohamed Cherif, A. Chebabhi, A. Kessal, M. F. Benkhoris, M, defdaf, 'Super-Twisting Sliding Mode Control of Interleaved Boost Converter Based Photovoltaic Applications', International Conference of Advanced Technology in Electronic and Electrical Engineering (ICATEEE), 26-27 November 2022, M'sila, Algeria. Doi: 10.1109/ICATEEE57445.2022.10093715

# *Table of Contents*

ACKNOWLEDGEMENT
ABSTRACT
LIST OF PUBLICATIONS
TABLE OF CONTENTS
LIST OF FIGURES
LIST OF TABLES
LIST OF ABBREVIATIONS AND SYMBOLS
GENERAL INTRODUCTION 1

CHAPTER I: AN OVERVIEW OF PHOTOVOLTAIC SYSTEMS FOR GRID-CONNECTED APPLICATIONS AND POWER QUALITY ENHANCEMENT

1 Introduction 6
2 Photovoltaic Systems 6
2.1 Photovoltaic Cells 6
2.2 Mathematical Modeling of PV Module 10
2.3 PV String and PV Array 11
2.4 Impact of Climatic Conditions on The Efficiency of PV Systems 13
2.5 Maximum Power Point Tracking Algorithms 15
3 Fundamentals of Grid-Connected PV System 21
3.1 GCPV Structure 22
3.2 Three-phase Three-wire GCPV topologies 26
3.3 Grid-Connection Standards and Recommendations 28
3.4 Grid Synchronization Technique 29
4 Power Quality Issue 30
4.1 Voltage Sags 30
4.2 Voltage Swells 31
4.3 Voltage Interruption 31
4.4 Voltage Imbalance 31
4.5 Voltage Flicker 32
4.6 Voltage Frequency Variation 32
4.7 Harmonics 32
5 Harmonics Sources, Impact and Mitigation Techniques 33
5.1 Sources and Impacts of Harmonics 33
5.2 Total Harmonics Distortion (THD) 34
5.3 IEEE Std-519 Standard for Harmonic Control in Electrical Power Systems 34
5.4 Harmonics Mitigating Techniques 35
6 Conclusion 40

CHAPTER II: STANDALONE PV SYSTEMS BASED ON IBC: DESIGN, CONTROL AND PERFORMANCE ANALYSIS

1 Introduction 42
2 Conventional Boost Converter 43
2.1 System Description and Modeling 43
2.2 Design of Conventional Boost Converter 45
2.3 Conventional Boost Converter Limitation 45
3 Four Legs Interleaved Boost Converter 46
3.1 System Description, Analysis and Modeling 46
3.2 Design of Interleaved Boost Converter 50

3.3 PV System Based on Four Legs Interleaved Boost Converter 51
4 Control Strategies 51
4.1 MPPT Controllers Design 52
4.2 Proportional Integral Controller 54
4.3 Backstepping Controller 56
4.4 Sliding Mode Controller 58
5 Simulation Results and Discussion 62
5.1 Performance Analysis of The FLIBC based on PI Controller 64
5.2 Performance Analysis of MPPT Algorithms 70
5.3 Performance Analysis of The FLIBC based on BS Controller 74
5.4 Performance analysis of The FLBIC based on SMC and STSMC 78
6 Conclusion 84

CHAPTER III: CLASSICAL CONTROL OF MULTIFUNCTIONAL GRID-CONNECTED PV SYSTEM BASED ON FLIBC

1 Introduction: 86
2 System Description and Modeling 87
2.1 Power Grid Modeling 87
2.2 Nonlinear Load (Three-Phase Uncontrolled Diode Rectifier) Modeling 88
2.3 Two-Level Voltage Source Inverter Modeling 88
3 Direct Power Control 90
3.1 Switching Table 91
3.2 DC-Bus Voltage Regulator Design 92
3.3 Phase Locked Loop Design 93
4 Simulation Results and Discussion 95
5 Conclusion 103

CHAPTER IV: DPC-SVM BASED ON GWO-BACKSTEPPING CONTROL OF MULTIFUNCTIONAL GRID-CONNECTED PV SYSTEM FED FLIBC

1 Introduction 106
2 Direct Power Control Based on Space Vector Modulation (DPC-SVM) 107
2.1 Active and Reactive Power Estimation 107
2.2 Power Control Loop Based on PI Controller 108
3 DPC-SVM Based on Backstepping Controller 110
3.1 Active and Reactive Power Controller based on BS Controller 110
3.2 DC-Bus Voltage Regulator Based on Optimized Anti-Windup PI Controller 112
4 Grey Wolf Optimizer Algorithm 113
5 Simulation Results and Discussion 115
6 Conclusion 124

GENERAL CONCLUSION 126
REFERENCES 128

# *List of Figures*

Figure I-1 Photovoltaic cell's p-n junction and n- and p-[4]. 7
Figure I-2 Silicon crystalline PV module: monocrystalline (a), polycrystalline (b). 7
Figure I-3 Thin-film PV module. 8
Figure I-4 Perovskites PV solar cell. 8
Figure I-5 Chart of best research-cell efficiencies from 1976 to 2022 provided by NRLE [19]. 9
Figure I-6 PV cell Single diode equivalent circuit. 10
Figure I-7 The electrical characteristic I-V and P-V curves of the PV module. 11
Figure I-8 PV system configuration: string (a), array (b). 12
Figure I-9 The electrical characteristic of the PV array. 12
Figure I-10 Solar radiation impact on I-V curve side view(a), top view (b), and P-V curve side view (c), top view (d). 13
Figure I-11 Temperature impact on I-V curve side view(a), top view (b), and P-V curve side view (c), top view (d). 14
Figure I-12 Partial shading impact on I-V curve (a), P-V curve (b). 15
Figure I-13 Conventional P&O flow chart. 16
Figure I-14 The flow chart of the incremental conductance algorithm. 17
Figure I-15 Phase portrait of a first-order sliding mode controller. 18
Figure I-16 Example of the structure of ANNs-based MPPT. 19
Figure I-17 Fuzzy logic controller’s block diagram. 19
Figure I-18 Particle swarm optimization algorithm. 20
Figure I-19 The main steps of the genetic algorithm. 21
Figure I-20 Grid-connected PV system classification based on power rating: small-scale (Sultan Qaboos University – Oman) (a), medium-scale (Jaen University – Spain) (b), and large-scale (Bhadla Solar Park– India) (c). 22
Figure I-21 GCPV system based on Central inverter: series (a), parallel (b), series-parallel (c), total-cross-tied (d), bridge linked (e), and honey-comb (f). 23
Figure I-22 GCPV system based on string inverter topology. 24
Figure I-23. GCPV system based on the multi-string inverter. 24
Figure I-24 GCPV based on AC module inverter. 25
Figure I-25 Schematics of the Single-stage (a) and Dual-stage GCPV. 25
Figure I-26 Two-level dual-stage GCPV system. 26
Figure I-27 Three-level dual-stage NPC GCPV system. 27
Figure I-28 Operating state of one leg of an NPC inverter: P (a), O (b), and N (c). 27
Figure I-29 Three-level T-type NPC GCPV system. 28
Figure I-30 The basic structure of PLL. 29
Figure I-31 The basic structure of SRF-PLL. 30
Figure I-32 Voltage sags waveform. 31
Figure I-33 Voltage swell waveform. 31
Figure I-34 Voltage interruption waveform. 31
Figure I-35 Voltage imbalance waveform. 32
Figure I-36 Voltage flicker waveform. 32
Figure I-37 Voltage frequency variation waveform. 32
Figure I-38 Example of a sinusoidal distorted waveform, its fundamental, and some harmonic components. 33
Figure I-39 PFs connection to the grid. 36

Figure I-40 Passive filter types: single tuning filter (a), first order (b), second order (c), and third order (d). 36
Figure I-41 Active filter topologies: SEAPF (a), SAPF (b), UPQC (c), series SEAPF and PF, in parallel with load (d); SEPAF and PF in parallel with load (e), parallel SAPF and PF, in parallel with load (f). 39
Figure I-42 The structure of the multifunctional grid-connected photovoltaic system. 40
Figure II-1 Conventional boost converter circuit. 43
Figure II-2 Conventional boost converter operating modes: switch closed (a), switch opened (b). 44
Figure II-3 Conventional boost converter waveforms. 44
Figure II-4 Four Legs interleaved boost converter circuit. 46
Figure II-5 FLIBC current waveforms (d=0.25). 47
Figure II-6 FLIBC current waveforms (d=0.375). 47
Figure II-7 FLIBC current waveforms (d=0.5). 47
Figure II-8 FLIBC current waveforms (d=0.675). 47
Figure II-9 FLIBC current waveforms (d=0.75). 47
Figure II-10 Normalized IBC input current ripple compared to CBC. 49
Figure II-11 Normalized output voltage ripple of the IBC compared to CBC. 50
Figure II-12 PV system fed four legs IBC. 51
Figure II-13 General scheme of the double loop control strategy. 52
Figure II-14 Fuzzy logic membership functions. 53
Figure II-15 PI Control scheme of PV system fed FLIBC. 56
Figure II-16 BS controller scheme for PV system fed FLIBC. 58
Figure II-17 SMC Control scheme of PV system fed FLIBC. 61
Figure II-18 ST-SMC Control scheme of PV system fed FLIBC. 62
Figure II-19 Simulation profile of the irradiation (a) and the temperature (b). 64
Figure II-20 The voltage of the PV system based on CBC. 65
Figure II-21 The voltage of the PV system based on FLIBC. 66
Figure II-22 The PV system current using the FLIBC and CBC. 67
Figure II-23 Converters input current $I_{IN}$. 68
Figure II-24 Equal current sharing between FLIBC legs. 68
Figure II-25 PV system produced power. 69
Figure II-26 Output voltage and current of the FLIBC compared with CBC. 70
Figure II-27 The curve of PV system voltage: InC (a) and Fuzzy logic (b) 71
Figure II-28 Zoom on Zone A and B of the curve of PV system voltage: InC (a) and Fuzzy logic (b) 72
Figure II-29 Zoom on Zone C and D of the curve of PV system voltage: InC (a) and Fuzzy logic (b). 73
Figure II-30 The PV system power curves using the InC and Fuzzy logic MPPT algorithms. 74
Figure II-31 PV system’s voltage curve using BS controller. 75
Figure II-32 PV system’s current curves using BS controller and PI controller. 76
Figure II-33 PV system’s power curves using BS controller and PI controller. 77
Figure II-34 Equal current sharing between FLIBC legs using BS controller. 78
Figure II-35 PV system's voltage curve using SMC. 80
Figure II-36 PV system's voltage curve using ST-SMC 81
Figure II-37 PV system's current curves using ST-SMC and SMC. 82
Figure II-38 PV system's power curve using ST-SMC and SMC. 83
Figure II-39 Equal current sharing between FLIBC legs using SMC. 83
Figure II-40 Equal current sharing between FLIBC legs using ST-SMC. 83
Figure III-1 Multifunctional Grid-Connected PV System basic configuration. 87

Figure III-2 AC power supply circuit. 88
Figure III-3 Nonlinear load: Three-phase full-wave rectifier circuit. 88
Figure III-4 2L-VSI circuit. 89
Figure III-5 Conventional direct power control of MGCPV system. 91
Figure III-6 Voltage space vector. 92
Figure III-7 The block diagram of the DC bus voltage regulator based on the PI controller. 92
Figure III-8 Conventional three-phase PLL block. 93
Figure III-9 STF-PLL block. 94
Figure III-10 The voltage sensed at PCC (a), the output of the conventional PLL (b), and the output of the STF-PLL (c). 94
Figure III-11 The phase angle (theta) detected by conventional PLL (a) and STF-PLL (b). 95
Figure III-12 Solar irradiation profile. 95
Figure III-13 DC bus voltage of the MGCPV based on conventional DPC. 97
Figure III-14 The MGCPV active and reactive power using CBC. 99
Figure III-15 The MGCPV active and reactive power using FIBC. 100
Figure III-16 The grid A-phase voltage and current using CBC. 101
Figure III-17 The grid A-phase voltage and current using FLIBC. 102
Figure III-18 Grid current spectrum before activating the MGCPV. 102
Figure III-19 Grid current spectrum after activating the MGCPV without a PV system. 103
Figure III-20 Grid current spectrum after activating the MGCPV with a PV system: CBC (a) and FLIBC (b). 103
Figure IV-1 d-axis aligned with the voltage vector. 108
Figure IV-2 Block diagram of the power control loop based on PI controller. 109
Figure IV-3 DPC-SVM strategy based on PI controller. 110
Figure IV-4 The block diagram of the power control loop is based on the optimized BS controller. 112
Figure IV-5 DPC-SVM strategy based on BS controller. 112
Figure IV-6 DC Bus voltage regulator based on GWO-Anti-Windup PI controller. 113
Figure IV-7 The flowchart of the grey wolf optimization algorithm. 114
Figure IV-8 The behavior of the OF $f_1$ during the power loop optimizing process. 115
Figure IV-9 The behavior of the OF $f_2$ during the DC bus voltage optimizing process. 115
Figure IV-10 Solar irradiation profile. 116
Figure IV-11 DC bus voltage of the MGCPV. 117
Figure IV-12 Grid's Active and Reactive power using MGCPV based on PI controller. 119
Figure IV-13 Grid's Active and Reactive power using MGCPV based on optimized BS controller. 120
Figure IV-14 Grid voltage and current of A-phase using PI controller. 121
Figure IV-15 Grid voltage and current of A-phase using the optimized BS controller. 122
Figure IV-16 Grid current spectrum before inserting the MGCPV system. 123
Figure IV-17 Grid current spectrum after activating the MGCPV without a PV system: PI controller (a) and GWO BS(b). 123
Figure IV-18 Grid current spectrum after inserting the MGCPV system with PV system using PI controller. 123
Figure IV-19 Grid current spectrum after inserting the MGCPV system with PV system using GWO-BS controller. 123

# *List of Tables*

Table I-1 A detailed comparison between the central-, string, multi-string- and AC module inverter [107]. 25
Table I-2 Single-stage and Dual-Stage topologies comparison. 26
Table I-3 Switching states and output voltage of two-level inverter. 26
Table I-4 The operating state and the output voltage of one leg of an NPC inverter. 27
Table I-5 Comparison between 2L-VSI and 3LNOC-VSI topologies. 28
Table I-6 Several international standards for the PV systems integration in the grid [124]. 29
Table I-7 Current distortion limits for general distribution systems (120 V - 69 KV). 35
Table I-8 Current distortion limits for general sub-transmission systems (69.001 kV - 161 kV). 35
Table I-9 Current distortion limits for general transmission systems, >161 kV. 35
Table I-10 Voltage distortion limits. 35
Table I-11 The main features of power filters [137], [147]. 39
Table II-1 Fuzzy MPPT rules. 54
Table II-2 PV system parameters. 63
Table II-3 The CBC and FLIBC parameters. 63
Table II-4 Parameters of the proposed controllers. 63
Table II-5 Comprehensive comparison of the control strategies. 84
Table III-1 Voltage vectors of 2L-VSI 89
Table III-2 Switching table of the DPC. 92
Table III-3 Simulation parameters. 95
Table IV-1 Simulation parameters. 116
Table IV-2 Comprehensive comparison of the performance standards between an Optimized BS and PI controller. 124

# *List of Abbreviations and Symbols*

***List of Abbreviations***

| | |
|---|---|
| Active Power Filters | APF |
| Artificial Neural Network | ANN |
| Backstepping Controller | BS |
| Conventional Boost Converter | CBC |
| Direct Current | DC |
| Direct Power Control | DPC |
| First-Order Sliding Mode Control | FOSMC |
| Four-Legs Interleaved Boost Converter | FLIBC |
| Genetic Algorithms | GA |
| Grey Wolf Optimizer | GWO |
| Grid-Connected PV | GCPV |
| Incremental Conductance | IC |
| Interleaved Boost Converter | IBC |
| Kirchhoff's Current Law | KCL |
| Kirchhoff's Voltage Law | KVL |
| Maximum Power Point | MPP |
| Maximum Power Point Tracking | MPPT |
| Multifunctional Grid-Connected PV | MGCPV |
| Particle Swarm Optimization | PSO |
| Passive Filters | PF |
| Perturb and Observe | P&O |
| Phase-Locked Loop | PLL |
| Photovoltaic | PV |
| Point of Common Coupling | PCC |
| Power Conversion Efficiencies | PEC |
| Proportional Integrator controller | PI |
| Renewable Energy Resources | RER |
| Self-Tuning Filter | STF |
| Series Active Power Filter | SEAPF |
| Shunt Active Power Filter | SAPF |
| Single-Diode Model | SD |
| Sliding Mode Control | SMC |
| Space Vector Modulation | SVM |
| Standard Test Conditions | STC |
| Synchronous Reference Frame | SRF |
| The Global Maximum Power Point | GMPP |
| Third-Order Sliding Mode Control | TOSMC |
| Total Harmonic Distortion | THD |
| Unified Power Quality Conditioner | UPQC |
| Voltage Source Inverter | VSI |
| Voltage-Oriented Control | VOC |

***List of Symbols***

| | |
|---|---|
| Active power (W) | $P$ |
| Active power reference (W) | $P_{ref}$ |
| Boltzmann constant (J/K) | $k$ |
| BS controller's gains of the boost converters | $K_1$, $K_2$, $\lambda_1$, $\lambda_2$ |
| Converter input current (A) | $I_{IN}$ |
| Converter output current (A) | $I_O$ |
| Converter output voltage (V) | $V_O$ |
| DC bus capacitor (F) | $C_{DC}$ |
| DC bus voltage (V) | $V_{DC}$ |
| DC bus voltage's PI controller gains | $K_{pdc}$, $K_{idc}$, $K_A$ |
| Duty cycle | $d$ |
| Electron charge (C) | $q$ |
| FLIBC's inductors (H) | $L_1$, $L_2$, $L_3$, $L_4$ |
| FLIBC 's inductors current (A) | $I_{L1}$, $I_{L2}$, $I_{L3}$, $I_{L4}$ |
| Grid currents (A) | $I_{sa}$, $I_{sb}$, $I_{sc}$ |
| Grid side inductor (H) | $L_s$ |
| Grid side resistor (Ω) | $R_s$ |
| Grid voltages (V) | $V_{sa}$, $V_{sb}$, $V_{sc}$ |
| Ideality factor of the diode | $\alpha$ |
| Inductor’s current (A) | $I_L$ |
| Inductor’s voltage (V) | $V_L$ |
| Input capacitor of the converter (F) | $C_{IN}$ |
| MGCPV's coupling inductor (H) | $L_f$ |
| MGCPV's coupling resistor (Ω) | $R_f$ |
| Nonlinear load inductor (H) | $L$ |
| Nonlinear load resistor (Ω) | $R$ |
| Nonlinear side inductor (H) | $L_c$ |
| Nonlinear side resistor (Ω) | $R_c$ |
| Number of parallel PV modules | $N_{pm}$ |
| Number of series cells in the PV module | $n_s$ |
| Number of series PV modules | $N_{sm}$ |
| Number of the IBC legs | $N$ |
| Open circuit voltage of the PV system in STC (V) | $V_{OC\text{-}STC}$ |
| Open circuit voltage temperature coefficient (V/K) | $K_V$ |
| Open-circuit voltage of the PV system (V) | $V_{OC}$ |
| Output capacitor of the converter (F) | $C_O$ |
| Output power of PV system (W) | $P_{PV}$ |
| PCC voltage (V) | $V_a$, $V_b$, $V_c$ |
| Photo-generated current (A) | $I_{ph}$ |
| Photo-generated current in the STC (A) | $I_{Ph\text{-}STC}$ |
| PI controller's gains of the boost converters | $K_{pv}$, $K_{iv}$, $K_{pc}$, $K_{ic}$ |
| PV cell diode current (A) | $I_D$ |
| PV cell equivalent parallel resistor (Ω) | $R_P$ |
| PV cell equivalent series resistor (Ω) | $R_S$ |
| PV cell output voltage (A) | $V_{PV}$ |

| | |
|---|---|
| PV cell parallel resistor current (A) | $I_P$ |
| PV module current at MPP (A) | $I_{MPP}$ |
| PV module power at maximum power point (W) | $P_{MPP}$ |
| PV module voltage at MPP (A) | $V_{MPP}$ |
| PV system output current (A) | $I_{PV}$ |
| Reactive power (VAR) | $Q$ |
| Reactive power reference (VAR) | $Q_{ref}$ |
| Saturation current of the diode (A) | $I_{SD}$ |
| Sampling time (s) | $T_s$ |
| Short circuit current of the PV system in STC (A) | $I_{SC\text{-}STC}$ |
| Short-circuit current of the PV system (A) | $I_{SC}$ |
| Short-circuit current temperature coefficient (A/K) | $K_I$ |
| Smc's gains of the boost converters | $K_3$, $K_4$, $\lambda_3$, $\lambda_4$ |
| Solar irradiation (W/m²) | $G$ |
| Solar irradiation in STC (W/m²) | $G_{STC}$ |
| Stsmc's gains of the boost converters | $\lambda_5$, $\lambda_6$, $\alpha_1$, $\alpha_2$, $\beta_1$, $\beta_2$ |
| Switching frequency (Hz) | $f_{SW}$ |
| Temperature of the PV cell (Kelvin) | $T$ |
| Temperature of the PV cell in STC (Kelvin) | $T_{STC}$ |
| The cell junction thermal potential (V) | $Vt$ |
| The current direct and quadratic components (A) | $I_d$, $I_q$ |
| The voltage direct and quadratic components (V) | $V_d$, $V_q$ |
| Time (s) | $t$ |
| VSI current (A) | $I_{fa}$, $I_{fb}$, $I_{fc}$ |
| VSI voltage (V) | $V_{fa}$,$V_{fb}$,$V_{fc}$ |

# General Introduction

The global transition toward sustainable energy systems has placed photovoltaic (PV) technology at the forefront of renewable energy integration. Grid-connected PV (GCPV) systems are becoming increasingly prevalent due to their potential to generate clean, reliable, and decentralized electricity [1]. These systems play a critical role in facilitating the integration of solar energy into the grid by ensuring efficient energy transfer. Additionally, GCPV systems can support ancillary services such as harmonic mitigation, reactive power compensation, and voltage regulation in utility grids [2].

However, this widespread adoption presents significant challenges, particularly concerning power quality [3]. Voltage instability, harmonic distortions, and grid synchronization issues are among the critical hurdles that compromise the performance and reliability of electrical grids [4]. The intermittency of solar energy exacerbates these challenges, as does the dynamic nature of grid conditions and the prevalence of widespread nonlinear loads. These factors necessitate the development of advanced control strategies and converter topologies capable of handling high-power rates. Addressing these issues is paramount for ensuring the seamless integration of PV systems into modern electrical grids, ultimately supporting a more resilient and sustainable energy future.

Conventional boost converters (CBC) have been widely used in PV systems due to their simplicity and cost-effectiveness [5], [6]. However, they exhibit several limitations when addressing the stringent requirements of modern grid-connected PV systems. These converters often suffer from high switching losses, significant current ripple, and limited efficiency, particularly under high power and dynamic operating conditions [7]. Additionally, the single-phase design of CBCs can lead to poor thermal management and increased stress on the components, ultimately reducing their reliability and lifespan. To overcome these drawbacks, the interleaved boost converter (IBC) presents a promising alternative. By distributing the input current across multiple phases, IBCs significantly reduce ripple, enhance thermal performance, and improve overall efficiency [8]. Furthermore, the structure of IBCs allows for better scalability and fault tolerance [9], [10], making them well-suited for both standalone and grid-connected PV applications. The use of IBCs addresses many of the challenges associated with conventional designs, offering a robust and efficient solution for modern PV systems.

Reliable Maximum power point tracking (MPPT) control strategies are crucial for maximizing the efficiency of PV systems, especially under varying environmental conditions. Traditional techniques, such as perturb and observe (P&O) [11] and incremental conductance (IC) [12], are commonly used due to their simplicity and ease of implementation. However, these methods often exhibit limitations, such as oscillations around the maximum power point, slow convergence under rapid changes in irradiance, and reduced tracking accuracy in partial shading conditions. In contrast, advanced strategies such as fuzzy logic-based MPPT [13], artificial neural network (ANN) MPPT [14], and bio-inspired

MPPT [15] provide superior performance compared to conventional techniques. One of the advantages of fuzzy logic-based MPPT is that it deals with the nonlinearity and uncertainties that characterize a PV system thanks to the fuzzy rules used in its operation, making it faster and more accurate in tracking the maximum power point (MPP) without the need for detailed system modeling [16]. These advanced MPPT techniques not only improve energy harvesting efficiency but also enhance the overall reliability and stability of PV systems, making them indispensable for modern applications.

In addition to reliable MPPT strategies, the implementation of robust control techniques for converters, particularly the IBC, is crucial for ensuring optimal performance in PV systems. The IBC's multi-phase structure requires precise control to maintain equal current sharing between its phases [17], which is essential for minimizing component stress and ensuring long-term reliability. Conventional PI controllers, while simple and widely used [18], often struggle to achieve the desired performance under dynamic conditions and fail to address the nonlinearities inherent in modern converters. Nonlinear control strategies, such as backstepping (BS) control [19], sliding mode control (SMC) [20], and super-twisting control (STSMC)[21], offer significant advantages by providing improved robustness, faster dynamic response, and enhanced disturbance rejection. These advanced techniques not only ensure equal current sharing in the IBC but also enhance the overall stability and efficiency of the PV system, making them critical components of modern control architectures.

The control strategies for grid-connected PV systems play a pivotal role in ensuring effective power quality management and reliable operation under dynamic grid conditions. Among these strategies, the instantaneous active and reactive power theory (PQ theory) [22], the synchronous reference frame (SRF) method [23], voltage-oriented control (VOC) [24] and Direct power control (DPC) [25], [26] are widely recognized. The DPC strategy has gained prominence due to its ability to directly regulate active and reactive power by employing a hysteresis comparator and switching table without using control loops. However, conventional DPC methods based on switching tables have limitations, including high power ripple, variable switching frequency, and high computational requirements. To address these drawbacks, an alternative DPC structure utilizing space vector modulation (SVM) has been proposed [27], offering smoother switching transitions, improved harmonic performance, and enhanced control precision. Moreover, the performance of power loop controllers within these systems is crucial. While PI controllers are commonly used [28], they often exhibit limitations in robustness and adaptability under grid disturbances. Alternative controllers, such as H-infinity controllers [29], sliding mode controllers [30], and backstepping controllers [31], have been introduced to overcome these challenges. These advanced control strategies provide superior disturbance rejection, faster response times, and improved stability, making them integral to modern grid-connected PV system designs.

The advantages of the backstepping controller have made it a popular choice for ensuring the precise and robust control of converters in PV systems. Its systematic design process, rooted in Lyapunov stability theory, enables it to handle nonlinearities and uncertainties effectively, providing excellent disturbance rejection and fast dynamic response [32]. By offering superior performance

compared to conventional control strategies, backstepping control has established itself as a robust solution for enhancing the efficiency and reliability of PV systems under dynamic operating conditions [19].

The application of meta-heuristic algorithms, such as particle swarm optimization (PSO) [33], genetic algorithms (GA) [34], and grey wolf optimizer (GWO) [35], has gained significant attention in optimizing the performance of PV systems [36], [37], [38], [39]. These algorithms are particularly effective in addressing complex, nonlinear, and multi-objective optimization problems inherent in modern PV system control. By fine-tuning control parameters, such as MPPT gains or converter controller settings, meta-heuristic algorithms enhance system efficiency, improve dynamic response, and ensure robust performance under varying environmental and grid conditions. Their adaptability and global search capabilities make them indispensable tools for advancing the state-of-the-art in PV system optimization, contributing to more reliable and sustainable energy solutions.

The primary objective of this research is to develop and validate advanced control strategies and converter designs aimed at improving the power quality and operational efficiency of both standalone and GCPV systems. To address the limitations of conventional topologies, this thesis proposes the adoption of IBC, which offers superior performance in terms of reduced ripple, fast response time, fault tolerance, and scalability. Complementing these hardware innovations, the study introduces advanced control strategies, including nonlinear controllers such as backstepping and sliding mode control, which provide enhanced robustness and dynamic response compared to traditional PI controllers. Additionally, the research focuses on the integration of fuzzy logic-based MPPT to optimize energy harvesting under varying environmental conditions. For grid-connected systems, the thesis emphasizes the use of a DPC approach, leveraging SVM to overcome the limitations of conventional switching table methods and employing the GWO to fine-tune controller parameters for optimal performance. These contributions collectively aim to mitigate harmonic distortions, ensure reliable grid synchronization, and enhance system stability under dynamic grid conditions.

This work begins with a comprehensive review of existing PV grid-integration architectures, emphasizing the power quality challenges and the limitations of current solutions. It identifies key gaps in the literature and sets the foundation for the proposed research. The focus then shifts to standalone PV systems utilizing IBC, comparing the fuzzy logic MPPT with classical techniques and demonstrating their superior tracking efficiency and adaptability. Additionally, the advantages of nonlinear controllers, such as BS control and SMC over conventional PI controllers, in enhancing system stability and performance are highlighted.

The research further transitions to grid-connected PV systems employing IBC, evaluating the performance of the classical DPC method with switching tables and the role of PI controllers in regulating DC bus voltage. A novel converter topology, IBC, is introduced to mitigate the drawbacks of traditional designs, such as high ripple and limited scalability. Finally, a control strategy combining DPC with SVM and a GWO-optimized BS controller is presented. This approach replaces PI controllers

in power loops, enhancing system stability and power quality under grid disturbances and demonstrating the effectiveness of the proposed strategy in optimizing harmonic mitigation and reactive power compensation.

The findings of this research present a holistic framework for improving the power quality of PV systems in modern electrical grids. The proposed innovations contribute to enhancing grid resilience, minimizing harmonic distortions, and enabling sustainable PV integration. Simulation tools, such as MATLAB/Simulink, are extensively used for validation, providing a robust platform to demonstrate the efficacy of the proposed methods. By addressing the identified gaps and challenges, this research advances the state-of-the-art in PV system control and converter design, paving the way for a more reliable and sustainable energy future.

# *Chapter I:*

## *An Overview of Photovoltaic Systems for Grid-Connected Applications and Power Quality Enhancement*

## 1 Introduction:

The rise in global energy consumption raises significant concerns regarding global warming caused by greenhouse gas emissions and the degradation of fossil fuel reserves. In this context, it is essential to focus on economic growth that respects sustainability principles. The modern generation of power systems prioritize the utilization of abundant, cost-effective, and clean energy resources called renewable energy resources (RERs) to produce environmentally friendly energy. Among these resources, solar energy is receiving extensive attention due to its benefits, such as sustainability, availability, and pollution-free operation [40]. The amount of solar energy that falls on the Earth is rated at about 175 petawatts ($175 \times 10^{12}$ KW) [41].

Over the past few years, many distributed generation systems have been integrated into the electrical grid, mainly aimed at boosting renewable energy production. From the various forms of energy, solar power integration refers to establishing a network that incorporates the sun's electricity into the utility grid. The integration of solar systems into grids is a significant technological advancement. It plays a crucial role in optimizing the energy balance of buildings, enhancing the economy, minimizing operating expenses, and offering additional benefits to consumers and utility providers. A GCPV system harnesses solar energy using PV panels, connects to the utility grid, benefits from energy exchange, and enhances grid stability, promoting sustainable and reliable renewable energy integration [39].

This chapter's organization is as follows: the 2nd section discusses the technologies of PV panels, their simulation modules, the impact of weather conditions on the PV panel performance, and the algorithms of maximum power tracking. The 3rd section overviews the grid-connected, including their structure, standards and recommendations, and synchronization techniques. In the 4th section, the power quality issues will be discussed in detail. The harmonics sources, their impact on the power systems, and the mitigation techniques will be shown in the 5th section.

## 2 Photovoltaic Systems:

Among the possible approaches for harvesting solar energy is the PV process, which involves converting solar radiation into electrical energy. PV energy is a sustainable and environmentally friendly source that does not deplete natural resources. Renewable energy is critical for effectively meeting the world's growing energy demands while mitigating greenhouse gas emissions and reducing pollution.

### 2.1 Photovoltaic Cells:

#### 2.1.1 The PV Cell Working Principle:

A PV cell is the fundamental component of a solar energy generation system, directly converting sunlight into electrical energy without involving a mechanical engine. PV cells are composed of p-n junctions. The presence of negatively charged electrons contributed by impurity elements functioning as donors can be recognized by the term "n-type." On the contrary, the designation p-type signifies the

presence of positively charged holes generated by acceptor impurity atoms. Stacking an n-type semiconductor layer on top of a p-type semiconductor layer forms a PV cell. In addition, a third area, known as a junction, forms between the two surfaces. Eventually, the electric field generated across the junction by the dispersed charges on the surfaces of the n and p-type materials stops the diffusion process. Considering the structure of the photovoltaic cell, light acts as an external energy source to generate an electric current. This description is in accordance with the PV structure depicted in Figure I-1.

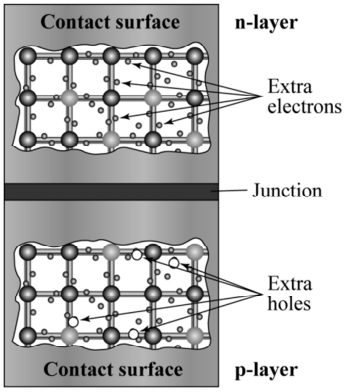


***Figure I-1 Photovoltaic cell's p-n junction and n- and p-***[42].

### *2.1.2 Type of PV Cell:*

**Silicon crystalline:** The first generation of solar PV cells comprises crystalline-silicon-based cells, including monocrystalline (m-crystalline) and polycrystalline (p-crystalline) variants (Figure I-2). The brand name given to photovoltaic cells that consist of crystalline silicon derives from their manufacturing process [43]. The monocrystalline cell is widely utilized, with over 80% of the market, and is expected to maintain its dominance until the development of a more efficient and economically competitive photovoltaic technology [44].

**(a)** **(b)**

***Figure I-2 Silicon crystalline PV module: monocrystalline (a), polycrystalline (b).***

**Thin-film:** The second generation is Thin-film solar cells (Figure I-3), which are more cost-effective because they require fewer components and a simpler production process than their crystalline

silicon counterparts [45]. The solar cell manufactured using this method is very thin (range of 35 to 260 nm) due to the reduced amount of material used. The main approaches of thin-film technology of PV cells are:

Amorphous Silicon.

Cadmium Telluride.

Gallium Arsenide.

Copper Indium Gallium Selenide.

**Emerging technologies:** Researchers are investigating third-generation photovoltaic technologies as an alternative to silicon solar cells. Third-generation solar cells (such as tandem cells, emerging concepts, dye-sensitized cells, perovskites (Figure I-4), and organic cells) take a wide variety of approaches, ranging from economic low-efficiency systems (such as organic solar cells) to costly high-efficiency systems (such as III-V multi-junction cells) with uses varying from building integration to space exploration [46], [47].

***Figure I-3 Thin-film PV module.***

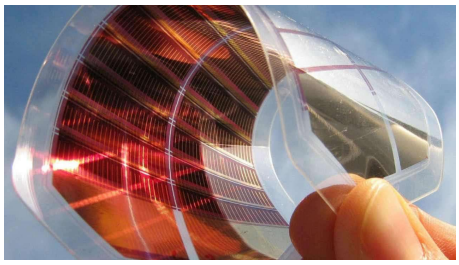

***Figure I-4 Perovskites PV solar cell.***

As depicted in Figure I-5, the power conversion efficiencies of emerging photovoltaic technologies have increased significantly in recent years due to the increased scientific interest in their development.

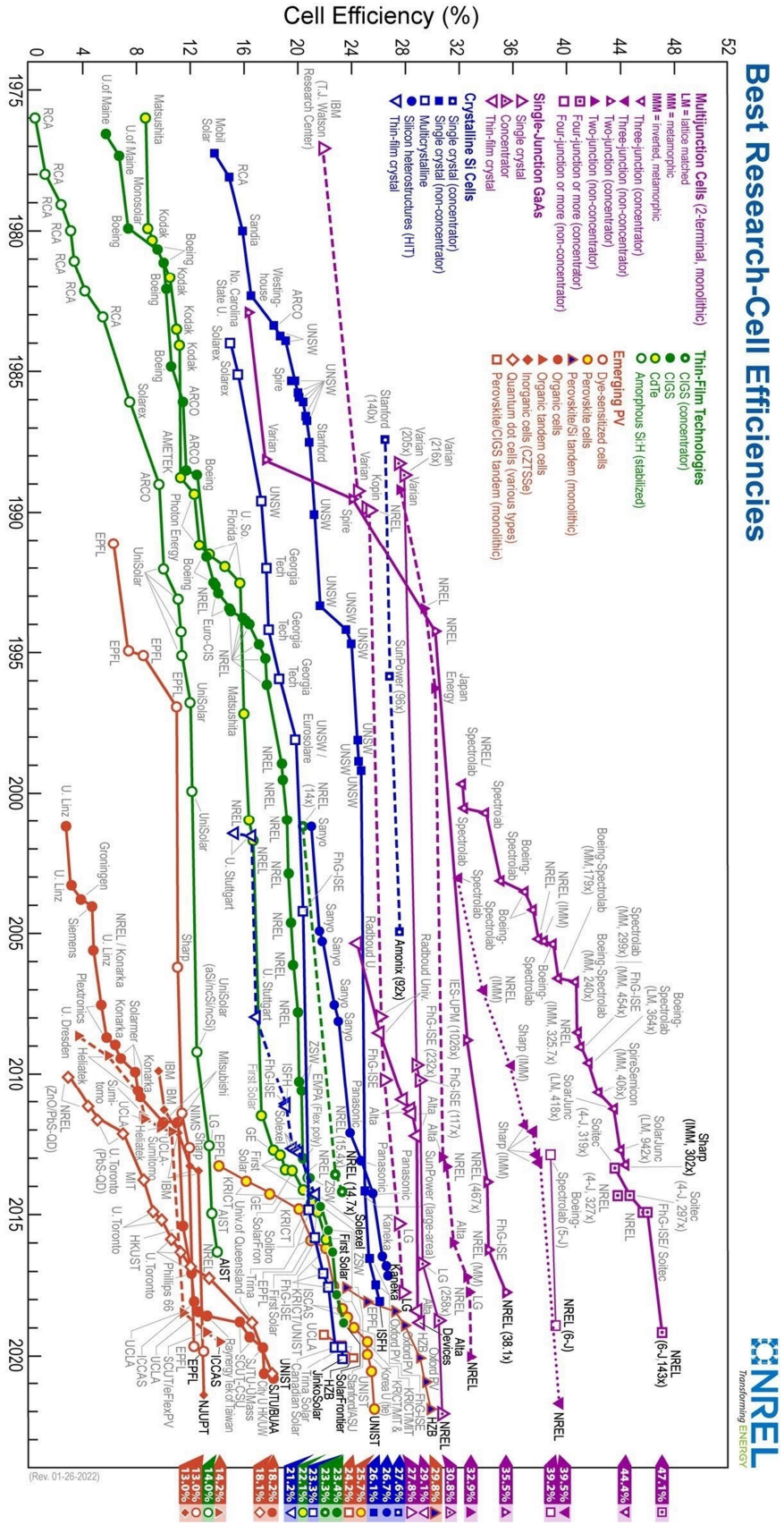


***Figure I-5 Chart of best research-cell efficiencies from 1976 to 2022 provided by NRLE*** [48]**.**

## 2.2 Mathematical Modeling of PV Module:

To simulate the nonlinear I-V characteristics of solar PV modules under various operating conditions (irradiance and temperature), in the literature, numerous equivalent circuits have been presented [49], [50], [51], [52], [53]. The single-diode (SD) [54] model is commonly used to simulate the characteristics of solar modules. The SD model consists of several electrical components, as Figure I-6 illustrates. The photo-generated current $I_{ph}$, which depends on temperature and solar radiation, is modeled as a current source. Furthermore, to simulate the semiconductor p-n junction, researchers employ an ideal diode connected in parallel with the current source. In addition, series and parallel resistors represent the internal cell resistance and the diode leakage current [55].

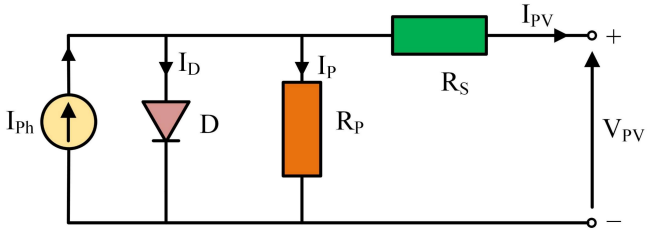


***Figure I-6 PV cell Single diode equivalent circuit.***

The PV module output current can be computed using the following equation [56]:

$$I_{PV} = I_{Ph} - I_D - I_P \tag{1.1}$$

$I_{PV}$, $I_{Ph}$, $I_D$, and $I_P$ denote the PV module's output current, the photo-generated current, the diode current, and the parallel resistor current, respectively. The photo-generated current $I_{Ph}$ by the PV module depends on the solar irradiance and temperature [55]:

$$I_{Ph} = \frac{G}{G_{STC}}\left(I_{Ph-STC} + K_I\left(T - T_{STC}\right)\right) \tag{1.2}$$

Where $K_I$ is the short-circuit current temperature coefficient (A/K), $G$ and $G_{STC}$ **= 1000 W/m²** define the solar irradiation (W/m²) and its nominal value in the standard test conditions (STC). $T$ and $T_{STC}$ **= 298.15 K** are the temperature and its nominal value in the STC in Kelvin (**K**), respectively.

$I_{Ph\text{-}STC}$ is the photo-generated current in the STC, and its value is approximately equal to the PV module short circuit current in STC. Equation (1.3) expresses the diode current using the Shockley equation [57]:

$$I_D = I_{SD}\left(\exp\left(\frac{V_{PV} + I_{PV}R_S}{\alpha V_t}\right) - 1\right) \tag{1.3}$$

Where $I_{SD}$ represents the diode's saturation current, $R_S$ is the series equivalent resistor, and $V_{PV}$ denotes the cell output voltage. $\alpha$ is the ideality factor of the diode, and $V_t$ is the cell junction thermal potential, which is given by [58]:

$$V_t = \frac{n_S kT}{q} \tag{1.4}$$

$k$= **1.38x10$^{-23}$ J/K** is the Boltzmann constant, $q$= **1.6x10$^{-19}$ C** represents the electron charge, and $n_S$ is the number of series cells in the PV module. In addition, the value of the saturation current of the diode $I_{SD}$ related to the solar radiation and cell temperature can be calculated using the following formula [59], [60]:

$$I_{SD} = \frac{I_{SC-STC} + K_I\left(T - T_{STC}\right)}{\exp\left(\frac{V_{OC-STC} + K_V\left(T - T_{STC}\right)}{\alpha V_t}\right) - 1} \tag{1.5}$$

Where $I_{SC\text{-}STC}$ is the short circuit current of the cell in STC, $V_{OC\text{-}STC}$ is the open circuit voltage in STC, and $K_V$ is the open circuit voltage temperature coefficient (V/K).

Using Kirchhoff's law, the parallel resistance current $I_P$ can be calculated as follows:

$$I_P = \frac{V_{PV} + R_S I_{PV}}{R_P} \tag{1.6}$$

Therefore, we can write equation (1-1) which describes the I-V characteristic of the PV module as:

$$I_{PV} = \frac{G}{G_{STC}}\left(I_{Ph-STC} + K_I\left(T - T_{STC}\right)\right) - I_{SD}\left(\exp\left(\frac{V_{PV} + I_{PV}R_S}{\alpha V_t}\right) - 1\right) - \frac{V_{PV} + R_S I_{PV}}{R_P} \tag{1.7}$$

Figure I-7 illustrates an example of the electrical characteristics of a PV panel. The figure shows the current-voltage (I-V) and power-voltage (P-V) curves. From the figure, $P_{MPP}$, $V_{MPP}$, and $I_{MPP}$ denote the panel's power in the maximum power point (MPP), the voltage in the MPP, and the current in the MPP, respectively.

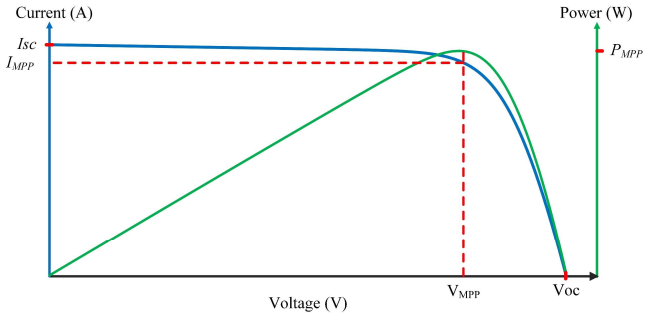


***Figure I-7 The electrical characteristic I-V and P-V curves of the PV module.***

### *2.3 PV String and PV Array:*

High-power applications with high voltage and/or current require a high-power source. PV strings or PV arrays (Figure I-8) are PV systems that consist of multi-PV panels, allowing high electrical power generation.

PV string is a number of PV panels wired in a series set. The aim of establishing a PV string is to raise the voltage of the PV system. The string's voltage is the sum of the PV panel's voltage and has the same current. Equations (1.8) and (1.9) formulate the PV string voltage and current:

$$V_{PV-string} = V_{PV} N_{sm} \tag{1.8}$$

$$I_{PV-string} = I_{PV} \tag{1.9}$$

$N_{sm}$: number of series PV modules.

A PV array is a number of PV panels connected in series and parallel. Its voltage is equal to the sum of the voltage of series panels, and its current is equal to the sum of parallel PV panels current as expressed in the following equation:

$$V_{PV-array} = V_{PV} N_{sm} \tag{1.10}$$

$$I_{PV-array} = I_{PV} N_{pm} \tag{1.11}$$

$N_{pm}$: number of parallel PV modules.

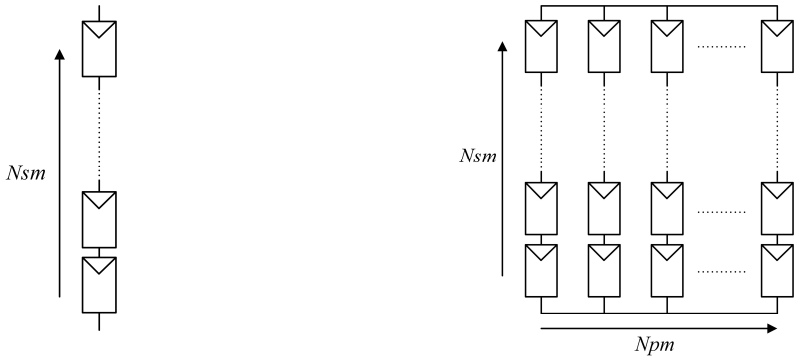


***Figure I-8 PV system configuration: string (a), array (b).***

In order to simulate the electrical characteristic of a PV array that consists of parallel and series PV modules, the following equation is used [61]:

$$I_{PV} = I_{Ph} N_{pm} - I_{SD} N_{pm} \left( \exp\left( \frac{V_{PV} + I_{PV} R_S \left( \frac{N_{sm}}{N_{pm}} \right)}{\alpha V_t N_{sm}} \right) - 1 \right) - \frac{V_{PV} + I_{PV} R_S \left( \frac{N_{sm}}{N_{pm}} \right)}{R_P \left( \frac{N_{sm}}{N_{pm}} \right)} \tag{1.12}$$

Figure I-9 shows the I-V and P-V curves of the PV array and compares them with the curves of the PV module.

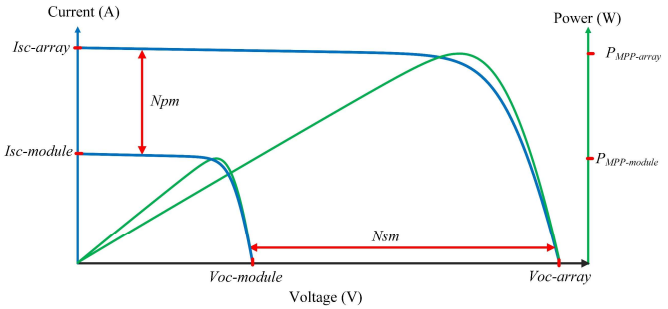


***Figure I-9 The electrical characteristic of the PV array.***

## 2.4 Impact of Climatic Conditions on The Efficiency of PV Systems:

The PV system's efficiency is mainly affected by the type of PV module and its manufacturing technique. Figure I-5 shows that the PV cell directly converts 13% - 47.1% of the solar radiance to electricity. However, climatic conditions (solar radiation and temperature) significantly impact the PV module efficiency.

### 2.4.1 Solar Radiance Influence on PV System's Electrical Characteristics:

Solar radiation significantly influences solar panels' electrical characteristics, as shown by the I-V (current-voltage) and P-V (power-voltage) curves in Figure I-10. These graphical depictions indicate how a solar panel will behave under different conditions. The main topic of this discussion, solar radiation, has the following effects:

The increase in radiation intensity leads to a rise in the number of photons hitting the panel, releasing more electrons and consequently increasing the current ($\boldsymbol{I_{PV}}$) generated by the panel. It is important to note that the fundamental shape of the I-V curve remains relatively constant. However, increased radiation levels lead to a significant increase in the output current.

Furthermore, solar radiation has a direct impact on the power ($P_{PV}$) output of a solar panel, which is calculated by multiplying voltage ($V$) and current ($I$) together ($P = V * I$). In most solar panels, the voltage at the maximum power point ($\boldsymbol{V_{MPP}}$) tends to exhibit a slightly stable behaviour as solar radiation levels increase. Nevertheless, there is a significant rise in the current at the maximum power point ($\boldsymbol{I_{MPP}}$). As radiation levels increase, there is a corresponding increase in solar panels' power output ($\boldsymbol{P_{MPP}}$), leading to an upward shift of the P-V curve.

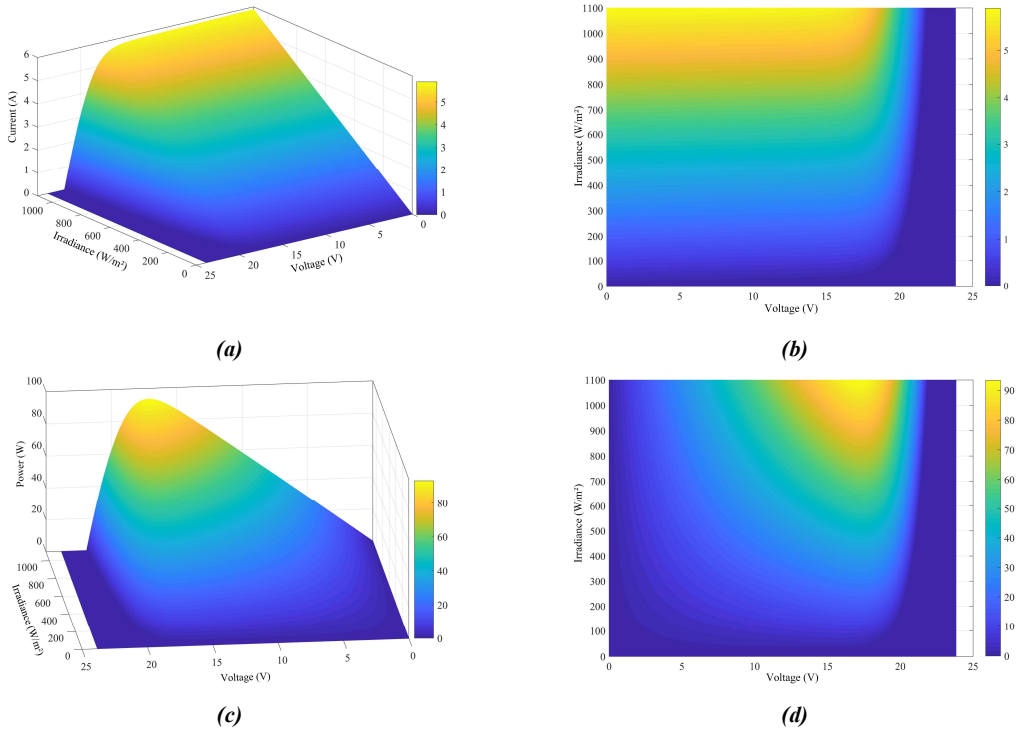


***Figure I-10 Solar radiation impact on I-V curve side view(a), top view (b), and P-V curve side view (c), top view (d).***

### 2.4.2 Temperature Influence on PV System's Electrical Characteristics:

The impact of temperature on the electrical characteristics of solar panels is a crucial factor to consider when analyzing and designing photovoltaic systems. This phenomenon is particularly evident in the I-V and P-V curves, as Figure I-11 illustrates.

An increase in temperature is commonly associated with a decrease in the open-circuit voltage ($V_{OC}$) and a slight increase in the short-circuit current ($I_{SC}$) on the I-V curve. This change in temperature causes a shift to the right along the voltage axis and a decrease in current and voltage. However, the P-V curve shows a more complex response to temperature changes. The primary aspect is a decrease in the maximum power ($P_{MPP}$) due to the simultaneous decline in voltage and current levels. The concurrent reduction in voltage at the maximum power point ($V_{MPP}$) and current at the maximum power point ($I_{MPP}$) results in a downward shift along the power axis. In order to precisely evaluate the impact of temperature on solar panels, manufacturers commonly include temperature coefficients. These coefficients are essential for optimizing photovoltaic systems and minimizing power losses caused by temperature.

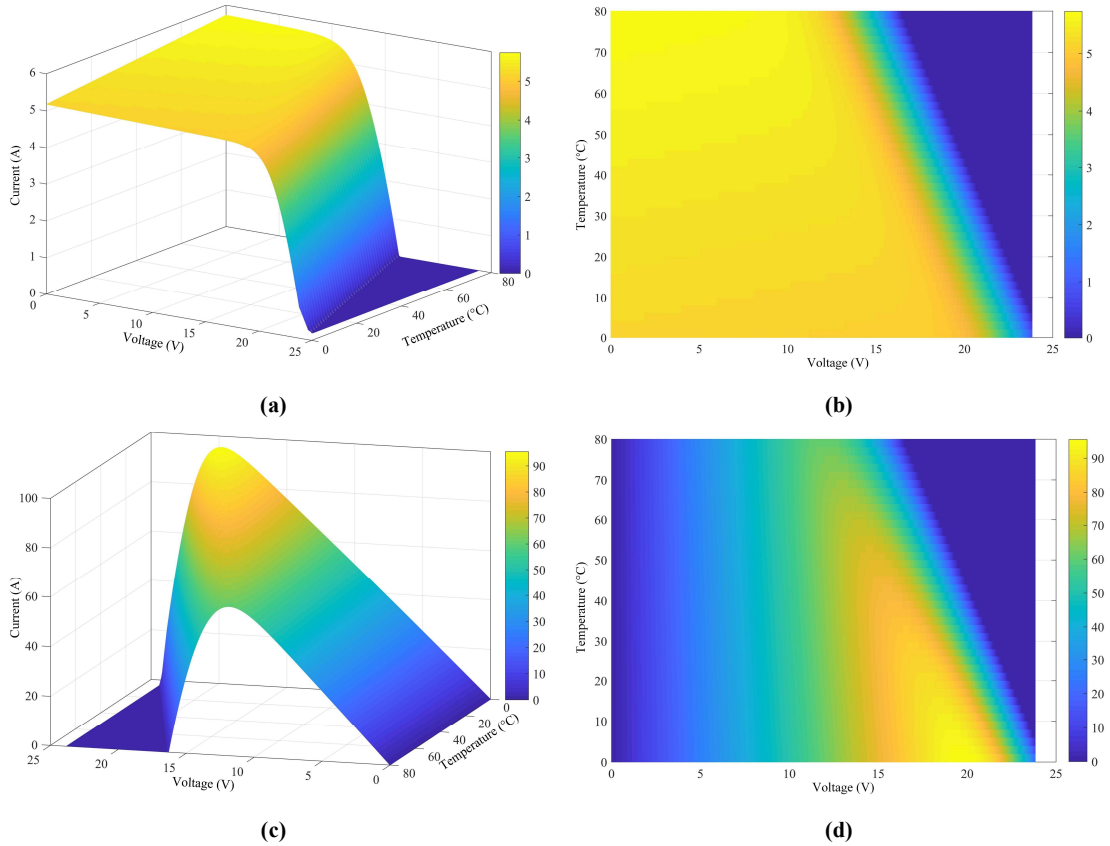


***Figure I-11 Temperature impact on I-V curve side view(a), top view (b), and P-V curve side view (c), top view (d).***

### 2.4.3 Partial Shading Influence on PV System's Electrical Characteristics:

Partial shading significantly affects the efficiency of solar panels. It reduces the amount of power generated, increases the mismatch losses, and can result in permanent damage, contributing to the panels' destruction over time [62], [63], [64]. Various factors influence the severity of these impacts, including the shading area, the arrangement of shaded panels within the array, the connections between panels, and the geometry of the shading [65]. Global maximum power point tracking, PV module reconfiguration, and bypass diodes are solutions proposed to mitigate the impact of partial shading. Figure I-12 shows the I-V and P-V curves during partial shading.

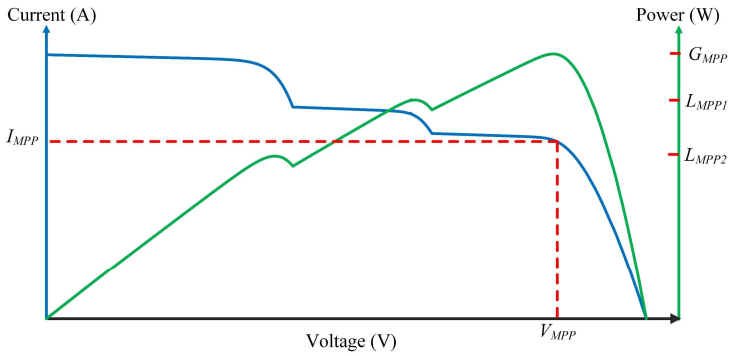


***Figure I-12 Partial shading impact on I-V curve and P-V curve.***

## 2.5 Maximum Power Point Tracking Algorithms:

MPPT algorithms have become popular in PV systems to optimize energy extraction from solar panels [66], [67]. The MPPT achieves a continuous adjustment of the aspects of the operation of the PV system through electronic converters to ensure operation at its MPP. The MPP refers to the specific operating point of a solar panel where it produces the highest amount of electrical power, considering changing conditions such as solar radiation intensity and temperature. There are many MPPT methods, each with different benefits and drawbacks. The following are many popular MPPT algorithms:

### 2.5.1 Perturb and Observe:

The P&O algorithm represents a fundamental and frequently employed approach for achieving MPPT in PV systems. Its main advantage lies in its inherent simplicity, making it a cost-effective option for implementation [68]. The P&O method continually adjusts the operational parameters of a solar panel by perturbing its operating point and subsequently monitoring the resultant variations in power output. It proceeds in the direction of enhanced power output when such enhancement is observed while altering the direction in the presence of power output reduction [69]. This iterative procedure facilitates its convergence toward the MPP.

Nonetheless, the P&O algorithm has certain limitations. Notably, there is a compromise concerning the step size and tracking speed [70]. An increase in step size enhances the tracking speed but causes an amplification in the ripples of the voltage close to the MPP and decreases the accuracy. Conversely,

the reduced step size can decrease oscillations but slow tracking speed and increase power loss. Furthermore, tracking the MPP is limited to only one direction, either during voltage increase or decrease. This constraint may lead to inaccurate monitoring and the possibility of missing the global maximum power point (GMPP) in cases where the P-V curve exhibits multiple peaks, particularly in partial shading [71]. Figure I-13 provides the flow chart of the conventional P&O algorithm.

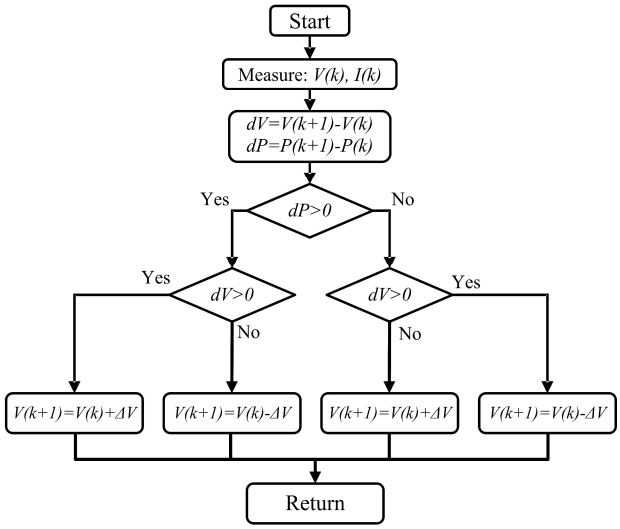


***Figure I-13 Conventional P&O flow chart.***

Various papers have proposed enhancements to improve the performance of the P&O algorithm. Altwallbah et al. [72] present an improved adaptive P&O algorithm that effectively and precisely tracks the GMPP in partial shading conditions. The algorithm overcomes the drawbacks of conventional P&O by employing variable step sizes and appropriate comparison sequences. In [73], Taibi et al. propose a variable step size P&O algorithm, which is determined using a fuzzy logic controller. The proposed algorithm performs better than the conventional P&O during changed climatic conditions.

### *2.5.2 Incremental Conductance:*

Hussain et al. proposed The incremental conductance algorithm in 1995 [74]. Its functionality principle depends on the relationship between a solar panel's incremental conductance (d$I$/d$V$) and instantaneous conductance ($I$/$V$). By comparing these two parameters, the IC is able to track the MPP voltage across increasing or decreasing the operating voltage of the solar panel, as shown in Figure I-14. The main equations express the IC algorithm given as follows:

$$\frac{dI}{dV} = -\frac{I}{V} \quad \text{Operating at the MPP} \tag{1.13}$$

$$\frac{dI}{dV} > -\frac{I}{V} \quad \text{Operating at the left side of MPP} \tag{1.14}$$

$$\frac{dI}{dV} < -\frac{I}{V} \quad \text{Operation at the right side of MPP} \tag{1.15}$$

The main benefits of the IC include efficiency, robustness, and ease of implementation. Nonetheless, the main criticism of the IC algorithm lies in the challenging task of the optimal step size [75], [76]. This choice involves finding a balance between the steady-state oscillation and the speed at which the system can accurately follow the desired tracking point. Moreover, the algorithm fails to track the GMPP during partial shading [77].

In this context, several papers propose improved IC algorithms to overcome the conventional IC drawbacks [78], [79], [80], [81]. In order to tackle issues related to accuracy and tracking speed, the authors in reference [82] suggest employing an IC algorithm with variable step sizes. Their approach involves dividing the I-V curve into four distinct sections and assigning a specific step size to each section. Mahmoud et al. introduce a variable step size IC algorithm that utilizes a fuzzy logic controller to adapt the step size [80]. An IC algorithm-based particle swarm optimization proposed in [81] aims to track the GMPP. The ICPSO algorithm shows a fast response and accurately tracks the GPMM during the partial shading condition.

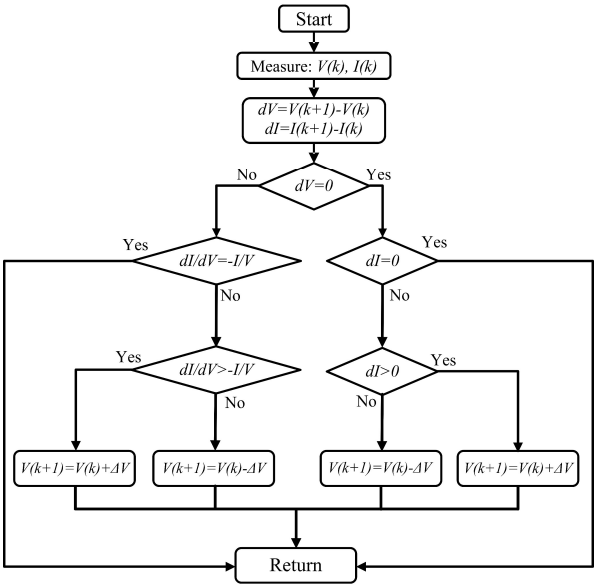


***Figure I-14 The flow chart of the incremental conductance algorithm.***

### *2.5.3 Sliding Mode MPPT Algorithm:*

Due to its notable characteristics, the SMC is a widely used nonlinear control technique. These include fast dynamic response, robustness, system order reduction, effective disturbance rejection, and ease of implementation. In the context of PV systems, SMC is frequently employed as an MPPT algorithm in standalone and grid-connected PV systems configuration [83], [84], [85], [86].

Yatimi and Aroudam [87] introduced a first-order sliding mode control (FOSMC) MPPT algorithm. It is a principle based on observing the power derivative concerning the voltage (d$P$/d$V$) equals zero at the MPP. Consequently, they select the sliding surface to force the system output to reach zero and optimize the power output. However, the FOSMC suffers from the chattering phenomena, which causes an oscillation around the MPP [21], as shown in the example in Figure I-15.

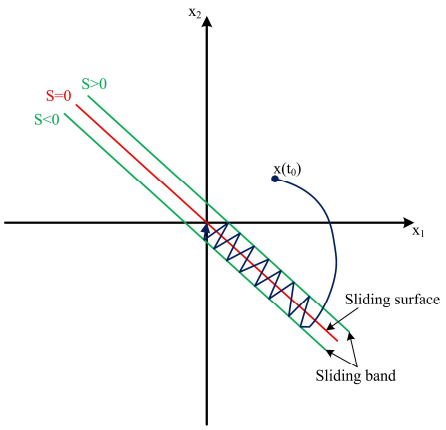


***Figure I-15 Phase portrait of a first-order sliding mode controller.***

Several papers propose a high-order sliding mode (HOSM) to mitigate the drawback of FOSMC [85], [86]. Kantas et al. suggest a third-order sliding mode control (TOSMC) for harvesting the MPP applied on a standalone PV system [86]. The results show the TOSM algorithm's superiority over the conventional FOSM in terms of maximum power output, reduced chattering, accuracy, and less fluctuation in the voltage and current.

### *2.5.4 Artificial Neural Network MPPT:*

ANNs are promising techniques that draw inspiration from the human brain's structure and operation. Recently, ANN has become an attractive solution adopted in PV systems [14]. It effectively addresses the limitations of the conventional iterative MPPT algorithm, including slow tracking speed, oscillation around the MPP, and accuracy tracking it during rapidly changing weather conditions or partial shading [88], [89], [90]. The MPPT based on ANNs provides the $V_{MPP}$ at its output. At the same time, various papers use different parameters in the input, such as PV voltage and current, temperature, irradiance, open circuit voltage, short circuit current, or a combination thereof [91], [92], [93].

However, The training of ANNs necessitates an extensive amount of data, which may not be accessible or accurate for some PV systems [14]. Moreover, ANNs can show poor performance during extreme conditions or noisy input. In addition, high computational costs and memory requirements may increase the implementation cost. Figure I-16 shows an example of the structure of ANNs-based MPPT with two inputs (irradiance and temperature), one hidden layer, and one output ($V_{MPP}$).

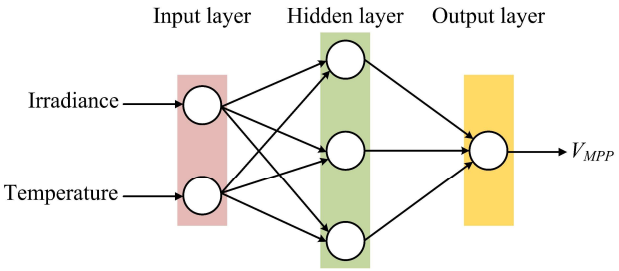


***Figure I-16 Example of the structure of ANNs-based MPPT.***

### *2.5.5 Fuzzy Logic Controller:*

Fuzzy logic is an extension of artificial intelligence specifically designed to manage inaccuracy and uncertainty by applying linguistic rules and fuzzy sets. The FL comprises three fundamental steps [94], as depicted in Figure I-17. The first step is fuzzification, which converts the real input values into linguistic terms through the membership function. The second step is the inference process, which applies the fuzzy rules to the fuzzified inputs and obtains the fuzzy output. The last step is defuzzification, which converts the fuzzy output values into real output values using the membership function defined for each output.

Fuzzy MPPT [95] adjusts the PV system's duty cycle or voltage to generate the peak power output in response to changing environmental factors such as temperature and solar irradiance. Unlike other MPPT techniques, fuzzy MPPT provides several benefits, including simplicity, robustness, fast convergence, and low oscillation [80].

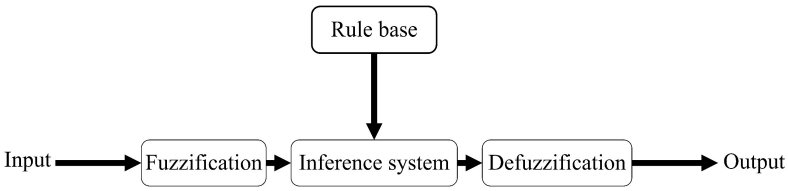


***Figure I-17 Fuzzy logic controller's block diagram.***

### *2.5.6 Meta-Heuristic and Bio-Inspired Techniques:*

Meta-heuristic and bio-inspired techniques are optimization methods used to track the MPP. These are practical solutions to track the GMPP under partial shading conditions. In this context, various MPPT algorithms inspired by nature are used, such as Particle swarm optimization [62], genetic algorithm [63], grey wolf optimization [64], ant colony optimization [65], artificial bee colony[66] [66], and cuckoo Search [96].

**Particle swarm optimization** is an optimization technique developed in 1995 by Kennedy and Eberhart [33]. They were inspired by the collective behavior of bird flocking and the schooling activities of fish. PSO allows the PV system to operate at the GMPP among all the MPPs, particularly when they encounter challenges such as partial shading or multiple peaks in the P-V curve [97].

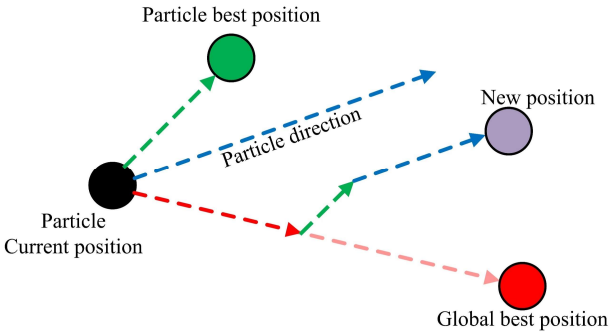


***Figure I-18 Particle swarm optimization algorithm.***

PSO utilizes a population of possible solutions represented as particles. These particles can take the form of duty cycles or PV voltages. Each particle has two fundamental properties: position and velocity. The particle properties are updated in each iteration based on the particle's best position and the swarm's global best position, and some random elements are introduced. Figure I-18 shows the process of particle movement toward the best solution.

The **genetic algorithm** is an optimization algorithm that mimics the process of natural evolution (Figure I-19). Its fundamental principle involves creating and improving of a population of possible solutions, guided by rules inspired by biology [98]. The main steps in the GA include initialization, evaluation, selection, crossover, mutation, and replacement [34].

Initially, the GA generates a random population, represented in binary form (in our case, this relates to PV voltage levels). Each binary element of the individual is called a gene. The evaluation step is pivotal, as it guarantees the survival of the fittest individual within the population. In this stage, the entire population is evaluated using a fitness function, which, in our context, aims to maximize power output. The selection process follows, where individuals are picked based on probability, and the fittest individuals closer to the optimal solutions have a greater chance of being selected. Subsequently, the crossover procedure creates new individuals by combining several of the selected parent's genes. Finally, the generation update is done using the replacement process, which uses techniques such as elitism (preserving the best individuals), generational (replacing all individuals), or steady-state (replacing few individuals). This process continues iteratively until a specific stopping condition is satisfied. Common stopping criteria include reaching a predefined maximum number of iterations or discovering an optimal solution.

The MPPT based on GA performs better than the conventional algorithm, especially during partial shading conditions [99].

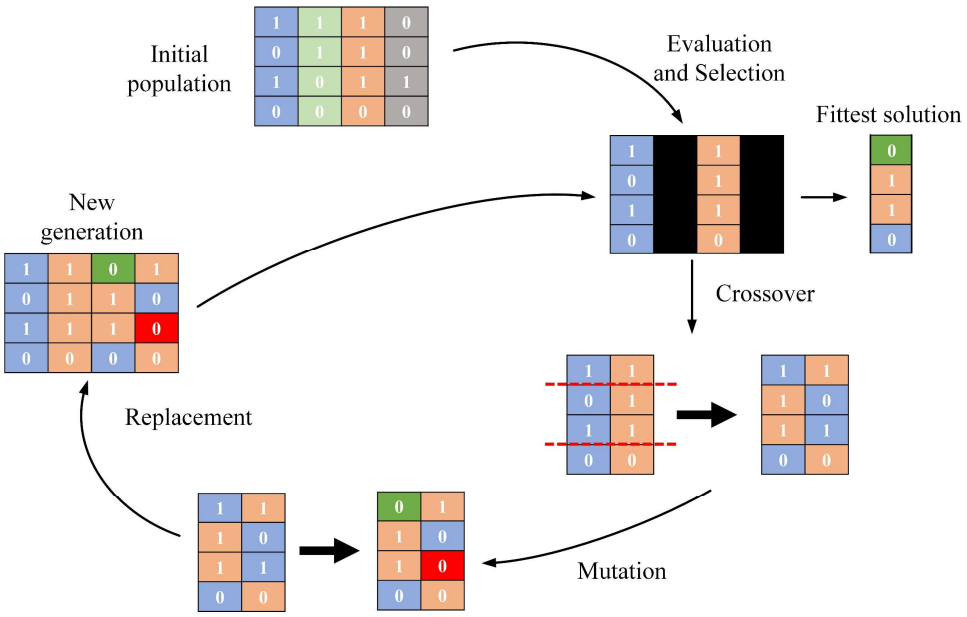


***Figure I-19 The main steps of the genetic algorithm.***

The **Grey Wolf Optimizer** is an optimization algorithm designed to emulate the hierarchical leadership structure and hunting behavior of grey wolves (Canis lupus) proposed by Mirjalili et al. in 2014 [35]. The GWO algorithm contains four different types of wolves, each possessing unique roles inside the pack. The alpha wolf is the dominant leader of the pack, and it is the best solution to the optimization problem. In contrast, the beta wolf is the subordinate of the alpha wolf, and its value presents the second-best solution. The delta (δ) is the third class in the pack and presents the third-best solution. The remaining candidate solutions are the omega (ω) wolves. The wolves exhibit cooperative behavior by effectively coordinating their actions to hunt their prey. The hunting process guides the alpha, beta, and delta, while the remaining omega wolves follow those three wolves.

In the GWO algorithm, three mathematical models emulate the hunting behaviors of wolves: encircling the prey, hunting the prey, and attacking the prey [100]. The alpha, beta, and delta wolves change their location using the encircling behavior based on the best solution discovered. The utilization of hunting behavior determines the calculation of the distance between each wolf and the prey. The attack behavior is employed to modify the position of each wolf by directing their movement towards the prey, utilizing a random coefficient.

Several papers propose an MPPT algorithm based on GWO to gather the GMPP of a PV system under partial shading. The technique performs better than conventional methods such as P&O, IC, PSO, and GA [101], [102].

### *3 Fundamentals of Grid-Connected PV System:*

GCPV systems are decentralized renewable energy sources connected to the grids to augment the efficiency of the electric network. This section will show a detailed overview of the GCPV.

### 3.1 GCPV Structure:

GCPV systems allow customers to reduce their reliance on the utility grid by supplying excess or unused power. The Classification of the GCPV structure depends on various factors such as the output power rating, the PV module arrangement, or the power processing stage. The following are some fundamental facts about the GCPV structure.

#### 3.1.1 Power Rating:

The particular application defines the size and configuration of the system. The GCPV systems can be classified into three levels depending on the power rating [103]: These categories include small-scale systems (Figure I-20 a), typically rated less than 20 kW, such as the eco-house rooftop GCPV in the Sultan Qaboos University (Oman) [104]; medium-scale systems (Figure I-20 b), covers the range of 20 kW to 1 MW, such as 200 kW PV system that carried out on the Jaen University (Spain) [105]; and large-scale systems (Figure I-20 c), covering a range that is higher than 1 MW, such as Bhadla Solar Park in India (2245 MW) [106].

*(a)* *(b)* *(c)*

***Figure I-20 Grid-connected PV system classification based on power rating: small-scale (Sultan Qaboos University – Oman) (a), medium-scale (Jaen University – Spain) (b), and large-scale (Bhadla Solar Park– India) (c).***

#### 3.1.2 PV Module Arrangement:

GCPV can be categorized into four distinct configurations (central-, string-, multi-string-, AC module) based on the PV module wiring to each other and the type of inverter system [107]:

**Central inverters** are typically interconnected with multiple PV arrays, comprising numerous PV panels that attach to the direct current (DC) link of the inverter, as depicted in

Figure I-21. Central inverters are widely used in large-scale PV systems (between 1 MW and 50 MW) due to their reduced cost and reliability since they may be installed in secure areas and have more excellent power handling capabilities [2]. Since the entire array is coupled with a single inverter, this particular arrangement is controlled using a single MPPT. Consequently, it is not considered an optimal solution for partial shading situations, as shaded parts within the PV array considerably decrease the

overall power output [108]. Moreover, if the central inverter malfunctions, the entire PV system will be inoperable.

The PV modules are connected with a central inverter in various combinations such as series, parallel, series-parallel, total-cross-tied, bridge-linked, and honey-comb [109]. Figure 1-21 presents the central inverter and the various PV module combinations. In [110], Pendem and Mikkili investigate various configurations under varied shade situations to maximize power harvest while minimizing mismatching power losses. The results show that the central inverter connected to the TCT PV array with bypass diodes generates the maximum power by reducing the mismatching power losses.

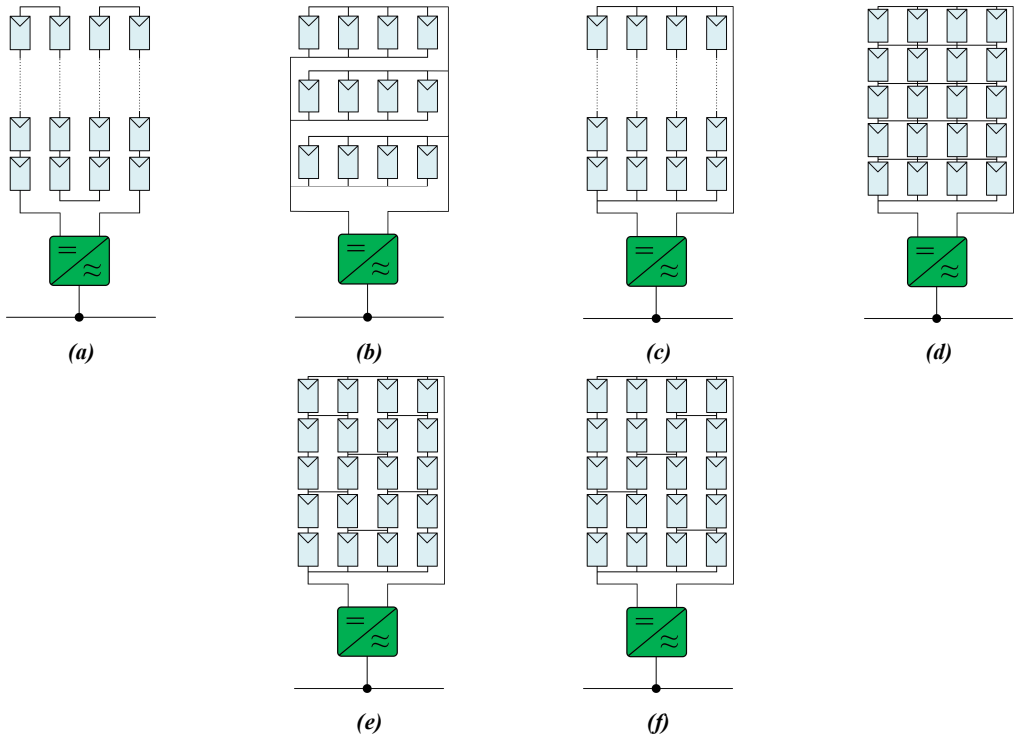


***Figure I-21 GCPV system based on Central inverter: series (a), parallel (b), series-parallel (c), total-cross-tied (d), bridge linked (e), and honey-comb (f).***

The **string inverter** is a topology consisting of a series of modules to form a string, whereas every single string is coupled to an inverter, as described in Figure I-22. The string inverter allows the use of an MPPT with each string. Therefore, partial shading and mismatching power losses significantly decrease, enhancing overall system efficiency [111]. This system maximizes energy harvesting for the grid, minimizes string diode losses, and reduces the size of the electrolyte capacitor, thereby extending the inverter's lifespan [112]. Furthermore, if one of the string inverters fails, the remaining strings continue to function, and replacing the faulty inverter with a new one is a simple procedure [113]. However, the installation cost is higher due to the use of several inverters.

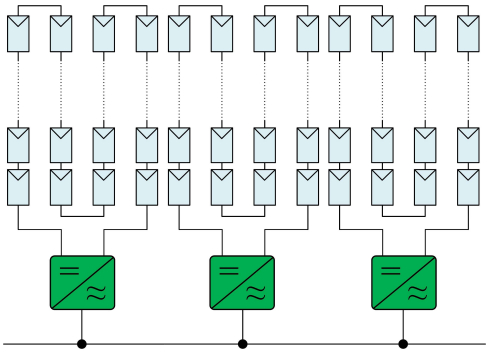

*Figure I-22 GCPV system based on string inverter topology.*

**A multi-string inverter** is a dual-stage system that effectively merges the benefits of central and string inverter configurations. Multiple strings are coupled directly to the voltage amplifier's converter, and each string is equipped with an independent MPPT algorithm. Figure I-23 depicts these strings combined and connected to a central or single inverter [114].

The overall efficiency is significantly higher because each PV string is controlled individually. Multi-string inverters offer numerous benefits, including cost reduction, increased flexibility, a smaller DC-link capacitor, and enhanced energy production due to local MPPT and optimal monitoring of the PV system [115]. Additionally, it facilitates improved performance of PV systems in scenarios of partial shading, especially when the PV strings are subject to varying levels of irradiance and operating temperatures [116].

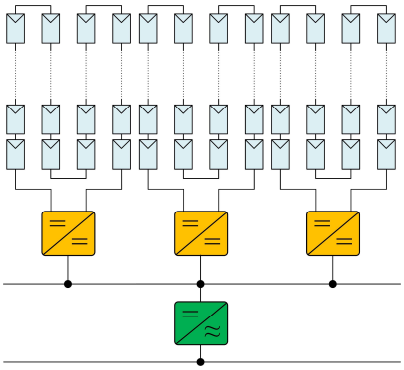

*Figure I-23. GCPV system based on the multi-string inverter.*

**AC module inverter** is a single PV module linked directly to the grid through an inverter, as shown in Figure I-24, generally used on the small scall GCPV [117]. Within the AC module, many functionalities, including MPPT, DC/DC voltage amplification, and DC-AC inversion, are combined into an individual device referred to as a module to eliminate the mismatch losses. The AC module topology is very beneficial to increasing system efficiency because it permits the optimal utilization of PV modules. Nevertheless, increasing the number of PV modules in a system can increase the costs and control requirements [118].

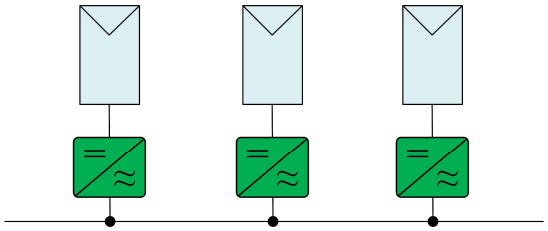

***Figure I-24 GCPV based on AC module inverter.***

A comprehensive comparative analysis of the performance evaluation of all four inverter configurations is conducted and presented in Table I-1.

***Table I-1 A detailed comparison between the central-, string, multi-string- and AC module inverter*** [107].

| *Configuration* | *Cost* | *Efficiency* | *Flexibility* | *Reliability* | *Maintenance* | *Power rating* |
|---|---|---|---|---|---|---|
| ***Central inverter*** | Lowest | Medium | Low | Low | Low | 1-50 MW |
| ***String inverter*** | Medium | High | High | High | Medium | 1-5 KW/string |
| ***Multi-string inverter*** | Medium | Medium | Medium | Medium | High | 1-50 KW |
| ***AC module*** | Highest | Highest | Highest | Highest | Highest | 600 W |

### *3.1.3 Power processing stage:*

Depending on the power processing stage, the different types of configuration systems of the GCPV are single-stage and dual-stage configurations [119]. In a single-stage system, the PV panels are directly connected to the inverter's input side, and the inverter's output side is connected to the grid, as illustrated in Figure I-25 (a). On the other hand, in a dual-stage configuration, the PV panels are integrated with the inverter's input side via a DC-DC converter, as shown in Figure I-25 (b). Table I-2 shows a detailed comparison analysis between the power processing stage configurations of GCPV.

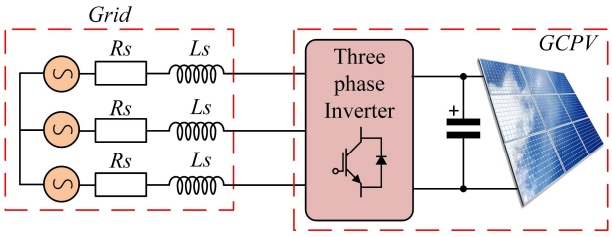


***(a)***

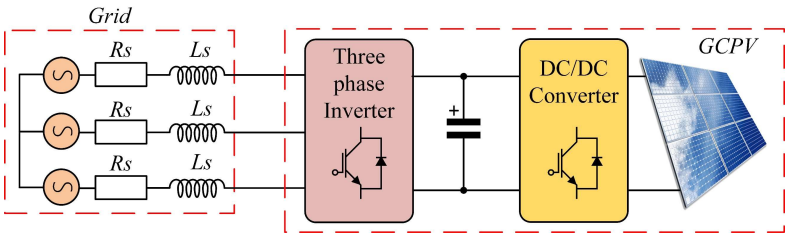


***(b)***

***Figure I-25 Schematics of the Single-stage (a) and Dual-stage GCPV.***

*Table I-2 Single-stage and Dual-Stage topologies comparison.*

| | *Single stage* | *Dual stage* |
|---|---|---|
| ***Components*** | Consists of only a grid-connected inverter (DC/AC converter). | Consists of an additional converter between the PV panels and the grid-connected inverter for the DC voltage regulation. |
| ***PV Array Connection*** | The PV panels are directly connected to the dc-bus of the grid-tied inverter. | A DC-DC converter is connected between the PV panels and inverter. |
| ***MPPT Performance*** | The grid-tied inverter assumes the task of performing the MPPT. | The grid-tied inverter is charged for performing the MPPT. |
| ***Efficiency and Cost*** | Cost-effective, but efficiency degrades. | Complex control but high efficiency can be achieved. |

## *3.2 Three-phase Three-wire GCPV topologies:*

### *3.2.1 Two-level GCPV:*

Figure I-26 shows a three-phase dual-stage, two-level GCPV consisting of PV panels, a DC/DC converter, and a two-level voltage source inverter (2L-VSI). The 2L-VSI consists of six switching devices. Each of the three legs comprises two IGBTs, which must operate complementarily [120]. It converts a DC to an AC voltage with a specified frequency and amplitude. This topology is simple to implement, highly efficient, and low-cost. However, it produces high harmonic distortion in the output voltage and current, high voltage stress on the switches, and high switching losses [121].

Table I-4 lists the possible operating states of a two-level inverter and its output voltage.

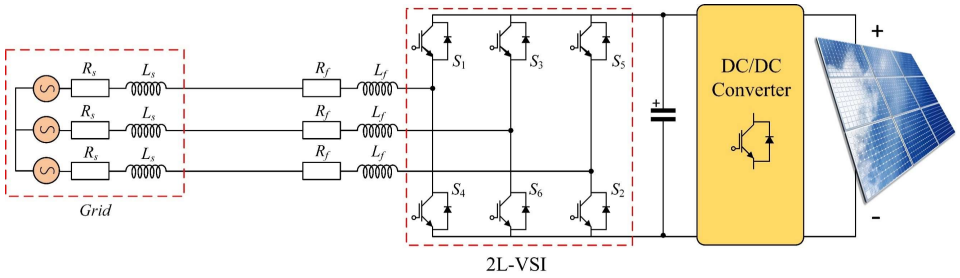


*Figure I-26 Two-level dual-stage GCPV system.*

*Table I-3 Switching states and output voltage of two-level inverter.*

| ***State*** | | ***V0*** | ***V1*** | ***V2*** | ***V3*** | ***V4*** | ***V5*** | ***V6*** | ***V7*** |
|---|---|---|---|---|---|---|---|---|---|
| $S_1$ | | 0 | 1 | 1 | 0 | 0 | 0 | 1 | 1 |
| $S_3$ | | 0 | 0 | 1 | 1 | 1 | 0 | 0 | 1 |
| $S_5$ | | 0 | 0 | 0 | 0 | 1 | 1 | 1 | 1 |
| ***Phase voltage*** | $V_{an}$ | **0** | $\frac{2}{3}V_{dc}$ | $\frac{1}{3}V_{dc}$ | $-\frac{1}{3}V_{dc}$ | $-\frac{2}{3}V_{dc}$ | $-\frac{1}{3}V_{dc}$ | $\frac{1}{3}V_{dc}$ | **0** |
| | $V_{bn}$ | **0** | $-\frac{1}{3}V_{dc}$ | $\frac{1}{3}V_{dc}$ | $\frac{2}{3}V_{dc}$ | $\frac{1}{3}V_{dc}$ | $-\frac{1}{3}V_{dc}$ | $-\frac{2}{3}V_{dc}$ | **0** |
| | $V_{cn}$ | **0** | $-\frac{1}{3}V_{dc}$ | $-\frac{2}{3}V_{dc}$ | $-\frac{1}{3}V_{dc}$ | $\frac{1}{3}V_{dc}$ | $\frac{2}{3}V_{dc}$ | $\frac{1}{3}V_{dc}$ | **0** |
| $V$ | | **0** | $\frac{2}{3}V_{dc}\angle 0$ | $\frac{2}{3}V_{dc}\angle 60$ | $\frac{2}{3}V_{dc}\angle 120$ | $\frac{2}{3}V_{dc}\angle 180$ | $\frac{2}{3}V_{dc}\angle 240$ | $\frac{2}{3}V_{dc}\angle 300$ | **0** |

### 3.2.2 Three-level Neutral Point clamped (NPC):

The three-level NPC (3L-NPC) inverter consists of four switching devices (e.g., MOSFET or IGBTs) and two power diodes in each leg, as illustrated in Figure I-27. The outer switches $S_{1a}$ and $S_{4a}$ operate at a high switching frequency, while the inner switches $S_{2a}$ and $S_{3a}$ operate at the grid frequency.

Table I-4 and Figure I-28 show the operating state and the output voltage of one leg of an NPC inverter. 3L-NPC inverters are becoming increasingly common as active interfaces for grid-connected PV systems due to their features, such as higher voltage operation, reduced harmonic, lower common mode voltage, and lower voltage stress on power switches [122]. However, the multilevel inverter requires more switching devices and complex control circuits than a two-level inverter; further, the cost of implementation, size, and complexity will rise.

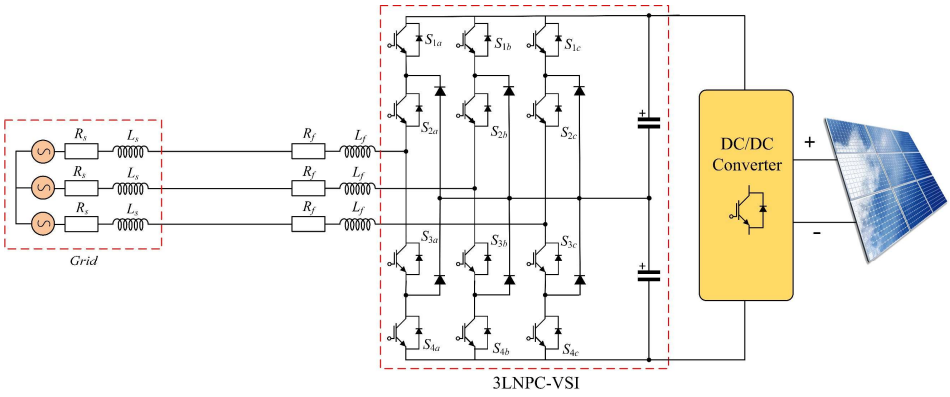


*Figure I-27 Three-level dual-stage NPC GCPV system.*

*Table I-4 The operating state and the output voltage of one leg of an NPC inverter.*

| *Operating state* | $S_{1a}$ | $S_{2a}$ | $S_{3a}$ | $S_{4a}$ | *Output voltage* |
|---|---|---|---|---|---|
| ***P state*** | ON | ON | OFF | OFF | $+V_{dc}/2$ |
| ***O state*** | OF | ON | ON | OFF | 0 |
| ***N state*** | OFF | OFF | ON | ON | $-V_{dc}/2$ |

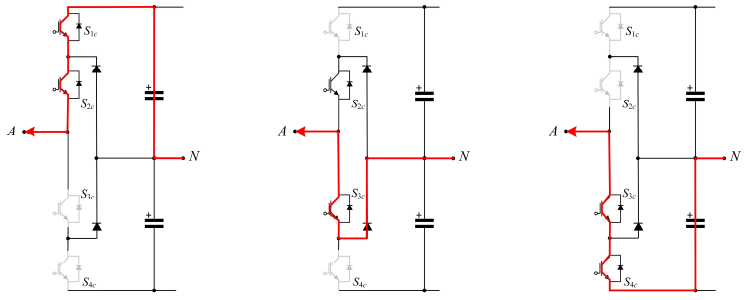


*(a)* *(b)* *(c)*

*Figure I-28 Operating state of one leg of an NPC inverter: P (a), O (b), and N (c).*

### 3.2.3 Three-Level T-Type NPC Inverter:

The three-level T-type NPC (3L-TNPC) inverters, a specialized form of the NPC inverter, are experiencing increased popularity. The T-type becomes an alternative solution to the complex three-

level inverter topologies due to its ability to eliminate clamping diodes, huge capacitors, and isolated sources. In addition, they have beneficial features such as low harmonic distortion, higher efficiency, and lower switching count [123]. Figure I-29 depicts the GCPV system based on a 3L-TNPC inverter. This topology is similar to 2L-VSI; the only difference is the inclusion of bi-directional switches connected to the neutral point of the DC link capacitor. Table I-5 compares the 2L-VSI and 3LNPC-VSI topology.

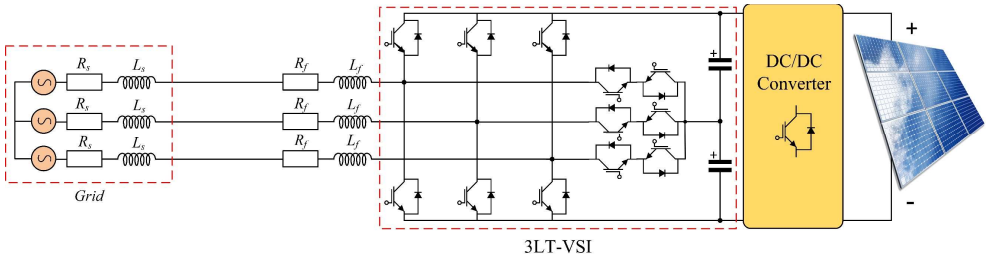


***Figure I-29 Three-level T-type NPC GCPV system.***

***Table I-5 Comparison between 2L-VSI and 3LNOC-VSI topologies.***

| | ***2L-VSI*** | ***3LNPC-VSI*** | ***3LTNPC-VSI*** |
|---|---|---|---|
| ***No. of switch*** | 6 | 12 | 12 |
| ***No. power diode*** | 0 | 6 | 0 |
| ***Line-to-Line Voltage Level*** | 3 | 5 | 5 |
| ***Total harmonic distortion*** | High | Low | Low |
| ***Cost*** | Low | Very high | High |
| ***Complexity*** | Low | High | High |
| ***implementation*** | Easy | Hard | Moderate |
| ***Commercial example*** | Semikron SK300GB063D | Semikron SK150MLI066T | Infineon F3L75r12W1h3 B27 |

## *3.3 Grid-Connection Standards and Recommendations:*

Significant developments in the photovoltaic industry in recent years have led to a rise in the proportion of solar power in distribution systems. Accordingly, many countries and international commissions (e.g., the International Electrotechnical Commission IEC and the Institute of Electrical and Electronics Engineers IEEE) have started establishing appropriate solar interconnection standards, modeling them after the interconnection standards and guidelines developed for wind generation [124]. Power quality, safety, and protection are the three main categories into which most interconnection standards fall. Researchers and engineers worldwide can benefit from a common technical language established by consensus standards and guidelines for the GCPV system. Table I-6 lists some standards and procedures for integrating PV systems with the grid.

***Table I-6 Several international standards for the PV systems integration in the grid*** [124].

| ***Standard*** | ***Title of the standard*** | ***Publication*** |
|---|---|---|
| IEEE Std 1547TM -2003 (R2008) (including amendment IEEE 1547a-2014) | IEEE Standard for Interconnecting Distributed Resources with Electric Power Systems | IEEE |
| IEEE Std 929-2000 | Recommended Practice for Utility Interface of Photovoltaic (PV) Systems | IEEE |
| IEC 61727-2004 | Photovoltaic (PV) systems - Characteristics of the utility interface | IEC |
| RD 1663/2000 | Interconnection of PV installations to the low-voltage grid | Spain |
| GB/T 19964-2012 | Technical requirements for connecting photovoltaic power station to power system | China |
| TPC Technical Guideline | Taiwan Power Company Technical Guideline for integrating renewable energy with the grid | Taiwan |

### *3.4 Grid Synchronization Technique:*

The current generated by the inverter and fed into the utility grid must be synchronized with the grid's voltage. The primary purpose of the synchronization method is to obtain the grid voltage's phase angle.

Currently, the phase-locked loop (PLL) is a widely used synchronization mechanism for extracting the phase angle of the grid voltage due to its efficiency and robustness, even in the presence of high-order harmonics in the grid. The main architecture of PLL illustrated in Figure I-30 consists of a phase detector (PD), a low-pass filter (LF), and a voltage-controlled oscillator (VCO).

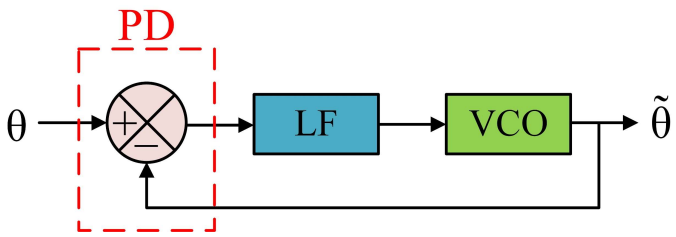


***Figure I-30 The basic structure of PLL.***

The synchronous reference frame PLL (SRF-PLL) is commonly employed in three-phase GCPV systems due to the accurate and fast estimation of the grid phase angle under ideal grid conditions. The architecture of the SRF-PLL is depicted in Figure I-31.

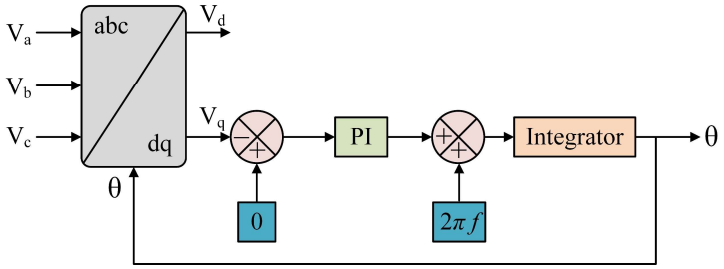


***Figure I-31 The basic structure of PLL.***

The Park transformation converts the measured grid voltage to the rotating synchronous frame dq, as shown in (1.16). The Proportional Integrator (PI) regulates the q elements, with the grid frequency being the resulting output of this PI. The utility grid phase angle is determined by integrating the grid frequency and subsequently providing this information as feedback to the PD (Park transformation) [125].

$$\begin{bmatrix} V_d \\ V_q \\ V_0 \end{bmatrix} = \frac{2}{3} \begin{bmatrix} \cos(\theta) & \cos(\theta - 2\pi/3) & \cos(\theta + 2\pi/3) \\ -\sin(\theta) & -\sin(\theta - 2\pi/3) & -\sin(\theta + 2\pi/3) \\ \frac{1}{2} & \frac{1}{2} & \frac{1}{2} \end{bmatrix} \begin{bmatrix} V_a \\ V_b \\ V_c \end{bmatrix} \tag{1.16}$$

## *4 Power Quality Issue:*

The term "power quality" refers to the level at which the supplied electrical power (voltage and current) meets the requirements of the system's equipment, hence assuring the system's ability to operate effectively and reliably. Poor power quality is a critical factor in modern electrical systems, as it can cause various operational problems, including decreased efficiency and lifespan of equipment, higher maintenance costs, equipment malfunctions, and safety risks. The ideal signals of a three-phase grid are:

- Three pure sinusoidal waveforms.
- Their amplitude and phase angle are constant.
- 2π/3 (rad/s) phase shift between them.

In this context, a variation of any signal from the ideal signal of voltages and currents is referred to as a power quality disturbance. The typical power quality disturbances are cited in the following:

### *4.1 Voltage Sags:*

Voltage sags, or voltage dips, refer to a temporary voltage amplitude reduction where the voltage levels drop between 10% and 90% below the usual operating range [126]. Voltage sags are a prevalent form of power quality disturbances that can cause significant disturbances to electrical and electronic devices. The causes of voltage sags are short circuit faults, connections to heavy loads, or lightning strikes. Figure I-32 shows the voltage sag waveform.

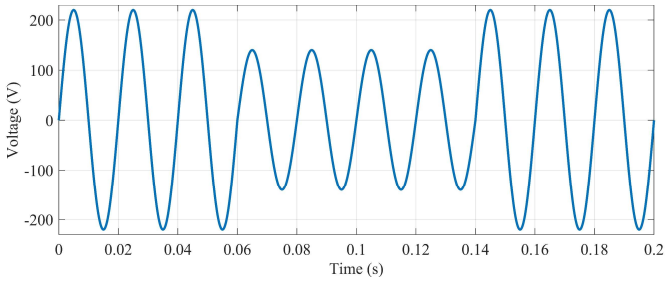


***Figure I-32 Voltage sags waveform.***

### *4.2 Voltage Swells:*

A voltage swell is a short-duration phenomenon of an increase in the grid voltage between 10% and 90%. Voltage swell is mainly caused by a single line-to-ground fault that switches off a heavy load and energizes a large bank of capacitors [127]. Figure I-33 illustrates the waveform of the voltage swell.

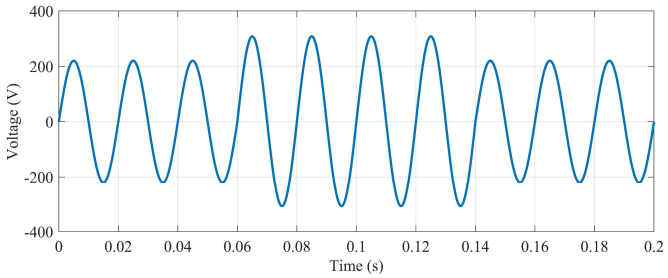


***Figure I-33 Voltage swell waveform.***

### *4.3 Voltage Interruption:*

Interruption is a complete loss of voltage supply level to less than 10% of the operating voltage [128]. Voltage interruption (as shown in Figure I-34) is classified into short-duration and long-duration. Short-duration interruption results from protective devices such as circuit breakers, a failure of a switching device, disturbances, or reclosers in response to faults. On the other hand, long-duration interruption is typically caused by storms, trees hitting the lines, or miscoordination of protective devices [129].

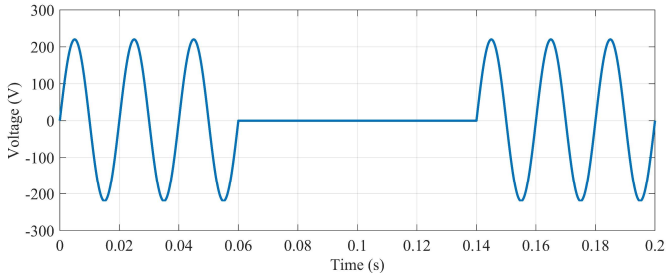


***Figure I-34 Voltage interruption waveform.***

### *4.4 Voltage Imbalance:*

A voltage imbalance occurs when the amplitude and/or phase of the three-phase voltages in a three-phase electric system deviates from the standard value of amplitude and a 120-degree phase shift between phases [130]. Several problems can produce a voltage imbalance, including asymmetrical

faults, unequal loads on different phases, an unbalanced transformer, or issues in the power distribution system. Figure I-35 shows the voltage imbalance waveform.

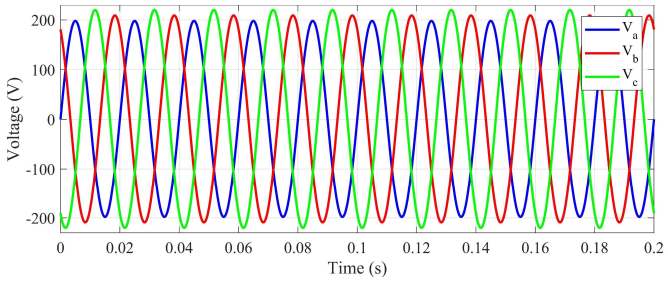


***Figure I-35 Voltage imbalance waveform.***

### *4.5 Voltage Flicker:*

Voltage flicker [131] refers to rapid and unpredictable variations in voltage levels in an electrical system. It is a temporary change in voltage caused by fluctuations in demand or equipment failures in the electrical grid. Fluctuations in the voltage waveform often characterize voltage flicker (as depicted in Figure I-36), and it can cause disruptions or disturbances in electrical equipment.

### *4.6 Voltage Frequency Variation:*

Voltage frequency variations are defined by the deviation of the fundamental frequency of the voltage from its nominal value, which may be 50 or 60 Hz [132]. The duration of a frequency variation might range from a few cycles to a few hours. Rapid changes in the connected loads generally cause such variances. The permitted range for variation in voltage frequency is typically limited to ±0.5 Hz.

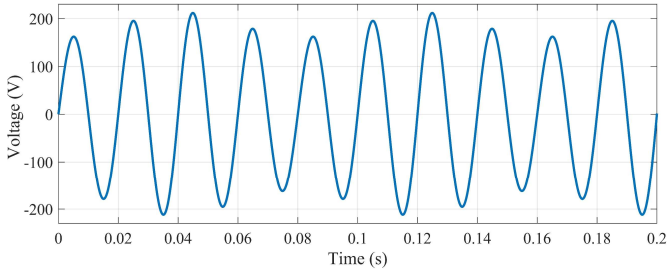


***Figure I-36 Voltage flicker waveform.***

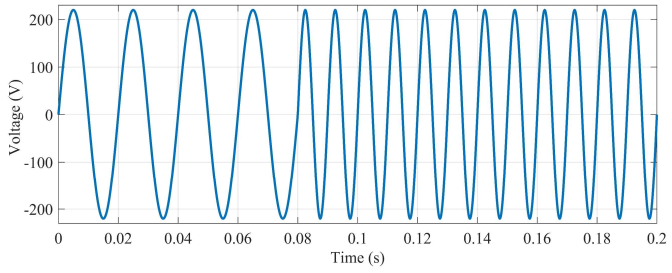


***Figure I-37 Voltage frequency variation waveform.***

### *4.7 Harmonics:*

Harmonics [133] refers to the voltage or current distortion. A harmonic is a component of a waveform of a frequency that is an integer multiple of the fundamental frequency of the electrical

system, generally 50 Hz or 60 Hz. For example, the fifth harmonic for the US electrical distribution system would be 5*60 Hz = 300 Hz. A sinusoidal distorted waveform and its components are shown in Figure I-38.

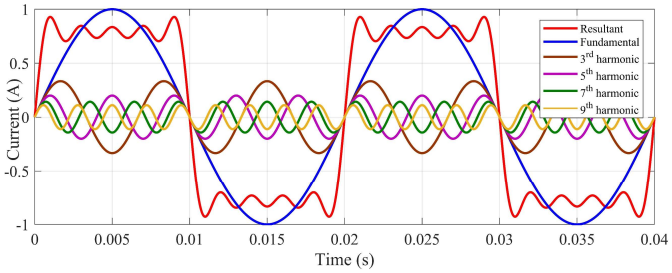


***Figure I-38 Example of a sinusoidal distorted waveform, its fundamental, and some harmonic components.***

## *5 Harmonics Sources, Impact and Mitigation Techniques:*

Nonlinear loads modify the sinusoidal characteristics of the AC power system, leading to the presence of harmonic currents in the AC power system.

### *5.1 Sources and Impacts of Harmonics:*

#### *5.1.1 Sources of Harmonics:*

Power system harmonics can be caused by several processes, including ferro-resonance, subsynchronous resonance, magnetic saturation, nonlinear loads, and electronically switched loads. The main source of harmonic distortion is from nonlinear loads. In the following some harmonics sources [134]:

- Static power converters include inverters, rectifiers, triacs, diacs, etc.
- Home appliances include fluorescent lighting, computers, variable-speed air conditioning, and televisions.
- Arc furnace.
- Induction heating.
- Adjustable speed drives.
- Wind and solar plants.
- Transformers.
- Rotating induction machines.
- Synchronous generators.

#### *5.1.2 Impacts of Harmonics:*

Electronic devices become exposed to the damaging effects of harmonics. The following is a list of the harmonics issues [134]:

- The capacitor bank failed due to excessive reactive power, resonance, and harmonic amplification, causing undesired fuse behavior.
- Induction and synchronous machines can experience overheating, harmonic torques, oscillations, and excessive losses, which can lead to torsional stress growth.
- A rise in negative sequence current loading damages windings and the rotor circuit of synchronous generators.
- Increase in flux density and generation of harmonic fluxes in transformers, followed by derating and eddy current heating.

- Resonance induces excessive currents and overvoltages in the power system.
- Derating of cables is the consequence of eddy current overheating and skin effect losses.
- Telecommunication circuits are exposed to inductive interference.
- Solid-state and microprocessor-controlled systems are susceptible to signal interference.
- Relay malfunctioning.
- The firing circuits that use zero-voltage crossing detection and latching may experience unstable functioning.
- Interference with power plant excitation systems and massive motor controllers.
- Subsynchronous resonance may occur.
- Flicker.

When capacitors are present, nonlinear loads can induce a resonant condition with one of the load-generated harmonics, creating a previously absent situation. This circumstance also gives rise to the following additional effects:

- Prolong the decay rate of the transformers and increase its transient inrush current.
- Rise the duty of the switching devices.

### *5.2 Total Harmonics Distortion (THD):*

Total harmonic distortion (THD) [135] is a factor that quantifies the harmonic distortion in voltage or current and allows systematic and comparable evaluations of power system quality to be carried out. Furthermore, THD plays a vital role in enhancing the quality and reducing distortion of power systems. The THD value quantifies the rate at which the measured signal deviates from its fundamental component, which is typically the most dominant in power systems, as expressed in the following equation:

$$THD = \frac{\sqrt{\sum_{n=2}^{\infty} X_n^2}}{X_f} \tag{1.17}$$

$X_n$ and $X_f$ are the harmonic components of rank n and the fundamental components' amplitude values.

### *5.3 IEEE Std-519 Standard for Harmonic Control in Electrical Power Systems:*

The IEEE Std-519 standard [136] is a vital reference in power quality, serving as guidelines for designing power systems and assuring harmonic interaction between power sources and loads. The main emphasis is on harmonics, which refer to undesired distortions in the AC waveform resulting from electronic devices. These distortions can cause significant damage to electrical equipment, resulting in malfunctions, overheating, and full failure. The IEEE 519-1992 harmonic limits for current and voltage at the point of common coupling (PCC) are shown in Table I-7, Table I-8, Table I-9, and Table I-10.

The IEEE 519-1992 document recommends setting even harmonics' upper limits at 25% of the upper limit for odd harmonics. In addition, deliver distortions leading to a direct current offset are restricted.

*Table I-7 Current distortion limits for general distribution systems (120 V - 69 KV).*

| *Maximum harmonic current distortion in percent of $I_L$* | | | | | | |
|---|---|---|---|---|---|---|
| *Individual harmonic order h (odd harmonics)* | | | | | | |
| **$I_{SC}/I_L$** | **< 11** | **11 ≤ h < 17** | **17 ≤ h < 23** | **23 ≤ h < 35** | **35 ≤ h** | **THD%** |
| **<20*** | 4.0 | 2.0 | 1.5 | 0.6 | 0.3 | 5.0 |
| **20<50** | 7.0 | 3.5 | 2.5 | 1.0 | 0.5 | 8.0 |
| **50<100** | 10.0 | 4.5 | 4.0 | 1.5 | 0.7 | 12.0 |
| **100<1000** | 12.0 | 5.5 | 5.0 | 2.0 | 1.0 | 15.0 |
| **>1000** | 15.0 | 7.0 | 6.0 | 2.5 | 1.4 | 20.0 |

Where

$I_{SC}$ is the maximum short-circuit current at PCC.

$I_L$ is PCC's maximum demand load current (fundamental frequency component).

*Table I-8 Current distortion limits for general sub-transmission systems (69.001 kV - 161 kV).*

| *Maximum harmonic current distortion in percent of $I_L$* | | | | | | |
|---|---|---|---|---|---|---|
| *Individual harmonic order (odd harmonics)* | | | | | | |
| **$I_{SC}/I_L$** | **< 11** | **11 ≤ h < 17** | **17 ≤ h < 23** | **23 ≤ h < 35** | **35 ≤ h** | **THD%** |
| **< 20*** | 2.0 | 1.0 | 0.75 | 0.3 | 0.15 | 2.5 |
| **20 < 50** | 3.5 | 1.75 | 1.25 | 0.5 | 0.25 | 4.0 |
| **50 < 100** | 5.0 | 2.25 | 2.0 | 0.75 | 0.35 | 6.0 |
| **100 < 1000** | 6.0 | 2.75 | 2.5 | 1.0 | 0.5 | 7.5 |
| **> 1000** | 7.5 | 3.5 | 3.0 | 1.25 | 0.7 | 10.0 |

*Table I-9 Current distortion limits for general transmission systems, >161 kV.*

| *Maximum harmonic current distortion in percent of $I_L$* | | | | | | |
|---|---|---|---|---|---|---|
| *Individual harmonic order (odd harmonics)* | | | | | | |
| **$I_{SC}/I_L$** | **< 11** | **11 ≤ h < 17** | **17 ≤ h < 23** | **23 ≤ h < 35** | **35 ≤ h** | **THD%** |
| **< 50*** | 2.0 | 1.0 | 0.75 | 0.3 | 0.15 | 2.5 |
| **≥ 50** | 3.0 | 1.5 | 1.15 | 0.45 | 0.22 | 3.75 |

*** All power generation equipment is limited to these values of current distortion, regardless of actual $I_{SC}/I_L$.**

*Table I-10 Voltage distortion limits.*

| *Bus voltage at PCC* | *Individual voltage distortion (%)* | *Total voltage distortion THD (%)* |
|---|---|---|
| **69 kV and below** | 3.0 | 5.0 |
| **69.0001 kV through 161 kV** | 1.5 | 2.5 |
| **161.001 kV and above** | 1.0 | 1.5 |

## *5.4 Harmonics Mitigating Techniques:*

Different filters have been utilized to eliminate the current harmonics in the context of harmonic mitigation techniques. In the following, the commonly used devices are discussed:

### *5.4.1 Passive Filter:*

In distribution systems, passive filters (PFs) have been utilized most frequently to minimize the flow of harmonic currents. Typically, they are custom-designed for specific applications. Its advantages include harmonic mitigation, reactive power compensation, and the absence of undesirable harmonics.

However, PFs possess disadvantages, such as inaccurate frequency tuning and demanding extensive calculations, the resonance with line impedance takes place, they cannot be used when harmonic components vary randomly, and they are also heavy and bulky in size. [137]

PFs comprise passive elements such as resistors, capacitors, and inductors. They are usually connected to the grid in parallel, as Figure I-39 shows. PFs are commonly used in industry and can be categorized into four types, as illustrated in Figure I-40: single tuning, first order, second order, and third order [138].

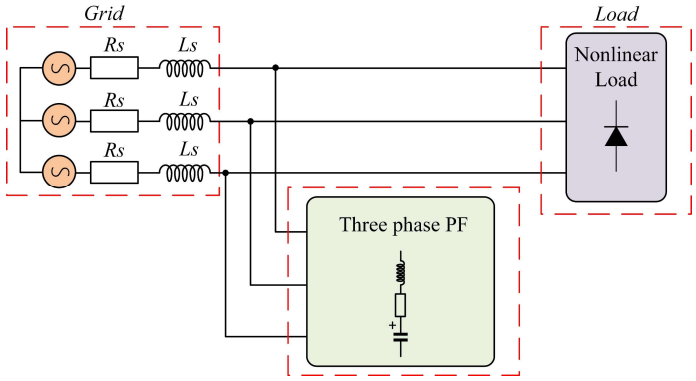


***Figure I-39 PFs connection to the grid.***

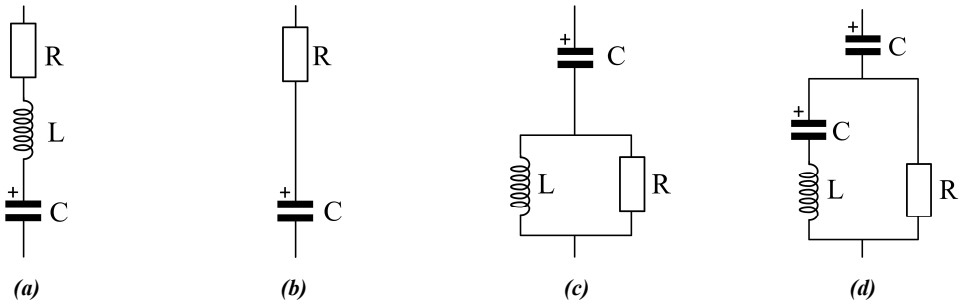


***Figure I-40 Passive filter types: single tuning filter (a), first order (b), second order (c), and third order (d).***

### *5.4.2 Active Power Filter:*

Power engineers are focusing on developing dynamic and adaptable solutions to power quality issues due to the increased severity of power quality in power networks. These devices, frequently called active power line conditioners or active power filters (APF), may enhance voltage balance in three-phase systems, control terminal voltage, decrease flicker, adjust current and voltage harmonics, and compensate for reactive power. A benefit of active filtering is its inherent ability to adapt to network and load variations dynamically. APFs can mitigate several harmonic frequencies and are not influenced by significant changes in network properties, reducing the possibility of resonance between the filter and network impedance. An additional advantage is that they occupy less space than conventional passive compensators. [139]

APF types can be categorized as series active power filters, shunt active power filters, unified power quality conditioners, and hybrid APFs [140], as shown in Figure I-41. Typically, the inverter component

of APFs can consist of either a voltage source inverter (VSI) or a current source inverter (CSI). VSIs are widely preferred due to their simple structure and ease of implementation [141].

Figure I-41(a) illustrates a **series active power filter (SEAPF)** connected in series with the nonlinear load. This configuration mitigates voltage signal disturbances, including voltage harmonics, unbalances, fluctuation, etc. The SEAPF can eliminate distortion in the voltage waveform caused by the load and regulate the voltage at the load terminals, regardless of voltage sag, swell, distortion, or unbalances in the supply voltages, through injecting harmonic voltage components into the grid using a coupling transformer [142]. The primary functions of SEAPFs are to act as a harmonic isolator and voltage regulator between a nonlinear load and the utility grid.

**Shunt active power filter (SAPF)** [139] mitigates current harmonics by injecting compensating currents that are identical in magnitude but opposite in direction to the harmonics. In this scenario, the SAPF functions as a current source by injecting the harmonic components produced by the load, but with a phase shift of 180 degrees. The SAPF effectively eliminates the load current's harmonic components, resulting in a source current that is in phase with the grid voltage and has a sinusoidal waveform. This principle can be applied to any load regarded as a harmonic source. Furthermore, using a suitable controller, the SAPF can effectively set the reactive power equal to zero. The power distribution system considers the SAPF and the nonlinear load as an ideal resistor. Figure I-41(b) illustrates the configuration of the SAPF.

Currently, hybrid power filters attract the researcher's interest due to the beneficial characteristics gained from the used filters. **Unified power quality conditioner (UPQC)** topology combines SEAPF and SAPF connected in parallel via a DC-link element [143]. This configuration improves the power quality by eliminating voltage disturbances in the grid and mitigating the current harmonics. The SEAPF component in the UPQC reduces the harmonics and disturbances of the voltage; on the other hand, the SAPF mitigates the current harmonics and reactive power compensation and enhances the DC-link regulation [144]. However, the high cost of this configuration is the main drawback. Figure I-41(c) shows the structure of the UPQC configuration.

To achieve the advantages of both active and passive filters in terms of cost, effectiveness, and stability. Figure I-41(d) shows an APF connected in series with a PF via a coupling transformer. APF improves the compensatory properties of PF by essentially forcing utility currents to become sinusoidal and in phase with the phase-to-neutral voltage [139]. Another hybrid topology proposed in [145] consists of a shunt PF and an APF connected in series with the source, as illustrated in Figure I-41(e). The proposed topology performs better than the hybrid technique that uses the SAPF and series PF. The parallel connection of an APF and a PF with the load is proposed in [146]. The hybrid filter presented comprises two single-tuned PFs, each tuned to the $5^{th}$ and $7^{th}$ harmonic of the fundamental frequency; on the other hand, a SAPF aims to mitigate higher-order harmonics. The basic structure of this type is depicted in Figure I-41(f). Table I-11 summarizes the characteristics of the various topologies of power filters.

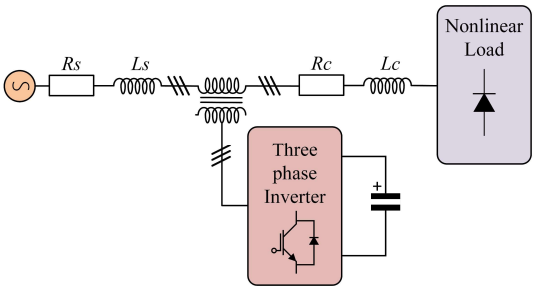
Rs
Ls
Rc
Lc
Nonlinear Load
Three phase Inverter
+

*(a)*

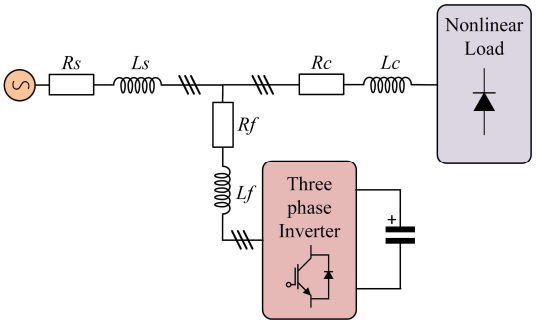
Rs
Ls
Rc
Lc
Nonlinear Load
Rf
Lf
Three phase Inverter
+

*(b)*

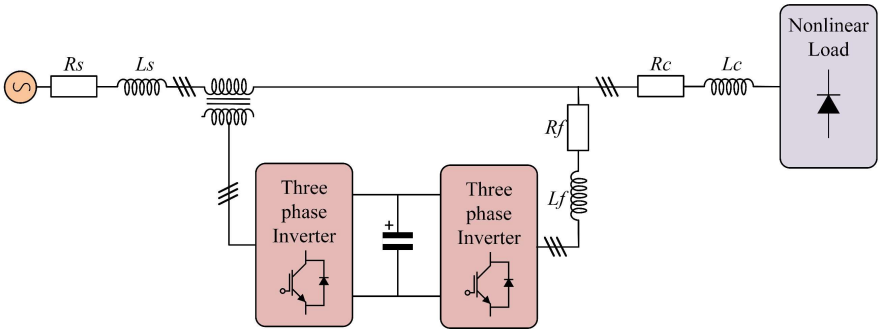
Rs
Ls
Rc
Lc
Nonlinear Load
Rf
Lf
Three phase Inverter
Three phase Inverter
+

*(c)*

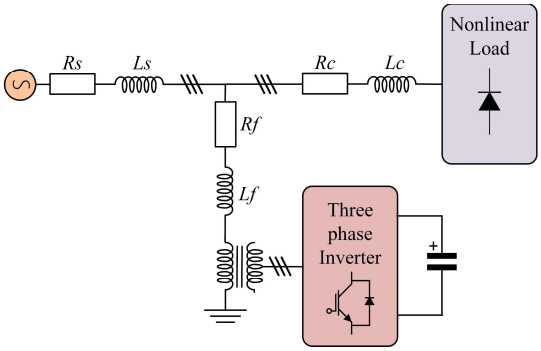
Rs
Ls
Rc
Lc
Nonlinear Load
Rf
Lf
Three phase Inverter
+

*(d)*

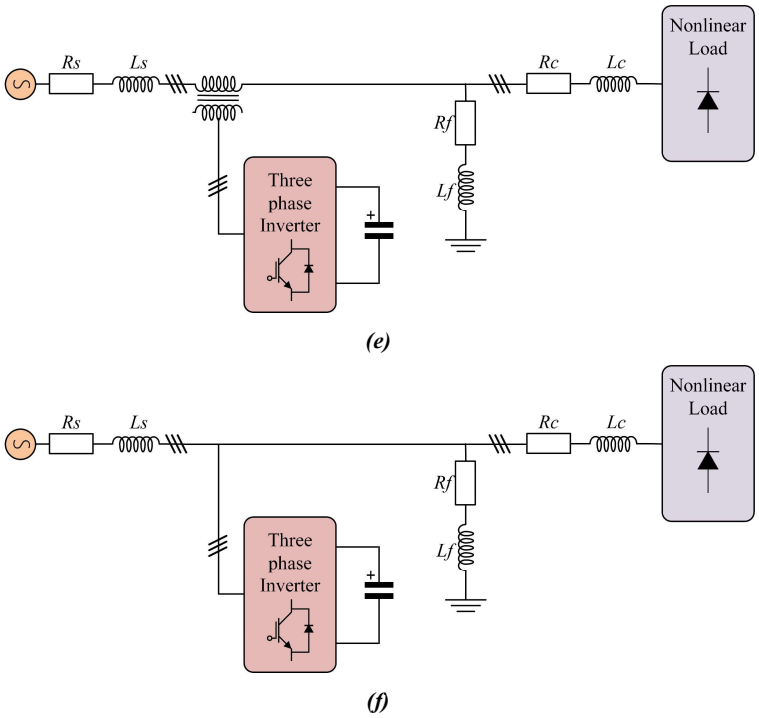


***Figure I-41 Active filter topologies: SEAPF (a), SAPF (b), UPQC (c), series SEAPF and PF, in parallel with load (d); parallel SEAPF and PF in parallel with load (e), parallel SAPF and PF, in parallel with load (f).***

***Table I-11 The main features of power filters*** [137], [147]**.**

| ***Functionality*** | ***Passive Filter*** | ***Active Power Filter*** | ***Hybrid Filter*** |
|---|---|---|---|
| ***Harmonic mitigation*** | Yes[1] | Yes | Yes |
| ***Reactive power compensation*** | Yes | Yes | Yes |
| ***Phase balancing*** | No | Yes | Yes |
| ***Advantages*** | The cheapest<br>Undesirable harmonics are absent. | Eliminate harmonics of any order.<br>Better harmonics mitigation[2].<br>Suitable for variable loads and harmonics varied randomly.<br>Reactive power management.<br>Easy to implement.<br>Small in size. | The same features of APFs.<br>Less voltage stress on switches.<br>Better harmonics mitigation[2].<br>Reactive power management. |
| ***Disadvantages*** | System requirements determine the design.<br>Tuning requires an extensive calculation.<br>Sensitive to overloads.<br>Resonance with the line impedance.<br>Not suitable for variable loads.<br>Heavy and bulky. | Expensive.<br>Complex. | Expensive.<br>The most complex.<br>High number of passive filters. |

**[1] Only the selected harmonics. [2] Compared with passive filters.**

### 5.4.3 Multifunctional GCPV:

Multifunctional grid-connected PV (MGCPV) system refers to a GCPV system that provides ancillary services beyond active power injection [148], such as reactive power compensation, harmonic mitigation, voltage regulation, energy storage in battery, and contributing to grid stability. Through those ancillary services, the MFGCPV system improves the power quality of the grid and guarantees a robust and stable electricity supply. Integrating MFGCPV with ancillary power quality enhancement services reduces the cost by eliminating the necessity for separate devices. Figure I-42 shows the structure of MFGCPV.

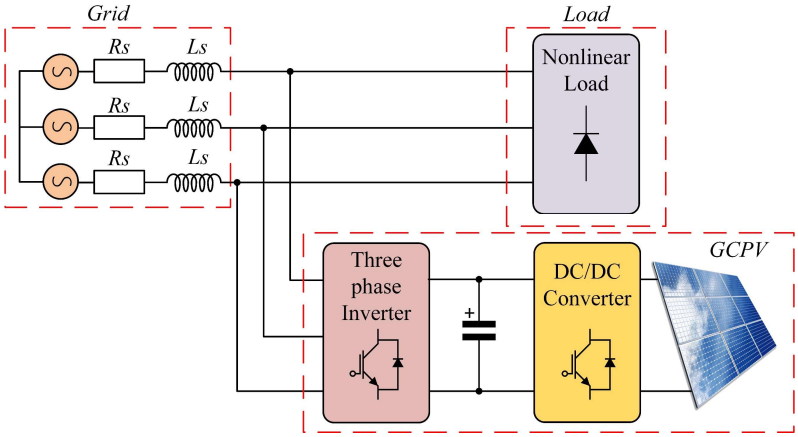


***Figure I-42 The structure of the multifunctional grid-connected photovoltaic system.***

## 6 Conclusion:

This chapter presents an overview of the GCPV system and the power quality issue. Initially, the photovoltaic technology is discussed in detail, including its operating principle, the technology of panels, the mathematical modeling of PV modules and arrays, and the impact of climatic conditions, including irradiation, temperature, and partial shading, on the panels' productivity, along with the commonly used MPPT algorithms.

In addition, an overview of the GCPV has been discussed. The structures of the GCPV depend on the power rating, photovoltaic panel arrangement, and power processing stages, which are listed and presented. Moreover, international standards of GCPV systems are shown. Then, we provide the common synchronization technique that is used to synchronize the GCPV with the voltage grid.

Then, we focus on power quality issues such as voltage sag and swell, voltage fluctuations and interrupt, flicker, frequency deviation, and harmonics. Further, the harmonic sources, their impact on the power systems, and the IEEE 519 standard are presented. Finally, the commonly used techniques that are used to mitigate the harmonics and improve the power quality, such as passive filters, active power filters, and multifunctional GCPV systems, are discussed.

In the next chapter, we will analyze, design, and control a photovoltaic system based on an interleaved boost converter to enhance the harvesting of the maximum power generated by the PV panels and compare its performance to that of a conventional boost converter.

# *Chapter II:*

## *Standalone PV Systems Based on IBC: Design, Control and Performance Analysis*

## 1 Introduction:

Concerns about renewable energy sources have increased globally due to declining conventional energy supplies. Renewable energy sources represent a solution to these concerns and a reliable alternative to fossil energy sources [149]. Solar energy is one of the most effective solutions for energy production. Sunlight can be converted directly into electrical energy through PV panels. It is characterized by ease of installation, does not require continuous maintenance, is environmentally friendly, and has low maintenance costs [150]. However, PV systems have several challenges, such as nonlinear behavior due to dynamically changing climatic conditions and the impact of partial shading on the output performance of the PV module. In addition, the main limitation of PV systems is the low output voltage. From this perspective, the power electronic converters have gained the interest of researchers because they play a vital role in the operation of MPPT algorithms, PV system injection on the grid, and the adoption of PV systems with high-power applications.

Several DC/DC converter topologies are commonly used in PV systems, including buck, boost, buck-boost, cuk, flyback, and single-ended primary-inductance converter (SEPIC) [151]. Recently, DC/DC converters have played a vital role in regulating the output voltage of the PV system to produce the maximum possible power, decrease it, or increase it.

In some applications, the load requires a high-magnitude voltage compared to the power source's output voltage. Therefore, the boost converter has been proposed as a voltage step-up in many applications such as PV systems, fuel cells, electrical vehicle charging, and battery power systems [152], [153], [154], [155]. In addition, the boost converter allows PV systems to track their maximum power points using MPPT algorithms. However, CBCs are unsuitable for high-power applications, have poor efficiency, and in high-duty cycles, the current and voltage ripples rise.

Researchers have grown their interest in raising the PV system's lifespan and efficiency in recent years while minimizing power losses, specifically in high-rating power applications. Several papers that improve the topologies of boost converters have been proposed to overcome the limitation of the CBC. The IBC [156] is a topology widely used to overcome the CBC topology. IBC is a suitable device for high-power applications such as fast electrical vehicle charging, industrial uses, and high PV plant applications due to its beneficial features, such as low input current and output voltage ripples, reduced voltage stress on the switches, reduced size of inductors and capacitors, and converting high amounts of power [157], [158].

This chapter discusses the topologies of CBC and IBC and their functioning principles. It also discusses the design of two topologies, including the selection of their components. Moreover, it presents the implementation of the MPPT algorithms with a 60-kW standalone PV system. Besides, it discusses the control linear and nonlinear strategies that enhance the efficiency and stability of the IBC-based PV system.

## 2 Conventional Boost Converter:

The conventional boost converter is a DC/DC step-up converter used to increase or boost the input DC voltage to a higher DC voltage level. Theoretically, a standard boost converter can gain high voltage as the duty cycle approaches unity [159].

This section will discuss the conventional boost converter's topology, modeling, principle of functioning, and design.

### 2.1 System Description and Modeling:

#### 2.1.1 Circuit Description:

Figure II-1 shows the conventional boost converter topology. The circuit contains a boost inductor $L$, diode $D$, controlled semiconductor switch $S$ (commonly used MOSFET or IGBT), and output filter capacitor $C_O$. In addition, resistor $R$ is utilized as a load. $V_{IN}$, $V_O$, $V_L$, $I_{IN}$, $I_L$, and $I_O$ represent the voltage source, the output voltage, the inductor voltage, the input current, the inductor current, and the output current, respectively.

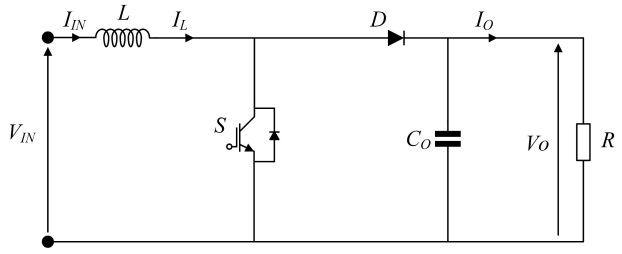


***Figure II-1 Conventional boost converter circuit.***

#### 2.1.2 Conventional Boost Converter Analysis:

To describe the CBC principle of operation, the converter is assumed to operate in a continuous conduction mode, with all components considered ideal (without parasitic resistance) and the diode's forward voltage. Figure II-2 shows two modes of functioning in a period of operation $T_S$. In the first mode, when the switch S is turned on ($t$=[0, $dT_S$]), diode $D$ is turned off, as depicted in Figure II-2 (a). The inductor current $I_L$ increases linearly while the capacitor supplies the load $R$. Therefore, the capacitor voltage decreases.

In the second mode, the switch $S$ is closed ($t$ = [ $dT_S$, $T_S$]). Where the power stored in the inductor is provided to the load $R$ through the diode $D$, and the output capacitor will charge. In this mode, the inductor current decreases until the next cycle, when switch $S$ is turned on again. Figure II-3 illustrates the boost converter waveforms.

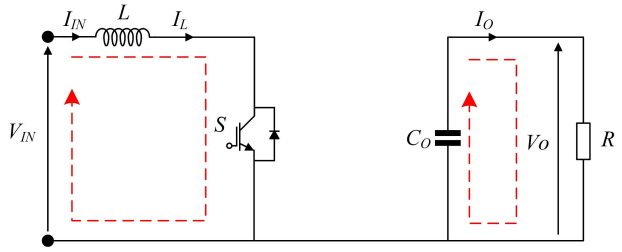

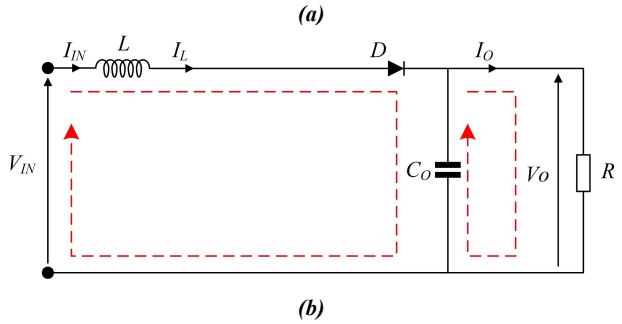


***Figure II-2 Conventional boost converter operating modes: switch closed (a), switch opened (b).***

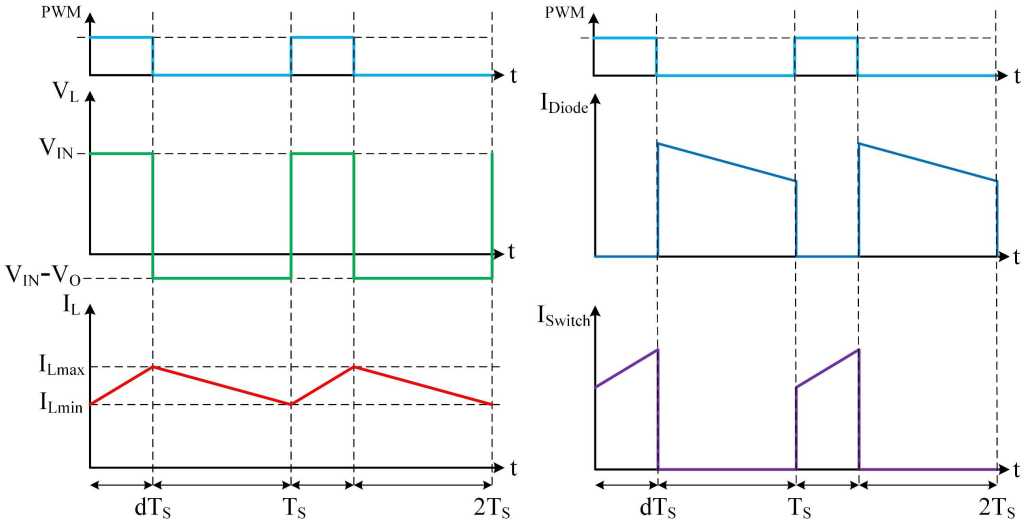


***Figure II-3 Conventional boost converter waveforms.***

### *2.1.3 Conventional Boost Converter Modeling:*

The differential equations that describe the operation of the boost converter are expressed using Kirchhoff's voltage law (KVL) and Kirchhoff's current law (KCL) in the following:

- Switch $S$ close ($S = 0$):

$$\begin{cases} V_L(t) = L\dfrac{dI_L(t)}{dt} = V_{IN}(t) \\ \dfrac{dV_O(t)}{dt} = \dfrac{-I_O(t)}{C_O} \end{cases} \tag{2.1}$$

- Switch $S$ open ($S = 0$):

$$\begin{cases} V_L(t) = L\dfrac{dI_L(t)}{dt} = V_{IN}(t) - V_O(t) \\ \dfrac{dV_O(t)}{dt} = \dfrac{I_L(t) - I_O(t)}{C_O} \end{cases} \tag{2.2}$$

Where $V_L$ is the inductor voltage (V), $I_L$ is the inductor current (A), $V_{IN}$ is the input voltage of the CBC, $I_O$ is the output current of the CBC, and $V_O$ is the output voltage of the CBC (V).

Combining the equations (2.1) and (2.2) and using the switch state function, we can write the differential equations of the conventional boost converter as follows:

$$\begin{cases} \dfrac{dI_L(t)}{dt} = \dfrac{V_{IN}(t) - [1-S]V_O(t)}{L} \\ C_O \dfrac{dV_O}{dt} = I_L(t)[1-S] - I_O(t) \end{cases} \tag{2.3}$$

Replacing the switch state $S$ by its average value $d$ (duty cycle) in a simple time. Therefore, the average module is provided in (2.4)

$$\begin{cases} \dfrac{dI_L(t)}{dt} = \dfrac{V_{IN}(t) - [1-d]V_O(t)}{L} \\ C_O \dfrac{dV_O(t)}{dt} = I_L(t)[1-d] - I_O(t) \end{cases} \tag{2.4}$$

## *2.2 Design of Conventional Boost Converter:*

The first step before the selection of the inductor and the output capacitor is calculating the duty cycle d using the following equation:

$$d = 1 - \frac{V_{IN}}{V_O} \tag{2.5}$$

### *2.2.1 Inductor Selection:*

The equation that allows the calculation of the inductor value is expressed as:

$$L > \frac{V_O}{f_{SW}\Delta I_L} d(1-d) \tag{2.6}$$

Where $f_{SW}$ is the switching frequency, and ΔIL is the inductor current ripple, chosen to be 20% to 40% of the output current $I_O$.

### *2.2.2 Capacitor Selection:*

The equation that allows the calculation of the inductor value is expressed in (2.7):

$$C_O > \frac{I_O d}{f_{SW}\Delta V_O} \tag{2.7}$$

Where $\Delta V_O$ is the output voltage ripple, its value can be 2% of the output voltage $V_O$.

## *2.3 Conventional Boost Converter Limitation:*

The most significant limitations of CBC are [21], [160], [161]:

- High input current and output voltage ripple.
- Unsuitable for high-power applications.
- The voltage gain is limited due to parasitic parameters.
- High voltage stress across the semiconductor switch.
- Low efficiency.
- Switching losses.
- Bulky size in high power applications.

## 3 Four Legs Interleaved Boost Converter:

The IBC is a promising choice for addressing the limitations of CBC [156]. These converters offer the benefits of decreasing the size of inductors, enhancing the power level, and minimizing the voltage stress on the power switches. This section will describe the four-legs interleaved boost converter (FLIBC) circuit and its modeling, investigate the mode of operation, and select the components.

### 3.1 System Description, Analysis and Modeling:

#### 3.1.1 Circuit Description:

Figure II-4 represents the FLIBC topology. It consists of four identical conventional boost converters connected in parallel to the same power source and load. The legs of the IBC operate with the same switching frequency and duty cycle $d$ with a phase shift equal to 90° degrees between them. The interleaving process allows the share of power among the legs, reduces the input current and output voltage ripple, and decreases the voltage stress of the switches [162].

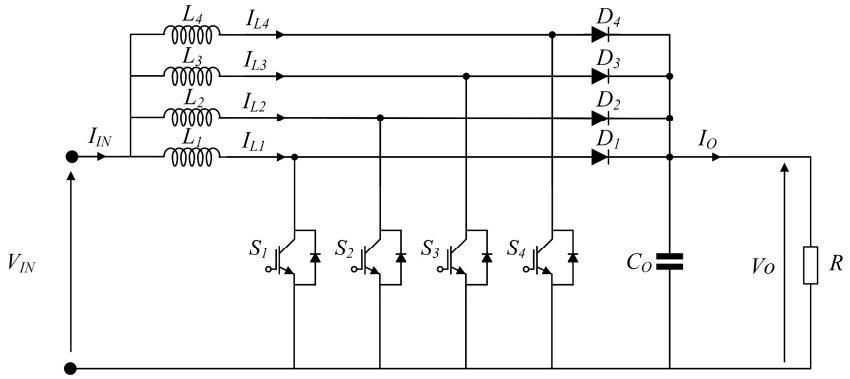


***Figure II-4 Four Legs interleaved boost converter circuit.***

#### 3.1.2 Interleaved Boost Converter Analysis:

The four-legs interleaved boost converter can operate in various cases depending on the duty cycle value. Our study will take the following value ($d$ = 0.25, $d$ = 0.375, $d$ = 0.5, $d$ = 0.675, $d$ = 0.75). The control signal waveforms, the inductors' current flow, and the FLIBC input current are illustrated in Figure II-5 and Figure II-9.

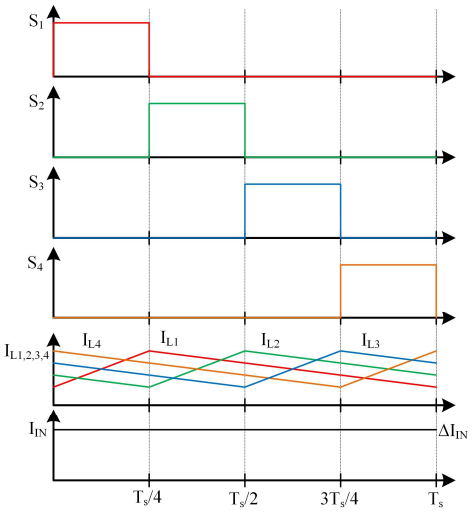


*Figure II-5 FLIBC current waveforms (d=0.25).*

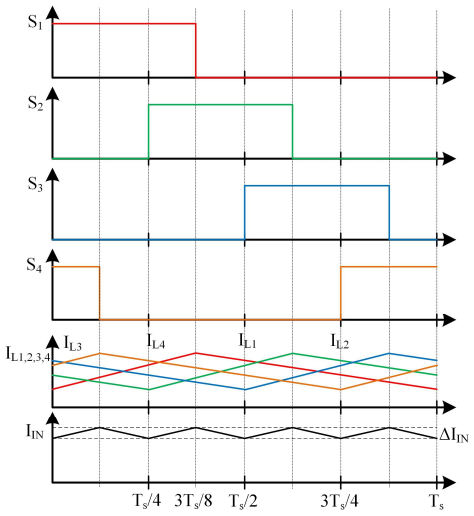


*Figure II-6 FLIBC current waveforms (d=0.375).*

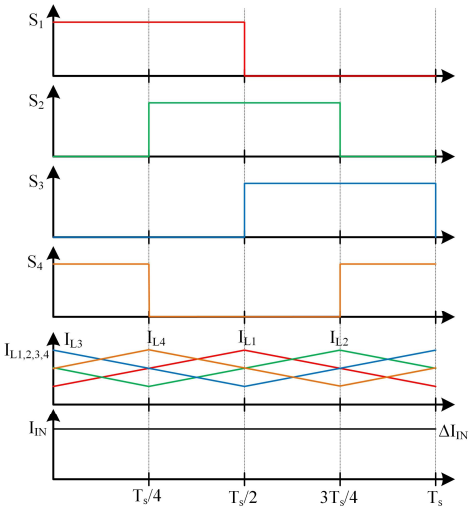


*Figure II-7 FLIBC current waveforms (d=0.5).*

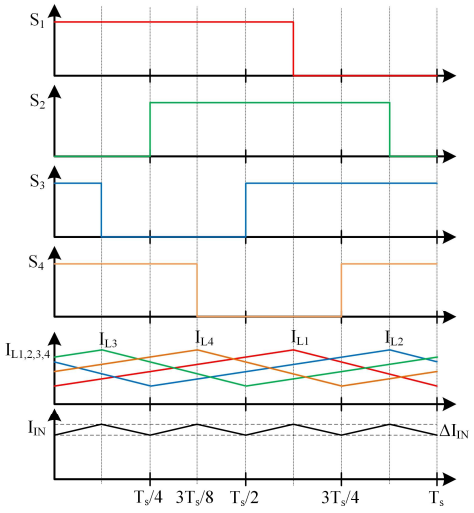


*Figure II-8 FLIBC current waveforms (d=0.675).*

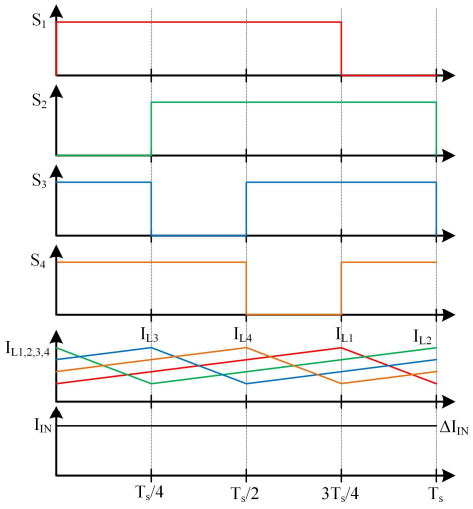


*Figure II-9 FLIBC current waveforms (d=0.75).*

The semiconductor switches of the FLIBC operate using a phase shift control signal between them. The equation that allows the calculation of the phase shift time considering the IBC legs can be written as follows:

$$\varphi_j = \frac{T_s}{N}(j-1); j = 1,2,...,N \tag{2.8}$$

Where $\varphi_j$ is the phase shift time of the concerned leg $j$, $T_s$ is the sample time value, and $N$ is the number of legs.

The input current ripple is a vital factor that affects the power source's efficiency and life span. The IBC inductors are assumed to be identical $L_1=L_2=\ldots=L_N$, and their internal resistances are negligible. The IBC input current ripple value can be calculated using the following general equation [163]:

$$\Delta I_{IN} = \frac{V_O}{Lf_{SW}}\left(d - \frac{j-1}{N}\right)\left(j - Nd\right); \quad \frac{j-1}{N} < d \le \frac{j}{N} \tag{2.9}$$

Where $j$=1, 2, …, $N$ is the subsection of the operating period, and $N$ is the number of IBC legs. Therefore, we can observe that the input current ripple $\Delta I_{IN}$= 0 when $d=j/N$ and the maximum value of the input current ripple of the IBC can be written as follows:

$$\Delta I_{IN,max} = \frac{V_O}{4NLf_{SW}}, \text{ for: } d = \frac{2j-1}{2N} \tag{2.10}$$

Then, the input current ripple expression of the FLIBC can be deduced using the equation (2.9) as below:

$$\Delta I_{IN} = \begin{cases} \dfrac{V_O}{Lf_{SW}} d\left(1-4d\right) & 0 < d \le \dfrac{1}{4} \\ \dfrac{V_O}{Lf_{SW}}\left(d-\dfrac{1}{4}\right)\left(2-4d\right) & \dfrac{1}{4} < d \le \dfrac{1}{2} \\ \dfrac{V_O}{Lf_{SW}}\left(d-\dfrac{1}{2}\right)\left(3-4d\right) & \dfrac{1}{2} < d \le \dfrac{3}{4} \\ \dfrac{V_O}{Lf_{SW}}\left(d-\dfrac{3}{4}\right)\left(4-4d\right) & \dfrac{3}{4} < d \le 1 \end{cases} \tag{2.11}$$

Meanwhile, the inductors' current ripple expression of the IBC is the same as that of the CBC.

$$\Delta I_{Lj} = \frac{V_O}{Lf_{SW}} d\left(1-d\right) \tag{2.12}$$

The normalized input current ripple variation of the IBC regarding the duty cycle is illustrated in Figure II-10. It is clear that the interleaving process ensures the decrease of the input current ripple of the IBC. Moreover, raising the number of legs leads to a reduction in the input current ripple.

On the other hand, the generalized equation of the output voltage ripple of the IBC is given in (2.13) [163]. Figure II-11 depicts the variation of the IBC output voltage ripple $\Delta V_O$ as a function of the duty cycle. It is noticed that the output voltage ripple decreases when the number of IBC legs increases. In addition, the $\Delta V_O$ becomes null for $d= k/N$ for $k$= 1,2, …, $N$-1, and its maximum value when $d$=1, where its value is given in (2.14).

$$\Delta V_O = \begin{cases} \dfrac{I_O}{C_O f_{SW}} \left( \dfrac{\left(d - \dfrac{j-1}{N}\right)\left(d - \dfrac{j}{N}\right)}{(d-1)} \right) & for: \dfrac{j-1}{N} \le d \le \dfrac{j}{N} \quad and: N \ge 2 \\ \dfrac{I_O}{C_O f_{SW}} \left( d - \dfrac{N-1}{N} \right) & for: \dfrac{N-1}{N} \le d \le 1 \end{cases} \tag{2.13}$$

$$\Delta V_{O\max} = \frac{I_O}{C_O f_{SW}} \left( 1 - \frac{N-1}{N} \right) \tag{2.14}$$

Then, the output voltage ripple of the FLIBC can be calculated using the following equation:

$$\Delta V_O = \begin{cases} \dfrac{I_O}{C_O f_{SW}} \left( \dfrac{d\left(d - \dfrac{1}{4}\right)}{(d-1)} \right) & 0 \le d \le \dfrac{1}{4} \\ \dfrac{I_O}{C_O f_{SW}} \left( \dfrac{\left(d - \dfrac{1}{4}\right)\left(d - \dfrac{1}{2}\right)}{(d-1)} \right) & \dfrac{1}{4} \le d \le \dfrac{1}{2} \\ \dfrac{I_O}{C_O f_{SW}} \left( \dfrac{\left(d - \dfrac{1}{2}\right)\left(d - \dfrac{3}{4}\right)}{(d-1)} \right) & \dfrac{1}{2} \le d \le \dfrac{3}{4} \\ \dfrac{I_O}{C_O f_{SW}} \left( d - \dfrac{3}{4} \right) & \dfrac{3}{4} \le d \le 1 \end{cases} \tag{2.15}$$

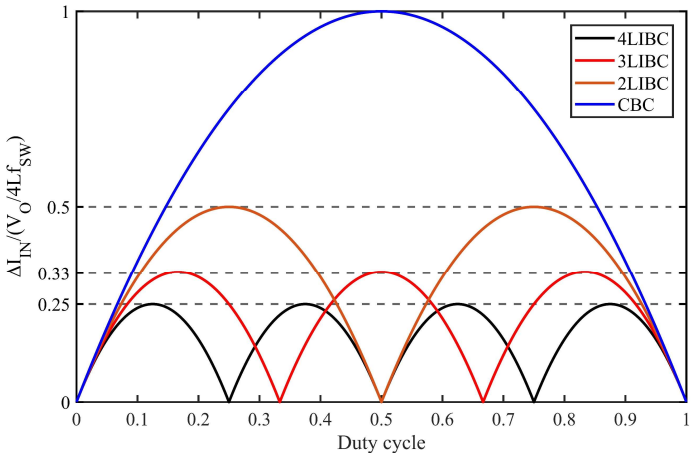


***Figure II-10 Normalized IBC input current ripple compared to CBC.***

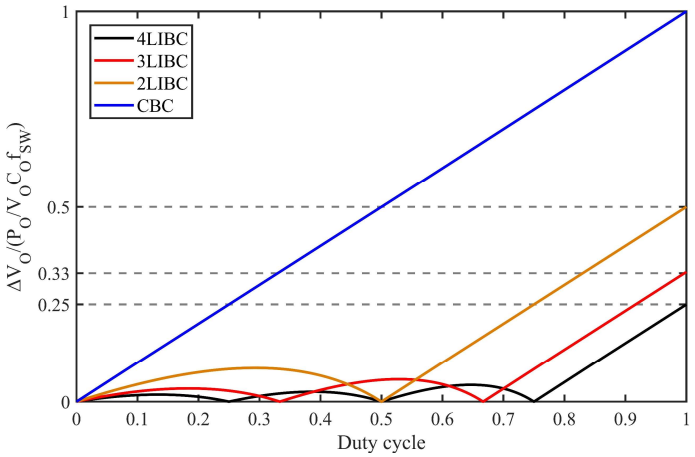


***Figure II-11 Normalized output voltage ripple of the IBC compared to CBC.***

### *3.1.3 IBC Modeling:*

As assumed above, the IBC inductors are identical ($L=L_1=L_2=\ldots=L_N$), and the diodes' internal resistance and forward voltage are neglected. The simplified average model of the IBC is presented according to the KVL and KCL using the following equations:

$$\begin{cases} \dfrac{dI_{Lj}(t)}{dt} = \dfrac{V_{PV}(t) - \left[1-d_j\right]V_O(t)}{L} \\ \dfrac{dV_O(t)}{dt} = \dfrac{\sum_{j=1}^{N} I_{Lj}(t)\left[1-d_j\right] - I_O(t)}{C_O} \end{cases} \quad j=1,2,\ldots,N \tag{2.16}$$

Where $V_{PV}$ is the PV panel voltage.

## *3.2 Design of Interleaved Boost Converter:*

The design of the interleaved boost converter is an important step in ensuring the optimal operation of the converter and maintaining the equal sharing of input current between the legs. The selection of the IBC component is subject to the system requirements, such as the maximum rated power, input voltage and current, output voltage and current, input current ripple, output voltage ripple, and the switching frequency.

### *3.2.1 Selection of Inductors:*

The equation that allows to calculate the value of the inductors $L$ of the IBC can be deduced from (2.10) the maximum input current ripple equation [164]:

$$L = \frac{V_O}{4N\Delta I_{IN,max} f_{SW}} \tag{2.17}$$

The inductance value can be decreased by increasing the switching frequency or increasing the number of IBC legs.

### *3.2.2 Selection of Capacitor CO:*

Using the equation of the maximum output voltage ripple (2.14), the expression of the output capacitor of the IBC can be given as follows:

$$C_O = \frac{I_O}{\Delta V_{O\max} f_{SW}} \left(1 - \frac{N-1}{N}\right) \tag{2.18}$$

### *3.3 PV System Based on Four Legs Interleaved Boost Converter:*

The PV systems have a major drawback represented in their nonlinear behavior. The power produced by PV systems depends on weather conditions such as solar radiation and temperature. Further, PV systems need to operate at their optimal performance, and a DC/DC converter and a reliable control strategy are necessary to track the maximum power point. In addition, large-scale PV systems require a suitable DC/DC converter to handle the high power. The IBC meets the abovementioned requirements due to its advantages. Figure II-12 shows the investigated PV system fed a FLIBC and connected to a load R.

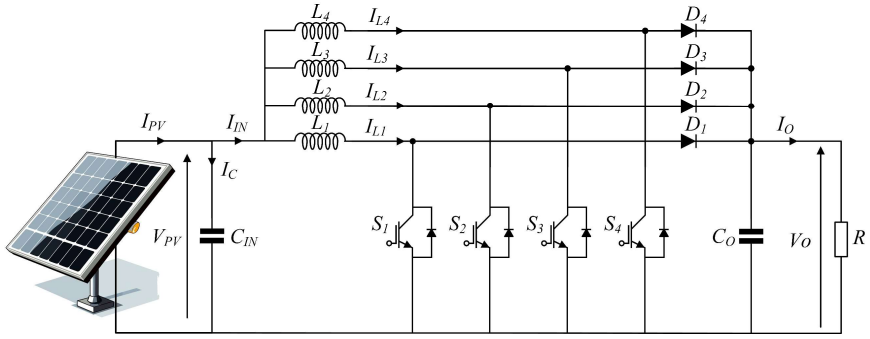


***Figure II-12 PV system fed four legs IBC.***

According to the circuit in Figure II-12, the differential equations that represent the legs current, the output voltage, and the PV system voltage are given by:

$$\begin{cases} \dfrac{dI_{Lj}(t)}{dt} = \dfrac{V_{PV}(t) - \left[1 - d_j\right] V_O(t)}{L} \\ \dfrac{dV_O(t)}{dt} = \dfrac{\sum_{j=1}^{4} I_{Lj}(t)\left[1 - d_j\right] - I_O(t)}{C_O} \quad j = 1,2,3,4 \\ \dfrac{dV_{PV}(t)}{dt} = \dfrac{I_{PV}(t) - I_{IN}(t)}{C_{IN}} \end{cases} \tag{2.19}$$

## *4 Control Strategies:*

A double-loop control strategy [165] is proposed to ensure the control objectives of an FLIBC, which are tracking the MPP of the PV system, equal current sharing between the legs, and obtaining a robust and fast response system. The general control scheme of the double loop control is illustrated in Figure II-13. It consists of an outer loop controlling the PV voltage to track its reference, provided by an MPPT algorithm. In addition, an inner loop guarantees equal current sharing between the FLIBC

legs, where the output controller of the outer loop serves as a current reference. The following will explain in detail the design of various parts of this controller.

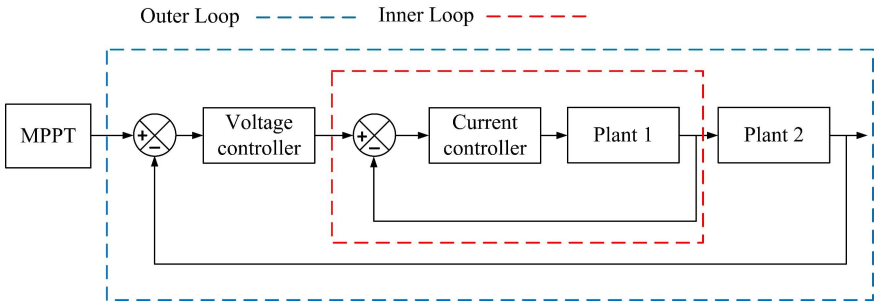


***Figure II-13 General scheme of the double loop control strategy.***

## *4.1 MPPT Controllers Design:*

As discussed in Chapter I, many algorithms are used to track the maximum power point of a PV system. This section will design the three most commonly used algorithms: incremental conductance and fuzzy MPPT.

### *4.1.1 Incremental Conductance:*

Incremental conductance is a method utilized to track the MPP of a PV system that has key differences compared to the P&O, such as fast tracking and high accuracy. The technique has been discussed in detail in the precedent chapter (Chapter I – section 2.5.2). The pseudocode of the incremental conductance is presented below.

***Pseudocode II-1 Incremental conductance algorithm steps.***

**1- Initialization:** define the initial values of the initial voltage reference $V_{PVref}(k)$, previous current $I_{PV}(k)$, step size $\Delta V > 0$, and the initial value of the measured voltage $V_{PV}(k)$ and current $I_{PV}(k)$.

**2- The measure of voltage and current:** acquire voltage $V_{PV}(k+1)$ and current $I_{PV}(k+1)$ measurements in real-time from the PV system. Then, calculate the difference between the current measurements and the previous measurements as follows: $\Delta V_{PV} = V_{PV}(k+1) - V_{PV}(k)$, $\Delta I_{PV} = I_{PV}(k+1) - I_{PV}(k)$

**3- Change the voltage reference according to the following conditions:**

- If $\Delta V_{PV} = 0$, & $\Delta I_{PV} = 0$ then ➔ $V_{Pvref}(k+1) = V_{PVref}(k)$.
- If $\Delta V_{PV} = 0$ & $\Delta I_{PV} > 0$, then ➔ $V_{Pvref}(k+1) = V_{PV}(k) + \Delta V$.
- If $\Delta V_{PV} = 0$ & $\Delta I_{PV} < 0$ & $\Delta I_{PV} / \Delta V_{PV} > -I_{PV}(k+1)/V_{PV}(k+1)$, then ➔ $V_{Pvref}(k+1) = V_{PV}(k) - \Delta V$.
- If $\Delta V_{PV} \neq 0$ & $\Delta I_{PV} / \Delta V_{PV} = -I_{PV}(k+1)/V_{PV}(k+1)$, then ➔ $V_{Pvref}(k+1) = V_{PV\,ref}(k)$.
- If $\Delta V_{PV} \neq 0$ & $\Delta I_{PV} / \Delta V_{PV} > -I_{PV}(k+1)/V_{PV}(k+1)$, then ➔ $V_{Pvref}(k+1) = V_{PV}(k) + \Delta V$.
- If $\Delta V_{PV} \neq 0$ & $\Delta I_{PV} / \Delta V_{PV} < -I_{PV}(k+1)/V_{PV}(k+1)$, then ➔ $V_{Pvref}(k+1) = V_{PV}(k) - \Delta V$.

**4- Update the previous variables with the current variables for the next iteration.**
$V_{PV}(k) = V_{PV}(k+1)$, $I_{PV}(k) = I_{PV}(k+1)$.

**5- Return the PV system voltage reference $V_{Pvref}(k+1)$.**

**6- Return to step 2 (voltage and current measurement) and continue the cycle.**

### *4.1.2 Fuzzy MPPT:*

The fuzzy MPPT is a controller that optimizes the operating point of the PV system to achieve the MPP and gather the peak power during varied climatic conditions [36]. As seen in (Chapter I- 2.5.5), the fuzzy logic controller consists of three essential stages: fuzzification, inference method, and defuzzification [166].

The fuzzification block is the process that converts the real input value into their corresponding degree of membership in the defined linguistic variable based on membership functions. In this controller, the size of the variation of the voltage reference is determined regarding the change of power with respect to the voltage (2.20) (the slope of the P-V curve $dP_{PV}/dV_{PV}$) and the rate of change of power (2.21) at a sampling time.

$$E(k) = \frac{P(k+1) - P(k)}{V_{PV}(k+1) - V_{PV}(k)} \tag{2.20}$$

$$CE = E(k+1) - E(k) \tag{2.21}$$

Therefore, the operating point of the PV system can be located using the slope of the P-V curve $E$ if it is on the right or the left side of the MPP, while $CE$ serves as an indicator of the change of $E$ over a sampling time, providing insights about the rate of acceleration or deceleration of the power change. On the other hand, the output of the fuzzy MPPT controller is the rate of variation of the PV system $\Delta V$ to track the optimal operating point where the slope $E$ equals zero. In the proposed controller, the input and output variables are divided into five fuzzy sets (linguistic variables), such as negative big (NB), negative small (NS), zero (Z), positive small (PS), and positive big (PB). Figure II-14 shows the membership functions of each fuzzy set of inputs and output.

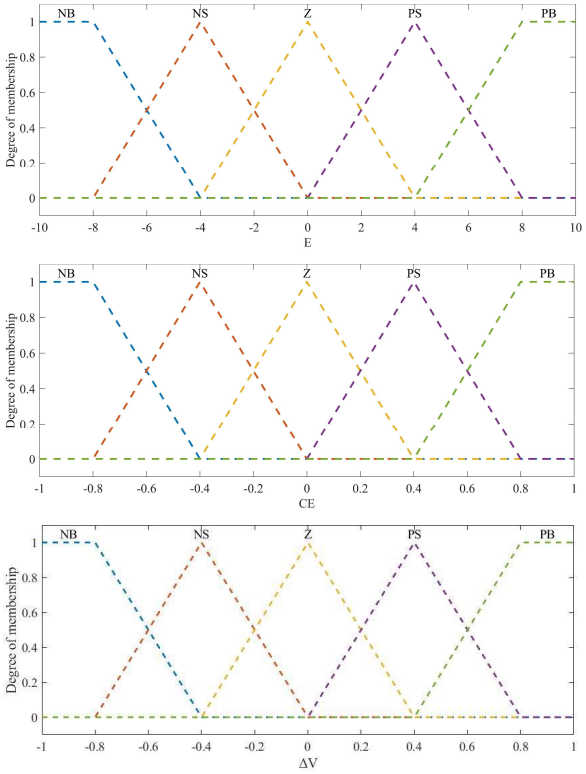


***Figure II-14 Fuzzy logic membership functions.***

The inference method is a process that applies the fuzzy rules to the fuzzy sets of the input in parallel to obtain the fuzzy set of the output corresponding to the rules [167]. The inference process is based on the Mamdani rule that uses the max-min operation. Where max is used for the operator (AND), and min

is used for the operator (OR). Table II-1 lists the proposed fuzzy MPPT rules based on the Mamdani method and the operation AND.

***Table II-1 Fuzzy MPPT rules.***

| E | CE | | | | |
|---|---|---|---|---|---|
| | **NB** | **NS** | **Z** | **PS** | **PB** |
| **NB** | Z | Z | NB | NB | NB |
| **NS** | Z | Z | NS | NS | NS |
| **Z** | NS | Z | Z | Z | PS |
| **PS** | PS | PS | PS | Z | Z |
| **PB** | PB | PB | PB | Z | Z |

The output of the proposed controller $\Delta V$ is obtained using the defuzzification step according to the output membership functions. Several methods have been proposed for the defuzzification process. The commonly used methods are the height method (HM), mean of maximum (MoM), and centroid of area (CoA) [167]. In this work, the designed fuzzy MPPT is implemented using the CoA, and its equation is given below:

$$\Delta V = \frac{\sum_{i=0}^{n} \Delta V_i \mu_z(\Delta V_i)}{\sum_{i=0}^{n} \mu_z(\Delta V_i)} \tag{2.22}$$

Here, $\Delta V_i$ represents the individual output values associated with each membership function, and $\mu_s$ represents the membership degree of $\Delta V_i$.

### *4.2 Proportional Integral Controller:*

The proportional integral is a linear feedback controller that adjusts a process or system to a desired setpoint. Due to its efficiency, low cost, and simple tuning, it is commonly used in various applications, such as industrial control systems, robotics, and automotive systems. The principle of operating the PI controller is based on the adjustment of the control signal *u(t)* based on the error between the setpoint and the measured output of the system. The time domain equation of the PI controller is composed of a proportional term and an integral term, as shown in equation (2.23):

$$u(t) = K_p\left(X_d(t) - X_m(t)\right) + K_i \int \left(X_d(t) - X_m(t)\right) dt \tag{2.23}$$

$K_p$, $K_i$, $X_d$, and $X_m$ denote the proportional and integral gain, the desired setpoint, and the system output, respectively.

#### *4.2.1 Design of The PV System Voltage Controller:*

According to the FLIBC module that is expressed in the equations (2.19), the deferential equation that describes the dynamic behavior of the PV system voltage is given below:

$$\frac{dV_{PV}(t)}{dt} = \frac{I_{PV}(t) - I_{IN}(t)}{C_{IN}} \tag{2.24}$$

Using the Laplace transform, the transfer function $G_V$ of the voltage open loop can be expressed as follows:

$$G_V(s) = \frac{V_{PV}(s)}{U_1(s)} = \frac{1}{C_{IN}s} \tag{2.25}$$

Where $U_1(s) = I_{PV}(s) - I_{IN}(s)$ is the output of the controller, and $s$ is a complex frequency domain parameter. On the other hand, the PI controller transfer function is given as below:

$$C_V(s) = \frac{u(s)}{E(s)} = K_{pv} + \frac{K_{iv}}{s} \tag{2.26}$$

Therefore, the voltage closed-loop transfer function is given in equation (2.27):

$$G_{VC}(s) = \frac{\frac{K_{pv}}{C_{IN}}s + \frac{K_{iv}}{C_{IN}}}{s^2 + \frac{K_{pv}}{C_{IN}}s + \frac{K_{iv}}{C_{IN}}} \tag{2.27}$$

Many methods of tuning the PI controller parameters include the Ziegler-Nicloas method, trial and error, pole placement, and artificial intelligence. To meet the desired performance, such as response time and overshoot, the closed-loop transfer function is compared to the canonical form transfer function of the second-order system. Equation (2.28) expresses the second-order system transfer function.

$$F(s) = \frac{\omega^2}{s^2 + 2\zeta\omega s + \omega^2} \tag{2.28}$$

Z denotes the damping ratio, and $\omega$ is the natural angular frequency. Therefore, the PI parameters of the voltage control loop can be calculated as follows:

$$K_{pv} = 2\xi_v\omega_v C_{IN} \quad K_{iv} = \omega_v^2 C_{IN} \tag{2.29}$$

### *4.2.2 Design of The Equal Current Sharing Controller:*

The inner loop controller aims to achieve balanced current distribution among the FLIBC legs. Each leg's current reference is derived by dividing the voltage controller's output by the number of legs (4 legs). The PI controller parameters are tuned using the previous manner in the voltage controller. The transfer function of the current open loop is written as below:

$$G_I(s) = \frac{I_{Lj}(s)}{U_{2j}(s)} = \frac{1}{Ls} \tag{2.30}$$

Where $U_{2j} = V_{PV} - (1 - d_j)\, V_O$. The closed-loop transfer function is expressed as follows:

$$G_{IC}(s) = \frac{\frac{K_{pc}}{L}s + \frac{K_{ic}}{L}}{s^2 + \frac{K_{pc}}{L}s + \frac{K_{ic}}{L}} \tag{2.31}$$

Therefore, the PI parameters are calculated using the following equations:

$$K_{pc} = 2\xi_c\omega_c L \quad K_{ic} = \omega_c^2 L \tag{2.32}$$

The duty cycle that fed the pulse width modulation block can be calculated using the following equation:

$$d_j = 1 + \frac{U_{2j} - V_{PV}}{V_O} \tag{2.33}$$

The control scheme of the FLIBC based on the PI controller is illustrated in Figure II-15.

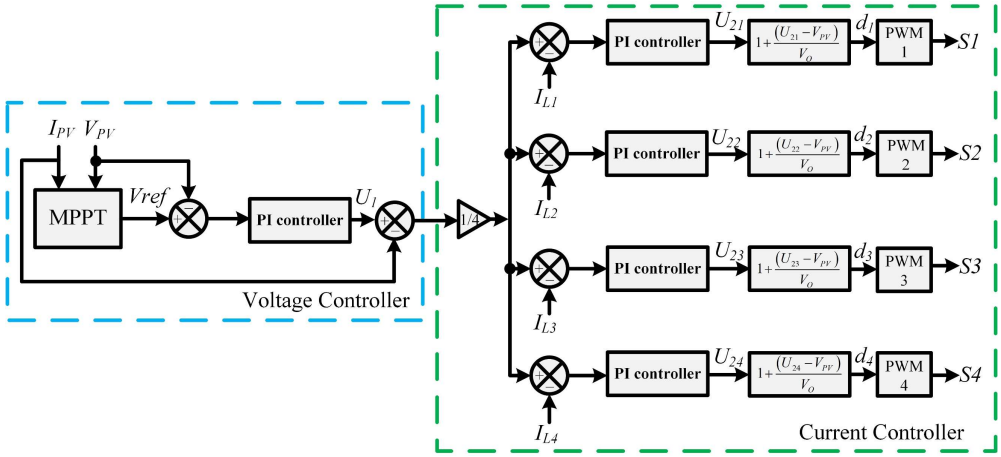


Figure II-15 PI Control scheme of PV system fed FLIBC.

### *4.3 Backstepping Controller:*

Backstepping control [32] is a powerful nonlinear control technique that stabilizes and regulates complex dynamical systems. It is particularly well-suited for systems that can be represented as a cascade of interconnected subsystems. In this section, we design a BS controller for the FLIBC-based PV system to achieve the desired control objectives:

- MPPT: The BS controller will ensure that the PV system operates at its maximum power point by tracking the reference voltage provided by the MPPT algorithm.
- Equal Current Sharing: The controller will guarantee balanced current distribution among the FLIBC legs, improving system efficiency and reliability.
- Robustness and Stability: The BS controller design will focus on achieving robust performance and stability against parameter variations and external disturbances.

The BS controller approach involves designing virtual control laws for each subsystem in the cascade, progressively "stepping back" from the final output to the input [168]. BS controller allows for the systematic construction of a Lyapunov function that guarantees the overall system's stability.

In the following, we will detail the design process of the BS controller for the FLIBC-based PV system, including the selection of Lyapunov functions, derivation of virtual control laws, and stability analysis.

The differential equations of the FLIBC used to design the backstepping controller are shown in (2.19). Let us define the tracking error of subsystem 1 as follows:

$$\begin{cases} e_1 = V_{PV} - V_{ref} \\ e_2 = \int \left( V_{PV} - V_{ref} \right) dt \end{cases} \tag{2.34}$$

Where $V_{ref}$ is the desired voltage given by the MPPT algorithm, then the derivative of the tracking errors is shown below:

$$\begin{cases} \dot{e}_1 = \dot{V}_{PV} - \dot{V}_{ref} = \dfrac{1}{C_{IN}}\left(I_{PV} - I_{IN}\right) - \dot{V}_{ref} \\ \dot{e}_2 = e_1 \end{cases} \tag{2.35}$$

The Lyapunov function $V_1$ and its derivative are defined as follows:

$$V_1 = \frac{1}{2}e_1^2 + \frac{\lambda_1}{2}e_2^2 \tag{2.36}$$

$$\dot{V}_1 = e_1\dot{e}_1 + \lambda e_2 e_1 = e_1\left[\frac{1}{C_{IN}}\left(I_{PV} - I_{IN}\right) - \dot{V}_{ref} + \lambda_1 e_2\right] \tag{2.37}$$

Where $V_1$ is a positive definite and $\lambda_1 > 0$ is a design parameter, to ensure the asymptotic stability of subsystem 1, the derivative of the Lyapunov function should be negatively defined ( $\dot{V}_1 < 0$ ). Therefore, the derivative of the Lyapunov function becomes as follows:

$$\dot{V}_1 = e_1\left[\frac{1}{C_{IN}}\left(I_{PV} - I_{IN}\right) - V_{ref} + \lambda e_2\right] = -K_1 e_1^2 \tag{2.38}$$

Then, the virtual control law $\delta$ that is considered as a setpoint of subsystem 2 can be deduced from (2.38) as follows:

$$\delta = \frac{I_{IN}}{4} = \frac{1}{4}\left[I_{PV} + C_{IN}(K_1 e_1 + \lambda e_2 - \dot{V}_{ref})\right] \tag{2.39}$$

Here, $K_1$ represents a positive constant that serves as a design parameter.

To design the BS controller of the equal current sharing, let us define the tracking errors of subsystem 2 as follows:

$$\begin{cases} e_{3j} = I_{Lj} - \delta \\ e_{4j} = \int\left(I_{Lj} - \delta\right)dt \end{cases} \tag{2.40}$$

The time derivative of $e_{3j}$ can be given as follows:

$$\dot{e}_{3j} = \dot{I}_{Lj} - \dot{\delta} = \frac{1}{L}\left(V_{PV} - \left(1 - d_j\right)\right)V_O - \dot{\delta} \tag{2.41}$$

Using equation (2.40), we find that:

$$I_{Lj} = e_{3j} + \delta \tag{2.42}$$

Replacing equation (2.42) in equation (2.35), the time derivative of the tracking error $e_1$ can rewritten as follows:

$$\dot{e}_1 = \frac{1}{C_{IN}}\left(I_{PV} - 4e_{3j} - 4\delta\right) - \dot{V}_{ref} \tag{2.43}$$

By the combination of equations (2.39) in (2.43), equation (2.43) can be reformulated as:

$$\dot{e}_1 = -K_1 e_1 - \lambda_1 e_2 - \frac{4}{C_{IN}}e_3 \tag{2.44}$$

Then, the time derivative of the Lyapunov function of subsystem 1 becomes as follows:

$$\dot{V}_1 = e_1\dot{e}_1 + \lambda_1 e_2 e_1 = e_1\left[-K_1 e_1 - \frac{4}{C_{IN}}e_{3j}\right] = -K_1 e_1^2 - \frac{4}{C_{IN}}e_{3j}e_1 \tag{2.45}$$

The Lyapunov function of subsystem 2 is a positive definite as follows:

$$V_2 = V_1 + \frac{1}{2}e_{3j}^2 + \frac{\lambda_2}{2}e_{4j}^2 \tag{2.46}$$

Where $\lambda_2$ is a positive design parameter, the derivative of $V_2$ with respect to time can written as:

$$\dot{V}_2 = \dot{V}_1 + e_{3j}\dot{e}_{3j} + \lambda_2 e_{4j}e_{3j} = -K_1 e_1^2 + e_3\left(\dot{e}_3 + \lambda_2 e_{4j} - \frac{4}{C_{IN}}e_1\right) \tag{2.47}$$

Then, for the asymptotic stability of subsystem 2, the derivative of the Lyapunov function should be negative definite $\dot{V}_2 < 0$ as follows:

$$\dot{V}_2 = -K_1 e_1^2 + e_3\left(\dot{e}_3 + \lambda_2 e_{4j} - \frac{4}{C_{IN}}e_1\right) = -K_1 e_1^2 - K_2 e_{3j}^2 \tag{2.48}$$

Where $K_2$ is a positively defined design parameter, then, from (2.48), we found:

$$\left(\dot{e}_3 + \lambda_2 e_{4j} - \frac{4}{C_{IN}}e_1\right) = \frac{1}{L}\left(V_{PV} - \left(1 - d_j\right)\right)V_O - \dot{\delta} + \lambda_2 e_{4j} - \frac{4}{C_{IN}}e_1 = -K_2 e_{3j} \tag{2.49}$$

Therefore, the virtual control law $d_j$ can be deduced using (2.49):

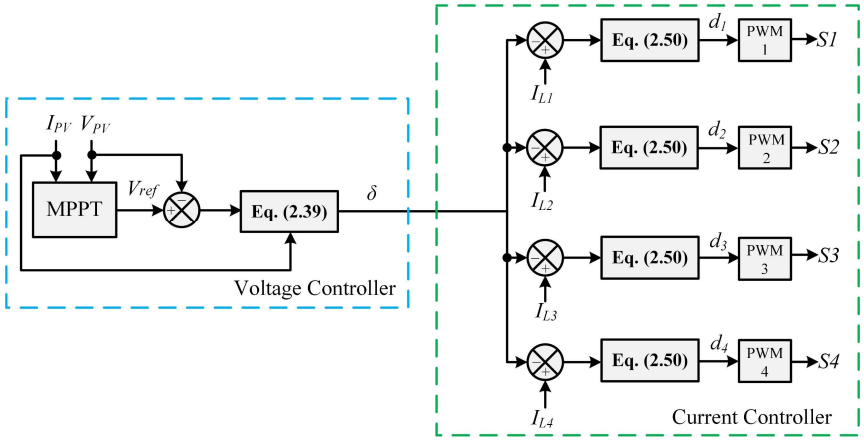


***Figure II-16 BS controller scheme for PV system fed FLIBC.***

$$d_j = 1 + \frac{L\left(\dot{\delta} - \lambda_2 e_{4j} + \frac{4}{C_{IN}}e_1 - K_2 e_{3j}\right) - V_{PV}}{V_O} \tag{2.50}$$

Finally, the control scheme of the BS controller-based FLIBC is shown in Figure II-16.

### *4.4 Sliding Mode Controller:*

SMC [169] is a nonlinear control for controlling variable structure systems. The objective of the SMC is to change a nonlinear system's behavior using a discontinuous control signal and ensure robust performance. SMC involves creating a control law that guides the system state to a chosen sliding surface and keeps it there. This sliding surface is a "boundary" separating various system behaviors. The SMC is widely used to control DC-DC boost converters due to its beneficial characteristics, such as high efficiency, fast transient response, stability, and robustness against parameter variation and

external disturbances [6]. The following SMC and super twisting SMC (STSMC) are designed for the FLIBC-based PV system.

### *4.4.1 First Order Sliding Mode Controller:*

The objective is to force the PV system's voltage to track the reference provided by the MPPT controller and ensure equal current sharing among the FLIBC legs. Implementing the SMC scheme involves two steps. The first is choosing the sliding surface that the system should follow to achieve the control objectives. The second step is designing the control law implemented to maintain the system's state trajectory on the sliding surface by adjusting its trajectory.

The sliding surface is selected as (2.51) to guarantee the gathering of maximum power of the PV system. The selected sliding surface is a combination of the error between the PV voltage and its setpoint value provided by the MPPT.

$$S_1 = e_1 + \lambda_3 e_2 \tag{2.51}$$

Here, $\lambda_3$ is a positive definite gain, $e_1$ and $e_2$ are the trajectory errors of subsystem 1, which are given by:

$$\begin{cases} e_1 = V_{PV} - V_{ref} \\ e_2 = \int \left( V_{PV} - V_{ref} \right) dt \end{cases} \tag{2.52}$$

The key advantages of this control approach are robustness and stability. This stability is demonstrated by the following Lyapunov function, which is relevant to the surface's attractiveness:

$$V_1 = \frac{1}{2} S_1^2 \tag{2.53}$$

The time derivative of equation (2.53) must be negative in order to guarantee asymptotic stability close to the equilibrium point.

$$\dot{V}_1 = S_1 \dot{S}_1 \leq 0 \tag{2.54}$$

The control law of the SMC consists of two parts, as shown in (2.55). The equivalent control law $u_{eq}$ is responsible for generating the control signal necessary to ensure the convergence of the system's trajectory toward the sliding surface during the reaching phase. On the other hand, the discontinuous part $u_{SW}$ acts as a switching control, ensuring that the system's trajectory is maintained on the sliding surface. It compensates for uncertainties and disturbances and guarantees the robustness of the SMC.

$$u_{SMC} = u_{eq} + u_{SW} \tag{2.55}$$

When designing the reaching control law $u_{eq}$, it should be ensured that the time derivative of the sliding surface equals zero, and solve the equation for the control law, as follows:

$$\dot{S}_1 = \dot{e}_1 + \lambda_3 \dot{e}_2 = 0 \tag{2.56}$$

Can rewrite (2.56) as follows:

$$\dot{S}_1 = \frac{1}{C_{IN}} \left( I_{PV} - I_{IN} \right) - \dot{V}_{ref} + \lambda_3 e_2 = 0 \tag{2.57}$$

Then, the reaching control law can be deduced as follows:

$$u_{eq} = I_{INeq} = I_{PV} + C_{IN}\left(\lambda_3 e_1 - \dot{V}_{ref}\right) \tag{2.58}$$

Moreover, the discontinuous control law can be given as follows [170]:

$$u_{SW} = I_{INSW} = K_3 sign(S_1) \tag{2.59}$$

$K_3 > 0$ is a positive design parameter, and sign is a switching function that checks the sign of the sliding surface. Then, the control law can be written as:

$$I_{IN} = I_{INeq} + I_{INSW} = I_{PV} + C_{IN}\left(\lambda_3 e_1 - \dot{V}_{ref}\right) + K_3 sign(S_1) \tag{2.60}$$

To prove the stability of the closed-loop voltage subsystem, it should be valid that the positive Lyapunov function is decreased along the sliding surface as follows:

$$\dot{V}_1 = S_1\dot{S}_1 = S_1\left(\frac{1}{C_{IN}}\left(I_{PV} - \left[I_{INeq} + I_{INSW}\right]\right) - \dot{V}_{ref} + \lambda_3 e_1\right) \tag{2.61}$$

Using (2.60), we can rewrite the time derivative of the Lyapunov function as follows:

$$S_1\dot{S}_1 = S_1\left(\frac{1}{C_{IN}}\left(I_{PV} - \left[I_{PV} + C_{IN}\left(\lambda_3 e_1 - \dot{V}_{ref}\right) + K_3 sign(S)\right]\right) - \dot{V}_{ref} + \lambda_3 e_1\right) \tag{2.61}$$

Then, equation (2.61) becomes as:

$$S\dot{S} = S\left(-\frac{K_3}{C_{IN}} sign(S)\right) < 0 \tag{2.62}$$

Therefore, the control law satisfies the stability analysis criteria, where the time derivative of the Lyapunov function is negative definite, indicating the system's asymptotic stability.

The SMC law of subsystem 2 can be designed following the precedent steps. Firstly, choosing the sliding surface as follows:

$$S_2 = e_3 + \lambda_4 e_4 \tag{2.63}$$

Where $e_3$ and $e_4$ are trajectory errors of subsystem 2 that are defined in equation (2.64):

$$\begin{cases} e_3 = I_{Lj} - \delta \\ e_4 = \int\left(I_{Lj} - \delta\right)dt \end{cases} \tag{2.64}$$

In which δ represents the inductors current reference ($\delta = 0.25 I_{IN}$). To ensure the robustness and stability of subsystem 2, let us define the following positive definite Lyapunov function:

$$V_2 = \frac{1}{2} S_2^2 \tag{2.65}$$

The Lyaponuv function stability and convergence of the trajectory errors to the sliding surface can be ensured by satisfying that the time derivative of the Lyapunov function $V_2$ is negative definite as follows:

$$\dot{V}_2 = S_2\dot{S}_2 \leq 0 \tag{2.66}$$

Initially formulating the equivalent control law $u_{eq}$ by assuming that the time derivative of the sliding surface is equal to zero allows for designing the control law satisfying the condition mentioned above. Subsequently, the equation can be solved for the equivalent control.

$$\dot{S}_2 = \dot{e}_3 + \lambda_4\dot{e}_4 = \dot{I}_{Lj} - \dot{\delta} + \lambda_4 e_3 = 0 \tag{2.67}$$

Then, substituting equation (2.19) in (2.67), we found:

$$\dot{S}_2 = \frac{V_{PV} - (1 - d_{jeq})V_O}{L} - \dot{\delta} + \lambda_4 e_3 = 0 \tag{2.68}$$

Therefore, the equivalent control law of subsystem 2 can be given as:

$$d_{jeq} = 1 + \frac{L\left(\dot{\delta} - \lambda_2 e_3\right) - V_{PV}}{V_O} \tag{2.69}$$

Moreover, adding a discontinuous control part is necessary to maintain the trajectory errors on the sliding surface.

$$d_{jSW} = -K_4 sign(S_2) \tag{2.70}$$

Therefore, the sliding mode control law of the subsystem 2 can be expressed as follows:

$$d_j = d_{jeq} + d_{jSW} = 1 + \frac{L\left(\dot{\delta} - \lambda_4 e_3\right) - V_{PV}}{V_O} - K_4 sign\left(S_2\right) \tag{2.71}$$

To prove the closed loop stability of subsystem 2, it should verify the Lyapunov function stability condition:

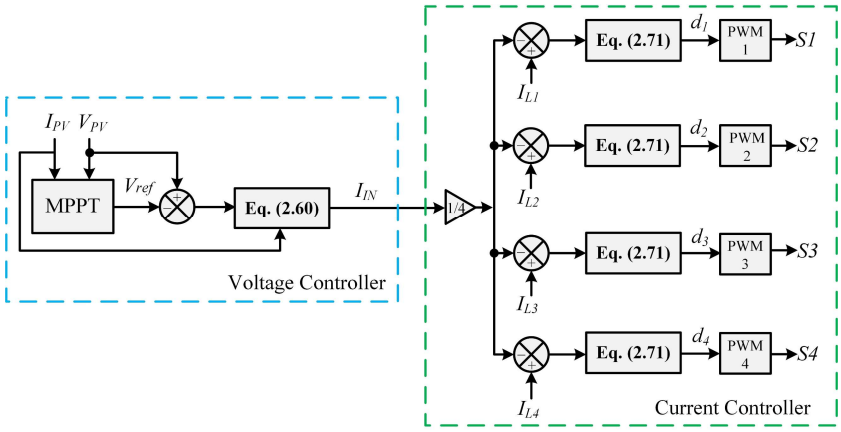


***Figure II-17 SMC Control scheme of PV system fed FLIBC.***

$$\dot{V}_2 = S_2\dot{S}_2 = S_2\left(\frac{V_{PV} - (1 - d_j)V_O}{L} - \dot{\delta} + \lambda_4 e_3\right) \tag{2.72}$$

By replacing the expression of $d_j$ (2.71) into the equation (2.72), we get:

$$\dot{V}_2 = S_2\dot{S}_2 = -S_2\frac{L}{V_O}K_4 sign\left(S_2\right) < 0 \tag{2.73}$$

The SMC diagram is depicted in Figure II-17.

### *4.4.2 Super Twisting Sliding Mode Controller:*

STSMC is a modern control approach utilized in a variety of applications, including power electronics [171] and renewable energy systems such as PV systems [172]. It is an improvement of conventional sliding mode control that aims to increase system performance, robustness, transient response, and reduce chattering. Moreover, STSMC also offers improved accuracy and superior tracking outcomes in dynamic environments. In the following, we will detail the design process of the ST-SMC for the FLIBC-based PV system. The STSMC control law can be expressed as follows:

$$u_{ST-SMC} = u_{eq} + u_{ST} \tag{2.74}$$

$u_{eq}$ is the equivalent control law, similar to the one derived for SMC in equation (2.58). Meanwhile, $u_{ST}$ is the super-twisting control law, defined as [67]:

$$u_{ST} = -\left(\alpha\sqrt{|S|}sign(S) + \beta\int sign(S)dt\right) \tag{2.75}$$

Here, α and β are positive design parameters that determine the STSMC's convergence rate and chattering reduction.

Then, the control law of the subsystem 1 can be given as follows:

$$I_{IN} = I_{PV} + C_{IN}\left(\lambda_5 e_1 - \dot{V}^*_{ref}\right) - \left(\alpha_1\sqrt{|S_1|}sign(S_1) + \beta_1\int sign(S_1)dt\right) \tag{2.76}$$

While the control law of the subsystem 2 is defined as:

$$d_j = 1 + \frac{L\left(\dot{\delta} - \lambda_6 e_3\right) - V_{PV}}{V_O} - \left(\alpha_2\sqrt{|S_2|}sign(S_2) + \beta_2\int sign(S_2)dt\right) \tag{2.77}$$

The STSMC control scheme is illustrated in Figure II-18.

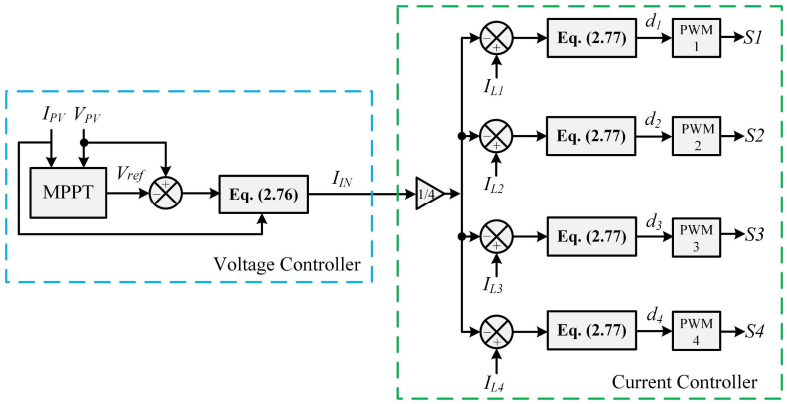


***Figure II-18 STSMC Control scheme of PV system fed FLIBC.***

## 5 *Simulation Results and Discussion:*

In this section, a comprehensive evaluation and comparison of the performance of the different proposed controllers is performed and implemented in MATLAB/Simulink. Firstly, the performance of the FLIBC and the CBC based on the PI controller is provided to prove the superiority of the FLIBC, as seen in section 3. In addition, a comparison between the proposed MPPTs is offered to analyze their performance. Secondly, the proposed BS controller, SMC, and STSMC will be compared with the PI controller to verify their performance. The simulation parameters of the PV system, CBC, FLIBC, and the proposed controllers are listed in Table II-2, Table II-3, and Table II-4. The irradiation and temperature profiles used in the simulation are illustrated in Figure II-19.

*Table II-2 PV system parameters.*

| PV System Parameters | Value |
|---|---|
| **Maximum power $P_{mpp}$ (1000 w/m², 25 °C)** | 85.14 W |
| **Maximum power voltage $V_{MPP}$** | 17.27 V |
| **Maximum power current $I_{MPP}$** | 4.93 A |
| **Open circuit voltage $V_{OC}$** | 21.83 V |
| **Short circuit current $I_{SC}$** | 5.33 A |
| **Short-circuit current temperature coefficient $K_I$** | 0.069 %/°C |
| **Open circuit voltage temperature coefficient $K_V$** | - 0.39 %/°C |
| **Number of series cells per module $n_s$** | 36 |
| **Number of series-connecter modules per string $N_{sm}$** | 35 |
| **Number of parallel strings $N_{pm}$** | 21 |

*Table II-3 The CBC and FLIBC parameters.*

| Parameters | Value | |
|---|---|---|
| | **CBC** | **FLIBC** |
| **Inductor $L$** | 5 mH | 5 mH |
| **The output capacitor $C_O$** | 46 µF | 46 µF |
| **The input capacitor $C_{IN}$** | 1200 µF | |
| **The load $R$** | 44 Ω | |
| **Switching frequency $f_{SW}$** | 25 kHz | |

*Table II-4 Parameters of the proposed controllers.*

| Controller | Parameters | FLIBC | CBC |
|---|---|---|---|
| **PI** | $K_{pv}$ | 36 | 12 |
| | $K_{iv}$ | $27x10^4$ | $3x10^4$ |
| | $K_{pc}$ | 280 | 56.56 |
| | $K_{ic}$ | $3.92x10^6$ | $32x10^4$ |
| **BS** | $K_1$ | $5.52x10^4$ | |
| | $K_2$ | $10x10^6$ | |
| | $\lambda_1$ | 2147.9 | |
| | $\lambda_2$ | $8x10^6$ | |
| **SMC** | $K_3$ | 3340 | |
| | $K_4$ | 20 | |
| | $\lambda_3$ | 0.1 | |
| | $\lambda_4$ | 0.4 | |
| **STSMC** | $\lambda_5$ | 0.001 | |
| | $\lambda_6$ | 6 | |
| | $\alpha_1$ | 20 | |
| | $\alpha_2$ | 198 | |
| | $\beta_1$ | 4 | |
| | $\beta_2$ | 2.2 | |

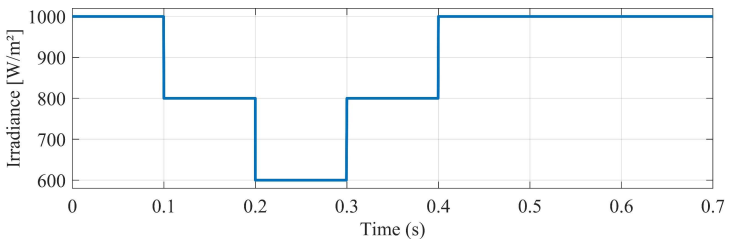


*(a)*

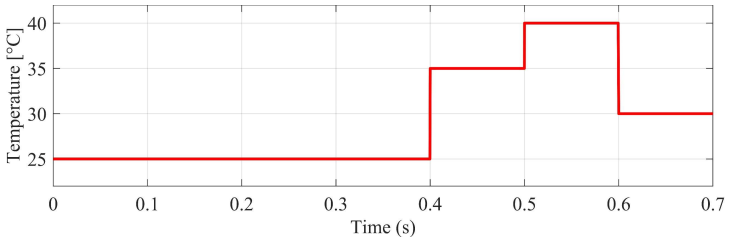


*(b)*

***Figure II-19 Simulation profile of the irradiation (a) and the temperature (b).***

## *5.1 Performance Analysis of The FLIBC based on PI Controller:*

The FLIBC power circuit (Figure II-12) and the PI controller scheme (Figure II-15) are implemented using MATLAB/Simulink environment. The IC MPPT algorithm is used to track the peak power of the PV system. The simulation results of the PV system based on FLIBC and CBC controlled using a PI controller are shown in Figure II-20 and Figure II-26.

According to the PV system voltage curves in Figure II-20 and Figure II-21, the PV system based on CBC or FLIBC tracks the reference voltage provided by the MPPT control. However, the FLIBC presents superior performance compared to the CBC in terms of response time, voltage ripple, and overshoot. In zone A, the FLIBC tracks the reference in 0.022 s, while the CBC tracks the reference in 0.026 s. In zone B, the voltage ripple presented using the FLIBC is 0.8 V. On the other hand, the CBC presents a high voltage ripple equal to 10.8 V, while in zone C, the FLIBC shows a faster response than the CBC.

Figure II-22 shows the PV system current; it is clear that the FLIBC reduces the PV system current ripples which improve the PV system's lifespan.

The input current of the FLIBC and CBC is illustrated in Figure II-23. The input current ripple of the FLIBC is less than the input current ripple in the CBC. The current ripple reduction is due to the interleaving technique (phase shift between FLIBC legs) used in the FLIBC. In addition, the FLIBC inductors current is shown in Figure II-24. The dual loop control based on the PI controller achieves equal current sharing among the legs.

Thanks to the IC algorithm, the FLIBC tracks the peak power. It presents a fast-tracking time and low power ripple compared to the CBC, as shown in the behavior of PV system power in Figure II-25.

Finally, the output voltage and current of the FLIBC and CBC are depicted in Figure II-26. The output voltage and current ripple are reduced significantly using the FLIBC. On the other hand, the CBC shows a high output voltage and current ripple. The reduction of the output ripples leads to an enhancement in the lifespan of loads and reduces the power losses.

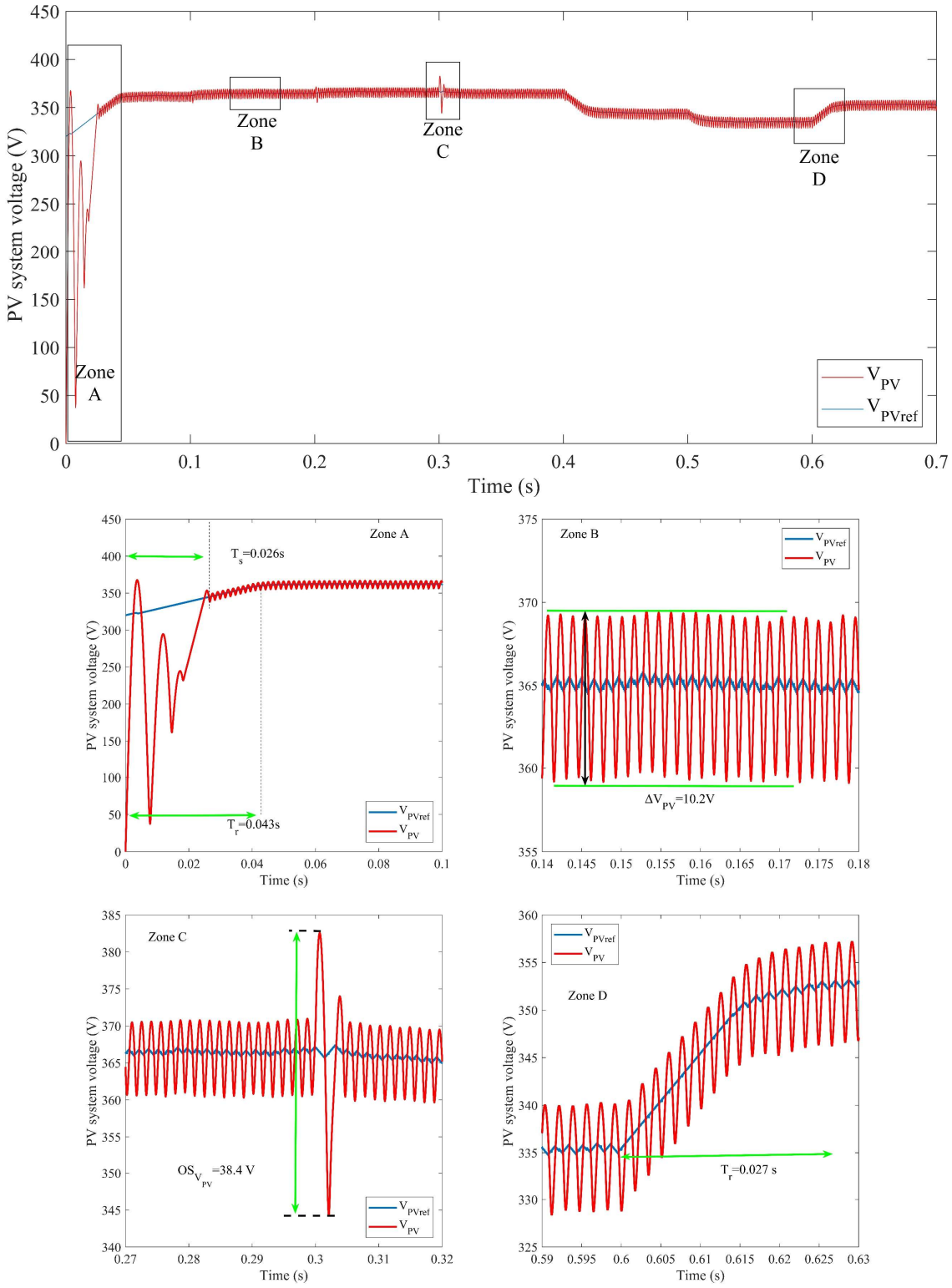


***Figure II-20 The voltage of the PV system based on CBC.***

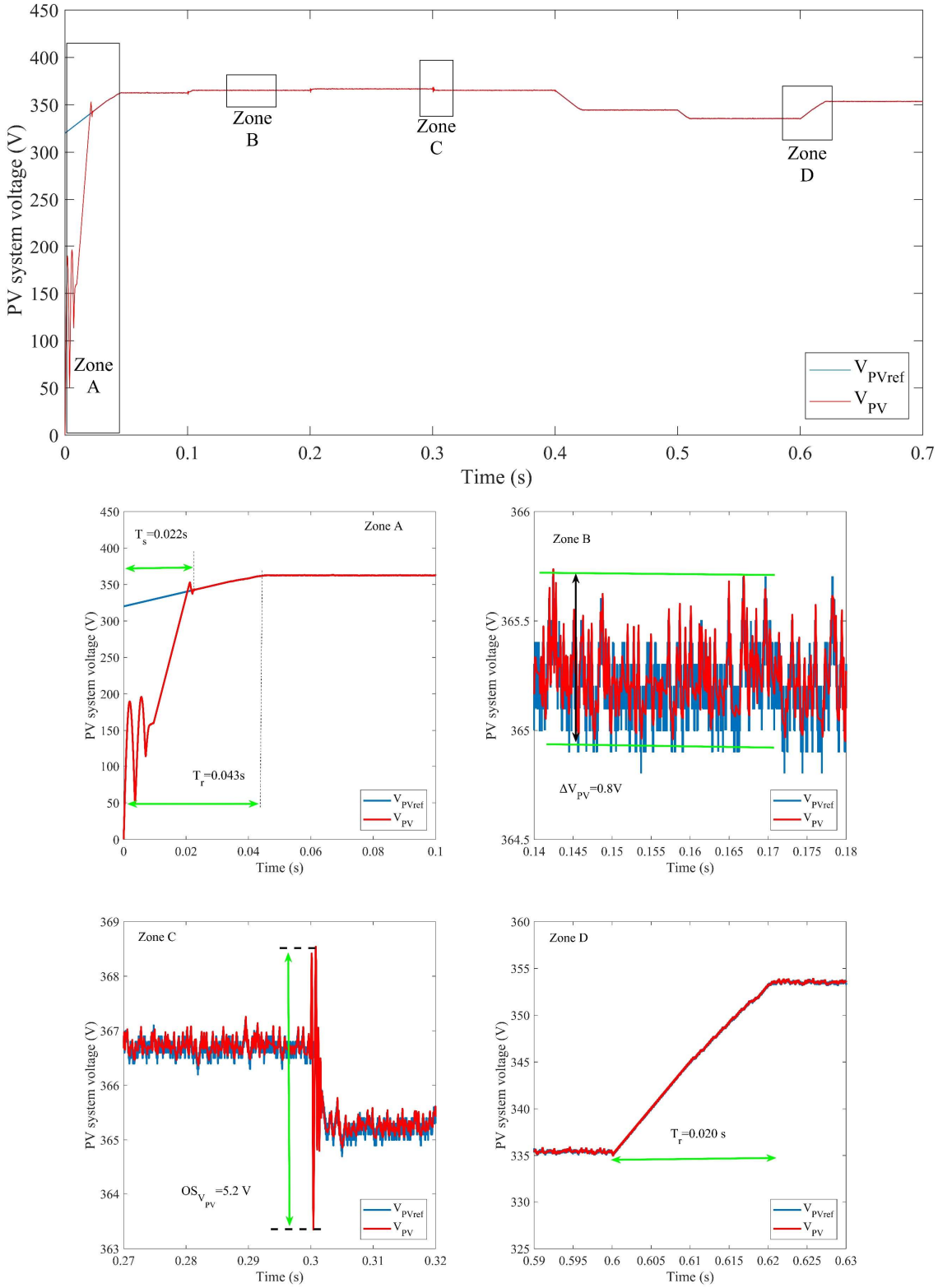


***Figure II-21 The voltage of the PV system based on FLIBC.***

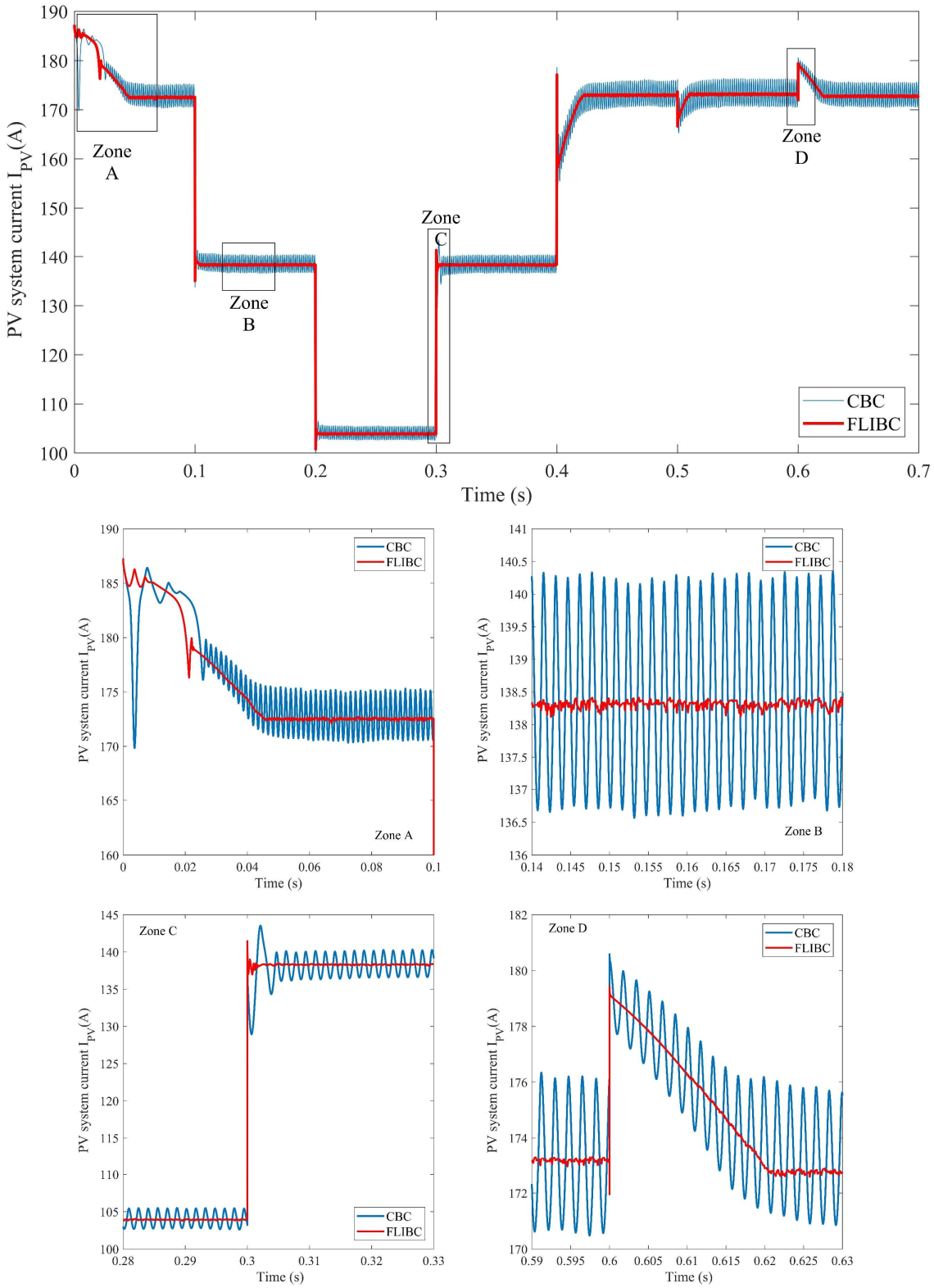


***Figure II-22 The PV system current using the FLIBC and CBC.***

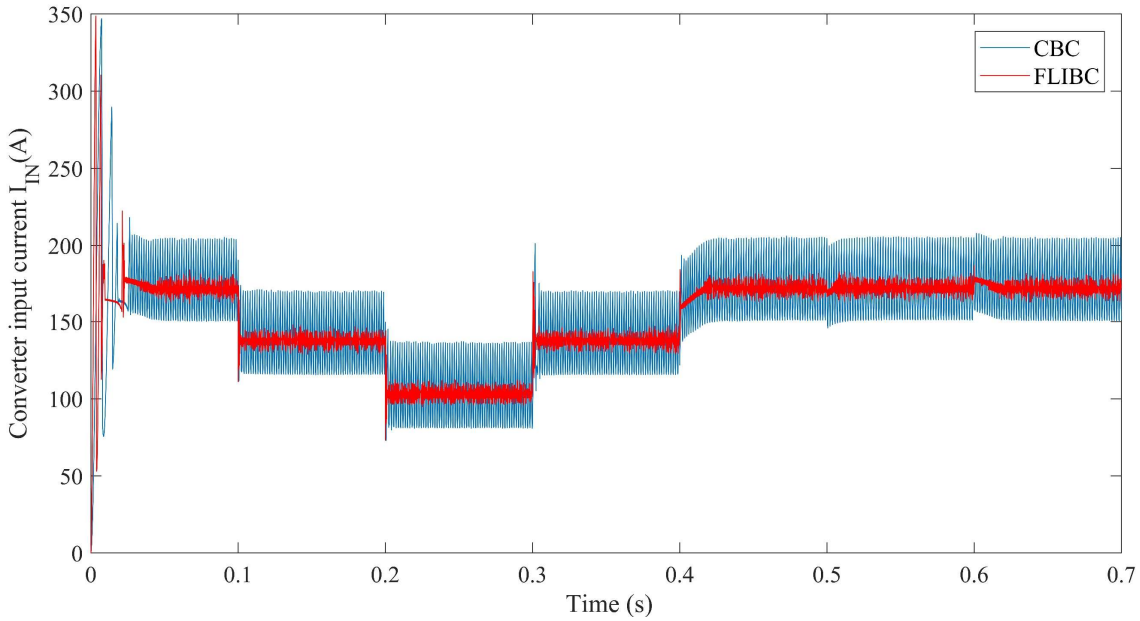


***Figure II-23 Converters input current $I_{IN}$.***

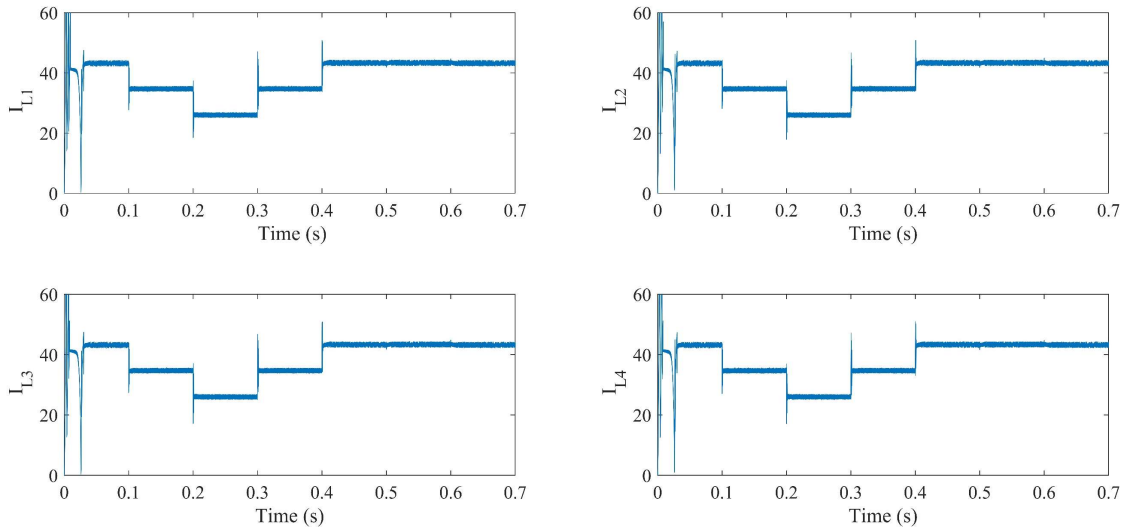


***Figure II-24 Equal current sharing between FLIBC legs.***

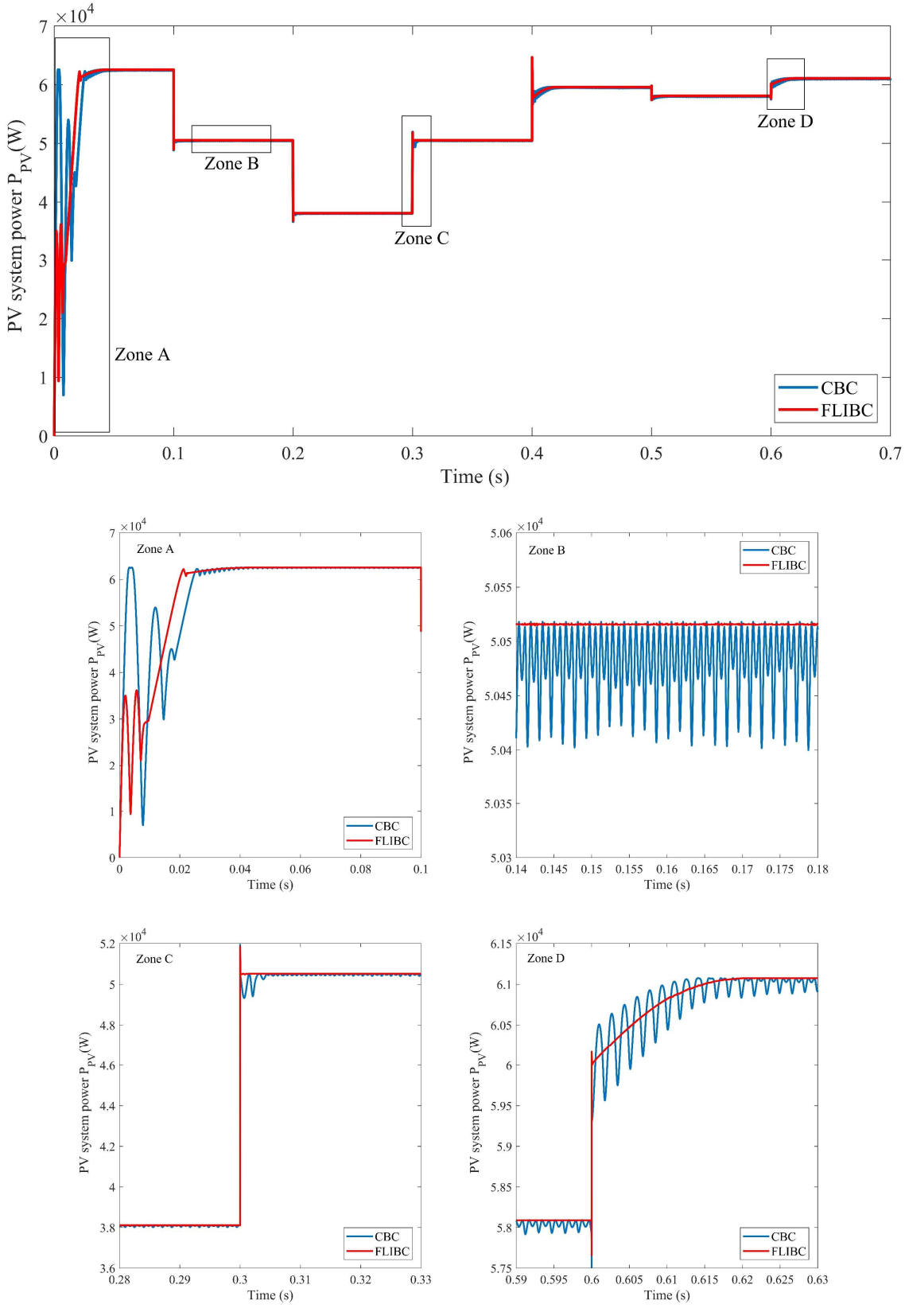


***Figure II-25 PV system produced power.***

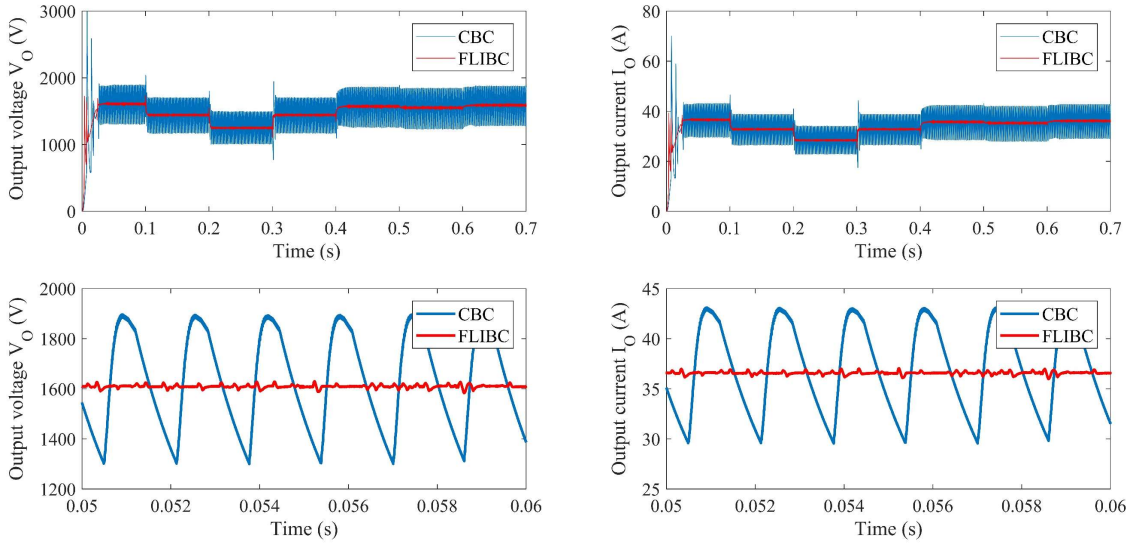


***Figure II-26 Output voltage and current of the FLIBC compared with CBC.***

## *5.2 Performance Analysis of MPPT Algorithms:*

The FLIBC-based PV system has been tested under the control of both the IC and fuzzy logic MPPT algorithms. Considering the aforementioned weather conditions, the test was conducted using MATLAB/Simulink. The comparison between the two algorithms considers the tracking time of the peak power and the power ripple. The voltage curves of the PV system are illustrated in Figure II-27, with further detail provided by zooming in on the zones, as shown in Figure II-28 and Figure II-29. As can be seen, the fuzzy logic MPPT exhibits faster convergence due to the quicker adjustment to weather changes and reduced voltage ripple around the maximum power voltage thanks to the continuous adjusting of the operating voltage based on the fuzzy logic mechanism. On the other hand, IC typically requires more iterations to converge to the MPP because it perturbs the operating point and compares changes in power to determine the direction of movement toward the MPP. As a result, it exhibits slightly longer tracking times compared to fuzzy logic.

In zone A, the fuzzy logic MPPT achieves a tracking time of 37 ms, faster than the IC algorithm's 43 ms. In comparison, the voltage ripple of the PV system decreased from 0.8 V to 0.35 V, which is attributed to the utilization of the fuzzy Logic MPPT, as seen in zone B. In zone C, the overshoot is almost similar in both algorithms. However, the IC algorithm exhibits a higher voltage ripple in the same zone than the fuzzy logic approach. The fast convergence to the $V_{MPP}$ using fuzzy logic MPPT is demonstrated in zone D, as shown in Figure II-29.

The PV system power curves using the Fuzzy logic MPPT and IC are illustrated in Figure II-30. It is clear that the fuzzy logic MPPT exhibits a fast convergence to the peak power during fast-changing weather conditions and has a reduced power ripple compared to the IC algorithm.

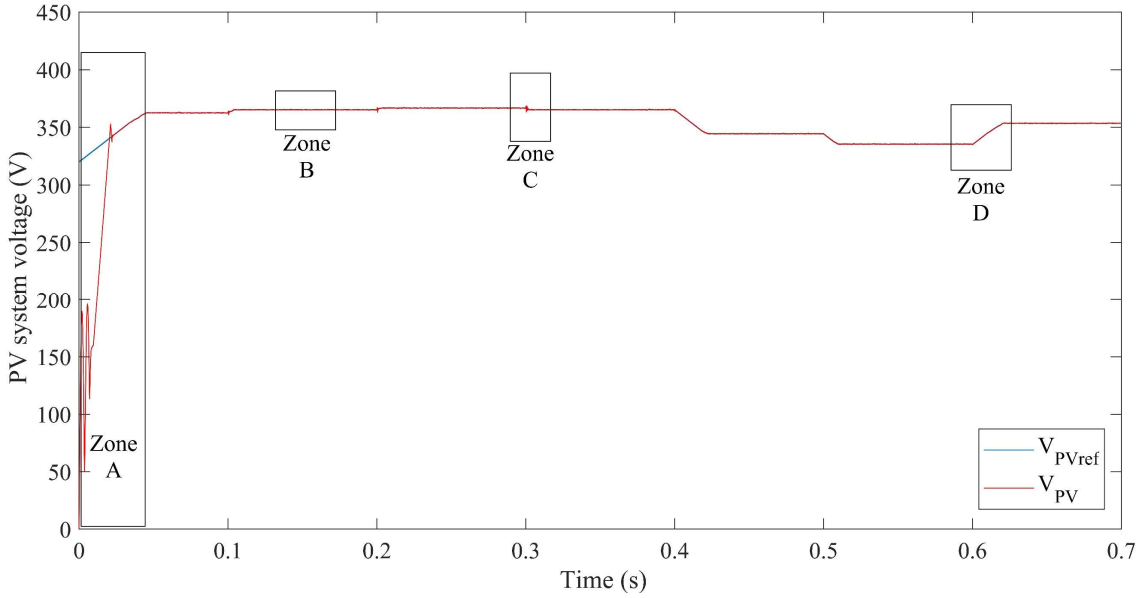


***(a)***

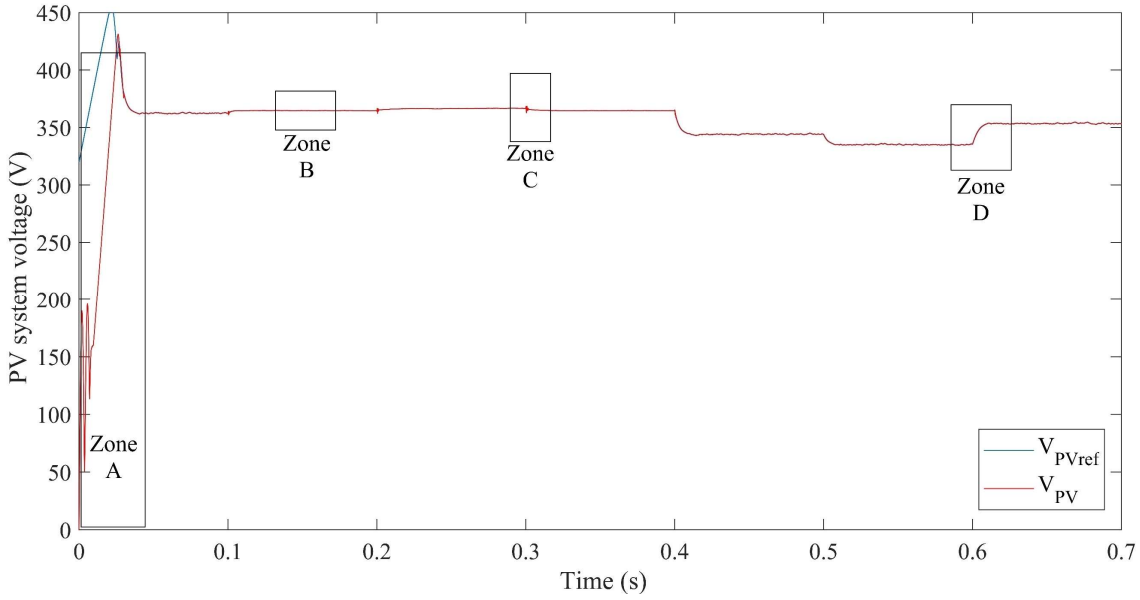


***(b)***

***Figure II-27 The curve of PV system voltage: IC (a) and Fuzzy logic (b)***

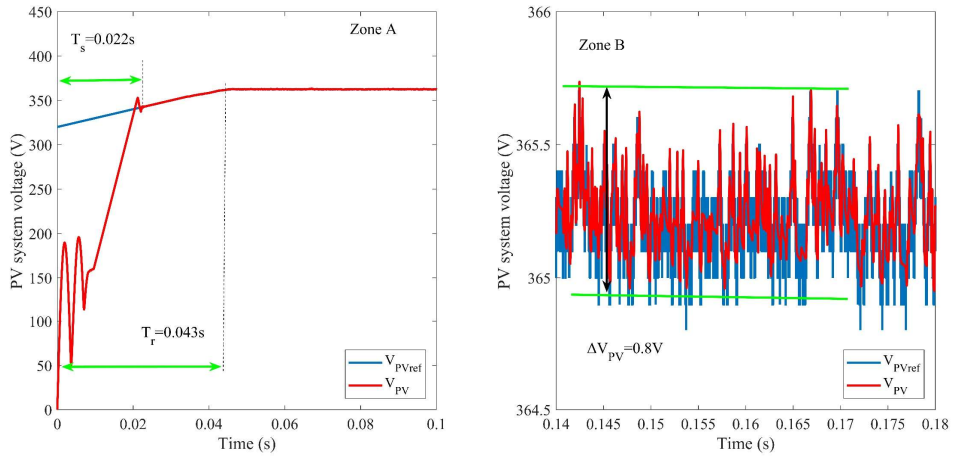


***(a)***

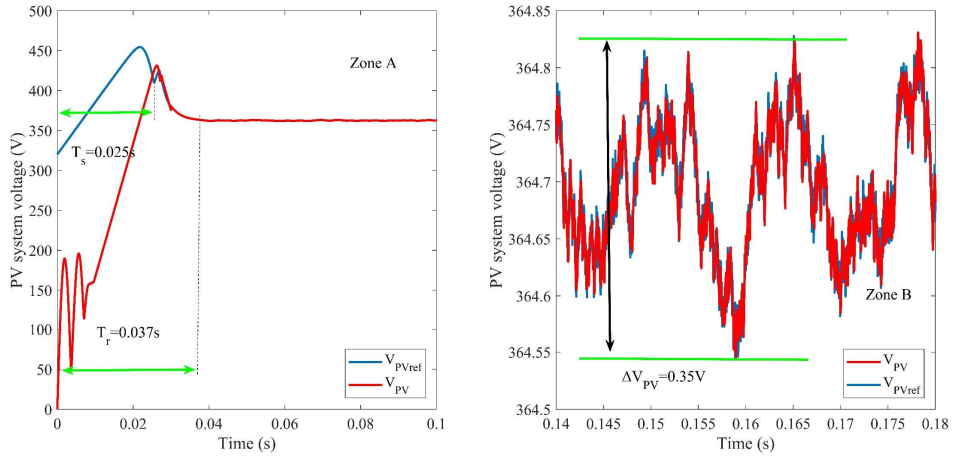


***(b)***

***Figure II-28 Zoom on Zone A and B of the curve of PV system voltage: IC (a) and Fuzzy logic (b)***

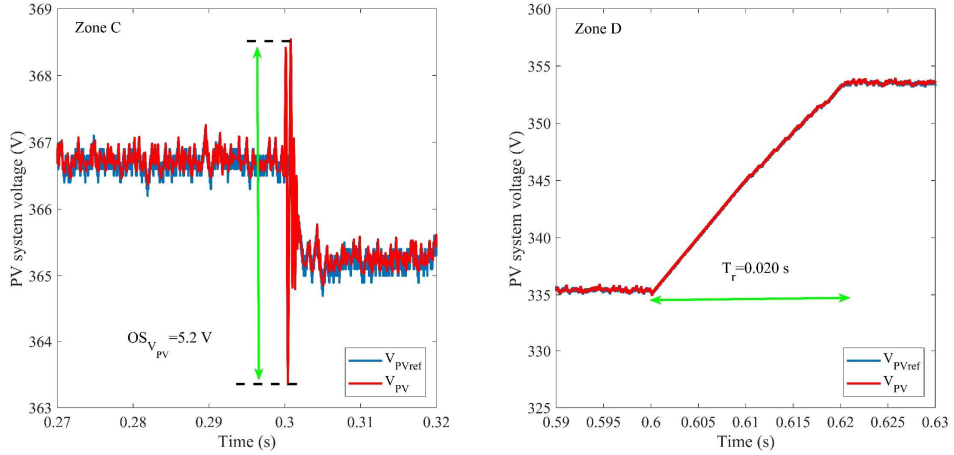


***(a)***

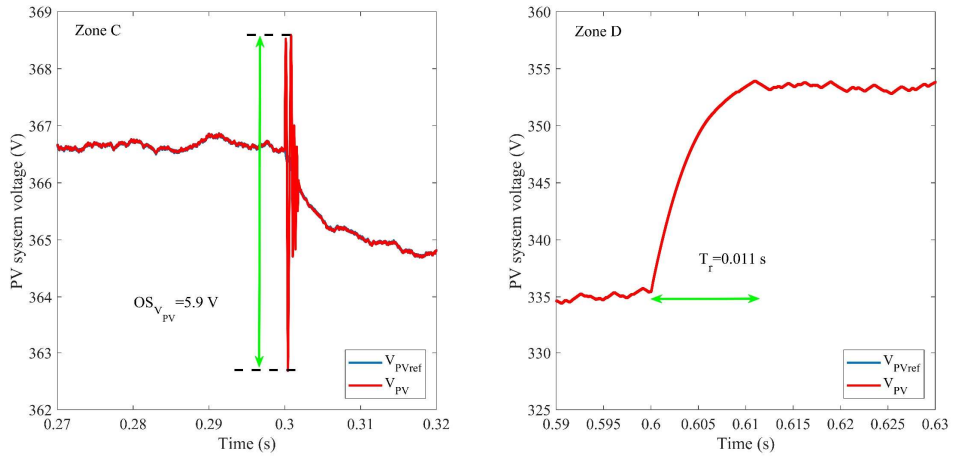


***(b)***

***Figure II-29 Zoom on Zone C and D of the curve of PV system voltage: IC (a) and Fuzzy logic (b)***

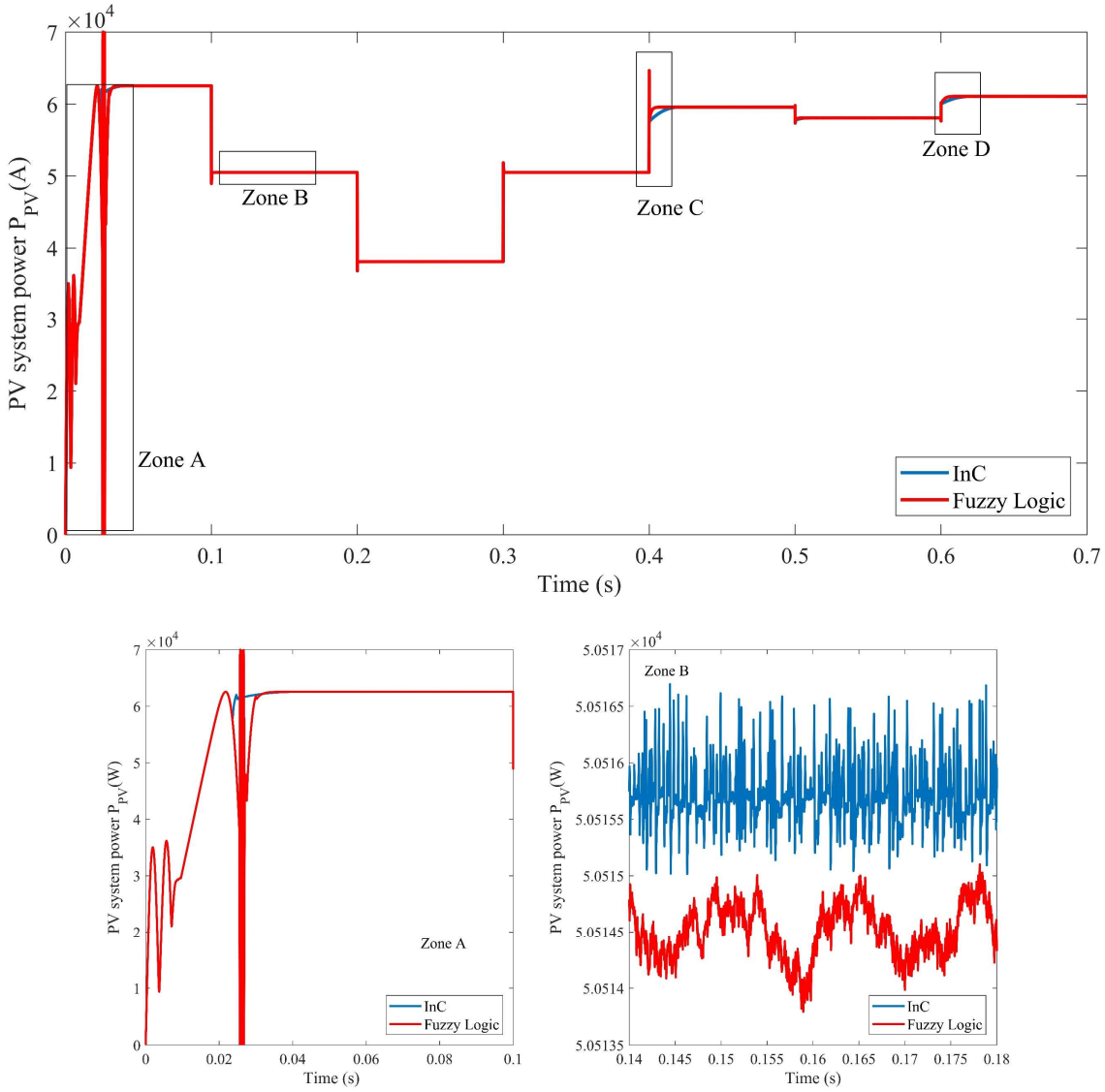

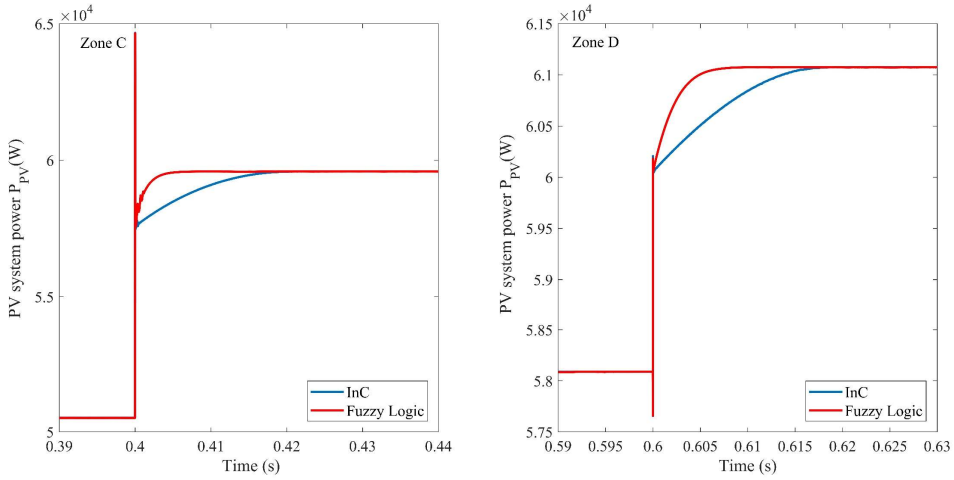


***Figure II-30 The PV system power curves using the IC and Fuzzy logic MPPT algorithms.***

## *5.3 Performance Analysis of The FLIBC based on BS Controller:*

This section investigates the FLIBC connected to a PV system and controlled using nonlinear backstepping control. The control scheme shown in Figure II-16 is applied to the system using MATLAB/Simulink. In this part, the fuzzy logic MPPT is utilized to track the MPP due to its superiority over the IC. The simulation parameters are listed in Table II-4. The simulation results of the BS controller are compared with those of the PI controller.

Figure II-31 shows the voltage behavior of the PV system fed a FLIBC and controlled using a fuzzy logic MPPT and BS controller. The BS controller demonstrates significant improvements in both response time $T_s$ and the tracking time $T_r$ compared to the PI controller. Moreover, voltage ripple around the operating voltage and overshoot during weather disturbances are considerably reduced. Specifically, the BS controller achieves a response time of 4 ms, while the PI controller lags at 22 ms. Similarly, the BS controller tracks the MPP in 6 ms, whereas the PI controller requires 43 ms, as seen in zone A. Zone B shows a reduction in voltage ripple with BS controller equal to 0.6 V compared to the PI controller 0.8 V. Overshoot in zone C is also significantly reduced from 5.2 V with PI control to 1.9 V with BS controller. Finally, zone D further confirms the optimized tracking time of BS controller (4.3 ms) compared to the PI controller (20 ms).

Figure II-32 compares the PV system's current curves under BS controller and PI control, again highlighting the BS controller's superior performance. Figure II-33 illustrates the PV system's power behavior, with zoomed-in zones showcasing the BS controller improves the MPP tracking time.

Finally, Figure II-34 shows the current of the FLIBC inductors, demonstrating that the BS controller contributes to an equal distribution of current between the FLIBC legs.

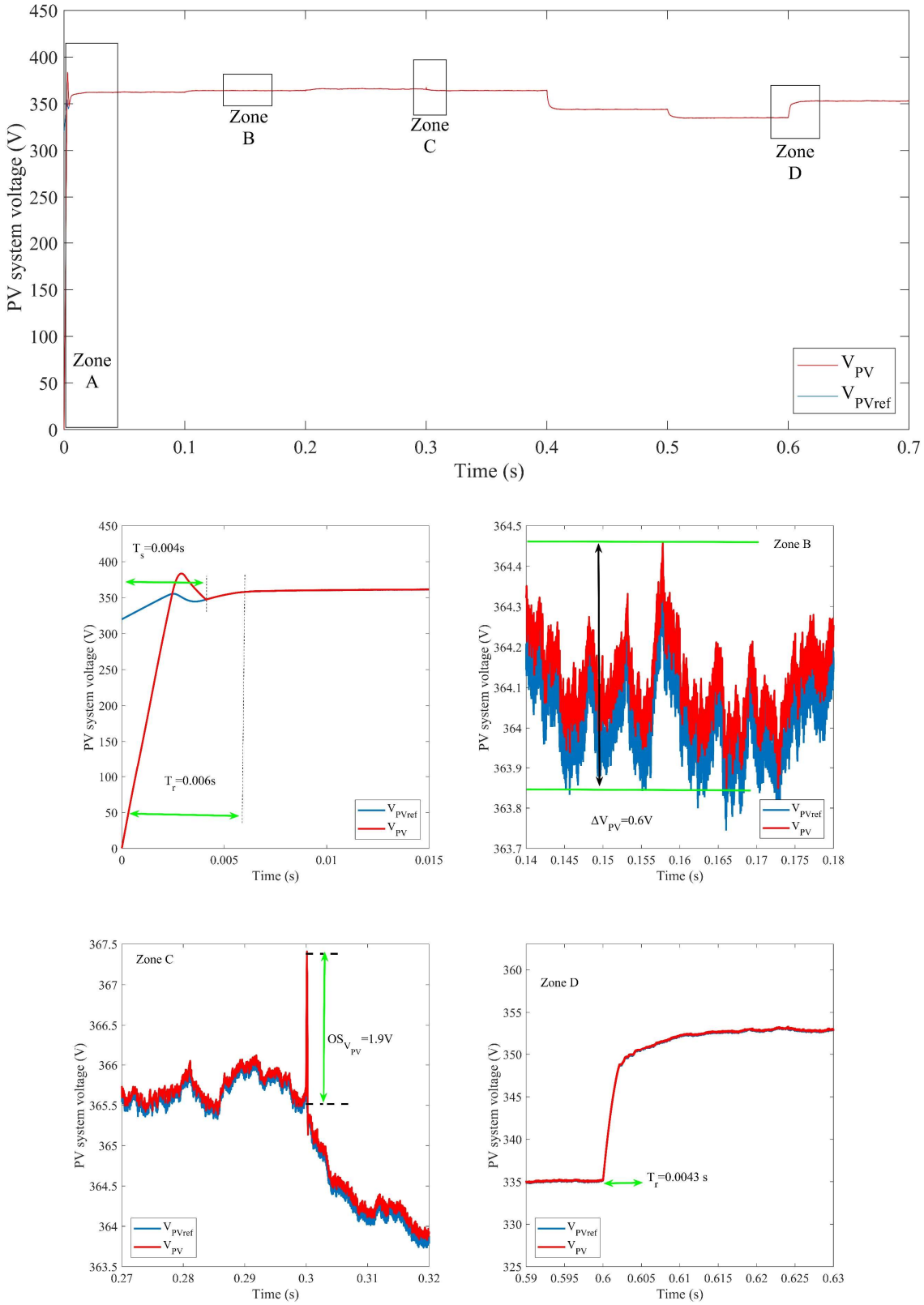


***Figure II-31 PV system's voltage curve using BS controller.***

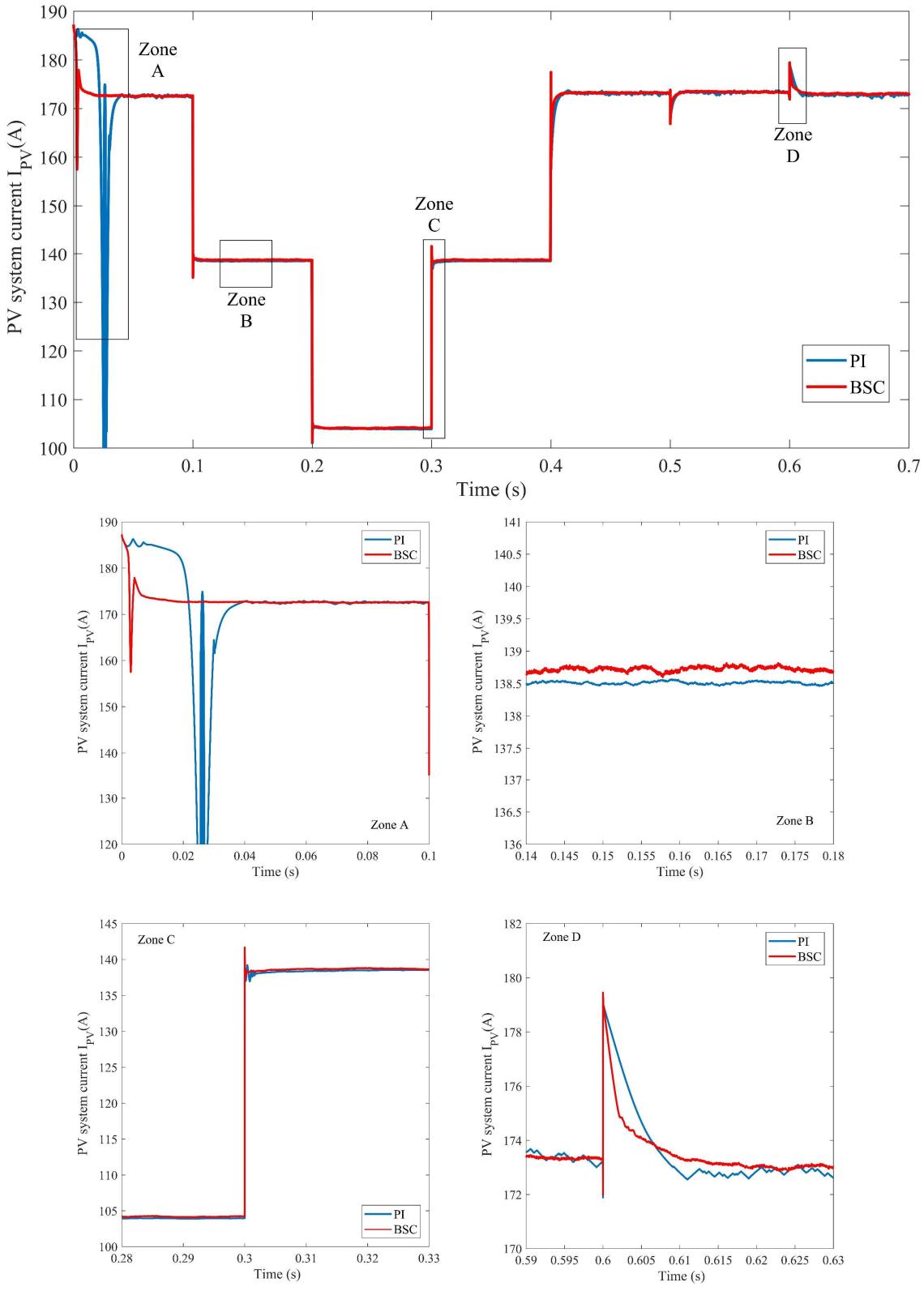


***Figure II-32 PV system's current curves using BS controller and PI controller.***

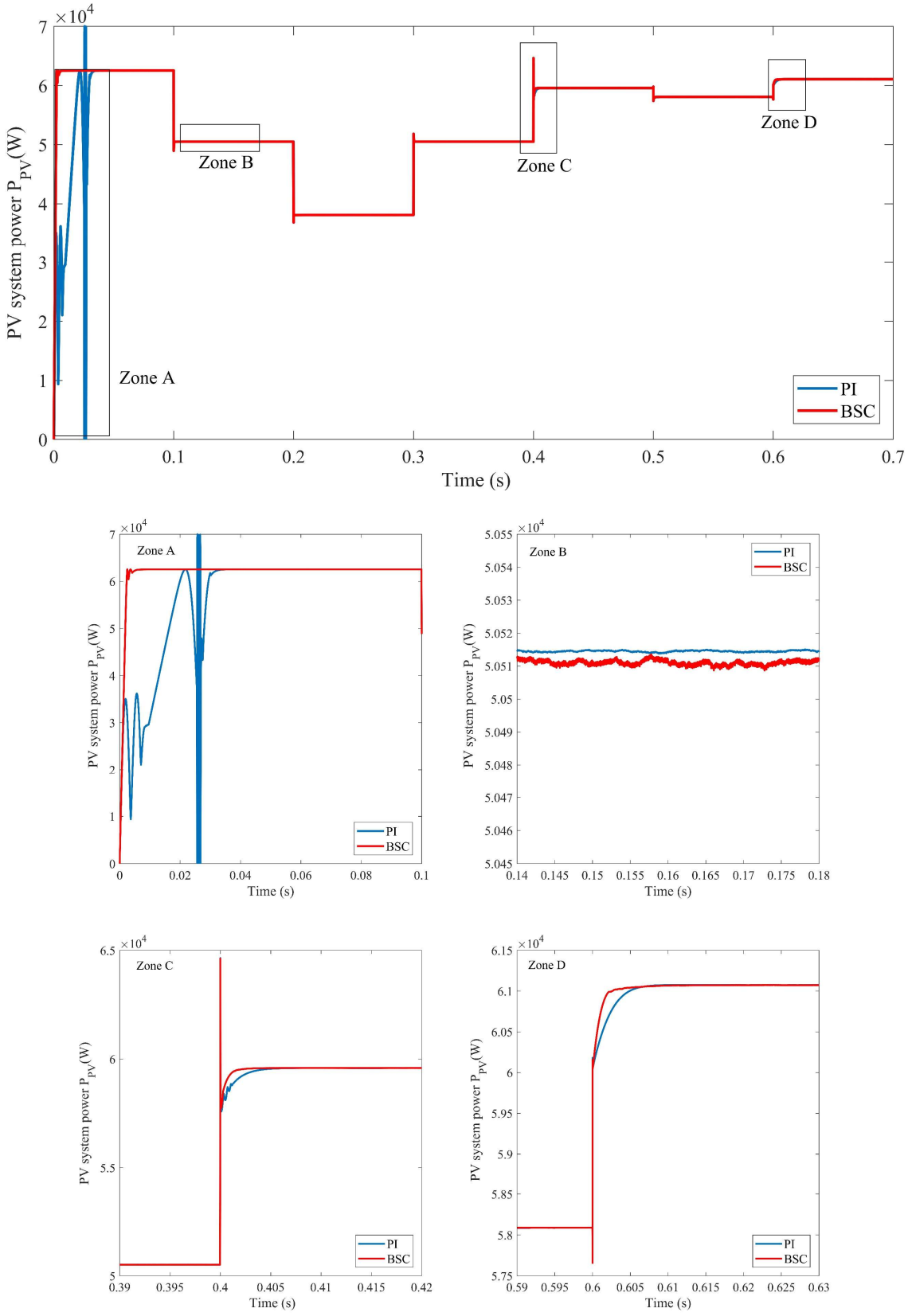


***Figure II-33 PV system's power curves using BS controller and PI controller.***

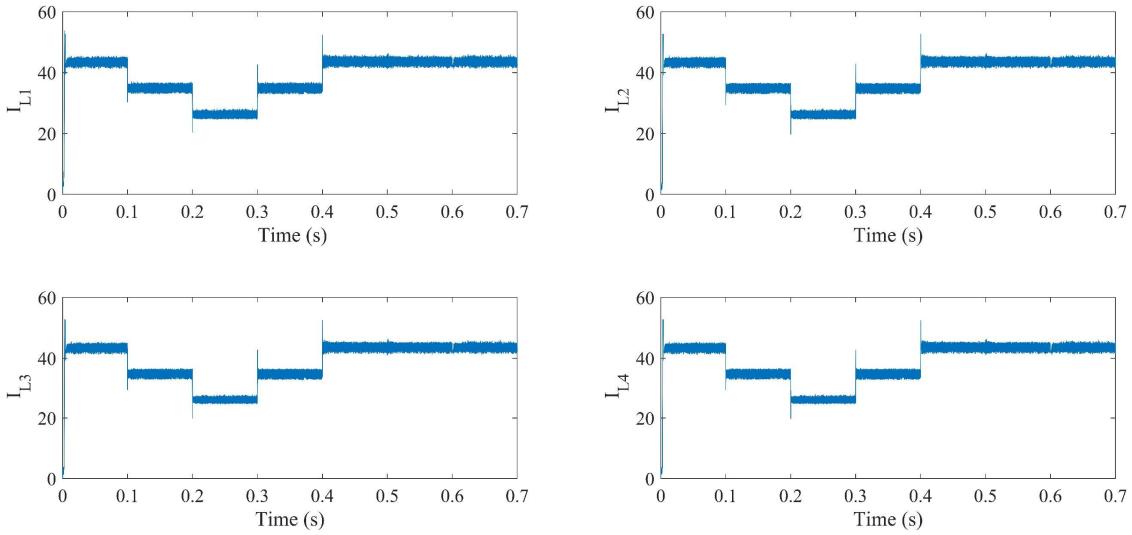


***Figure II-34 Equal current sharing between FLIBC legs using BS controller.***

## *5.4 Performance analysis of The FLBIC based on SMC and STSMC:*

In the following, the performance of a PV system fed FLIBC and controlled using both SMC and STSMC has been investigated. The control scheme presented in Figure II-17 and Figure II-18 are carried out using MATLAB/Simulink environment. The fuzzy logic MPPT is used to track the peak power of the PV system during fast-changing weather conditions. The simulation parameters of the controllers are listed in Table II-4. The simulation results are shown in Figure II-35 – Figure II-40.

The voltage curves of the PV system that fed FLIBC and controlled using SMC and STSMC are illustrated in Figure II-35 and Figure II-36. The SMC presents a faster response and tracking time than the PI controller. However, the SMC shows a chattering phenomenon, which is not seen when the PI controller is used.

The STSMC is proposed to address the chattering issue. The voltage curve of the PV system based on FLIBC controlled using STSMC is depicted in Figure II-36. As can be seen, the performance of the PV system is enhanced thanks to the STSMC. In which the chattering phenomena are eliminated, the response time is improved, and the tracking time of the MPP voltage is reduced compared to the SMC.

Specifically, in zone A, the STSMC exhibits a response time of 2.8 ms, significantly faster than the 6.7 ms response time of the SMC. Additionally, zone B highlights the effectiveness of STSMC in reducing voltage ripple, decreasing it from 5.5 V with SMC to 0.8 V. Furthermore, STSMC successfully minimizes overshoot in zone C, bringing it down from 8.3 V with SMC to 1.6 V. Finally, zone D confirms the rapid MPP tracking capability of STSMC, achieving the MPP voltage within 6 ms, compared to 6.7 ms for the SMC.

Figure II-37 shows the PV system's current curves, where conventional SMC displays slower response and higher current ripple. In contrast, STSMC achieves faster response and significantly reduced current ripple.

Figure II-38 illustrates the PV system's power curves using SMC and STSMC. The superiority of the STSMC over the SMC can be observed clearly. Zone A shows the MPP's fast-tracking when the STSMC is employed. In addition, zone B shows a reduction of the power ripple thanks to the STSMC. The fast response time of the STSMC is confirmed through zone C and zone D.

Finally, equal current sharing among the legs is achieved using both controllers, as seen in Figure II-39 and Figure II-40. The figures demonstrate that the STSMC exhibits less current ripple compared to the SMC.

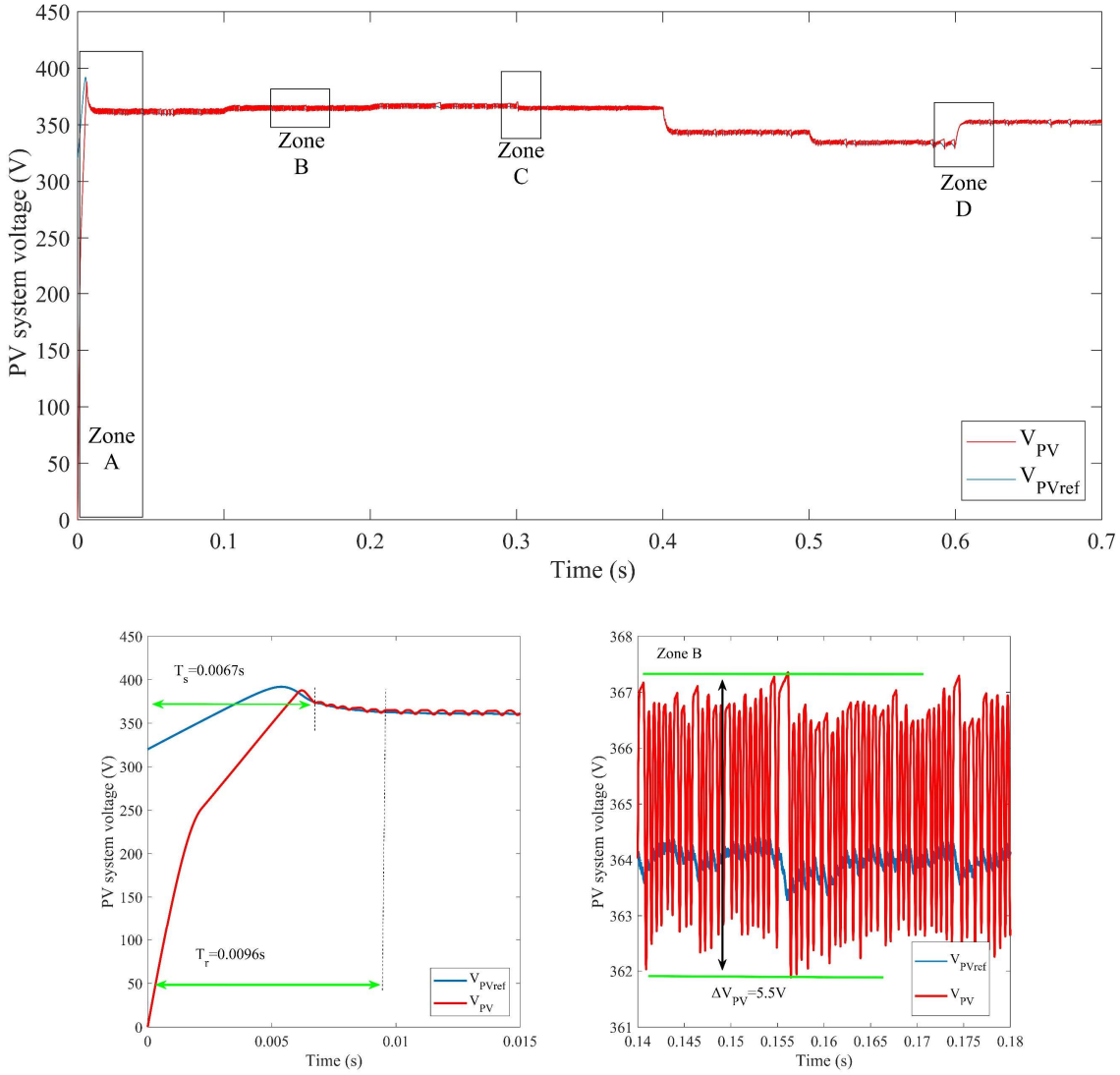

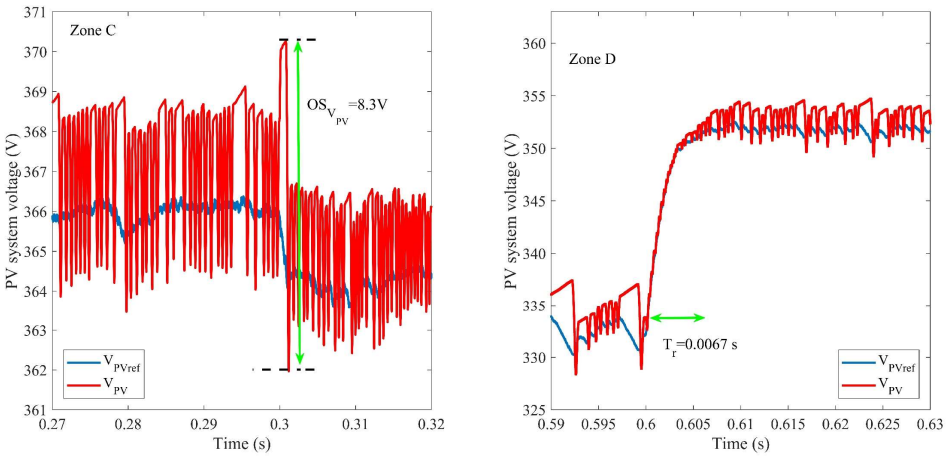


***Figure II-35 PV system's voltage curve using SMC.***

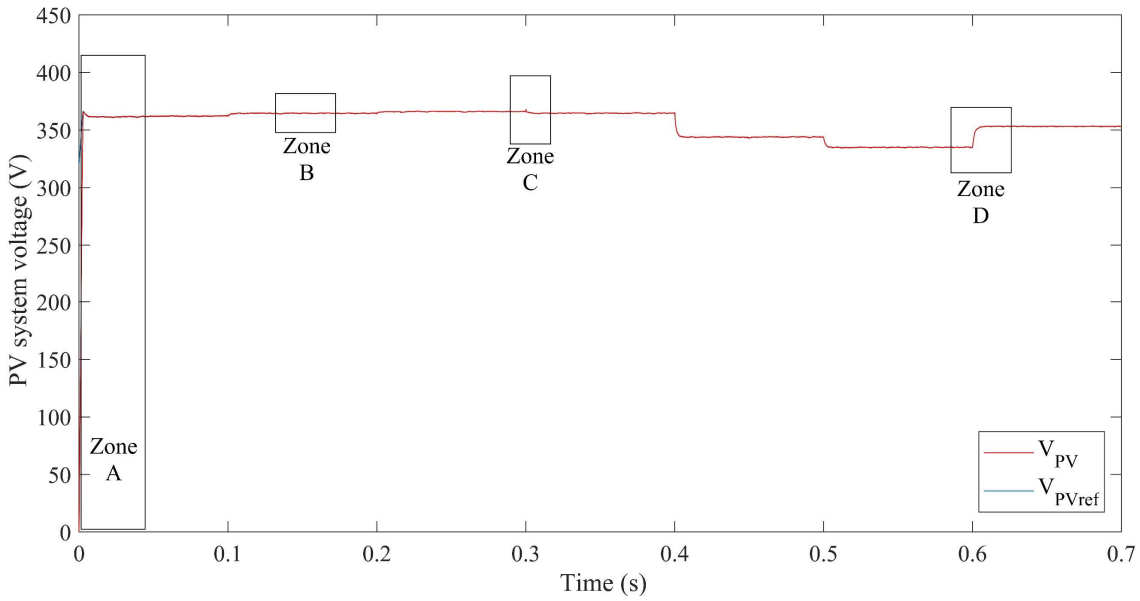


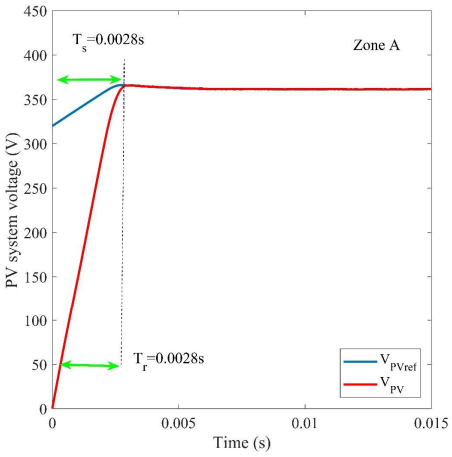


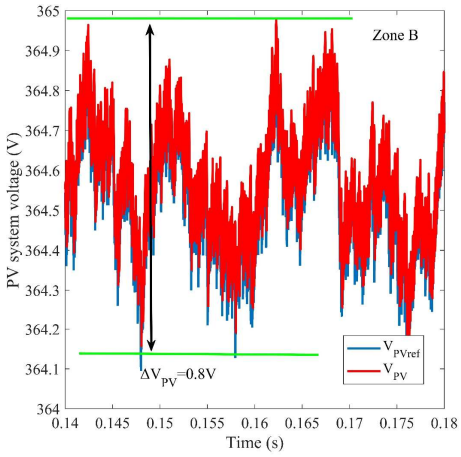

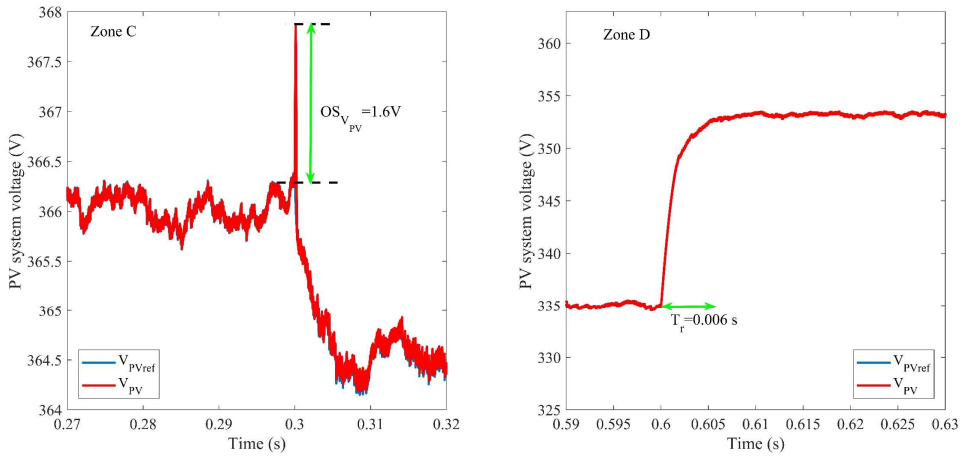


***Figure II-36 PV system's voltage curve using STSMC***

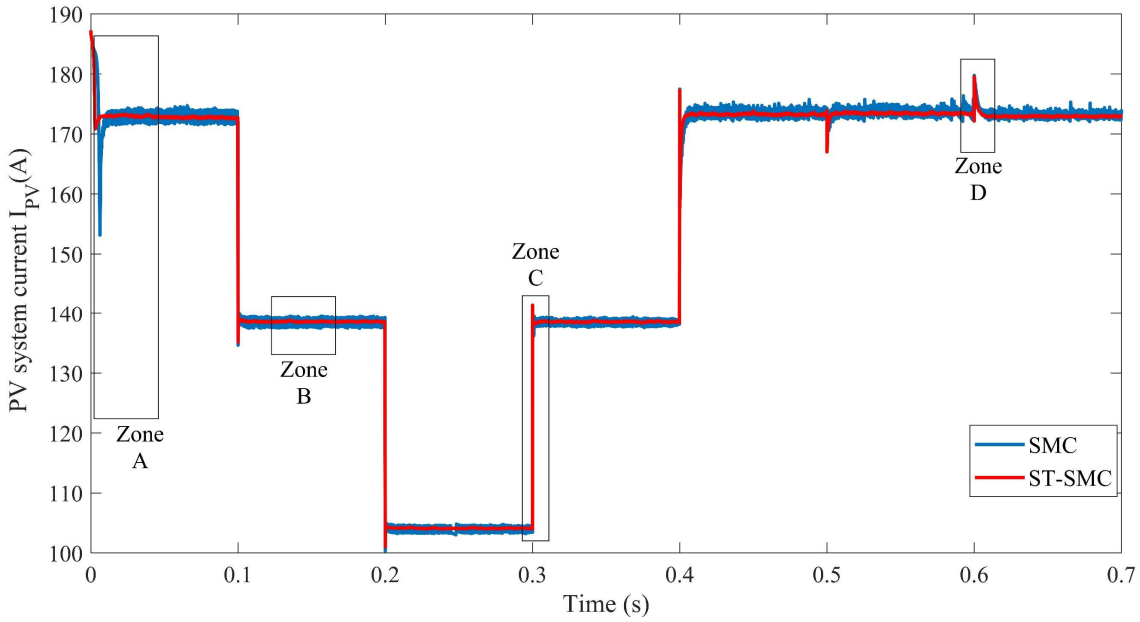


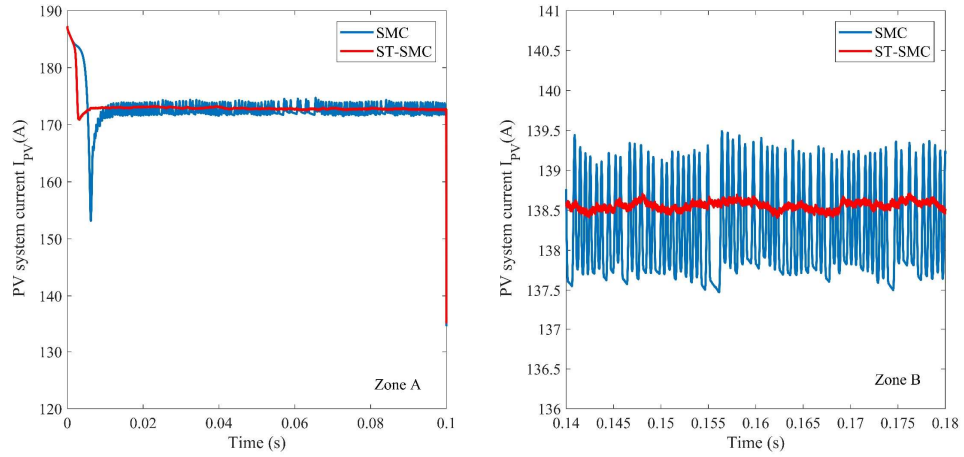

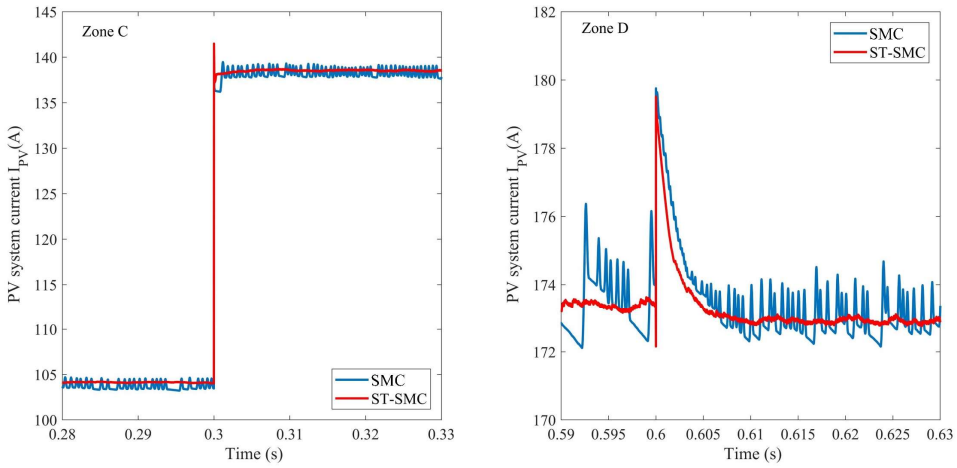


***Figure II-37 PV system's current curves using STSMC and SMC.***

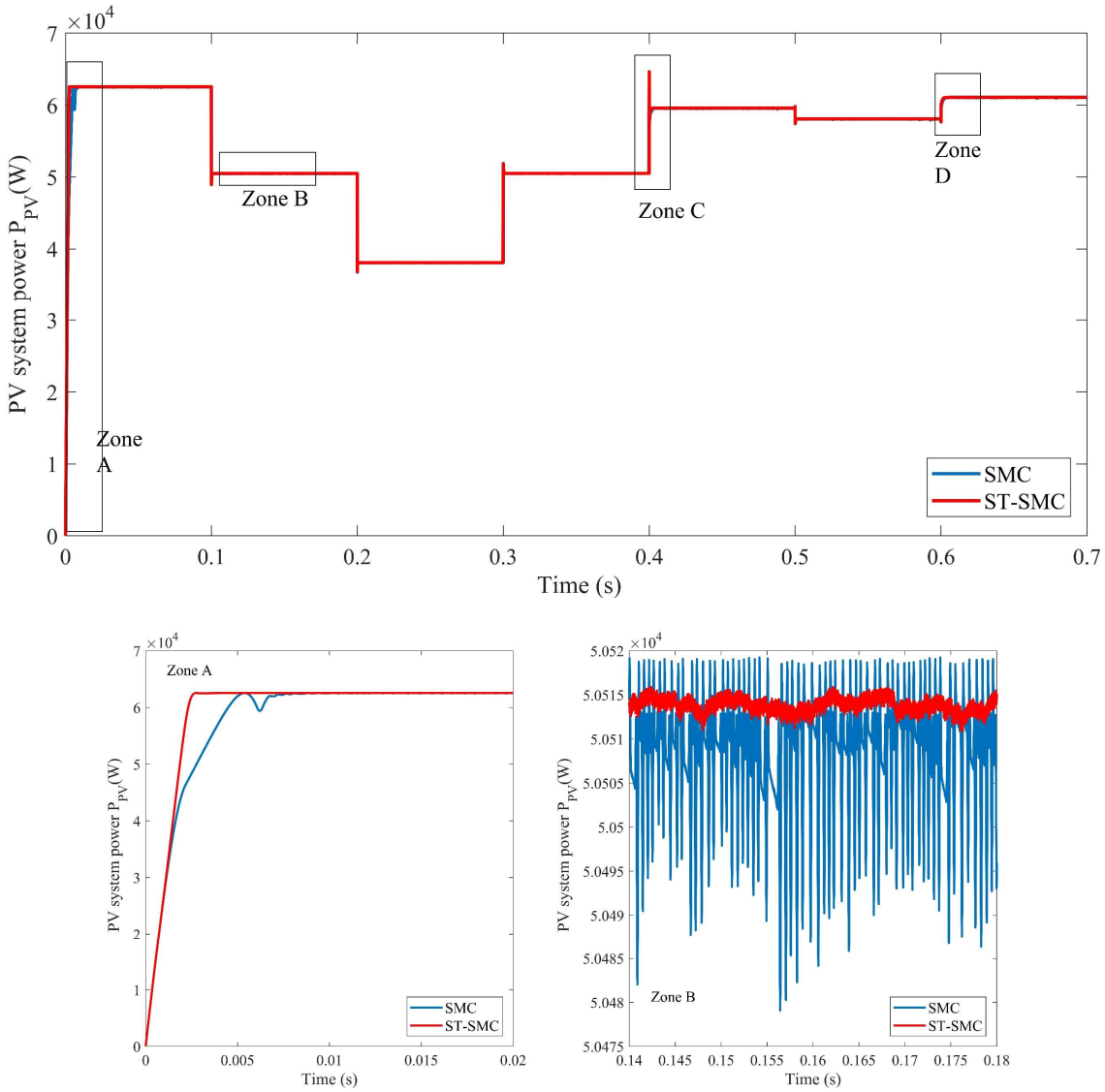

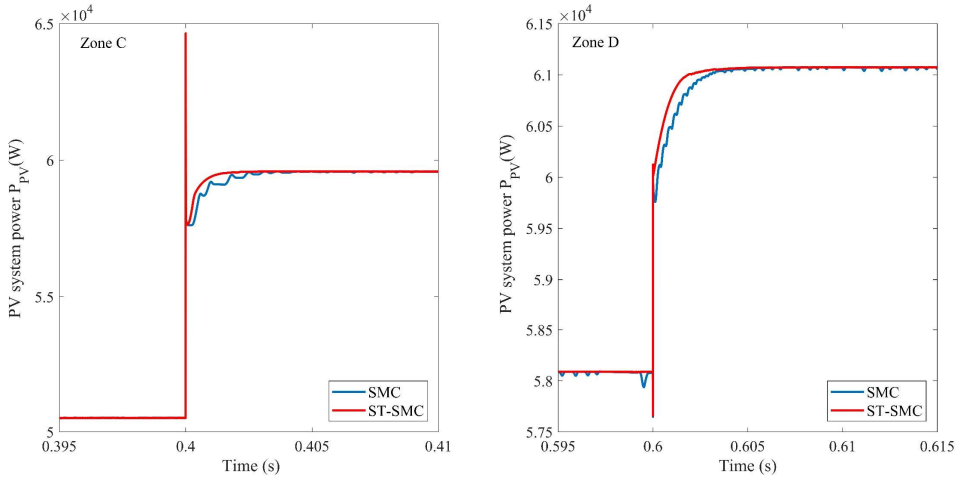


***Figure II-38 PV system's power curve using STSMC and SMC.***

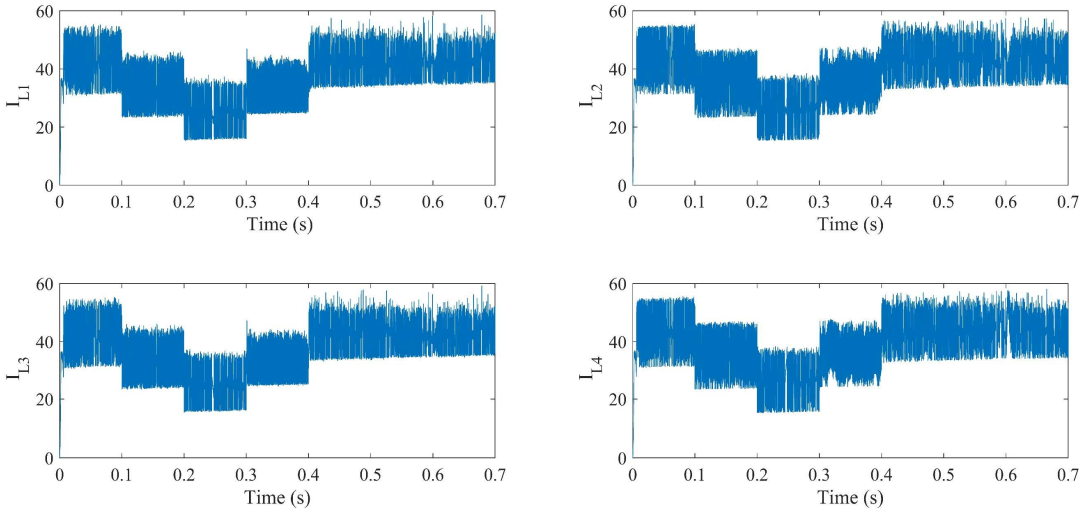


***Figure II-39 Equal current sharing between FLIBC legs using SMC.***

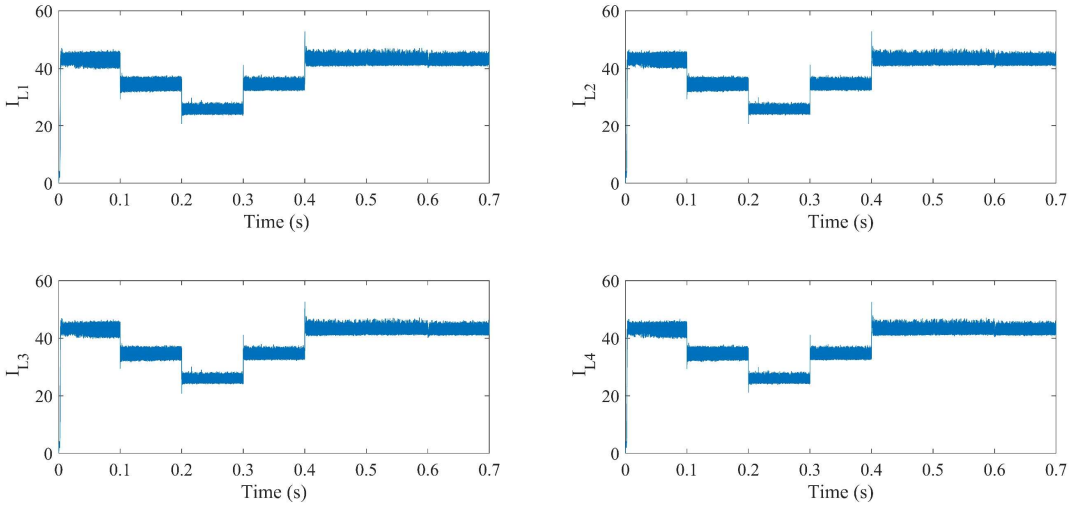


***Figure II-40 Equal current sharing between FLIBC legs using STSMC.***

To evaluate the effectiveness of these strategies, a comprehensive comparison of the control strategies is presented in Table II-5, focusing on key performance indicators derived from the simulation results. The comparison specifically examines the transient response time, MPP tracking speed, PV voltage ripple, overshoot magnitude, and the perfermence index (IAE, ISE, ITAE and ITSE), contrasting the conventional PI controller with advanced nonlinear techniques such as BS controller, SMC, and ST-SMC, all implemented within the FLIBC topology under identical conditions.

***Table II-5 Comprehensive comparison of the control strategies.***

| *Controller* | *PI* | *BS* | *SMC* | *ST-SMC* |
|---|---|---|---|---|
| ***Response time in Zone A*** | 22 ms | 4 ms | 6.7 ms | **2.8 ms** |
| ***MPP tracking time in Zone A*** | 37 ms | 6 ms | 9.6 ms | **2.8 ms** |
| ***PV voltage ripple (V) in Zone B*** | 0.35 | **0.6** | 5.5 | 0.8 |
| ***PV voltage overshoot (V) Zone C*** | 5.9 | 1.9 | 8.3 | **1.6** |
| ***IAE of the PV voltage*** | 3.610 | 0.481 | 2.359 | **0.467** |
| ***ISE of the PV voltage*** | 692.7 | **82.88** | 301.2 | 84.97 |
| ***ITAE of the PV voltage*** | 0.048 | 0.021 | 0.130 | **0.019** |
| ***ITSE of the PV voltage*** | 4.751 | **0.055** | 1.576 | 0.057 |

## *6 Conclusion:*

This chapter presents a comprehensive analysis of the design, control, and performance of a standalone PV system using a four-leg interleaved boost converter. The study compares various control strategies such as PI, backstepping, SMC, and STSMC to achieve optimal system performance.

The simulation results demonstrated that:

- The FLIBC offers significant advantages over the conventional boost converter in terms of reduced input and output current ripple, improved efficiency, and suitability for high-power applications.
- The fuzzy logic MPPT algorithm exhibits faster and more accurate MPP tracking than the incremental conductance algorithm.
- Nonlinear control strategies, such as backstepping, SMC, and STSMC, provide superior performance compared to the PI controller concerning the response time, tracking time, and voltage ripple and overshoot reduction.
- The STSMC eliminates chattering, improving efficiency and smoother operation.

The study concludes that the FLIBC, combined with a fuzzy logic MPPT and a nonlinear control strategy like STSMC, provides a highly efficient and robust solution for standalone PV systems. This configuration ensures optimal power extraction from the PV panels, even under varying weather conditions, and improves system stability and performance.

# *Chapter III:*

## *Classical Control of Multifunctional Grid-Connected PV System Based on FLIBC*

## 1 Introduction:

The significance of MGCPV is increasingly recognized within the context of evolving energy demands and the expanding integration of solar energy sources. These systems extend beyond their conventional role of power generation, offering additional functionalities such as reactive power compensation and harmonic mitigation, thereby supporting grid stability and efficiency. Their capacity to regulate voltage levels and mitigate harmonic distortions is pivotal for ensuring stable grid operation and enhancing power quality.

The MGCPV is typically composed of a two-stage power conversion scheme [173]. In the first stage, the highest DC power possible from the PV system is provided, usually using DC-DC converters. In contrast, this DC power is transported to the grid by converting it to AC power in the second stage, using VSI [174]. The VSI is used as a SAPF to reduce harmonic current, compensate for reactive power, and integrate the PV-generated energy into the grid [175].

The solar panels are commonly coupled with a DC-DC boost converter to raise their voltage and bring it up to the desired level by the DC link voltage. Moreover, it maintains the PV power close to the peak power using an MPPT controller. Generally, the researchers employ the CBC topology within the PV system conversion chain [173], [176], [177]. However, the CBC topology is associated with various inherent limitations, such as high current stress on components, large inductor size, reduced efficiency at high power levels, slow transient response, and significant power ripple levels [19]. Despite these drawbacks, the interleaved boost converter has emerged as a preferred topology to overcome the constraints of the conventional boost converter. This is due to its advantages, which include lower power ripple, higher efficiency, compact size, and enhanced suitability for high-power applications [178], [179].

Generally, each stage of the MGCPV structure consists of two control loops: the PV voltage and inductor current control loops in the first stage (PV-IBC), as discussed in the second chapter. While the DC-bus voltage and grid power control loops in the inversion stage (grid-connected inverter) [180]. Several control strategies have been adopted for controlling the active and reactive power of the MGCPV system, such as instantaneous reactive power theory (PQ theory), voltage-oriented control [24], synchronous reference frame control [181], and direct power control [182].

Direct power control strategy is one of the common techniques used in power electronics applications, particularly in shunt active power filters, PWM rectifiers, Microgrids, etc [176], [182], [183], [184]. In 1998, Noguchi et al. [185] pioneered the development of DPC, an innovative control strategy derived from the principles of direct torque control (DTC). In DPC, there are no internal current control loops and no PWM modulator block because a switching table appropriately selects the converter switching states based on the instantaneous errors between the commanded and estimated values of active and reactive power.

In this chapter, the MGCPV topology based on FLIBC and controlled using the DPC strategy employing a switching table is investigated to handle the high power rate and drawbacks of the CBC topology. Extensive simulation tests are carried out using the MATLAB/Simulink environment to verify and compare the proposed topology with the performance of the MGCPV topology that uses the CBC.

## 2 System Description and Modeling:

In this study, a multifunctional grid-connected PV system goes beyond simply generating power from sunlight. By incorporating additional functionalities, it actively participates in maintaining grid stability and power quality. This section explores the configuration of such a system, highlighting its key components and finally providing their modeling.

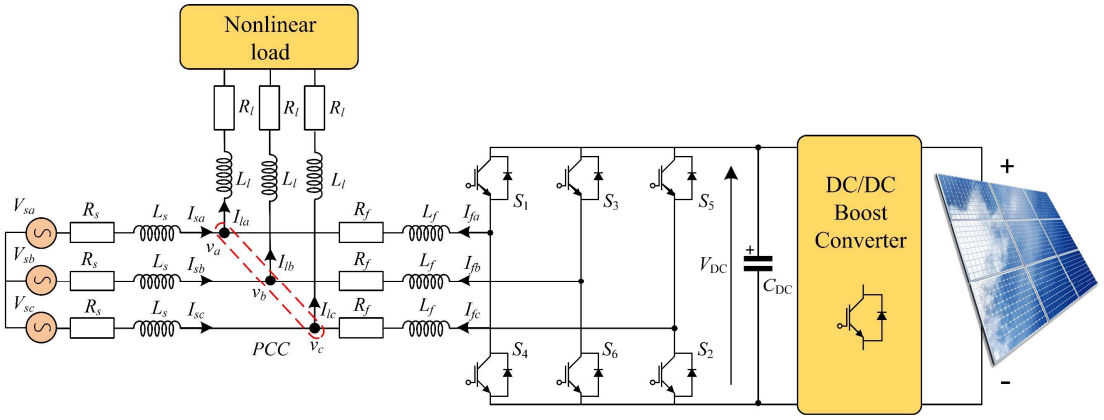


*Figure III-1 Multifunctional Grid-Connected PV System basic configuration.*

As seen in Figure III-1, the studied system is composed of four main parts: PV modules fed a DC/DC boost converter, voltage source inverter (VSI), AC power supply, and nonlinear load. The DC/DC boost converter connects the PV modules to the VSI and operates the MPPT algorithm. The two-level VSI consists of six switches and a capacitor connected to the DC side. Moreover, it is connected to the grid at the PCC via an R-L coupling filter. The 2L-VSI operates as a shunt active power filter; its main objectives are for the reactive power compensation and to mitigate the current harmonic distortion caused by the nonlinear loads. In addition, VSI allows the injection of the PV power generated into the load and/or the grid. The nonlinear load is connected to the grid across three inductors. The nonlinear load is a harmonic current source composed of a three-phase uncontrolled diode rectifier connected to an R-L load.

### 2.1 Power Grid Modeling:

A three-phase power supply (Figure III-2) is usually modeled with three voltage sources having their own voltage and phase waveforms. If the voltage waveforms are purely sinusoidal with the same amplitude and the phase angle between the voltages is 120°, then the source is balanced. Otherwise, the source is unbalanced. The mathematical equations that describe the behaviour of the grid voltages can be given as follows:

$$\begin{cases} V_{sa} = R_s i_{sa} + L_s \dfrac{di_{sa}}{dt} + v_a \\ V_{sb} = R_s i_{sb} + L_s \dfrac{di_{sb}}{dt} + v_b \\ V_{sc} = R_s i_{sc} + L_s \dfrac{di_{sc}}{dt} + v_c \end{cases} \tag{3.1}$$

Where $V_{sa,b,c}$ is the grid voltage, $i_{sa,b,c}$ is the grid current, and $v_{a,b,c}$ is the PCC voltage.

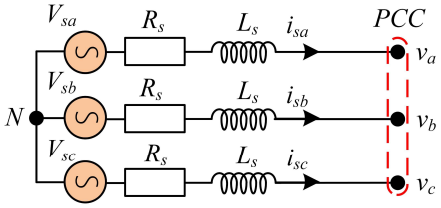


***Figure III-2 AC power supply circuit.***

## 2.2 Nonlinear Load (Three-Phase Uncontrolled Diode Rectifier) Modeling:

Recently, the growth of nonlinear electronic loads has increased significantly worldwide. The most common nonlinear loads are AC/DC converters, such as three-phase and single-phase rectifiers. In the proposed system, a three-phase full-wave rectifier is employed as a nonlinear load. This type of three-phase nonlinear load (Figure III-3) is widely used in industrial zones and high-power applications, such as the converters of direct current distribution systems (HVDC).

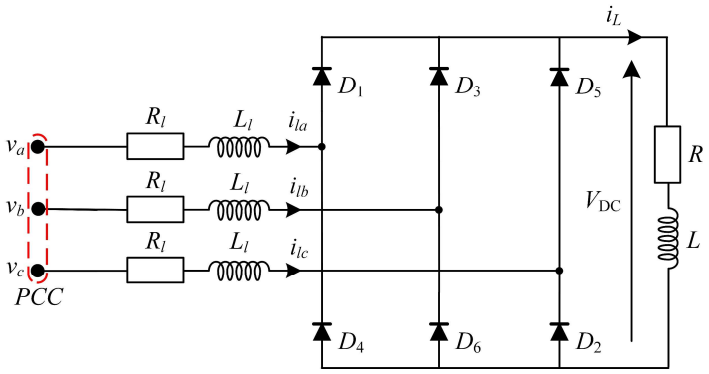


***Figure III-3 Nonlinear load: Three-phase full-wave rectifier circuit.***

## 2.3 Two-Level Voltage Source Inverter Modeling:

The schematic of the three-phase 2L-VSI topology is shown in Figure III-4. The VSI consists of an R-L coupling filter, six semiconductor switches, and a DC link capacitor. The 2L-VSI is connected to a three-phase power supply through an R-L coupling filter. The 2L-VSI includes two zero voltage and six zero voltage vectors, as listed in Table III-1. The mathematical equation of the voltage of the 2L-VSI can be expressed using the switching functions as follows:

$$\begin{bmatrix} V_{faN} \\ V_{fbN} \\ V_{fcN} \end{bmatrix} = \frac{V_{DC}}{3} \begin{bmatrix} 2 & -1 & -1 \\ -1 & 2 & -1 \\ -1 & -1 & 2 \end{bmatrix} \begin{bmatrix} S_a \\ S_b \\ S_c \end{bmatrix} \tag{3.2}$$

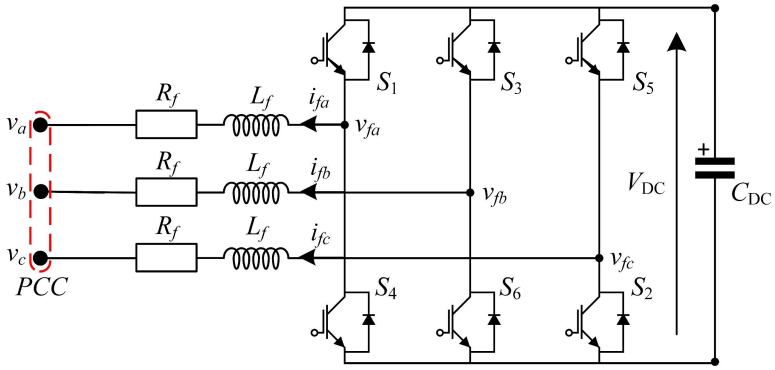


***Figure III-4 2L-VSI circuit.***

***Table III-1 Voltage vectors of 2L-VSI***

| $V_{fi}$ | $S_a$ | $S_b$ | $S_c$ | $V_{faN}$ | $V_{fbN}$ | $V_{fcN}$ | $V_{fab}$ | $V_{fbc}$ | $V_{fac}$ |
|---|---|---|---|---|---|---|---|---|---|
| **0** | 0 | 0 | 0 | 0 | 0 | 0 | 0 | 0 | 0 |
| **1** | 1 | 0 | 0 | $2V_{DC}/3$ | $-V_{DC}/3$ | $-V_{DC}/3$ | $V_{DC}$ | 0 | $V_{DC}$ |
| **2** | 1 | 1 | 0 | $V_{DC}/3$ | $V_{DC}/3$ | $-2V_{DC}/3$ | $V_{DC}/2$ | $V_{DC}/2$ | $V_{DC}$ |
| **3** | 0 | 1 | 0 | $-V_{DC}/3$ | $2V_{DC}/3$ | $-V_{DC}/3$ | $V_{DC}$ | $V_{DC}$ | 0 |
| **4** | 0 | 1 | 1 | $-2V_{DC}/3$ | $V_{DC}/3$ | $V_{DC}/3$ | $V_{DC}$ | $V_{DC}/2$ | $V_{DC}/2$ |
| **5** | 0 | 0 | 1 | $-V_{DC}/3$ | $-V_{DC}/3$ | $2V_{DC}/3$ | 0 | $V_{DC}$ | $V_{DC}$ |
| **6** | 1 | 0 | 1 | $V_{DC}/3$ | $-2V_{DC}/3$ | $V_{DC}/3$ | $V_{DC}/2$ | $V_{DC}$ | $V_{DC}/2$ |
| **7** | 1 | 1 | 1 | 0 | 0 | 0 | 0 | 0 | 0 |

According to Kirchhoff's laws, the differential equations that describe the dynamic model of the 2L-VSI, as illustrated in Figure III-4, can be given below:

$$\begin{cases} \dfrac{di_{fa}}{dt} = \dfrac{1}{L_f}\left(v_a - v_{fa} - v_{Rfa}\right) = -\dfrac{R_f}{L_f} i_{fa} - \dfrac{1}{L_f} v_{fa} + \dfrac{1}{L_f} v_a \\ \dfrac{di_{fb}}{dt} = \dfrac{1}{L_f}\left(v_b - v_{fb} - v_{Rfb}\right) = -\dfrac{R_f}{L_f} i_{fb} - \dfrac{1}{L_f} v_{fb} + \dfrac{1}{L_f} v_b \\ \dfrac{di_{fc}}{dt} = \dfrac{1}{L_f}\left(v_c - v_{fc} - v_{Rfc}\right) = -\dfrac{R_f}{L_f} i_{fc} - \dfrac{1}{L_f} v_{fc} - \dfrac{1}{L_f} v_c \\ \dfrac{dV_{DC}}{dt} = \dfrac{1}{C_{DC}}\left[S_a i_{fa} + S_b i_{fb} + S_c i_{fc}\right] \end{cases} \tag{3.3}$$

Where $v_{a,b,c}$ is the PCC's measured voltage, $v_{fa,b,c}$ is the output voltage of the VSI, $i_{fa,b,c}$ is the output current of the VSI, and $S_{a,b,c}$ are the VSI switching functions.

The previous equations can be rewritten in the rotating reference frame using the following Park transformation:

$$X_{dq0} = T_{dq0} X_{abc} = \sqrt{\frac{2}{3}} \begin{bmatrix} \cos(\omega t) & \cos(\omega t) & \cos(\omega t) \\ -\sin(\omega t) & -\sin(\omega t) & -\sin(\omega t) \\ \dfrac{1}{\sqrt{2}} & \dfrac{1}{\sqrt{2}} & \dfrac{1}{\sqrt{2}} \end{bmatrix} X_{abc} \tag{3.4}$$

Using (3.3) and (3.4), the 2L-VSI model on the rotating reference frame can be given as:

$$\begin{cases} \dfrac{di_{fd}}{dt} = -\dfrac{R_f}{L_f} i_{fd} - \omega i_{fq} - \dfrac{1}{L_f} v_{fd} + \dfrac{1}{L_f} v_d \\ \dfrac{di_{fq}}{dt} = -\dfrac{R_f}{L_f} i_{fq} + \omega i_{fd} - \dfrac{1}{L_f} v_{fq} + \dfrac{1}{L_f} v_q \\ \dfrac{dV_{DC}}{dt} = \dfrac{1}{C_{DC}} \left[ S_d i_{fd} + S_q i_{fq} \right] \end{cases} \tag{3.5}$$

Meanwhile, the modeling of the 2L-VSI in the stationary frame using Clarck transformation that is given in (3.6)

$$X_{\alpha\beta 0} = T_{\alpha\beta 0} X_{abc} = \sqrt{\frac{2}{3}} \begin{bmatrix} 1 & -0.5 & -0.5 \\ 0 & \dfrac{\sqrt{3}}{2} & -\dfrac{\sqrt{3}}{2} \\ \dfrac{1}{\sqrt{2}} & \dfrac{1}{\sqrt{2}} & \dfrac{1}{\sqrt{2}} \end{bmatrix} X_{abc} \tag{3.6}$$

Therefore, the 2L-VSI model on the stationary frame can be expressed as follows:

$$\begin{cases} \dfrac{di_{f\alpha}}{dt} = -\dfrac{R_f}{L_f} i_{f\alpha} - \dfrac{1}{L_f} v_{f\alpha} + \dfrac{1}{L_f} v_{\alpha} \\ \dfrac{di_{f\beta}}{dt} = -\dfrac{R_f}{L_f} i_{f\beta} - \dfrac{1}{L_f} v_{f\beta} + \dfrac{1}{L_f} v_{\beta} \\ \dfrac{dV_{DC}}{dt} = \dfrac{1}{C_{DC}} \left[ S_{\alpha} i_{f\alpha} + S_{\beta} i_{f\beta} \right] \end{cases} \tag{3.7}$$

### *3 Direct Power Control:*

DPC stands out among the several control approaches investigated for the regulation of MGCPV systems exhibiting various characteristics. Ohnishi et al. propose the basic concept of the DPC strategy to control a three-phase PWM rectifier [186], which is derived from the direct torque control of the induction machines proposed by Takahashi and Noguchi in 1986 [187]. In DTC, the amplitudes of the torque and flux are used as controlled inputs. Meanwhile, in DPC, the active and reactive power amplitudes are used as controlled inputs.

DPC allows the control of the MGCPV without using any internal control loops or PWM block. Its fundamental concept involves choosing the suitable switching states using a predefined optimal switching table, which is based on the errors limited by hysteresis bands observed in the active and reactive powers and the position of the source voltage space vector, as depicted in Figure III-5.

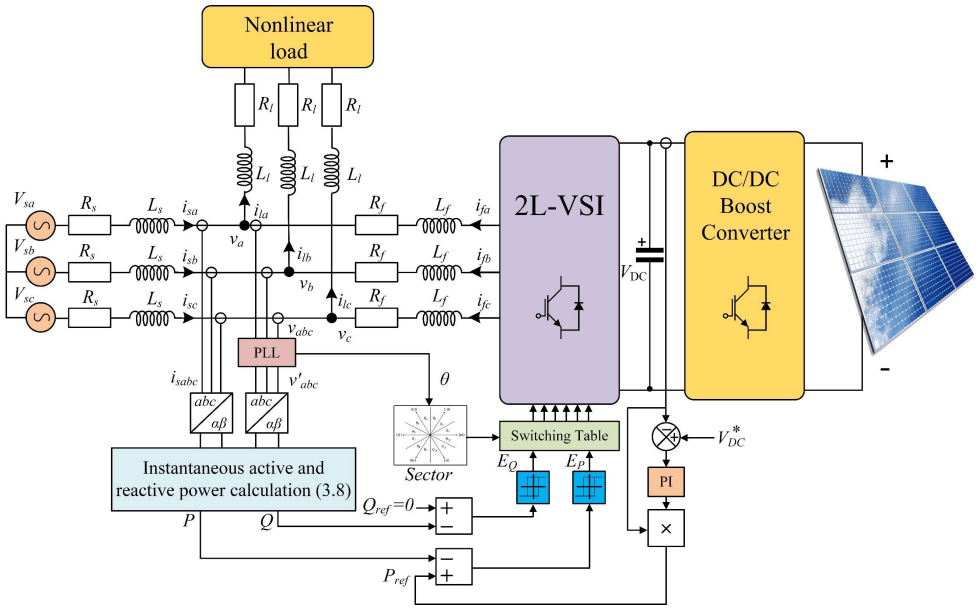


***Figure III-5 Conventional direct power control of MGCPV system.***

The active power P and reactive power Q are calculated using the voltage and current of the grid across the following expressions:

$$\begin{cases} P = V_{S\alpha} I_{S\alpha} + V_{S\beta} I_{S\beta} \\ Q = V_{S\alpha} I_{S\beta} - V_{S\beta} I_{S\alpha} \end{cases} \tag{3.8}$$

The active power reference is delivered by the output of the DC bus voltage controller. At the same time, the reactive power set point is equal to zero to guarantee unity power factor operation [29].

The power errors are calculated as follows:

$$\begin{cases} \Delta P = P_{ref} - P \\ \Delta Q = Q_{ref} - Q \end{cases} \tag{3.9}$$

Then, the power is fed into the hysteresis controller to calculate the digitized signals $E_p$ and $E_q$ as follows:

$$\begin{cases} \Delta P > \varepsilon : E_P = 1 \\ \Delta P < \varepsilon : E_P = 0 \\ \Delta Q > \varepsilon : E_Q = 1 \\ \Delta Q < \varepsilon : E_Q = 0 \end{cases} \tag{3.10}$$

## *3.1 Switching Table:*

The switching table used in DPC consists of the optimal switching states that allow the control of active and reactive power. The switching states are determined by the power error signals provided by the hysteresis controllers and the position of the voltage in the space vector. Noguchi et al. proposed the widely used switching table in [185]. The voltage space vector is illustrated in Figure III-6, and the switching table is listed in Table III-2.

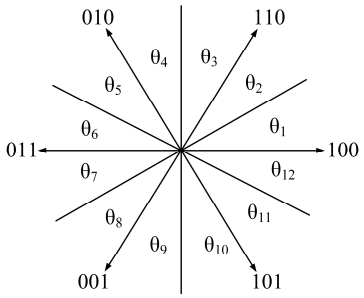


***Figure III-6 Voltage space vector.***

***Table III-2 Switching table of the DPC.***

| $E_P$ | $E_Q$ | Sector | | | | | | | | | | | |
|---|---|---|---|---|---|---|---|---|---|---|---|---|---|
| | | $\theta_1$ | $\theta_2$ | $\theta_3$ | $\theta_4$ | $\theta_5$ | $\theta_6$ | $\theta_7$ | $\theta_8$ | $\theta_9$ | $\theta_{10}$ | $\theta_{11}$ | $\theta_{12}$ |
| **1** | **1** | 111 | 111 | 000 | 000 | 111 | 111 | 000 | 000 | 111 | 111 | 000 | 000 |
| | **0** | 101 | 111 | 100 | 000 | 110 | 111 | 010 | 000 | 011 | 111 | 001 | 000 |
| **0** | **1** | 100 | 110 | 110 | 010 | 010 | 011 | 011 | 001 | 001 | 001 | 101 | 100 |
| | **0** | 101 | 100 | 100 | 110 | 110 | 010 | 010 | 011 | 011 | 011 | 001 | 101 |

## *3.2 DC-Bus Voltage Regulator Design:*

In order to maintain the DC bus voltage in the desired setpoint and decrease its fluctuations, an anti-windup compensator-based PI controller is suggested in several papers, such as [29], [188]. The control scheme is depicted in Figure III-7. The PI controller contains a proportional gain $K_{pdc}$ and an integral gain $K_{idc}$, which minimize the steady-state error. In addition, an anti-windup compensator has been employed to avoid saturation of the controller output with a gain $K_A$.

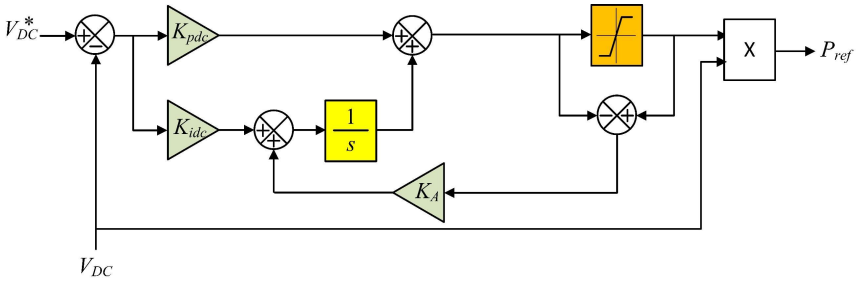


***Figure III-7 The block diagram of the DC bus voltage regulator based on the Anti-windup PI controller.***

The closed-loop transfer function of the DC bus voltage regulator can be expressed as follows:

$$G_{V_{DC}}(s)=\frac{V_{DC}}{V_{DC}^*}=\frac{\frac{K_{pdc}}{C_{DC}}s+\frac{K_{idc}}{C_{DC}}}{s^2+\frac{K_{pdc}}{C_{DC}}s+\frac{K_{idc}}{C_{DC}}} \tag{3.11}$$

To calculate the PI controller gains $K_p$ and $K_i$, we can use the transfer function of the second-order system, which is given as:

$$F(s)=\frac{\omega_n}{s^2+2\zeta\omega_n s+\omega_n^2} \tag{3.12}$$

Then, by equalizing (3.11) and (3.12), the PI controller gains can be deduced in the following:

$$\begin{cases} K_{pdc} = 2\zeta\omega_n C_{DC} \\ K_{idc} = \omega_n^2 C_{DC} \end{cases} \tag{3.13}$$

### *3.3 Phase Locked Loop Design:*

Synchronizing a PV system with the electrical grid requires accurately determining the grid voltage characteristics, including the amplitude, phase shift, and frequency of the grid voltage component. A commonly used method in power electronics for this purpose is the phase-locked loop (PLL) technique. The PLL block enables the MGCPV system to synchronize effectively with both balanced and disturbed grid conditions. The three-phase PLL [189] processes the three-phase voltage signals and transforms them into a two-axis representation commonly achieved using a Park transformation, as shown in Figure III-8. The phase detector compares the phases of the converted input signal with the VCO output. The resultant error signal is subsequently transmitted to the loop filter. The loop filter analyses the error signal to provide a control voltage that reduces phase error using a PI controller, hence regulating the VCO. As a result, the VCO modifies its frequency and phase according to the control signal received from the loop filter, therefore synchronizing with the reference signal.

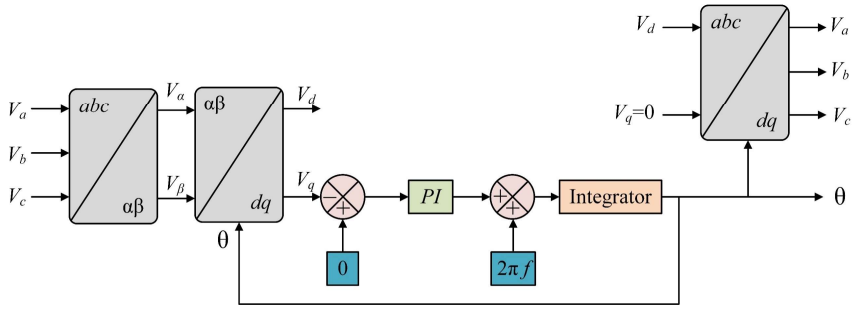


***Figure III-8 Conventional three-phase PLL block.***

To improve the performance of the three-phase PLL, a self-tuning filter (STF) is used to extract the fundamental components of the three-phase voltage signals, as illustrated in Figure III-9. The PLL based on STF is insensitive to disturbances and allows the filtering of the sensed voltages suitably using the αβ axis, which improves the obtained results during distorted voltages.

The transfer function that describes the dynamics of the STF block can be given as follows [190]:

$$F(s) = \frac{V'_{\alpha\beta}}{V_{\alpha\beta}} = k\frac{(s+k)+j\omega_c}{(s+k)^2+\omega_c^2} \tag{3.14}$$

$k$ and $\omega_c$ are parameter gain and cut-off frequency. The fundamental component $V_{\alpha\beta}$ can be given as follows:

$$\begin{cases} V'_\alpha = \dfrac{k}{s}\left[V_\alpha(s) - V'_\alpha(s)\right] - \dfrac{\omega_c}{s}V'_\beta \\ V'_\beta = \dfrac{k}{s}\left[V_\beta(s) - V'_\beta(s)\right] + \dfrac{\omega_c}{s}V'_\alpha \end{cases} \tag{3.15}$$

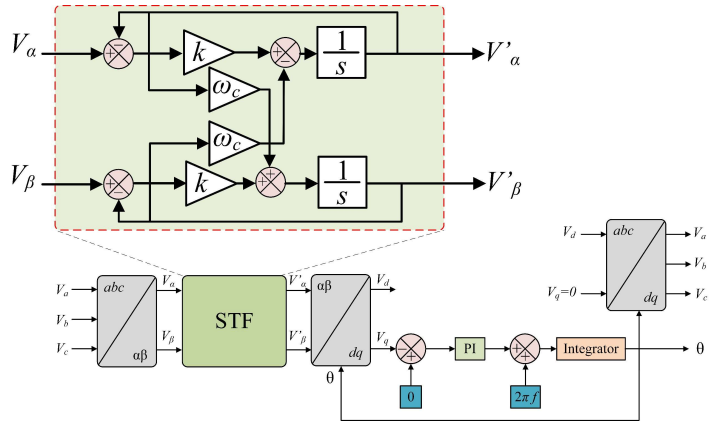


***Figure III-9 STF-PLL block.***

The performance of the proposed PLL techniques is investigated using distorted voltage source signals. The obtained results are shown in Figure III-10 and Figure III-11. The STF-PLL technique provides better performance than the conventional PLL, where the distorted voltages are well-filtrated and quickly estimate their position angular (theta θ).

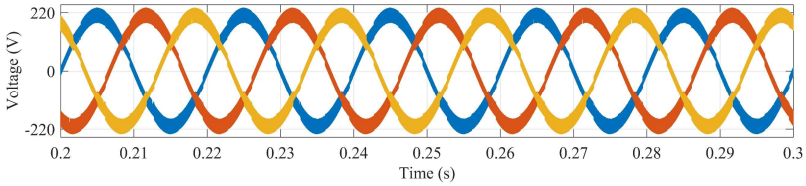


***(a)***

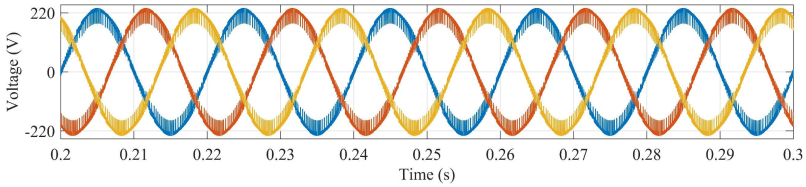


***(b)***

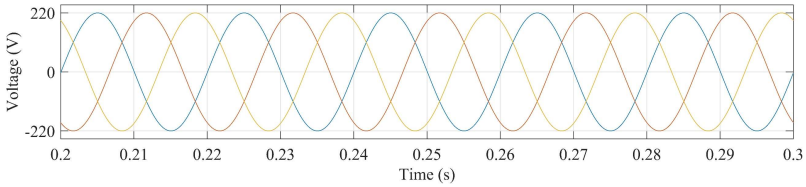


***(c)***

***Figure III-10 The voltage sensed at PCC (a), the output of the conventional PLL (b), and the output of the STF-PLL (c).***

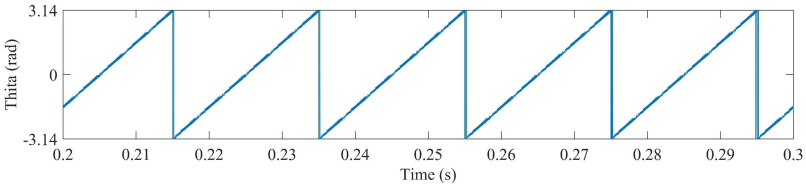


***(a)***

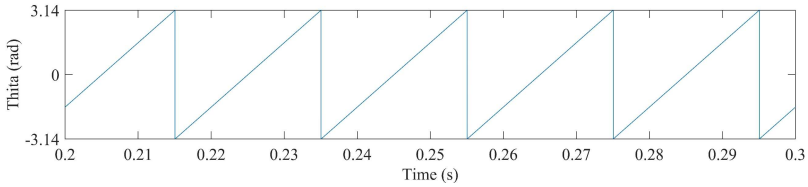


***(b)***

***Figure III-11 The phase angle (theta) detected by conventional PLL (a) and STF-PLL (b).***

## *4 Simulation Results and Discussion:*

Numerous simulations have evaluated the proposed system, as shown in Figure III-5. The simulations focused on the properties of the conventional DPC of an MGCPV based on FLIBC during transient and steady-state operation.

The simulation model has been developed using the MATLAB/Simulink environment. Its simulation parameters are presented in Table III-3. The proposed system has been investigated using various solar irradiation values during constant temperature (25 °C). Figure III-12 shows the irradiation profile.

***Table III-3 Simulation parameters.***

| ***MGCPV Parameters*** | |
|---|---|
| ***Parameter*** | ***Value*** |
| ***Source Voltage $V_{max}$*** | 220 *V* |
| ***Source frequency*** | 50 *Hz* |
| ***$R_s$, $L_s$*** | 10 *m*Ω, 0.6 *mH* |
| ***$R_f$, $L_f$*** | 0.6 *m*Ω, 2 *mH* |
| ***$R_c$, $L_c$*** | 1 *m*Ω, 0.3 *mH* |
| ***$R_{L1}$, $R_{L2}$, $L_L$*** | 10 Ω, 8.5 Ω, 1 *mH* |
| ***DC bus voltage $V_{DC}$*** | 800 *V* |
| ***$C_{DC}$*** | 4000 *uF* |
| ***DC Bus Voltage Controller Parameters*** | |
| ***Parameter*** | ***Value*** |
| ***$K_{pdc}$*** | 0.88 |
| ***$K_{idc}$*** | 48.4 |

Finally, the system is investigated under load variation in t = [ 1.6 s, 1.8 s] range, where a second resistive load decreased from 10 Ω to 8.5 Ω in $t$ =1.6 s and vice versa in 1.8 s.

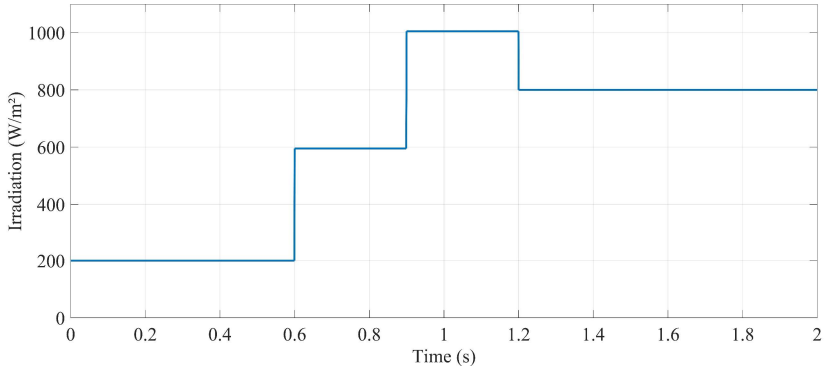


***Figure III-12 Solar irradiation profile.***

The performance of the DC bus voltage for both topologies, relative to their reference values, is depicted in Figure III-13. Before the integration of the PV panels, the DC bus voltage of both topologies stabilizes at 66 ms. After the PV panels are integrated at t = 0.3 s with irradiation equal to 200 W/m², the CBC topology exhibits notable fluctuations, including an overshoot of 48.8 V and an undershoot of 3.3 V, with a response time of 52.5 ms. In contrast, the FLIBC topology shows enhanced performance, with significantly reduced fluctuations, presenting an overshoot of 8 V, an undershoot of 2 V, and the same response time of 52.5 ms.

At $t$ = 0.6 s, the irradiation level is increased from 200 W/m² to 600 W/m². Both topologies recover their reference values within 60 ms, experiencing a 13.2 V overshoot. However, the FLIBC exhibits less voltage ripple ($\Delta V_{DC}$ = 0.7 V) compared to the voltage ripple in the CBC topology ($\Delta V_{DC}$ = 2 V).

The solar radiation rises from 600 W/m² to 1000 W/m² at $t$ = 0.9 s; the two topologies exhibit an overshoot of 13 V with a response time of 61 ms. In this period, the voltage ripple $\Delta V_{DC}$ is 2.7 V and 0.9 V for the CBC and FLIBC, respectively.

At t = 1.2 s, after the solar irradiation decreases from 1000 W/m² to 800 W/m², the converters show an undershoot of 6.4 V and a response time of 55 ms. In contrast, the FLIBC topology reduces the voltage ripple to 0.9 V, while the CBC topology's voltage ripple is 2.3 V.

In the time interval $t$ = [1.6 s,1.8 s], the system was subjected to a load variation, wherein the resistive load was decreased from 10 Ω to 8.5 Ω and then reverted to 10 Ω at $t$=1.8 s. The MGCPV system responded promptly to this transient, quickly recovering its reference voltage value within 55 ms with an undershoot of 2.7 V and an overshoot of 2.7 V.

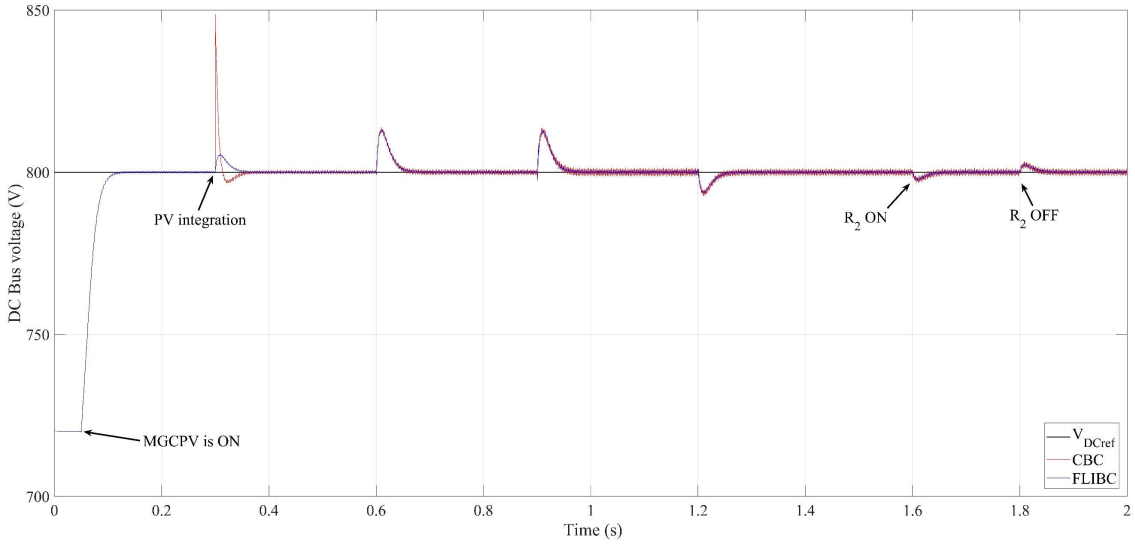

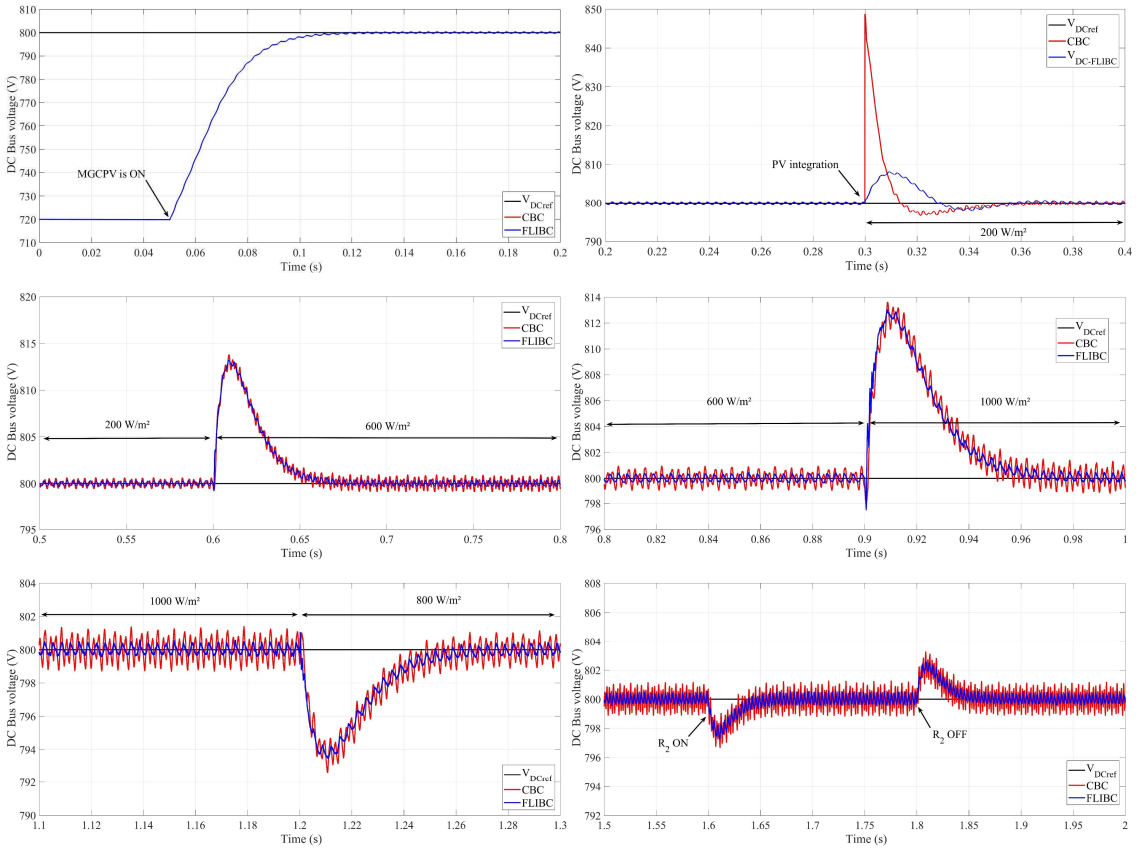


***Figure III-13 DC bus voltage of the MGCPV based on conventional DPC.***

The active power, reactive power, and PV power curves for both topologies are depicted in Figure III-14 and Figure III-15. At $t$ = 0.05s, after integrating the MGCPV system (without the PV array), the active power *Ps* rapidly aligns with its reference value. Simultaneously, the reactive power *Qs* drop to zero, indicating that the DC bus capacitor fully compensates the reactive power demand from the nonlinear load. As a result, unity power factor operation is achieved, reflecting the power efficiency. In this mode, the MGCPV is employed as a SAPF, which only mitigates the harmonics and eliminates the reactive power.

At $t$ = 0.3s, the PV system of the MGCPV is activated. Between $t$ = [0.3s, 0.6s], with a solar irradiation of 200 W/m², the power generated by the PV system (6.43 kW) is less than the nonlinear load's power demand. Consequently, the grid's active power decreases while the reactive power remains zero. This period demonstrates the PV system's role in enhancing power quality by supplying power to the nonlinear load, reducing grid consumption, and compensating for reactive power through the DC bus capacitor. Notably, during this interval, the FLIBC topology exhibits a lower power ripple compared to the CBC topology.

During the period $t$ = [0.6s, 0.9s], as solar irradiation increases from 200 W/m² to 600 W/m², the PV system's power output rises accordingly from 6.43 kW to 19.4 kW. As shown in the curves, the power generated by the PV system exceeds the demand for the nonlinear load. Consequently, the

MGCPV system meets the load's power requirements, with the excess power being fed back into the grid, as indicated by the negative grid power value.

As the irradiation increases from 600 W/m² to 1000 W/m², the power produced by the PV system rises from 19.4 kW to 32.3 kW during the period $t$ = [0.9s, 1.2s]. In this interval, the power generated by the PV system exceeds the demand of the nonlinear load, allowing the MGCPV system to supply energy to the load and feed the surplus power back into the grid. During this process, reactive power is effectively managed. At this power level, the FLIBC topology demonstrates superior performance, exhibiting significantly lower power ripples compared to the CBC topology.

Between t = [1.2s, 1.6s], as irradiation levels decrease from 1000 W/m² to 800 W/m², the PV system's power output grows from 32.3 kW to 26 kW. During this time, the power produced by the PV system exceeds the demands of the nonlinear load, enabling the MGCPV system to supply the necessary energy to the load while feeding the surplus back into the grid. Throughout this period, reactive power remains equal to zero to achieve the power factor unity. From the figures, we can observe that the power ripple of the CBC topology rises when the solar irradiation increases. At the same time, the FLIBC can handle high-power levels efficiently with reduced power ripples.

Finally, the nonlinear load resistance decreased during the interval t=[1.6s,1.8s]. During this period, the power produced by the PV system connected to the grid successfully met the load's power demand.

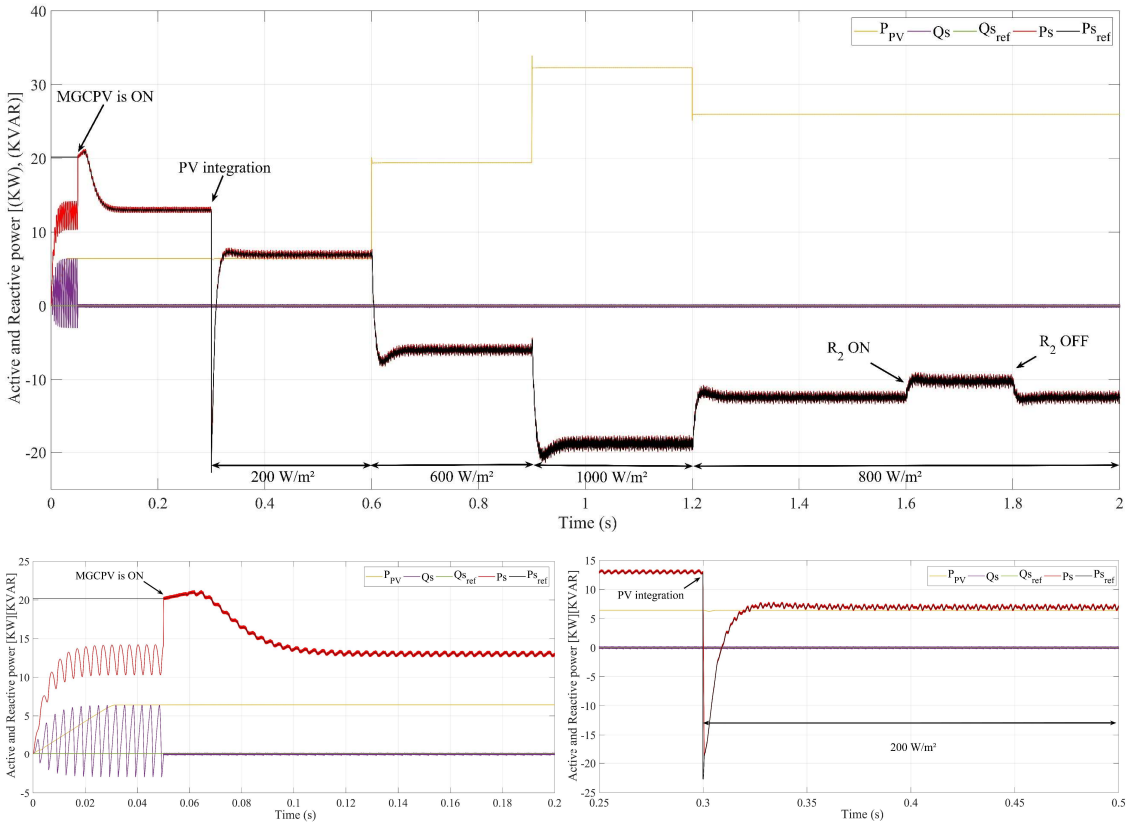

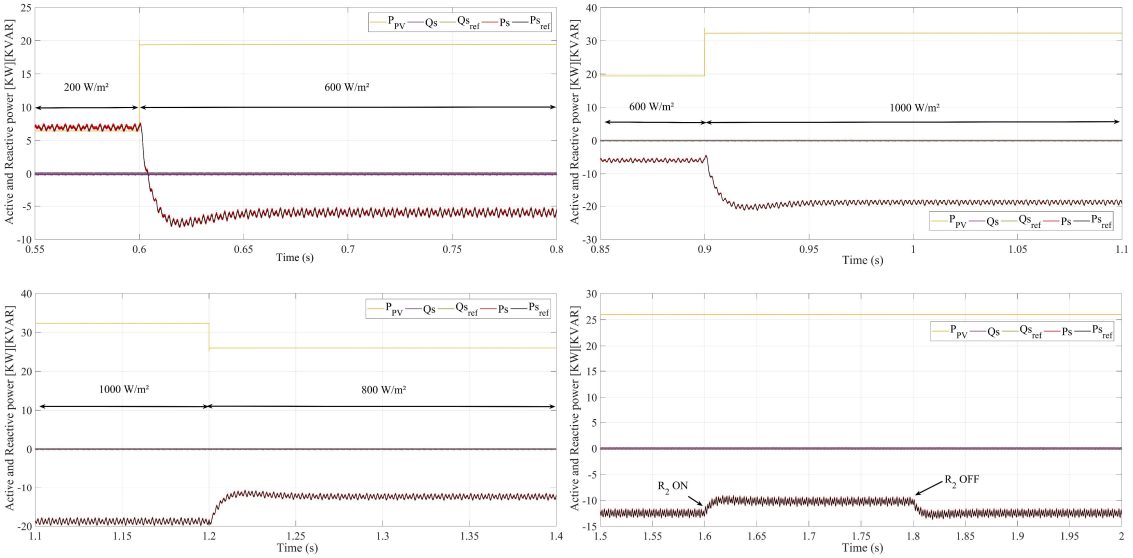


***Figure III-14 The MGCPV active and reactive power using CBC.***

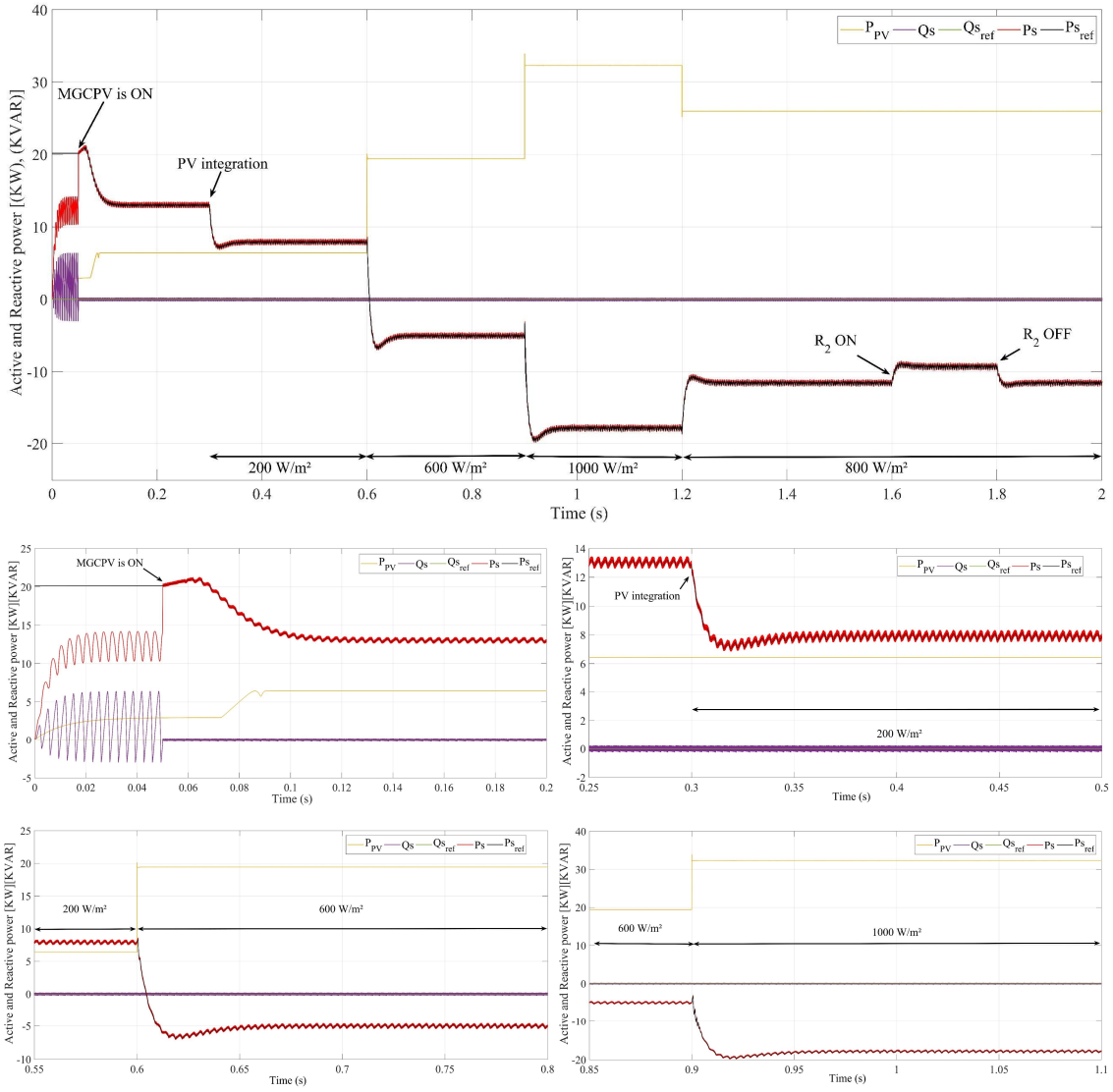

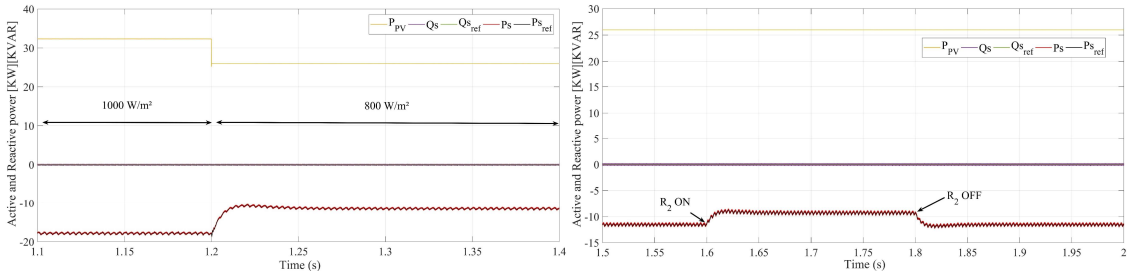


***Figure III-15 The MGCPV active and reactive power using FIBC.***

Figure III-16 and Figure III-17 illustrate the grid voltage and current for phase A. Before the MGCPV is activated, the current waveform is distorted and out of phase with the voltage due to reactive power that is consumed by the load. However, once the MGCPV is activated at $t$= 0.05s, it immediately begins injecting the filtering currents. As a result, the harmonic components are removed at the PCC, and the source current becomes a sinusoidal wave in phase with the source voltage, which indicates the power factor's unity.

At $t$=0.3s, the PV system is integrated with the MGCPV with solar radiation equal to 200 W/m², then increased to 600 W/m², 1000 W/m², then decreased to 800 W/m², respectively. In the interval $t$ = [0.3, 0.6], the grid current decreases thanks to the current injected by the PV system to the nonlinear load.

Then, the power produced using the PV system during the remaining interval is surplus to the nonlinear load power demand. Therefore, the source current becomes on the opposite side of the voltage and has no significant peaks, which means that the current is injected into the utility grid.

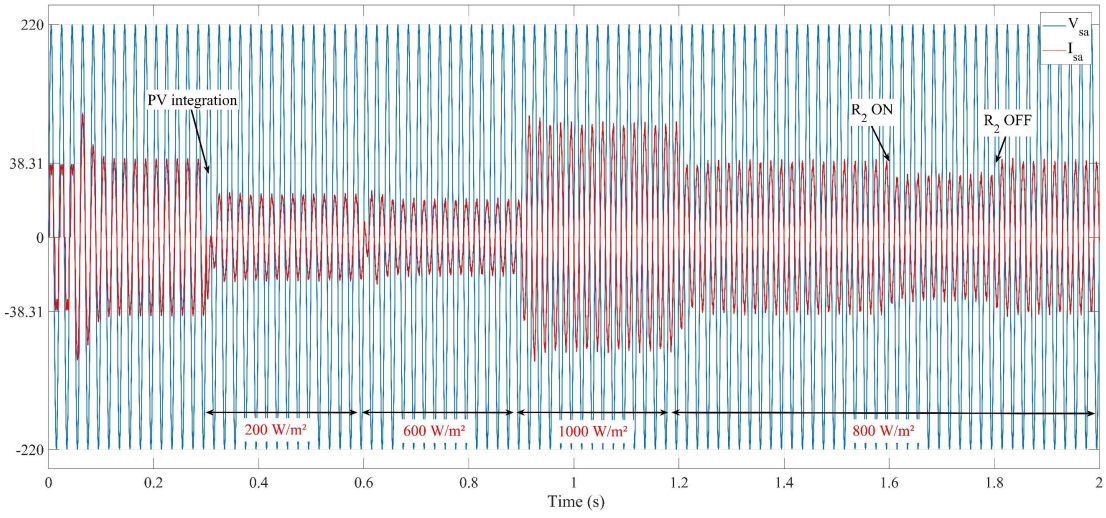

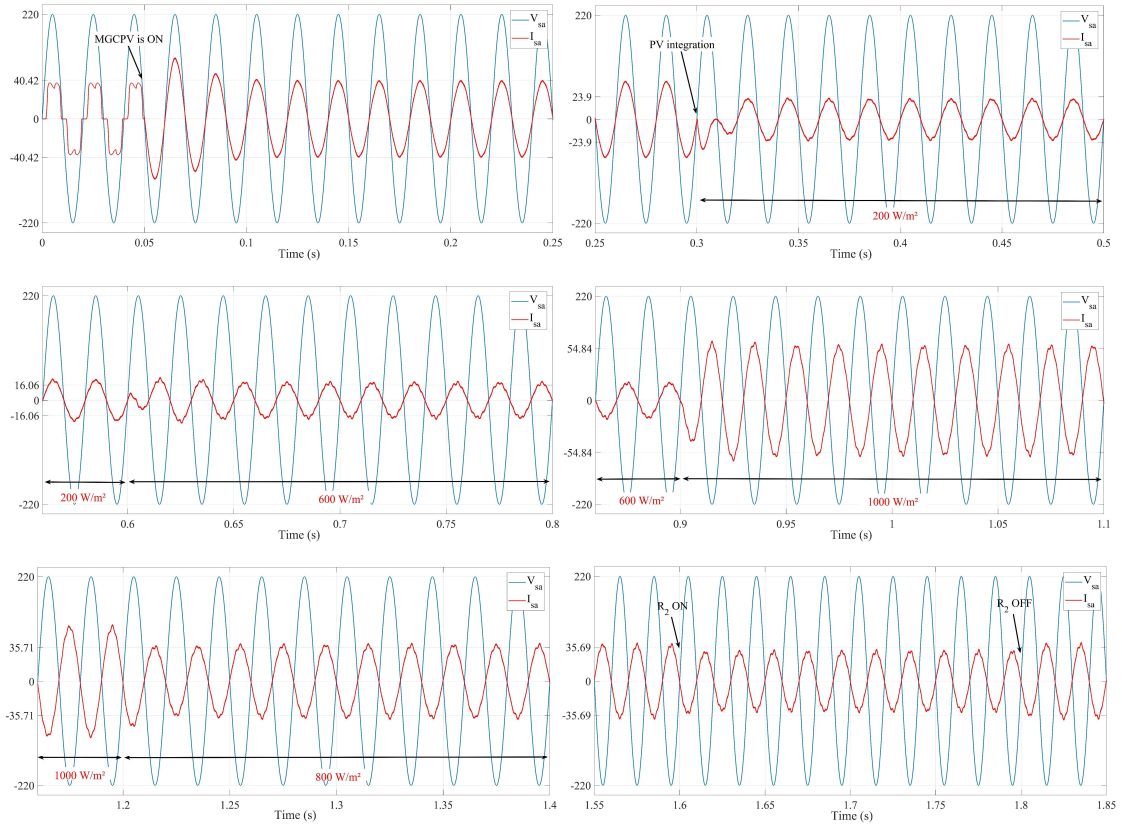


***Figure III-16 The grid A-phase voltage and current using CBC.***

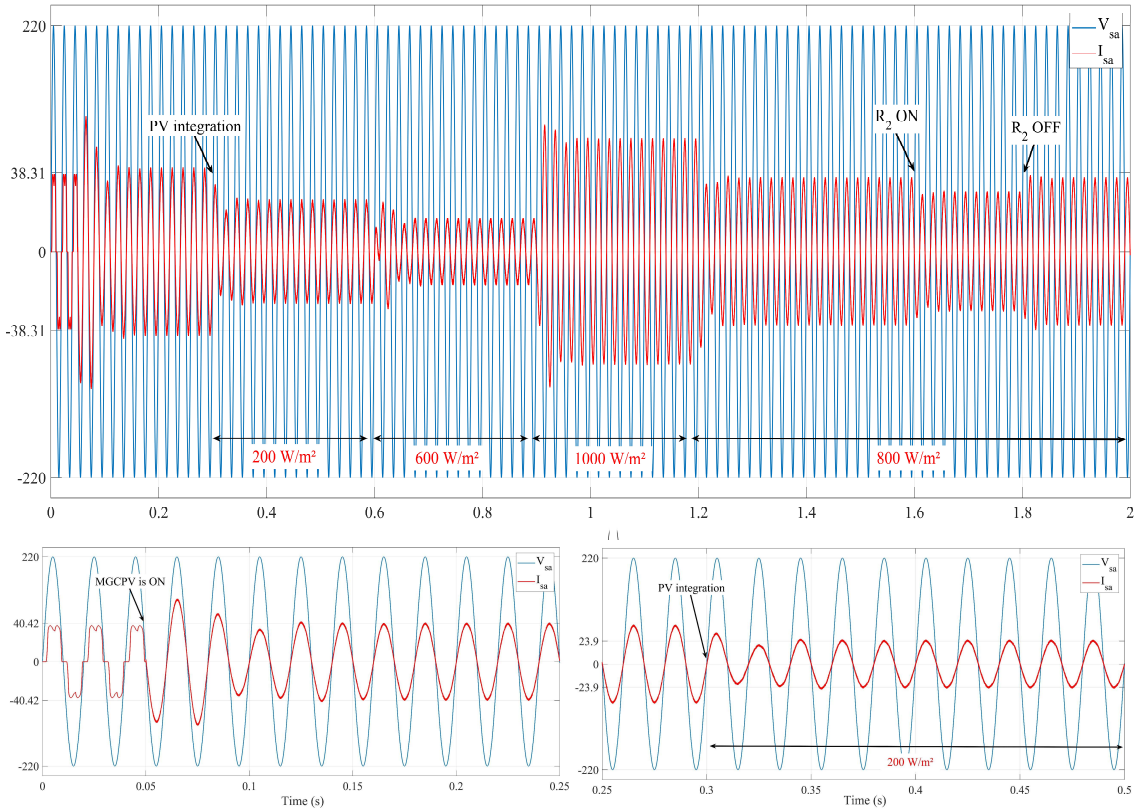

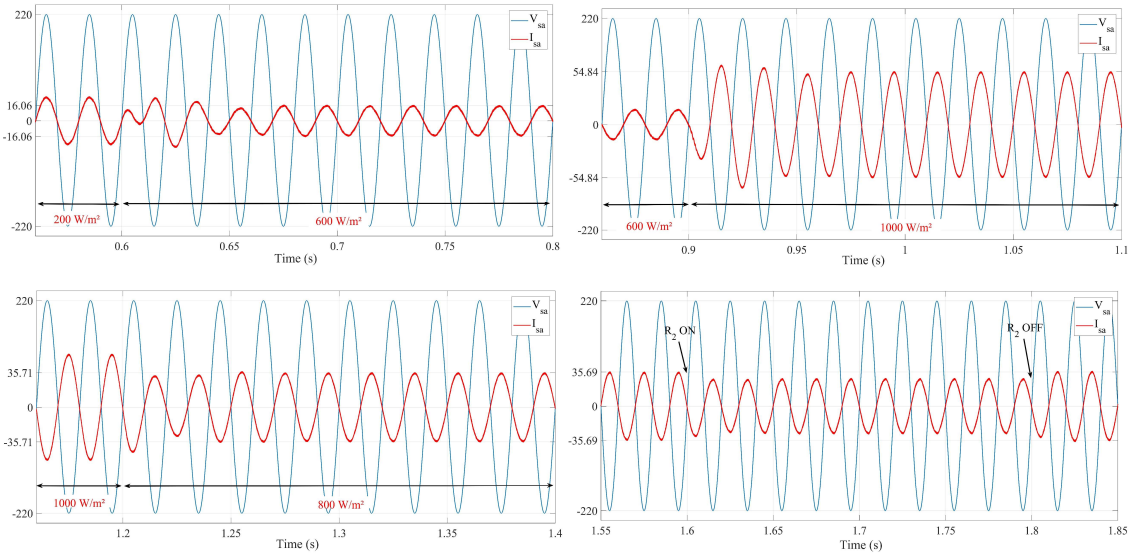


***Figure III-17 The grid A-phase voltage and current using FLIBC.***

The current spectrums are illustrated in Figure III-18-Figure III-20. Initially, before activating the MGCPV, the total harmonic distortion (THD) is measured at 25.31%, as seen in Figure III-18.

At t = 0.05s, the harmonic currents are significantly reduced due to the MGCPV, resulting in a THD of 1.80% without the PV system ( Figure III-19).

Once the PV system is introduced, the recorded THD varies between the two topologies, as depicted in Figure III-20. For the CBC topology, the THD values are 4.06%, 6.23%, 3.43%, and 2.60% at irradiance levels of 200 W/m², 600 W/m², 800 W/m², and 1000 W/m², respectively. In comparison, the FLIBC topology outperforms the CBC in terms of THD reduction, with values of 2.89%, 4.47%, 1.91%, and 1.26% for the same irradiance levels.

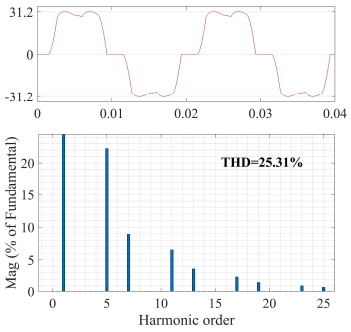


***Figure III-18 Grid current spectrum before activating the MGCPV.***

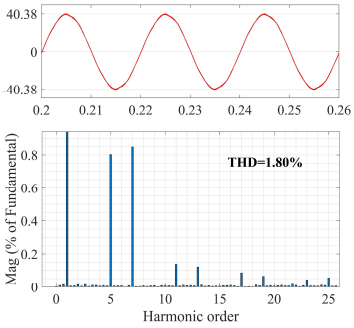


***Figure III-19 Grid current spectrum after activating the MGCPV without a PV system.***

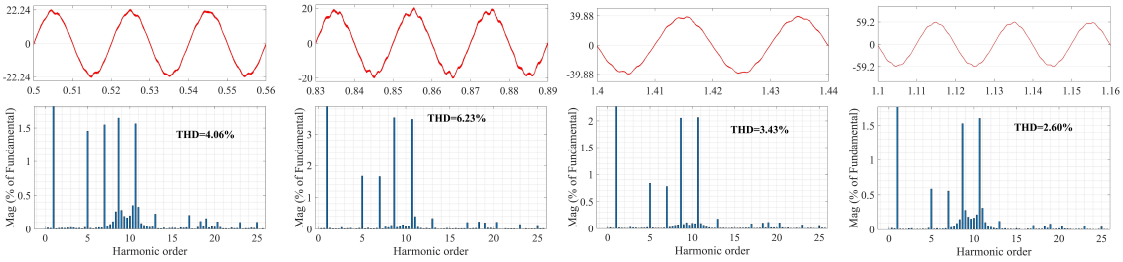


***(a)***

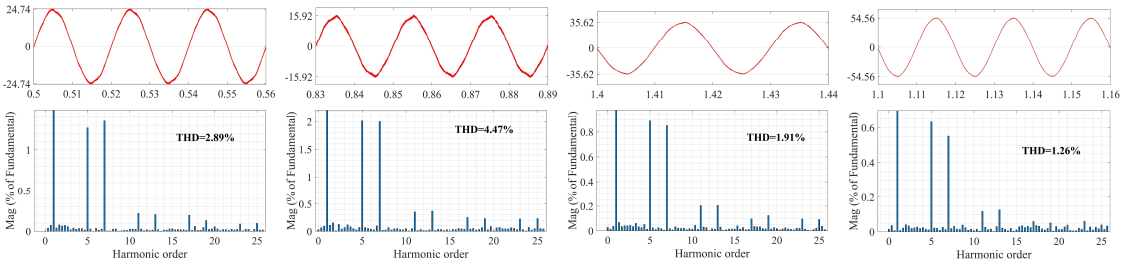


***(b)***

***Figure III-20 Grid current spectrum after activating the MGCPV with a PV system: CBC (a) and FLIBC (b).***

## *5 Conclusion:*

This chapter presents the classical control of a multifunctional grid-connected PV system based on the FLIBC topology. It details the system configuration and modeling of the key components, including the power grid, nonlinear load, and two-level voltage source inverter.

The DPC strategy was adopted to regulate the MGCPV system's active and reactive power. The design of the DC bus voltage regulator and the phase-locked loop was also discussed. Extensive simulations were carried out to evaluate the proposed system's performance under various operating conditions, such as changes in solar irradiation and load disturbances.

The results demonstrate that the FLIBC topology exhibits superior performance compared to the CBC in terms of lower power ripple and less voltage regulation of the DC bus. Specifically, the FLIBC showed reduced DC bus voltage ripple. Additionally, the MGCPV system was able to effectively compensate for reactive power and mitigate current harmonics caused by the nonlinear load.

Overall, the classical control of the MGCPV system based on the FLIBC topology provides an efficient solution for integrating solar energy into the grid while maintaining power quality and grid stability.

In the next chapter, an optimized nonlinear BS control strategy based on fixed switching DPC will investigated to overcome the drawbacks of the conventional DPC.

# *Chapter IV:*

## *DPC-SVM Based on GWO-Backstepping Control of Multifunctional Grid-Connected PV System Fed FLIBC*

## 1 Introduction:

The increasing demand for clean energy has led to the widespread integration of PV systems into the power grid. Advanced control strategies are necessary to ensure high efficiency, stability, and multifunctional capabilities to optimize the performance of these grid-connected systems. Conventional DPC with a switching table and hysteresis controller has been widely used for controlling grid-connected converters. However, this approach has several disadvantages, such as variable switching frequency, increased switching losses, high sampling frequency, and higher current harmonics, which degrade power quality [191].

DPC combined with SVM has emerged as a promising solution to overcome these limitations [188]. The DPC-SVM approach provides a fast-dynamic response, reduces power ripple, and ensures a fixed switching frequency, which enhances power quality and reduces switching losses [192]. This makes it particularly suitable for multifunctional PV systems that require high performance and reliability.

However, using a PI controller in the DPC-SVM strategy presents some limitations [29]. The PI controller is sensitive to parameter variations and has difficulty handling nonlinearities and external disturbances, which can lead to reduced control accuracy and degraded system performance, particularly when the system's performance requirements are stringent. To mitigate these limitations, a BS controller is proposed as an alternative. The BS controller offers a systematic design approach that can handle system nonlinearities effectively [193]. It improves robustness against parameter uncertainties and external disturbances, improving stability and dynamic performance [194]. Using the BS controller, the DPC-SVM strategy can achieve enhanced power regulation, improved transient response, and greater overall reliability for grid-connected PV systems.

The grey wolf optimizer [195] can further optimize the BS controller. GWO is a nature-inspired optimization algorithm that mimics grey wolves' social hierarchy and hunting behavior [37]. By using GWO to optimize the parameters of the BS controller, the system can achieve even better performance in terms of faster convergence, reduced steady-state error, and improved robustness [152].

This chapter presents the design and implementation of an enhanced DPC-SVM control scheme for a MGCPV system. The proposed method addresses the challenges associated with power quality improvement, harmonic compensation, and effective energy injection to the grid. By employing DPC-SVM with a BS controller optimized by the GWO algorithm, the control system achieves precise power regulation, improved transient response, and enhanced robustness. This comprehensive approach mitigates common issues such as grid disturbances and power quality degradation, ultimately demonstrating how this sophisticated control strategy can significantly improve PV-based power systems' overall performance, reliability, and efficiency in a modern grid environment.

The performance of the proposed control scheme is evaluated using the Matlab/Simulink environment. The MATLAB/Simulink model allows for detailed simulation of the grid-connected PV system, incorporating realistic system parameters and operating conditions. Various scenarios,

including changes in solar irradiance, grid disturbances, and load variations, are simulated to test the robustness and effectiveness of the control strategy. Key performance metrics such as power quality, transient response, harmonic distortion, and steady-state error are analyzed to validate the superiority of the DPC-SVM with a BS controller optimized by GWO.

## *2 Direct Power Control Based on Space Vector Modulation (DPC-SVM):*

DPC is a widely used strategy for controlling power systems [27], [182], [196], [197], particularly in applications such as shunt active power filters, grid-connected inverters, and PWM Rectifiers. While conventional DPC based on a switching table and hysteresis controller is widely used for its simplicity and fast dynamic response [198], it also has some limitations that may impact its performance in certain applications [199]. DPC-SVM is an improved version of conventional DPC that incorporates to address the limitations of conventional DPC proposed by Malinowski et al. [27]. By using SVM, DPC-SVM offers more precise control over the switching patterns of the power converter, resulting in a fixed switching frequency, reduced power ripples, and improved overall performance. The DPC-SVM control method comprises an instantaneous active and reactive power estimator, an external DC bus voltage control loop that establishes the active power setpoint $P_{ref}$ using a PI controller, and two internal active and reactive power loops based on PI controllers. The reactive power reference $Q_{ref}$ is set to zero to ensure the unity power factor operation. Finally, the output of the power controller is transformed into the rotating reference frame (d-q frame) and then fed to the SVM block, which determines the appropriate switching states of the VSI.

### *2.1 Active and Reactive Power Estimation:*

According to instantaneous reactive power theory, the instantaneous active and reactive power using the rotating reference frame component can be expressed as follows:

$$\begin{cases} P = V_d I_{sd} + V_q I_{sq} \\ Q = V_q I_{sd} - V_d I_{sq} \end{cases} \tag{4.1}$$

$V_d$ and $V_q$ are the PCC voltage components, and $I_{sd}$ and $I_{sq}$ are the source current. To simplify the control system and decouple the control of active and reactive power, the rotating reference frame's direct axis (d-axis) is aligned with the voltage vector, as shown in Figure IV-1 [200]. As a result, the voltage along the quadrature axis (q-axis) becomes zero while the entire voltage vector is concentrated along the d-axis. The equations below describe the voltage components in the rotating reference frame when the d-axis is aligned with the voltage vector.

$$\begin{cases} V_d = \sqrt{\frac{2}{3}} V_{\max} = U \\ V_q = 0 \end{cases} \tag{4.2}$$

Therefore, the active and reactive power can be calculated as follows:

$$\begin{cases} P = UI_{sd} \\ Q = -UI_{sq} \end{cases} \tag{4.3}$$

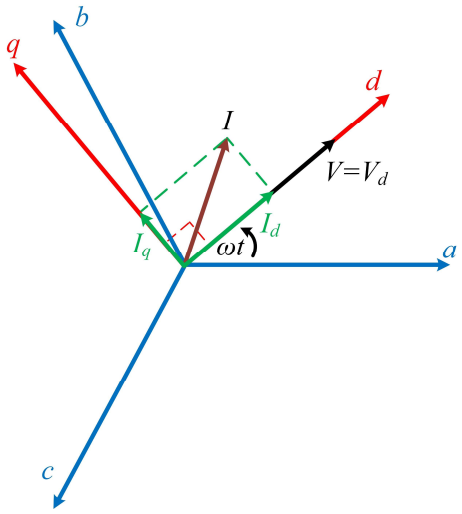


***Figure IV-1 d-axis aligned with the voltage vector.***

## *2.2 Power Control Loop Based on PI Controller:*

PI controllers of the power control loop can be analytically designed using a simplified model of the grid in the rotating reference frame as given in (4.4)

$$\begin{cases} L_s \dfrac{di_{sd}}{dt} = -R_s i_{sd} + L_s \omega i_{sq} - v_d + v_{sd} \\ L_s \dfrac{di_{sq}}{dt} = -R_s i_{sq} - L_s \omega i_{sd} - v_q + v_{sq} \end{cases} \tag{4.4}$$

Where $i_{sd,q}$ are the grid current, $v_{sd,q}$ are the grid voltage and $v_{d,q}$ are the PCC voltage.

When the direct component of the grid voltage is considered aligned with the voltage vector, the model becomes as follows:

$$\begin{cases} L_s \dfrac{di_{sd}}{dt} = -R_s i_{sd} + L_s \omega i_{sq} - v_d + U \\ L_s \dfrac{di_{sq}}{dt} = -R_s i_{sq} - L_s \omega i_{sd} - v_q \end{cases} \tag{4.5}$$

The transfer function of the active ($P$) and reactive ($Q$) power can be expressed using (4.5) as follows:

$$\begin{cases} p(s) = \dfrac{i_{sd}(s)}{u_1(s)} = \dfrac{1}{L_s s + R_s} \\ q(s) = \dfrac{i_{sq}(s)}{u_2(s)} = \dfrac{1}{L_s s + R_s} \end{cases} \tag{4.6}$$

Where $u_1(s) = L_s \omega i_{sq} - v_d + U$ and $u_2(s) = -L_s \omega i_{sd} - v_q$

Thus, from the transfer functions (4.6), the coupling between the dynamics of the grid current $i_{sd}$ and $i_{sq}$ has been transformed into decoupled dynamics. Consequently, the grid currents $i_{sd}$ and $i_{sq}$ can be controlled independently by acting on the quantities $u_1$ and $u_2$, respectively. The block diagram of the power control loop is illustrated in Figure IV-2.

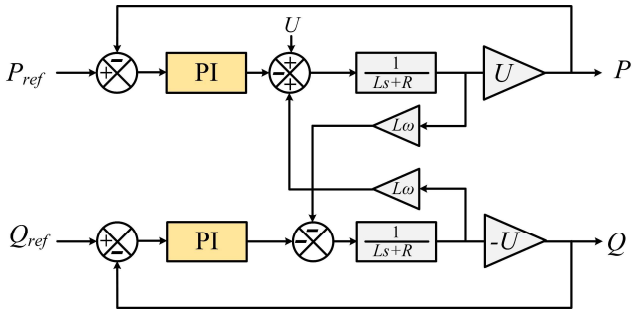


***Figure IV-2 Block diagram of the power control loop based on PI controller.***

Let's consider that the control quantities $u_1$ and $u_2$ are expressed as:

$$\begin{cases} u_1(s) = \left( \dfrac{K_i}{s} + K_p \right) \left( P_{ref} - P \right) \\ u_2(s) = \left( \dfrac{K_i}{s} + K_p \right) \left( Q_{ref} - Q \right) \end{cases} \tag{4.7}$$

Therefore, the closed-loop transfer function, which is identical for both power components, is given by:

$$P,Q(s) = \frac{\dfrac{K_p s}{L_s} + \dfrac{K_i}{L_s}}{s^2 + \dfrac{K_p + R_s}{L_s} s + \dfrac{K_i}{L_s}} \tag{4.8}$$

Thus, the gains $K_p$ and $K_i$ can be calculated as:

$$\begin{cases} K_p = 2\xi\omega L_s - R_s \\ K_i = L_s \omega^2 \end{cases} \tag{4.9}$$

Then, the PCC voltage reference is given as follows:

$$\begin{cases} v_d^* = U + L_s \omega i_{sq} - u_1(s) \\ v_q^* = -L_s \omega i_{sd} - u_2(s) \end{cases} \tag{4.10}$$

Consequently, the VSI voltage reference can be calculated as:

$$\begin{cases} v_{fd}^* = v_d^* - R_f i_{fd} - L_f \dfrac{di_{fd}}{dt} + L_f \omega i_{fq} \\ v_{fq}^* = v_q^* - R_f i_{fq} - L_f \dfrac{di_{fq}}{dt} - L_f \omega i_{fd} \end{cases} \tag{4.11}$$

The block diagram of the DPC-SVM strategy based on the PI controller is shown in Figure IV-3.

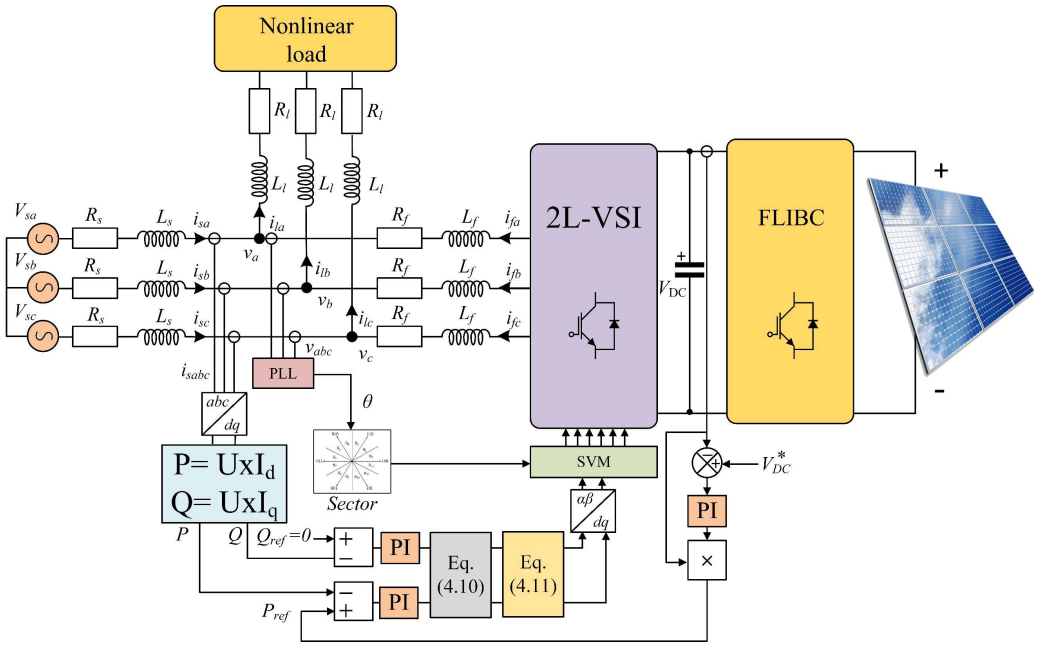


***Figure IV-3 DPC-SVM strategy based on PI controller.***

## *3 DPC-SVM Based on Backstepping Controller:*

Recently, nonlinear control approaches have been an alternative solution to linear control drawbacks. Kanellakopoulos [201] and Kokotovic [202] developed the BS control, a systematic and flexible approach that can effectively control nonlinear systems in the presence of uncertainties.

In the field of power electronics, BS control is widely used. Chebabhi et al. present a comprehensive control strategy that integrates three-level three-dimensional modulation techniques with BS control to enhance the performance of SAPFs based on a three-level NPC four-leg inverter [32]. The proposed approach significantly improves power quality and system stability, making it a valuable contribution to power electronics. In [203] a DPC strategy for a PWM rectifier is suggested for achieving the unity power factor where the BS control was employed to control the DC bus voltage. The simulation results demonstrate the feasibility and adaptability of the BS controller and its effectiveness in regulating transient or stationary voltage with an almost sinusoidal current source with low THD. In the following sections, the design process of the BS control strategy is detailed for both the active and reactive power control loops.

### *3.1 Active and Reactive Power Controller based on BS Controller:*

The foundation of the BS control strategy lies in the precise modeling of the active and reactive power dynamics of an MGCPV system. Using the voltage components $v_d$ and $v_q$ as control inputs, the power equations are defined as:

$$\begin{cases} L_e \dfrac{dP}{dt} = -R_e P - L_e \omega Q - v_d + U \\ L_e \dfrac{dQ}{dt} = -R_e Q + L_e \omega P + v_q \end{cases} \tag{4.12}$$

Where $L_e = \frac{L_s}{e}$ and $R_e = \frac{R_s}{e}$.

The tracking errors for active and reactive power are expressed as:

$$\begin{cases} e_P = P - P_{ref} \\ e_Q = Q - Q_{ref} \end{cases} \tag{4.13}$$

Their time derivatives, critical for control design, are given by:

$$\begin{cases} \dot{e}_P = \dot{P} - P_{ref} = -\frac{R_e}{L_e}P - \omega Q - \frac{v_d}{L_e} + \frac{U}{L_e} - P_{ref} \\ \dot{e}_Q = \dot{Q} - Q_{ref} = -\frac{R_e}{L_e}Q + \omega P + \frac{v_q}{L_e} - Q_{ref} \end{cases} \tag{4.14}$$

To ensure system stability, Lyapunov functions are defined for each subsystem:

$$\begin{cases} V_P = \frac{1}{2}e_P^2 + \frac{\lambda_P}{2}\left(\int e_P dt\right)^2 \\ V_Q = \frac{1}{2}e_Q^2 + \frac{\lambda_Q}{2}\left(\int e_Q dt\right)^2 \end{cases} \tag{4.15}$$

Where $\lambda_P$ and $\lambda_Q$ are design parameters.

The derivatives of these functions are expressed as follows:

$$\begin{cases} \dot{V}_P = e_P\left(\dot{e}_P + \lambda_P \int e_P dt\right) \\ \dot{V}_Q = e_Q\left(\dot{e}_Q + \lambda_Q \int e_Q dt\right) \end{cases} \tag{4.16}$$

To ensure the asymptotic stability of the system, the Lyapunov functions derivative with respect to time must be negative definite as:

$$\begin{cases} \dot{V}_P = -K_P e_P^2 \\ \dot{V}_Q = -K_Q e_Q^2 \end{cases} \tag{4.17}$$

Therefore, substituting (4.9) with (4.10) results in the following:

$$\begin{cases} -K_P e_P^2 = e_P\left(\dot{e}_P + \lambda_P \int e_P dt\right) \\ -K_Q e_Q^2 = e_Q\left(\dot{e}_Q + \lambda_Q \int e_Q dt\right) \end{cases} \tag{4.18}$$

Then,

$$\begin{cases} -K_P e_P = \left(\dot{e}_P + \lambda_P \int e_P dt\right) \\ -K_Q e_Q = \left(\dot{e}_Q + \lambda_Q \int e_Q dt\right) \end{cases} \tag{4.19}$$

To design the control law $v_d$ and $v_q$, must replace (4.14) in (4.19), then:

$$\begin{cases} v_d^* = -R_e P - L_e \omega Q + U - L_e \dot{P}_{ref} + L_e K_P e_P + L_e \lambda_P \int e_P dt \\ v_q^* = R_e Q - L_e \omega P + L_e \dot{Q}_{ref} - L_e K_Q e_Q - L_e \lambda_Q \int e_Q dt \end{cases} \tag{4.20}$$

Finally, the VSI voltage references can deduced as follows:

$$\begin{cases} v_{fd}^{*} = v_{d}^{*} - R_f i_{fd} - L_f \dfrac{di_{fd}}{dt} + L_f \omega i_{fq} \\ v_{fq}^{*} = v_{q}^{*} - R_f i_{fq} - L_f \dfrac{di_{fq}}{dt} - L_f \omega i_{fd} \end{cases} \tag{4.21}$$

The block diagram of the power control loop is illustrated in Figure IV-4, and the block diagram of the DPC-SVM strategy based on the BS controller is shown in Figure IV-5.

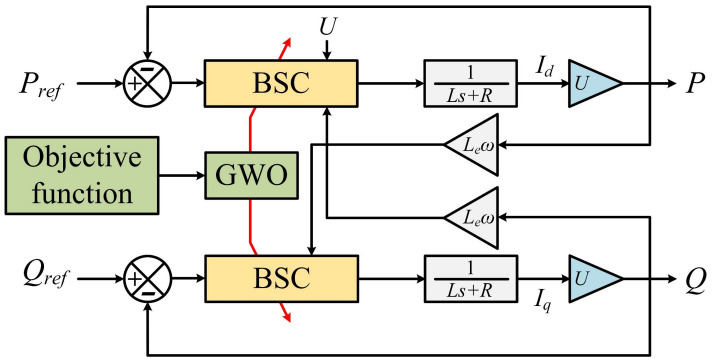


***Figure IV-4 The block diagram of the power control loop is based on the optimized BS controller.***

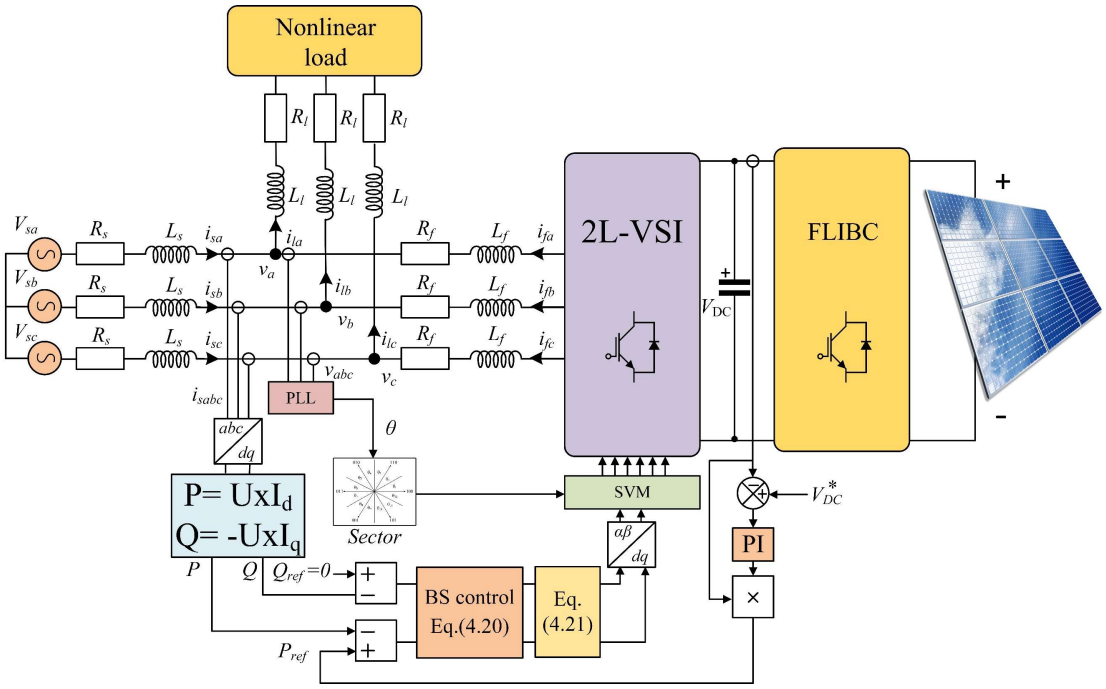


***Figure IV-5 DPC-SVM strategy based on BS controller.***

### *3.2 DC-Bus Voltage Regulator Based on Optimized Anti-Windup PI Controller:*

In this chapter, the DC bus voltage regulator based on PI controller and optimized using the grey wolf optimization technique is proposed. The controller gains are tuned across an objective function (OF) (Figure IV-6). The GWO allows to choose the gains that give the minimum value of the OF.

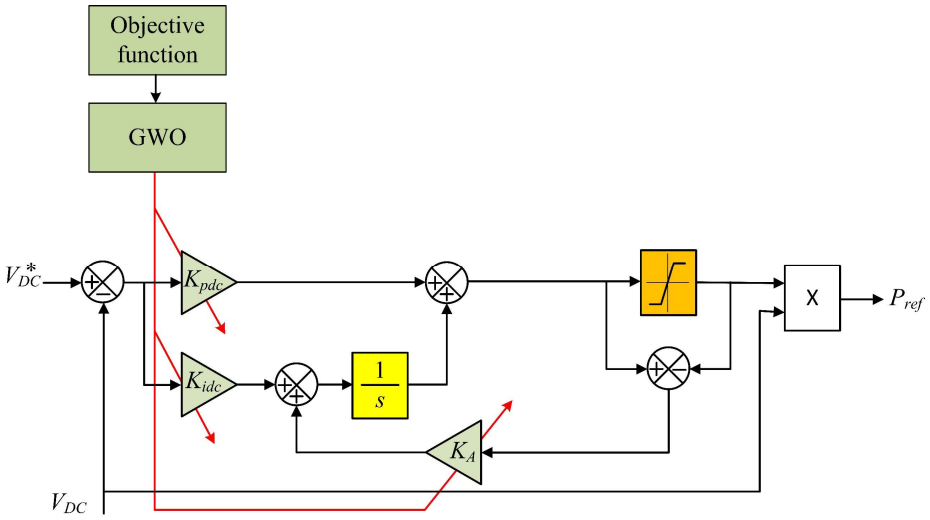


***Figure IV-6 DC Bus voltage regulator based on GWO-Anti-Windup PI controller.***

## 4 *Grey Wolf Optimizer Algorithm:*

The GWO [35] is a bio-inspired method that mimics the hunting behavior of the grey wolf group. Generally, the group size ranges from 5 to 12 wolves [204]. The hierarchical system of there are four tiers in the grey wolf social hierarchy: alpha ($\alpha$), beta ($\beta$), delta ($\delta$), and omega ($\omega$), where alpha is the leader level, and the three lower levels must follow it. The second-level beta can provide feedback and help the alpha-level make decisions. In addition, lead the two lower levels. The delta level dominates the lowest omega and submits to the alpha and beta levels. The rest of the wolves are the last level of omega, and they are not important in the group but are required to protect the dominant structure. Muro et al. [205] describe the principal steps of grey wolf hunting behavior, which are as follows

1. Approaching, tracking, and pursuing the prey;
2. Pursuit, harass, and encircling maneuvers, tracking and hunting the prey;
3. Attack and hunt the prey.

The following mathematical equations describe the procedures mentioned above.

$$\vec{D} = \left|\vec{C}.\vec{X}_p(i) - \vec{X}(i)\right| \tag{4.24}$$

$$\vec{X}(i+1) = \left|\vec{X}_P(i) - \vec{A}.\vec{D}\right| \tag{4.25}$$

Where $X_P$ is the position vector of the prey, $i$ is the recent iteration, $X$ is the vector of the grey wolves' position, and $D$ is a vector that refers to the distance between the prey and wolves. $A$ and $C$ are coefficient vectors which can be computed using the following equations:

$$\vec{C} = 2\vec{r}_1 \tag{4.26}$$

$$\vec{A} = 2\vec{a}\vec{r}_2 - \vec{a} \tag{4.27}$$

On the other hand, $r_1$ and $r_2$ are random numbers that vary in each iteration in the range [0, 1]. In addition, $a$ is a vector decreased during iterations from 2 to 0. According to the grey level, the distance of each level can be given as:

$$\begin{cases} \vec{D}_\alpha = \left| \vec{C}_1 . \vec{X}_\alpha - \vec{X} \right| \\ \vec{D}_\beta = \left| \vec{C}_2 . \vec{X}_\beta - \vec{X} \right| \\ \vec{D}_\delta = \left| \vec{C}_3 . \vec{X}_\delta - \vec{X} \right| \end{cases} \tag{4.28}$$

$D_\alpha$, $D_\beta$, and $D_\delta$ are the distances between wolves of alpha level and prey, wolves of beta level and prey, and wolves of delta level and prey. $C_1$, $C_2$, and $C_3$ are the coefficient vectors of the first three best fittest positions: $X_1$, $X_2$, and $X_3$. And $X_\alpha$, $X_\beta$, and $X_\delta$ are the best search agents. The equations that represent the three best positions of grey wolves are expressed as follows:

$$\begin{cases} \vec{X}_1 = \vec{X}_\alpha - \vec{A}_1 (\vec{D}_\alpha) \\ \vec{X}_2 = \vec{X}_\beta - \vec{A}_2 (\vec{D}_\beta) \\ \vec{X}_3 = \vec{X}_\delta - \vec{A}_3 (\vec{D}_\delta) \end{cases} \tag{4.29}$$

The formula below can be used to compute the position of the prey for the best search agent.

$$\vec{X}(i+1) = \frac{\vec{X}_1 + \vec{X}_2 + \vec{X}_3}{3} \tag{4.30}$$

The flowchart of the GWO algorithm is presented in Figure IV-7.

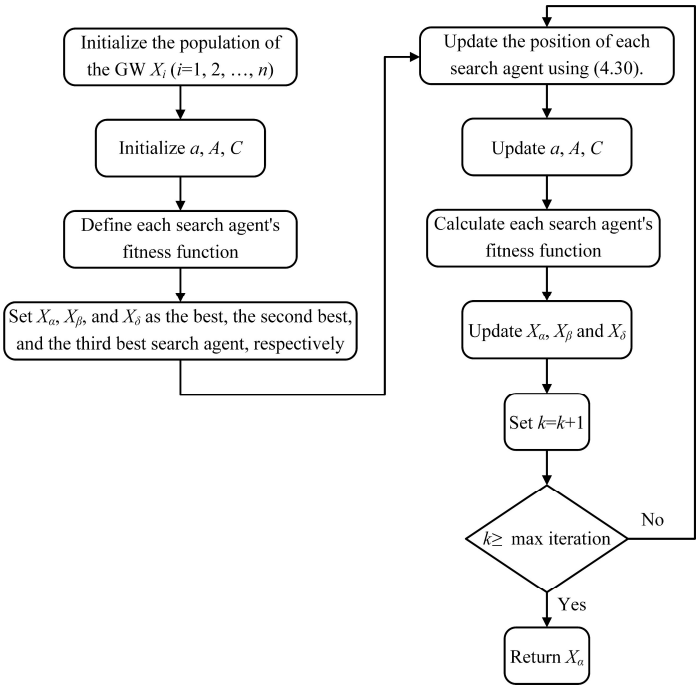


***Figure IV-7 The flowchart of the grey wolf optimization algorithm.***

The objective function used in the optimization is described as follows:

For the power loops, the integral time square error is used as an objective function, and its equation is given as:

$$f_1 = ITSE(P_{ref} - P) = \int T \left( P_{ref} - P \right)^2 dt \tag{4.31}$$

For the DC bus voltage:

$$f_2 = w_1 ITSE(V_{DC}) + w_2 (\max(V_{DC}) - V_{DCref}) / V_{DCref} + w_3 THD \tag{4.32}$$

Where $w_1$, $w_2$, and $w_3$ are positive definite weighting factors. Figure IV-8 and Figure IV-9 show the OF curves during the optimization process. Using the trial and error method, the obtained gains of the DC bus voltage controller are tuned using the following weighting factors: $w_1 = 0.3$, $w_2 = 0.7$, and $w_3 = 6$.

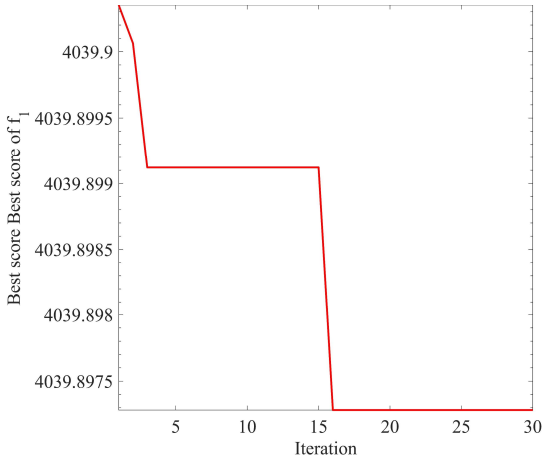


***Figure IV-8 The behavior of the OF $f_1$ during the power loop optimizing process.***

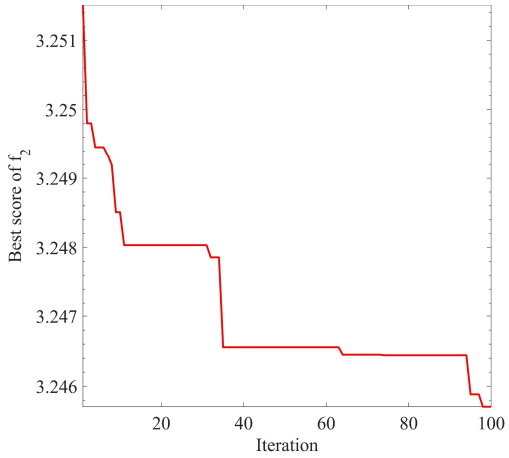


***Figure IV-9 The behavior of the OF $f_2$ during the DC bus voltage optimizing process.***

## *5 Simulation Results and Discussion:*

The proposed system was analyzed through comprehensive simulations conducted using MATLAB/Simulink software. Extensive tests were performed under various operating conditions to assess the system's performance and ensure a thorough evaluation of its capabilities.

The simulation results focused on the performance of the MGCPV system based on FLIBC, which employed DPC-SVM in conjunction with an optimized BS controller achieved through a GWO algorithm. These results were compared to those obtained using a DPC-SVM based on a PI controller. The parameters used in the simulations are listed in Table IV-1. In addition, the solar irradiation profile used to evaluate the system is presented in Figure IV-10.

***Table IV-1 Simulation parameters.***

| *MGCPV Parameters* | | *Controller Parameters* | | |
|---|---|---|---|---|
| *Parameter* | *Value* | *Parameter* | *Value* | |
| *Source Voltage* $V_{max}$ | 220 *V* | *Optimized BS controller* | | |
| *Source frequency* | 50 *Hz* | $K_P$, $K_Q$ | 9.2145x10$^6$ | 10x10$^6$ |
| $R_s$, $L_s$ | 10 *m*Ω, 0.6 *mH* | $\lambda_P$, $\lambda_Q$ | 4.1541x10$^3$ | 1.7147x10$^3$ |
| $R_f$, $L_f$ | 0.6 *m*Ω, 2 *mH* | *Optimized PI controller* | | |
| $R_c$, $L_c$ | 1 *m*Ω, 0.3 *mH* | $K_{pdc}$ | 0.592 | |
| $R_{L1}$, $R_{L2}$, $L_L$ | 10 Ω, 8.5 Ω, 1 *mH* | $K_{idc}$ | 75.66 | |
| | | $K_A$ | 973 | |
| *DC bus voltage* $V_{DC}$ | 800 *V* | *GWO Parameters* | | |
| $C_{DC}$ | 4000 *uF* | *Search Agent* | 50 | |
| *Switching frequency* | 20 *KHz* | *Max iteration* | 100 | |

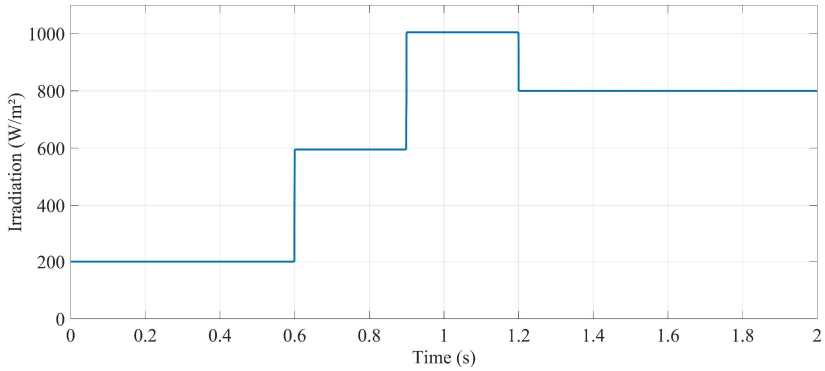


***Figure IV-10 Solar irradiation profile.***

Figure IV-11 illustrates the DC bus voltage of the MGCPV using both controllers (PI and GWO-PI). At $t$ = 0.05 s, the MGCPV without the PV system is connected to the grid. The DC bus voltage rapidly tracks its reference value. The PI controller reaches the reference value in 66 ms without overshoot, whereas the optimized PI controller achieves its reference value in 44 ms with a 6 V overshoot.

After integrating the PV system at $t$ = 0.3 s, the DC bus voltage perturbation was rectified using both controllers. The PI controller exhibits an overshoot of 4.8 V and a response time of 54 ms. In contrast, the GWO-tuned PI controller achieves a faster response time of 29 ms and an overshoot of 5.3 V.

At $t$ = 0.6, the solar irradiation increases from 200 W/m² to 600 W/m². The optimized PI controller's behavior is faster than the PI controller's, with response times of 32 ms and 61 ms, respectively. Regarding overshoot, the GWO-PI controller exhibits 12.9 V, while the PI controller shows 11.3 V.

After increasing the solar irradiation in $t$ = 0.9 from 600 W/m² to 1000 W/m², the DC bus voltage experiences a perturbation quickly rectified by the DC bus voltage controller. The PI controller exhibits an overshoot of 11.2 V and a response time of 60 ms. The response of the GWO-PI controller is faster than that of the PI controller, whose response time is 38 ms and an overshoot of 12.5 V.

When the solar irradiation decreased from 1000 W/m² to 800 W/m² at $t$ = 1.2 s, the DC bus voltage exhibited an undershoot for both controllers. The GWO-PI controller recovered its reference with a response time of 38 ms and an undershoot of 6.4 V, while the PI controller regained its reference value at 55 ms with an undershoot of 5.5 V.

For the load variation that occurred at $t$ =1.6 s and $t$ = 1.8 s, the DC bus voltage controllers rejected that perturbation and quickly recovered the reference value.

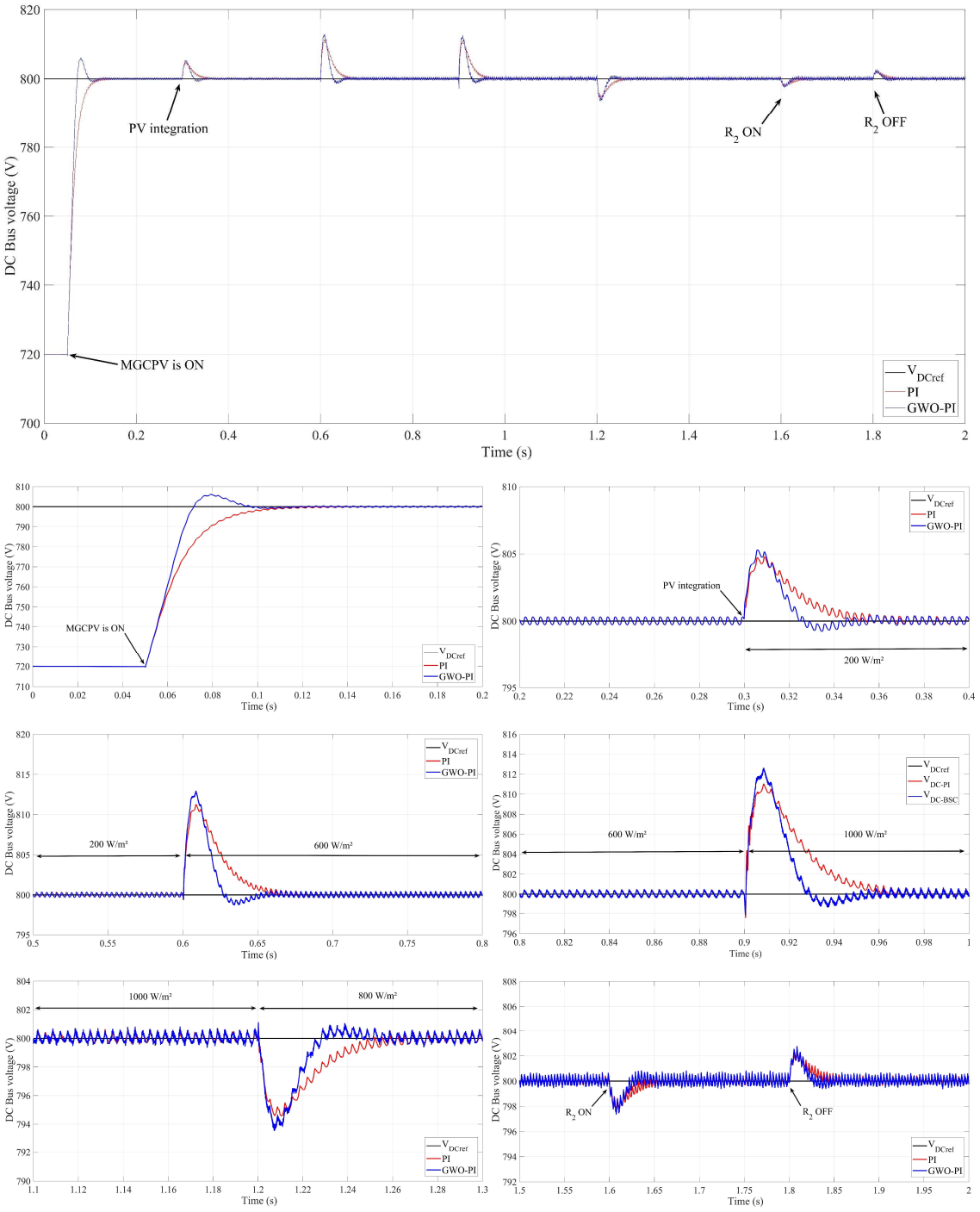


***Figure IV-11 DC bus voltage of the MGCPV.***

The power curves of the system, including the grid active and reactive powers and the PV system power, are illustrated in Figure IV-12 and Figure IV-13. After connecting the MGCPV to the grid without the PV system at $t = 0.05$, the DPC-SVM strategy, based on both controllers, allows the system to track the reference values of active and reactive power. The reactive power drops to zero, indicating that the unity power factor is achieved. During this period, the active power ripple is 580.7 W for the PI controller and 404.8 W for the optimized BS.

At t = 0.3 s, the PV system is integrated with the MGCPV system, where the PV system's produced power is 6.43 kW. When the PV system is integrated, the active power absorbed by the grid decreases from 10.7 kW to 6.58 kW. The power ripple in the MGCPV system using DPC-SVM with an optimized BS controller is 450.3 W, while the power ripple with a PI controller is 617.5 W.

When the irradiation increases from 200 W/m² to 600 W/m², the controllers smoothly track the power references. The power injected by the PV system causes the grid's active power consumed by the load to become negative. In this case, the power injected into the grid exceeded the load power demand. The negative active power value signifies that the PV system's excess power is being fed into the grid. The optimized system demonstrates a lower power ripple (590 W) compared to the DPC-SVM strategy based on a PI controller (696.2 W).

After $t = 0.9$ s, the solar irradiation increased from 600 W/m² to 1000 W/m², causing the PV system's power output to rise from 19.44 kW to 32.31 kW. In this period, the power ripples of the PI controller and the optimized BS controller are 853.4 W and 753.5 W, respectively.

Decreasing the solar irradiation to 800 W/m² at $t = 1.2$ decreased the PV system's power output, which in turn reduced the power injected into the grid. In this period, the power generated by the PV system is 25.97 kW, which surplus the grid's power demand (10.7 kW). The power ripples, in this case, are 731.1 W for the PI controller and 655 W for the optimized BS controller.

Finally, in the event of load variation, the system rejects that perturbation and rectifies the load power demand.

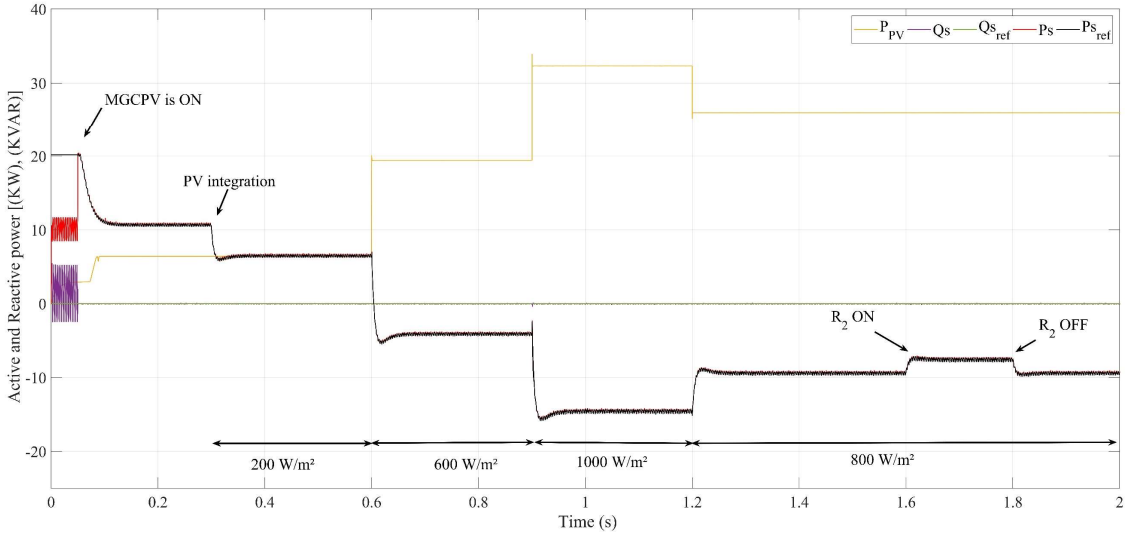

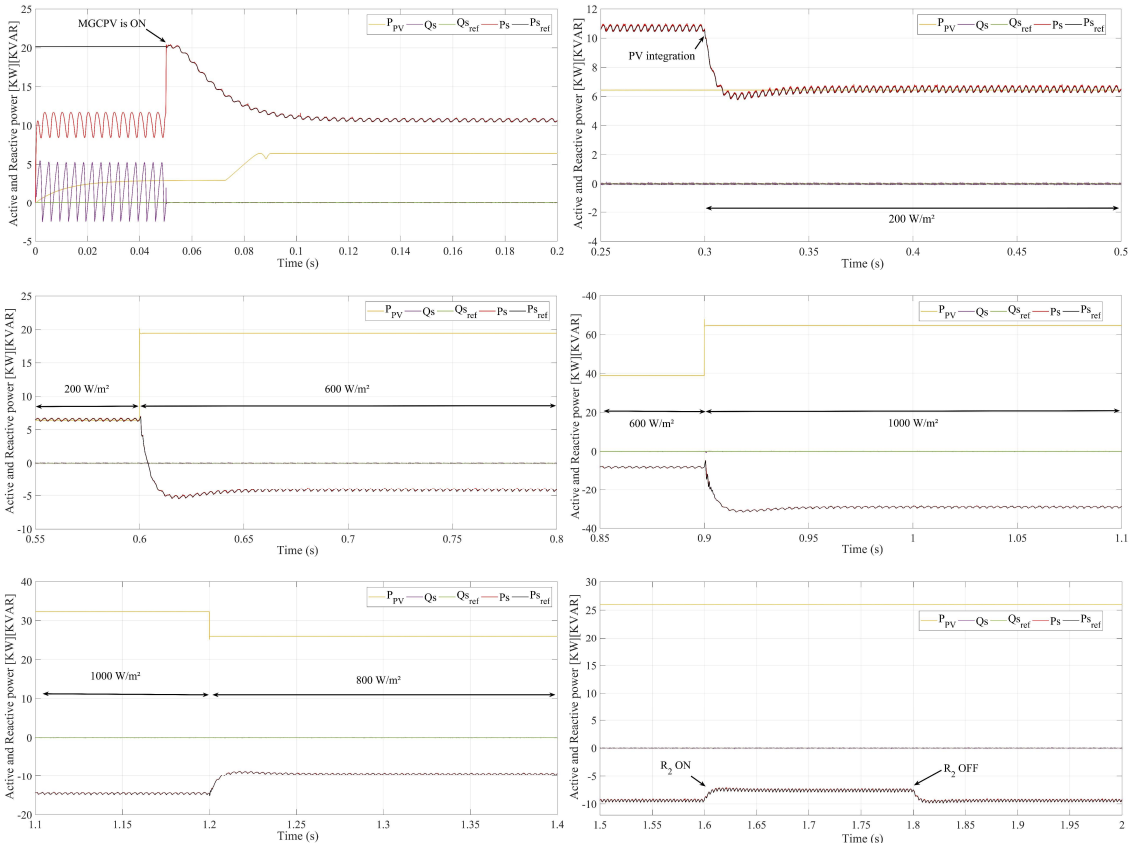


***Figure IV-12 Grid's Active and Reactive power using MGCPV based on PI controller.***

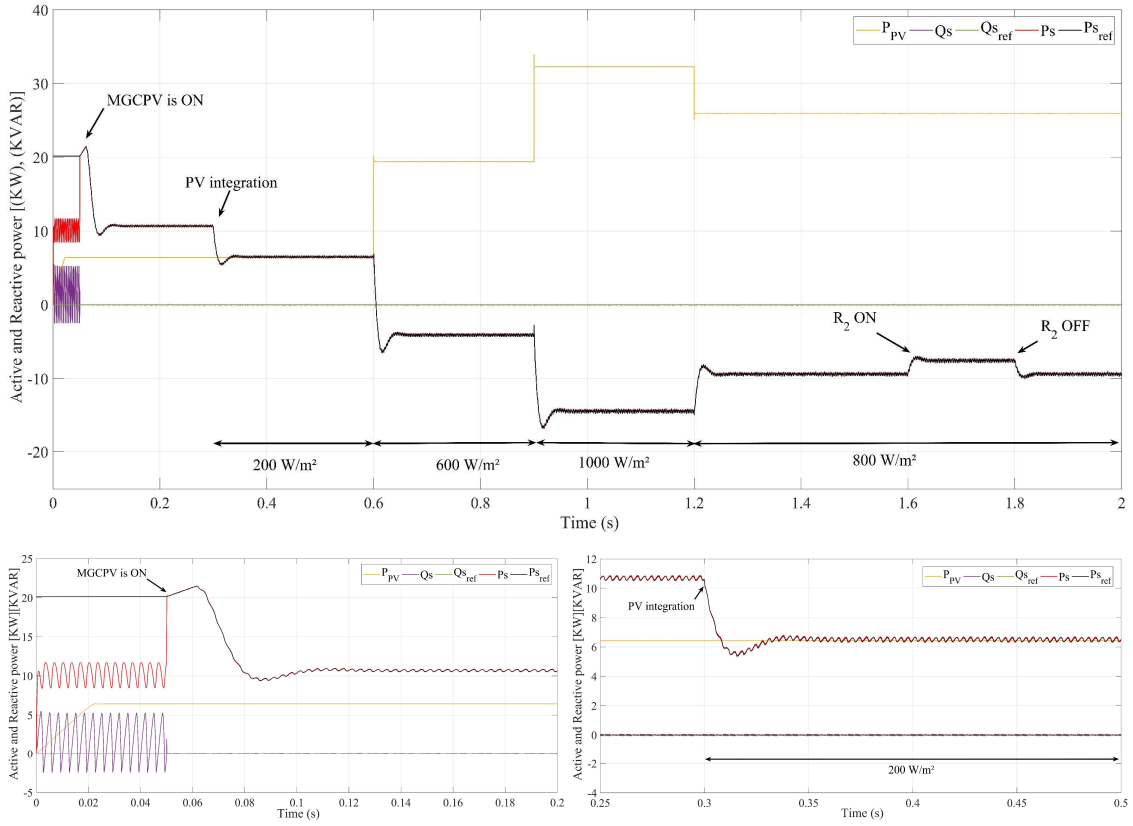

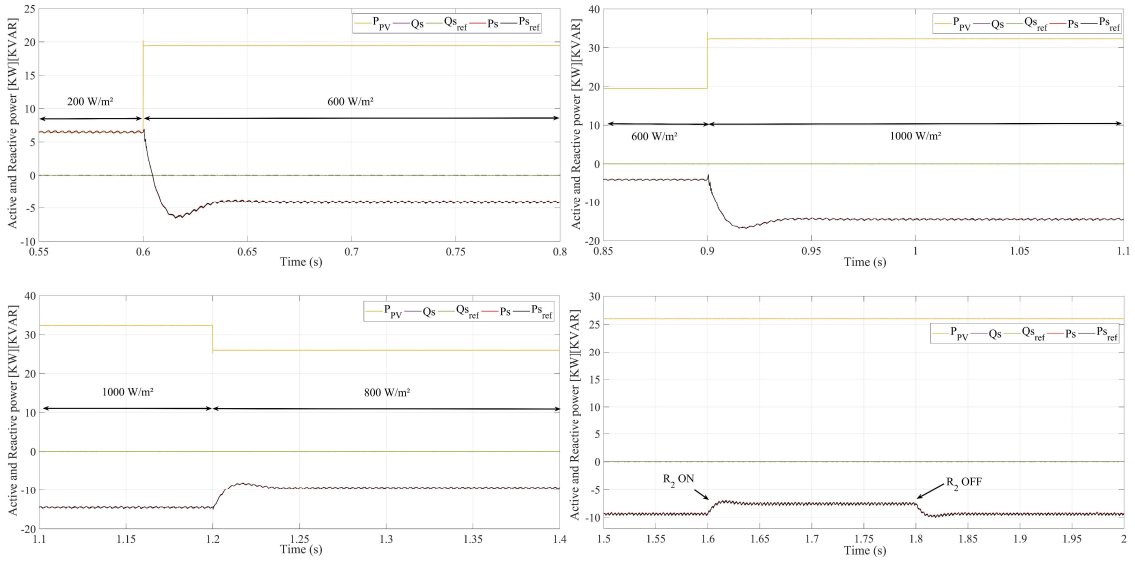


***Figure IV-13 Grid's Active and Reactive power using MGCPV based on optimized BS controller.***

The grid's current and voltage for phase A are illustrated in Figure IV-14 and Figure IV-15. The curves in Figure IV-14 are derived from the topology employing the PI controller, while Figure IV-15 presents the simulation results from the optimized BS controller topology. From the figures, it is evident that the current is distorted and phase-shifted relative to the grid voltage before integrating the MGCPV system. During this period, a significant amount of harmonics in the source current with a THD value equal to 25.31%, as shown in the current spectrum before inserting the MGCPV system in Figure IV-16.

After integrating the MGCPV system into the grid at $t = 0.05$ s, the grid current assumes a sinusoidal waveform and aligns in phase with the grid voltage. This indicates that harmonics have been effectively suppressed and reactive power has been compensated. The optimal BS controller performs better than the PI controller, whereas the response time is 50 ms and 65 ms, respectively. In this case, the grid supplies the load, and the inverter works as SAPF.

At $t = 0.3$ s, the PV system is integrated with 200 W/m² of irradiation. During this period, the grid current remains sinusoidal and in phase with the grid voltage. However, the amplitude of the grid current decreases because the PV system's generated power is being injected into the grid.

When solar irradiation increases from 200 W/m² to 600 W/m² at $t = 0.6$ s, the power generated by the PV system exceeds the demand from the nonlinear load. Consequently, the grid current becomes 180 degrees out of phase with the voltage, indicating that power is being injected into the grid. A similar behavior is observed when irradiation increases at $t = 0.9$ s from 600 W/m² to 1000 W/m²; the amplitude of the grid current becomes more negative, suggesting an increase in power injection due to higher PV system power generation. At $t = 1.2$ s, solar irradiation decreases to 800 W/m², leading the PV system to reduce its power output, which in turn decreases the amplitude of the current injected into the grid.

During load variation events at $t = 1.6$ s and $t = 1.8$ s, the system quickly rectifies the load demand without current spikes.

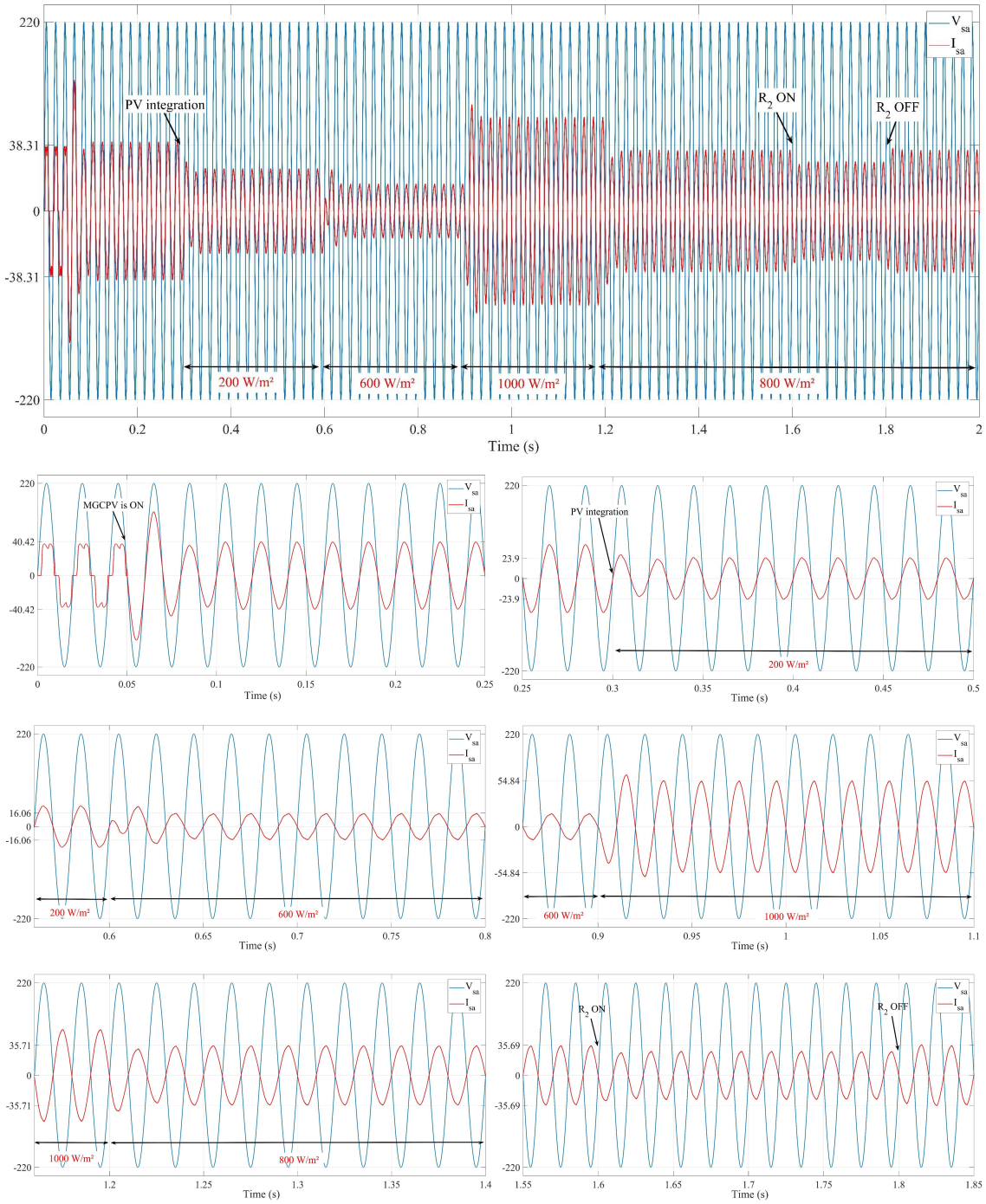


***Figure IV-14 Grid voltage and current of A-phase using PI controller.***

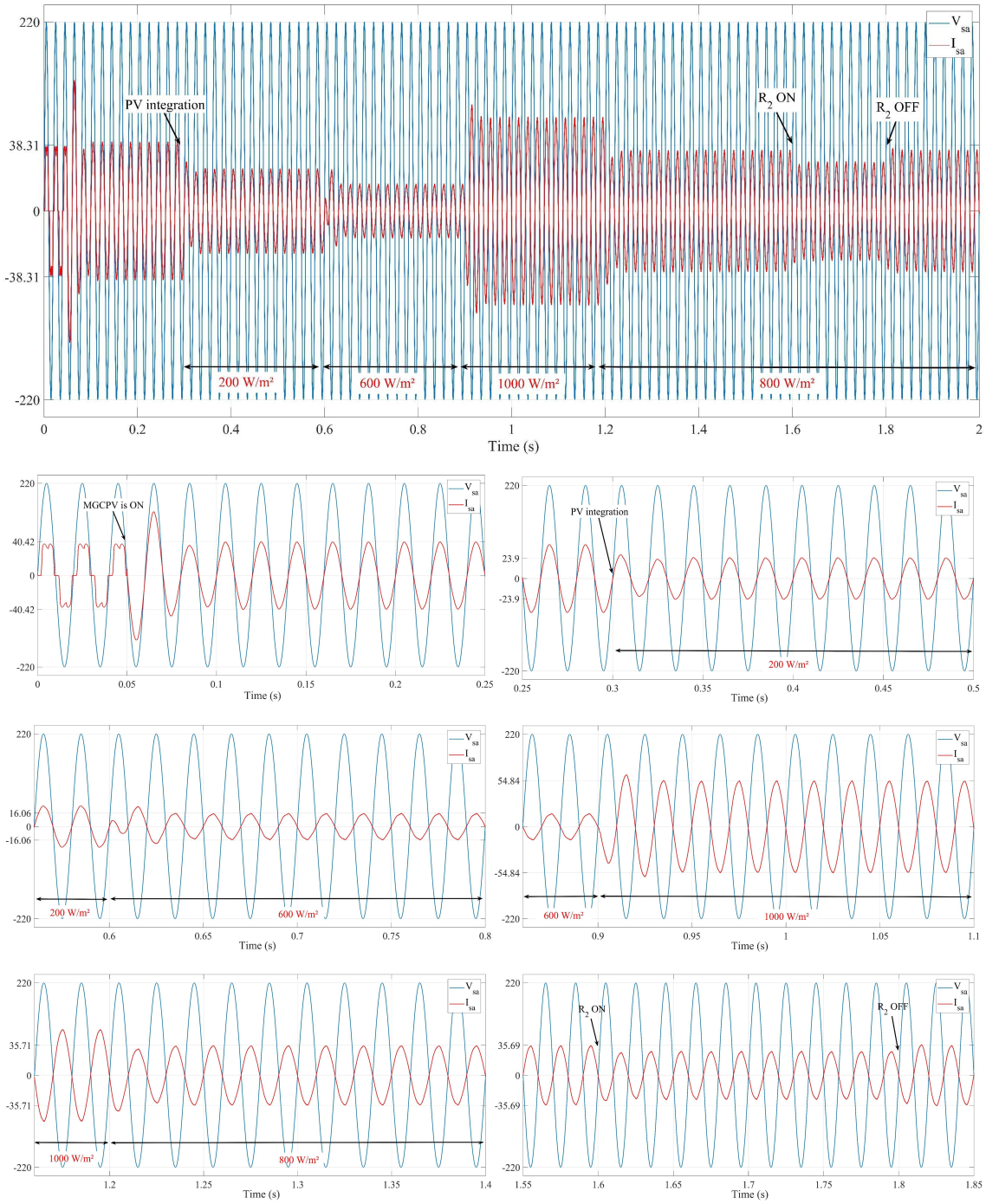


***Figure IV-15 Grid voltage and current of A-phase using the optimized BS controller.***

The grid current spectrums are shown in Figure IV-16 -Figure IV-19. The THD of the distorted grid current before inserting the MGCPV is 25.31%, as seen in Figure IV-16. At t = 0.05s, the MGCPV system is integrated with the grid without the PV system. The THD observed in the topology of the DPC-SVM based on the optimized controllers is 1.04% compared to the PI controller, whereas the THD is 1.45%, as illustrated in Figure IV-17.

After integrating the PV system, both topologies meet the IEEE-514 standards, as the grid current spectrums show in Figure IV-18 and Figure IV-19. Where the PI controller THDs are 2.35%, 3.69%, 1.71% and 1.19% for irradiations 200 W/m², 600 W/m², 800 W/m² and 1000 W/m², respectively. On the other hand, the optimized topology using the BS controller shows THD values of 1.68%, 2.80%, 1.31%, and 0.91% for solar irradiations of 200 W/m², 600 W/m², 800 W/m², and 1000 W/m², respectively.

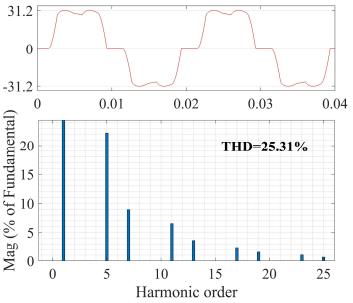


***Figure IV-16 Grid current spectrum before inserting the MGCPV system.***

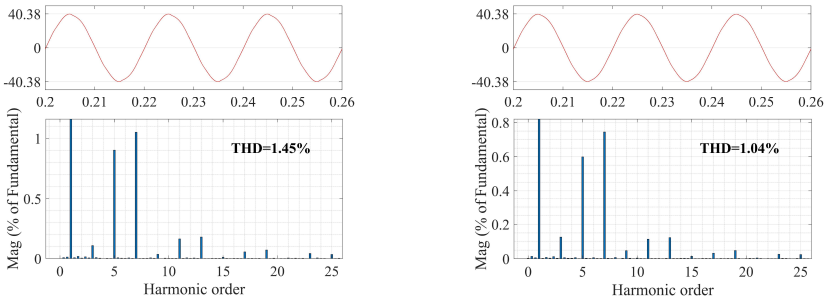


***(a)*** ***(b)***

***Figure IV-17 Grid current spectrum after activating the MGCPV without a PV system: PI controller (a) and GWO BS(b).***

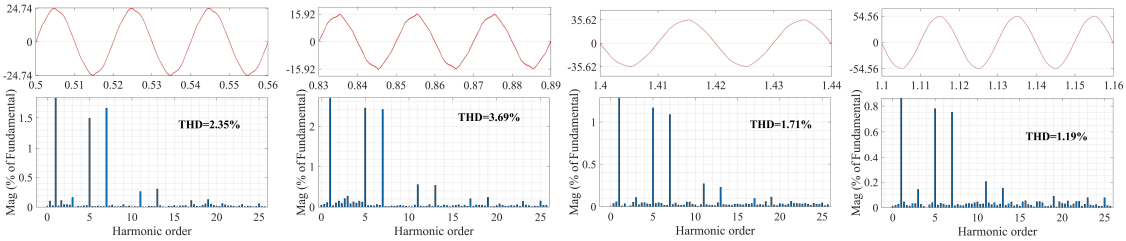


***Figure IV-18 Grid current spectrum after inserting the MGCPV system with PV system using PI controller.***

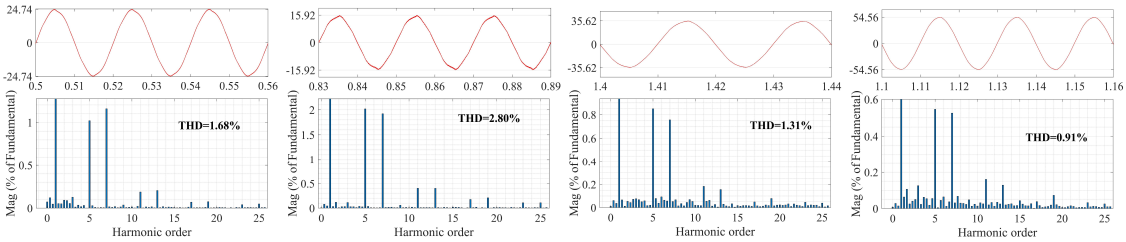


***Figure IV-19 Grid current spectrum after inserting the MGCPV system with PV system using GWO-BS controller.***

Finally, Table IV-2 provides a comprehensive comparison of the two controllers. The results clearly show that the DPC-SVM system with BS controller optimized using GWO outperforms the conventional DPC-SVM with PI controller in terms of the performance indexes (IAE, ISE, ITAE, and ITSE), power ripple reduction, and THD values.

***Table IV-2 Comprehensive comparison of the performance standards between an Optimized BS and PI controller.***

| | ***Controller*** | | ***IAE*** | ***ISE*** | ***ITAE*** | ***ITSE*** |
|---|---|---|---|---|---|---|
| ***DC bus voltage*** | ***PI*** | | 6.345 | 376.6 | 1.260 | 14.87 |
| | ***GWO-PI*** | | 5.892 | 368.0 | 1.096 | 13.94 |
| ***Power loop*** | ***CDPC*** | *P* | 687.6 | $4.720x10^6$ | 251.4 | $2.115x10^5$ |
| | | *Q* | 350.6 | $6.208x10^5$ | 215.9 | $4.628x10^4$ |
| | ***DPC-SVM-PI*** | *P* | 558 | $4.994x10^6$ | 70.29 | $1.271x10^5$ |
| | | *Q* | 170 | $4.820x10^5$ | 43.22 | $1.321x10^4$ |
| | ***DPC-SVM-BS*** | *P* | 547.7 | $4.981x10^6$ | 67.39 | $1.251x10^5$ |
| | | *Q* | 169 | $4.779x10^5$ | 41.66 | $1.295x10^4$ |
| ***Irradiation (W/m²)*** | | **0** | **200** | **600** | **800** | **1000** |
| ***Power ripples (W)*** | ***CDPC*** | 873.2 | 915.7 | 994.5 | 1079 | 1119 |
| | ***DPC-SVM-PI*** | 580.7 | 617.5 | 696.2 | 731.1 | 853.4 |
| | ***DPC-SVM-BS*** | 404.8 | 450.3 | 590.0 | 655.0 | 753.5 |
| ***Irradiation (W/m²)*** | | **0** | **200** | **600** | **800** | **1000** |
| ***THD (%)*** | ***CDPC*** | 1.80 | 2.89 | 4.47 | 1.91 | 1.26 |
| | ***DPC-SVM-PI*** | 1.45 | 2.35 | 3.69 | 1.71 | 1.19 |
| | ***DPC-SVM-BS*** | 1.10 | 1.78 | 2.94 | 1.38 | 0.98 |

## *6 Conclusion:*

This chapter meticulously presents and validates an enhanced DPC-SVM strategy tailored for MGCPV systems. The core innovation lies in substituting the PI controller within the DPC-SVM with a sophisticated BS controller, further optimized through the GWO algorithm with the DC bus voltage regulator. Through MATLAB/Simulink simulations, the proposed control scheme's performance has been comprehensively evaluated against the traditional DPC-SVM with a PI controller, demonstrating its superior capabilities across a spectrum of operational scenarios.

The simulation results robustly confirm the efficacy of the BS controller, particularly when its parameters are fine-tuned using the GWO. The optimized BS controller consistently outperformed the conventional PI controller in several critical performance metrics. Notably, the system exhibited significantly faster transient responses under various disturbances, including step changes in solar irradiation and load variations. This rapid response is crucial for maintaining grid stability and ensuring seamless integration of PV systems, especially in dynamic grid and weather conditions. Furthermore, the proposed control demonstrably achieved reduced power ripples in both active and reactive power, contributing to enhanced power quality injected into the grid. This reduction in power fluctuations translates to smoother operation and minimized stress on grid infrastructure.

Perhaps most importantly, the optimized BS controller effectively mitigated harmonic distortion, consistently achieving lower THD values in the grid current compared to the PI-based DPC-SVM. This improvement is vital for complying with stringent grid codes and ensuring the reliable operation of sensitive equipment connected to the power network. The lower THD values directly reflect the enhanced power quality delivered by the PV system, a key requirement for modern grid integration.

The GWO's success in optimizing the BS controller's parameters is noteworthy. GWO's nature-inspired approach enabled efficient searching of the parameter space, leading to gains that minimized objective functions related to transient response, steady-state error, and harmonic content. This highlights the potential of bio-inspired optimization algorithms in enhancing the performance of complex control systems in power electronics.

In conclusion, this chapter convincingly demonstrates that the proposed DPC-SVM control strategy, incorporating a GWO-optimized BS controller, represents a significant advancement in the control of MGCPV systems. It offers a robust, high-performance solution that addresses key challenges related to power quality, transient response, and grid stability.

# General Conclusion

This thesis has undertaken a comprehensive investigation into advanced control strategies for PV systems dedicated to enhancing the electrical grid's power quality. The core objective has been to address the critical challenges of efficient energy injection and power quality, which are paramount for the seamless integration of PV systems into electrical grids and the realization of a sustainable energy future.

Chapter I laid the groundwork for this research by providing an overview of photovoltaic systems for grid-connected applications and power quality enhancement. It established the context of increasing PV integration and the associated power quality challenges, reviewed fundamental PV technologies and their modeling, and analyzed the impact of environmental conditions on PV performance. Furthermore, Chapter I surveyed various MPPT algorithms, including conventional and advanced techniques, and provided a detailed overview of GCPV system structures, relevant standards, and synchronization methods. Crucially, this chapter comprehensively outlined key power quality issues, such as voltage sags, swells, and harmonics, and explored mitigation techniques, highlighting the limitations of current solutions and identifying critical research gaps that this thesis aims to address.

Chapter II focused on standalone photovoltaic systems based on the interleaved boost converter, delving into their design, control, and performance analysis. This chapter introduced both CBC and FLIBC topologies, demonstrating through modeling and simulation the inherent advantages of the FLIBC, particularly in reducing current and voltage ripple and improving efficiency in standalone applications. A comparative analysis of fuzzy logic and incremental conductance MPPT algorithms revealed the superior performance of fuzzy logic in terms of convergence speed and reduced voltage ripple. Furthermore, this chapter compared linear (PI) and nonlinear (BS, SMC, STSMC) controllers for the FLIBC, demonstrating the enhanced performance of nonlinear control strategies, with the STSMC showing particular promise due to its chattering reduction and fast response.

Moving to grid-connected applications, Chapter III investigated the classical control of the MGCPV system based on the FLIBC. This chapter implemented a conventional DPC strategy with a switching table and PI controllers for an MGCPV system employing the FLIBC. Through detailed modeling of grid components, nonlinear loads, and a two-level VSI, the chapter evaluated the performance of this classical DPC approach. The simulation results confirmed the effectiveness of the FLIBC-based MGCPV system in enhancing power quality through harmonic mitigation and reactive power compensation. Crucially, Chapter III demonstrated the superior performance of the FLIBC topology compared to the CBC within a classical DPC framework in grid-connected scenarios.

Building upon the classical approach, Chapter IV presented the core innovation of the thesis: DPC-SVM Based on GWO-BS Control of MGCPV Systems Fed FLIBC. This chapter meticulously designed and validated an advanced DPC-SVM strategy incorporating a BS controller optimized using the GWO.

Extensive comparative simulations against a traditional PI-based DPC-SVM system convincingly demonstrated the significant performance enhancements achieved by the proposed GWO-optimized BS controller. The results highlighted superior transient response, reduced harmonic distortion, minimized power ripple, and enhanced robustness against disturbances for the advanced control strategy. This chapter definitively showcased the effectiveness of the proposed DPC-SVM with GWO-optimized BS control in achieving precise power regulation, reduced current harmonics that meet the IEEE-514 standards and reactive power compensation.

The findings of this thesis carry significant implications for the field of grid-connected PV systems. The successful implementation of the FLIBC, coupled with fuzzy logic MPPT and the GWO-optimized BS-based DPC-SVM, offers a holistic framework for achieving superior performance, reliability, and efficiency in PV energy injection. These advancements directly contribute to enhancing grid resilience, minimizing harmonic pollution, and facilitating a more seamless and sustainable integration of solar energy into the power grid.

Furthermore, this research paves the way for future investigations in several directions. Practical implementation and experimental validation of the proposed control scheme on a hardware prototype are crucial next steps. Further research could explore the system's performance under more complex and realistic grid conditions, including unbalanced grid voltages and frequency variations. Extending the control strategy's capabilities to incorporate advanced grid support functions, such voltage and frequency regulation, anti-islanding protection and fault management, would further enhance the value and applicability of the proposed solution for modern power grids.

# References


[1] I. Jamal, M. F. Elmorshedy, S. M. Dabour, E. M. Rashad, W. Xu, and D. J. Almakhles, "A Comprehensive Review of Grid-Connected PV Systems Based on Impedance Source Inverter," *IEEE Access*, vol. 10, pp. 89101–89123, 2022, doi: 10.1109/ACCESS.2022.3200681.

[2] M. Morey, N. Gupta, M. M. Garg, and A. Kumar, "A comprehensive review of grid-connected solar photovoltaic system: Architecture, control, and ancillary services," *Renew. Energy Focus*, vol. 45, pp. 307–330, Jun. 2023, doi: 10.1016/j.ref.2023.04.009.

[3] M. Shafiullah, S. D. Ahmed, and F. A. Al-Sulaiman, "Grid Integration Challenges and Solution Strategies for Solar PV Systems: A Review," *IEEE Access*, vol. 10, pp. 52233–52257, 2022, doi: 10.1109/ACCESS.2022.3174555.

[4] Z. M. Ali, M. Ćalasan, F. Jurado, and S. H. E. Abdel Aleem, "Complexities of Power Quality and Harmonic-Induced Overheating in Modern Power Grids Studies: Challenges and Solutions," *IEEE Access*, vol. 12, pp. 151554–151597, 2024, doi: 10.1109/ACCESS.2024.3477729.

[5] A. I. M. Ali *et al.*, "An Enhanced P&O MPPT Algorithm With Concise Search Area for Grid-Tied PV Systems," *IEEE Access*, vol. 11, pp. 79408–79421, 2023, doi: 10.1109/ACCESS.2023.3298106.

[6] G. Vargas Gil, L. Lima Rodrigues, R. Inomoto, A. Sguarezi, and R. Machado Monaro, "Weighted-PSO Applied to Tune Sliding Mode Plus PI Controller Applied to a Boost Converter in a PV System," *Energies*, vol. 12, no. 5, p. 864, Mar. 2019, doi: 10.3390/en12050864.

[7] A. Amir, A. Amir, H. S. Che, A. Elkhateb, and N. A. Rahim, "Comparative analysis of high voltage gain DC-DC converter topologies for photovoltaic systems," *Renew. Energy*, vol. 136, pp. 1147–1163, Jun. 2019, doi: 10.1016/j.renene.2018.09.089.

[8] S. Zhuo, "Control of Interleaved DC-DC Converter with Switch Fault Consideration for Fuel Cell Application," Université Bourgogne Franche-Comté, 2020. [Online]. Available: https://theses.hal.science/tel-03894942

[9] L. Xu, R. Ma, R. Xie, J. Xu, Y. Huangfu, and F. Gao, "Open-Circuit Switch Fault Diagnosis and Fault- Tolerant Control for Output-Series Interleaved Boost DC–DC Converter," *IEEE Trans. Transp. Electrif.*, vol. 7, no. 4, pp. 2054–2066, Dec. 2021, doi: 10.1109/TTE.2021.3083811.

[10] Z. Liu, Z. Xu, and X. Zhang, "A Novel Real-Time Fast Fault-Tolerance Diagnosis and Fault Adjustment Strategy for m-Phase Interleaved Boost Converter," *IEEE Access*, vol. 9, pp. 11776–11786, 2021, doi: 10.1109/ACCESS.2021.3050705.

[11] Z. Fan, S. Li, H. Cheng, and L. Liu, "Perturb and Observe MPPT Algorithm of photovoltaic System: A Review," in *2021 33rd Chinese Control and Decision Conference (CCDC)*, IEEE, May 2021, pp. 1413–1418. doi: 10.1109/CCDC52312.2021.9602272.

[12] T. V. Muni and S. V. N. L. Lalitha, "Implementation of Control Strategies for Optimum Utilization of Solar Photovoltaic System with Energy Storage Systems," *Int. J. Renew. Energy Res.*, vol. 10, no. v10i2, pp. 716–726, 2020, doi: 10.20508/ijrer.v10i2.10565.g7943.

[13] A. Kouzou, A. Teta, M. M. Rezaoui, and S. Khadar, "Interactive PV-Shunt Active Power Filter with Fuzzy-MPPT Controller for Power Quality Improvement," *Proc. - 2022 5th Int. Conf. Power Electron. their Appl. ICPEA 2022*, no. March, pp. 29–31, 2022, doi: 10.1109/ICPEA51060.2022.9791143.

[14] C. G. Villegas-Mier, J. Rodriguez-Resendiz, J. M. Álvarez-Alvarado, H. Rodriguez-Resendiz, A. M. Herrera-Navarro, and O. Rodríguez-Abreo, "Artificial Neural Networks in MPPT Algorithms for Optimization of Photovoltaic Power Systems: A Review," *Micromachines*, vol. 12, no. 10, p. 1260, Oct. 2021, doi: 10.3390/mi12101260.

[15] S. Pathy, C. Subramani, R. Sridhar, T. M. Thamizh Thentral, and S. Padmanaban, "Nature-Inspired MPPT Algorithms for Partially Shaded PV Systems: A Comparative Study," *Energies*, vol. 12, no. 8, p. 1451, Apr. 2019, doi: 10.3390/en12081451.

[16] G.-I. Giurgi, L. A. Szolga, and D.-V. Giurgi, "Benefits of Fuzzy Logic on MPPT and PI Controllers in the Chain of Photovoltaic Control Systems," *Appl. Sci.*, vol. 12, no. 5, p. 2318, Feb. 2022, doi: 10.3390/app12052318.

[17] W. Wu, J. Chen, Z. Chen, Z. Li, and C. Xiao, "Parallel Current Sharing Control Algorithm Of Four Phase Interleaved Boost Converter," in *2021 China Automation Congress (CAC)*, IEEE,

Oct. 2021, pp. 1860–1864. doi: 10.1109/CAC53003.2021.9728115.

[18] M. C. Daia Eddine O, C. Ali, and K. Abdelhalim, "Four leg Interleaved DC/DC boost Converter based PV system using PSO Algorithm based PI controller," in *2022 19th International Multi-Conference on Systems, Signals & Devices (SSD)*, IEEE, May 2022, pp. 1415–1421. doi: 10.1109/SSD54932.2022.9955647.

[19] D. E. O. MOHAMED CHERIF, A. CHEBABHI, and A. KESSAL, "An Integral-Backstepping Controller for Interleaved Boost Converter based on Photovoltaic Systems," *Electroteh. Electron. Autom.*, vol. 71, no. 1, pp. 13–21, Mar. 2023, doi: 10.46904/eea.23.71.1.1108002.

[20] K. Bouguerra, S. Latreche, M. Khemliche, and H. Khemliche, "Sliding Mode Control for Interleaved DC-DC Boost Converter based Photovoltaic Energy System," in *2024 International Conference on Advances in Electrical and Communication Technologies (ICAECOT)*, IEEE, Oct. 2024, pp. 1–7. doi: 10.1109/ICAECOT62402.2024.10828944.

[21] D. E. O. Mohamed Cherif, A. Chebabhi, A. Kessal, M. F. Benkhoris, and M. Defdaf, "Super-Twisting Sliding Mode Control of Interleaved Boost Converter Based Photovoltaic Applications," in *2022 International Conference of Advanced Technology in Electronic and Electrical Engineering (ICATEEE)*, IEEE, Nov. 2022, pp. 1–5. doi: 10.1109/ICATEEE57445.2022.10093715.

[22] M. Jauhari, D. C. Riawan, and M. Ashari, "Control Design For Shunt Active Power Filter Based On p-q Theory In Photovoltaic Grid-Connected System," *Int. J. Power Electron. Drive Syst.*, vol. 9, no. 3, p. 1064, Sep. 2018, doi: 10.11591/ijpeds.v9.i3.pp1064-1071.

[23] T. Sathiyanarayanan and S. Mishra, "Synchronous Reference Frame Theory based Model Predictive Control for Grid Connected Photovoltaic Systems," *IFAC-PapersOnLine*, vol. 49, no. 1, pp. 766–771, 2016, doi: 10.1016/j.ifacol.2016.03.149.

[24] M. Ahmed, M. Abdelrahem, A. Farhan, I. Harbi, and R. Kennel, "DC-link sensorless control strategy for grid-connected PV systems," *Electr. Eng.*, vol. 103, no. 5, pp. 2345–2355, 2021, doi: 10.1007/s00202-021-01228-2.

[25] S. Ouchen, S. Abdeddaim, A. Betka, and A. Menadi, "Experimental validation of sliding mode-predictive direct power control of a grid connected photovoltaic system, feeding a nonlinear load," *Sol. Energy*, vol. 137, pp. 328–336, 2016, doi: 10.1016/j.solener.2016.08.031.

[26] A. Benzahia, R. Boualaga, A. Moussi, L. Zellouma, M. Meriem, and B. Chaima, "A PV powered shunt active power filter for power quality improvement," *Glob. Energy Interconnect.*, vol. 2, no. 2, pp. 143–149, Apr. 2019, doi: 10.1016/j.gloei.2019.07.001.

[27] M. Malinowski, M. Jasinski, and M. P. Kazmierkowski, "Simple Direct Power Control of Three-Phase PWM Rectifier Using Space-Vector Modulation (DPC-SVM)," *IEEE Trans. Ind. Electron.*, vol. 51, no. 2, pp. 447–454, Apr. 2004, doi: 10.1109/TIE.2004.825278.

[28] M. Armstrong and F. Mulolani, "Space Vector Modulation Direct power control of Grid-Connected Photovoltaic Converter with Reactive Power Compensation," in *7th IET International Conference on Power Electronics, Machines and Drives (PEMD 2014)*, Institution of Engineering and Technology, 2014, pp. 4.6.04-4.6.04. doi: 10.1049/cp.2014.0451.

[29] S. Ouchen, H. Steinhart, M. Benbouzid, and F. Blaabjerg, "Robust DPC-SVM control strategy for shunt active power filter based on H∞ regulators," *Int. J. Electr. Power Energy Syst.*, vol. 117, no. May 2019, p. 105699, 2020, doi: 10.1016/j.ijepes.2019.105699.

[30] N. Debdouche, Z. Laid, C. Ali, and S. Ouchen, "DPC-SVM Controlled Strategy for a Three-Level Shunt Active Power Filter Grid Connected Photovoltaic System Optimized by Super Twisting Sliding Mode Technique," 2022, pp. 245–255. doi: 10.1007/978-3-030-92038-8_25.

[31] B. Youcefa, A. Massoum, S. Barkat, and P. Wira, "Backstepping Direct Power Control for Power Quality Enhancement of Grid-connected Photovoltaic System Implemented with PIL Co-simulation Technique," *Adv. Model. Anal. C*, vol. 74, no. 1, pp. 1–14, Mar. 2019, doi: 10.18280/ama_c.740101.

[32] A. Chebabhi, M. Karim, A. Kessal, and M. F. Benkhoris, "A new balancing three level three dimensional space vector modulation strategy for three level neutral point clamped four leg inverter based shunt active power fi lter controlling by nonlinear back stepping controllers," *ISA Trans.*, pp. 1–15, 2016, doi: 10.1016/j.isatra.2016.03.001.

[33] J. Kennedy and R. Eberhart, "Particle swarm optimization," in *Proceedings of ICNN'95 - International Conference on Neural Networks*, IEEE, pp. 1942–1948. doi:

10.1109/ICNN.1995.488968.
[34] S. Mirjalili, “Genetic Algorithm,” in *Evolutionary Algorithms and Neural Networks. Studies in Computational Intelligence, vol 780*, Springer, Cham, 2019, ch. Evolutiona, pp. 43–55. doi: 10.1007/978-3-319-93025-1_4.
[35] S. Mirjalili, S. M. Mirjalili, and A. Lewis, “Grey Wolf Optimizer,” *Adv. Eng. Softw.*, vol. 69, pp. 46–61, Mar. 2014, doi: 10.1016/j.advengsoft.2013.12.007.
[36] R. Kumar, “Fuzzy particle swarm optimization control algorithm implementation in photovoltaic integrated shunt active power filter for power quality improvement using hardware-in-the-loop,” *Sustain. Energy Technol. Assessments*, vol. 50, no. May 2021, p. 101820, Mar. 2022, doi: 10.1016/j.seta.2021.101820.
[37] N. Aouchiche, “Meta-heuristic optimization algorithms based direct current and DC link voltage controllers for three-phase grid connected photovoltaic inverter,” *Sol. Energy*, vol. 207, no. June, pp. 683–692, Sep. 2020, doi: 10.1016/j.solener.2020.06.086.
[38] M. Nicola and C. I. Nicola, “Improved Performance of Grid-Connected Photovoltaic System Based on Fractional-Order PI Controller and Particle Swarm optimization,” *Proc. 2021 9th Int. Conf. Mod. Power Syst. MPS 2021*, 2021, doi: 10.1109/MPS52805.2021.9492707.
[39] O. M. C. Daia Eddine, A. Chebabhi, and A. Kessal, “Backstepping Based Grey Wolf and DPC for Power Quality Improvement and Active Power Injection in PV Grid-connected System Based on Interleaved Boost Converter,” *Period. Polytech. Electr. Eng. Comput. Sci.*, vol. 67, no. 3, pp. 268–280, Jul. 2023, doi: 10.3311/PPee.21852.
[40] T. T. E. Vo, H. Ko, J.-H. Huh, and N. Park, “Overview of Solar Energy for Aquaculture: The Potential and Future Trends,” *Energies*, vol. 14, no. 21, p. 6923, Oct. 2021, doi: 10.3390/en14216923.
[41] A. Kleidon, “How the Earth generates renewable energy,” *Eur. Energy Clim. J.*, vol. 6, no. 2, pp. 18–31, Sep. 2016, doi: 10.4337/eecj.2016.02.01.
[42] *Photonics Principles in Photovoltaic Cell Technology*. OP-TEC: The National Center for Optics and Photonics Education, 2009.
[43] S. Sharma, K. K. Jain, and A. Sharma, “Solar Cells: In Research and Applications—A Review,” *Mater. Sci. Appl.*, vol. 06, no. 12, pp. 1145–1155, 2015, doi: 10.4236/msa.2015.612113.
[44] L. El Chaar, L. A. Lamont, and N. El Zein, “Review of photovoltaic technologies,” *Renew. Sustain. Energy Rev.*, vol. 15, no. 5, pp. 2165–2175, Jun. 2011, doi: 10.1016/j.rser.2011.01.004.
[45] J. A. M. Vrielink, R. M. Tiggelaar, J. G. E. Gardeniers, and L. Lefferts, “Applicability of X-ray fluorescence spectroscopy as method to determine thickness and composition of stacks of metal thin films: A comparison with imaging and profilometry,” *Thin Solid Films*, vol. 520, no. 6, pp. 1740–1744, Jan. 2012, doi: 10.1016/j.tsf.2011.08.049.
[46] M. Giannouli, “Current Status of Emerging PV Technologies: A Comparative Study of Dye-Sensitized, Organic, and Perovskite Solar Cells,” *Int. J. Photoenergy*, vol. 2021, pp. 1–19, May 2021, doi: 10.1155/2021/6692858.
[47] J. Pastuszak and P. Węgierek, “Photovoltaic Cell Generations and Current Research Directions for Their Development,” *Materials (Basel).*, vol. 15, no. 16, p. 5542, Aug. 2022, doi: 10.3390/ma15165542.
[48] “NREL’s Best Research-Cell Efficiency Chart.,” The National Renewable Energy Laboratory. [Online]. Available: https://www.nrel.gov/pv/assets/pdfs/best-research-cell-efficiencies-rev220126b.pdf
[49] S. Gallardo-Saavedra and B. Karlsson, “Simulation, validation and analysis of shading effects on a PV system,” *Sol. Energy*, vol. 170, no. May, pp. 828–839, 2018, doi: 10.1016/j.solener.2018.06.035.
[50] M. Ahmed, I. Harbi, R. Kennel, and M. Abdelrahem, “Dual-Mode Power Operation for Grid-Connected PV Systems with Adaptive DC-link Controller,” *Arab. J. Sci. Eng.*, vol. 47, no. 3, pp. 2893–2907, 2022, doi: 10.1007/s13369-021-05916-w.
[51] M. R. Mostafa, N. H. Saad, and A. A. El-sattar, “Tracking the maximum power point of PV array by sliding mode control method,” *Ain Shams Eng. J.*, vol. 11, no. 1, pp. 119–131, 2020, doi: 10.1016/j.asej.2019.09.003.
[52] M. K. Singla and P. Nijhawan, “Triple diode parameter estimation of solar PV cell using hybrid algorithm,” *Int. J. Environ. Sci. Technol.*, vol. 19, no. 5, pp. 4265–4288, May 2022, doi:

10.1007/s13762-021-03286-2.

[53] H. Rezk and M. A. Abdelkareem, "Optimal parameter identification of triple diode model for solar photovoltaic panel and cells," *Energy Reports*, vol. 8, pp. 1179–1188, Apr. 2022, doi: 10.1016/j.egyr.2021.11.179.

[54] J. Gosumbonggot and G. Fujita, "Partial Shading Detection and Global Maximum Power Point Tracking Algorithm for Photovoltaic with the Variation of Irradiation and Temperature," *Energies*, vol. 12, no. 2, p. 202, Jan. 2019, doi: 10.3390/en12020202.

[55] M. Kermadi and E. M. Berkouk, "Artificial intelligence-based maximum power point tracking controllers for Photovoltaic systems: Comparative study," *Renew. Sustain. Energy Rev.*, vol. 69, no. February 2019, pp. 369–386, Mar. 2017, doi: 10.1016/j.rser.2016.11.125.

[56] R. Ben Messaoud, "Extraction of uncertain parameters of single-diode model of a photovoltaic panel using simulated annealing optimization," *Energy Reports*, vol. 6, pp. 350–357, Nov. 2020, doi: 10.1016/j.egyr.2020.01.016.

[57] W. Gong and Z. Cai, "Parameter extraction of solar cell models using repaired adaptive differential evolution," *Sol. Energy*, vol. 94, pp. 209–220, Aug. 2013, doi: 10.1016/j.solener.2013.05.007.

[58] A. Bouraiou, M. Hamouda, A. Chaker, M. Sadok, M. Mostefaoui, and S. Lachtar, "Modeling and Simulation of Photovoltaic Module and Array Based on One and Two Diode Model Using Matlab/Simulink," *Energy Procedia*, vol. 74, pp. 864–877, Aug. 2015, doi: 10.1016/j.egypro.2015.07.822.

[59] M. G. Villalva and E. R. F., "ANALYSIS AND SIMULATION OF THE P&OMPPT ALGORITHMUSING A LINEARIZED PV ARRAY MODEL," in *2009 35th Annual Conference of IEEE Industrial Electronics*, IEEE, Nov. 2009, pp. 231–236. doi: 10.1109/IECON.2009.5414780.

[60] C. Hussaian Basha, C. Rani, R. M. Brisilla, and S. Odofin, "Mathematical Design and Analysis of Photovoltaic Cell Using MATLAB/Simulink," 2020, pp. 711–726. doi: 10.1007/978-981-15-0035-0_58.

[61] W. Long, S. Cai, J. Jiao, M. Xu, and T. Wu, "A new hybrid algorithm based on grey wolf optimizer and cuckoo search for parameter extraction of solar photovoltaic models," *Energy Convers. Manag.*, vol. 203, no. June 2019, p. 112243, 2020, doi: 10.1016/j.enconman.2019.112243.

[62] S. Murkute and V. A. Kulkarni Deodhar, "New high performance PV system architecture for mitigation of partial shading effects," *e-Prime - Adv. Electr. Eng. Electron. Energy*, vol. 5, p. 100189, Sep. 2023, doi: 10.1016/j.prime.2023.100189.

[63] M. Sharma, S. Pareek, and K. Singh, "Robust reconfiguration strategies for maximum output power from large-scale photovoltaic arrays under partial shading conditions," *Phys. Scr.*, vol. 98, no. 3, p. 035215, Mar. 2023, doi: 10.1088/1402-4896/acb112.

[64] A. K. Sahu and S. Gupta, "A Comparative Study on Effects of Shading on a Solar Photovoltaic System," in *2023 International Conference for Advancement in Technology (ICONAT)*, IEEE, Jan. 2023, pp. 1–5. doi: 10.1109/ICONAT57137.2023.10080679.

[65] S. Nofal, B. E. Pieters, M. Hülsbeck, C. Zahren, A. Gerber, and U. Rau, "A direct measure of positive feedback loop-gain due to reverse bias damage in thin-film solar cells using lock-in thermography," *EPJ Photovoltaics*, vol. 14, p. 3, Jan. 2023, doi: 10.1051/epjpv/2022030.

[66] R. Alik and A. Jusoh, "An enhanced P&O checking algorithm MPPT for high tracking efficiency of partially shaded PV module," *Sol. Energy*, vol. 163, pp. 570–580, Mar. 2018, doi: 10.1016/j.solener.2017.12.050.

[67] S. Ahmed, H. M. Muhammad Adil, I. Ahmad, M. K. Azeem, Z. e Huma, and S. Abbas Khan, "Supertwisting Sliding Mode Algorithm Based Nonlinear MPPT Control for a Solar PV System with Artificial Neural Networks Based Reference Generation," *Energies*, vol. 13, no. 14, p. 3695, Jul. 2020, doi: 10.3390/en13143695.

[68] T. M. Chung, H. Daniyal, M. H. Sulaiman, and M. S. Bakar, "Comparative study of P&O and modified incremental conductance algorithm in solar maximum power point tracking," in *4th IET Clean Energy and Technology Conference (CEAT 2016)*, Kuala Lumpur, Malaysia, 2016, pp. 1–6. doi: 10.1049/cp.2016.1300.

[69] J. J. Nedumgatt, K. B. Jayakrishnan, S. Umashankar, D. Vijayakumar, and D. P. Kothari,

"Perturb and observe MPPT algorithm for solar PV systems-modeling and simulation," in *2011 Annual IEEE India Conference*, Hyderabad, India, Dec. 2011, pp. 1–6. doi: 10.1109/INDCON.2011.6139513.

[70] A. A. Elbaset, H. Ali, M. Abd-El Sattar, and M. Khaled, "Implementation of a modified perturb and observe maximum power point tracking algorithm for photovoltaic system using an embedded microcontroller," *IET Renew. Power Gener.*, vol. 10, no. 4, pp. 551–560, Apr. 2016, doi: 10.1049/iet-rpg.2015.0309.

[71] R. Kumar, B. Kumar, and S. D., "Fuzzy Logic based Improved P&O MPPT Technique for Partial Shading Conditions," in *2018 International Conference on Computing, Power and Communication Technologies (GUCON)*, Greater Noida, India, Sep. 2018, pp. 775–779. doi: 10.1109/GUCON.2018.8674917.

[72] A. N. Mahmod Mohammad, M. A. Mohd Radzi, N. Azis, S. Shafie, and M. A. Atiqi Mohd Zainuri, "An Enhanced Adaptive Perturb and Observe Technique for Efficient Maximum Power Point Tracking Under Partial Shading Conditions," *Appl. Sci.*, vol. 10, no. 11, p. 3912, Jun. 2020, doi: 10.3390/app10113912.

[73] D. Taibi, T. Amieur, T. Laamayad, and M. Sedraoui, "Improvement of the Standard Perturb & Observe MPPT control strategy by the proposed Fuzzy Logic Mechanism for a Cascade Regulation of a PMSM-based PV pumping system," *Arab. J. Sci. Eng.*, vol. 48, no. 5, pp. 6631–6647, May 2023, doi: 10.1007/s13369-022-07496-9.

[74] K. H. Hussein, I. Muta, T. Hoshino, and M. Osakada, "Maximum photovoltaic power tracking: an algorithm for rapidly changing atmospheric conditions," *IEE Proc. Gener. Transm. Distrib.*, vol. 142, no. 1, pp. 59–64, 1995, doi: 10.1049/ip-gtd:19951577.

[75] S. Necaibia, M. S. Kelaiaia, H. Labar, A. Necaibia, and E. D. Castronuovo, "Enhanced auto-scaling incremental conductance MPPT method, implemented on low-cost microcontroller and SEPIC converter," *Sol. Energy*, vol. 180, pp. 152–168, Mar. 2019, doi: 10.1016/j.solener.2019.01.028.

[76] R. I. Putri, S. Wibowo, and M. Rifa'i, "Maximum power point tracking for photovoltaic using incremental conductance method," *Energy Procedia*, vol. 68, pp. 22–30, 2015, doi: 10.1016/j.egypro.2015.03.228.

[77] M. Kermadi *et al.*, "Recent developments of MPPT techniques for PV systems under partial shading conditions: a critical review and performance evaluation," *IET Renew. Power Gener.*, vol. 14, no. 17, pp. 3401–3417, Dec. 2020, doi: 10.1049/iet-rpg.2020.0454.

[78] L. Xu, R. Cheng, and J. Yang, "A New MPPT Technique for Fast and Efficient Tracking under Fast Varying Solar Irradiation and Load Resistance," *Int. J. Photoenergy*, vol. 2020, pp. 1–18, Feb. 2020, doi: 10.1155/2020/6535372.

[79] M. Alsumiri, "Residual Incremental Conductance Based Nonparametric MPPT Control for Solar Photovoltaic Energy Conversion System," *IEEE Access*, vol. 7, pp. 87901–87906, 2019, doi: 10.1109/ACCESS.2019.2925687.

[80] M. N. Ali, K. Mahmoud, M. Lehtonen, and M. M. F. Darwish, "An Efficient Fuzzy-Logic Based Variable-Step Incremental Conductance MPPT Method for Grid-Connected PV Systems," *IEEE Access*, vol. 9, pp. 26420–26430, 2021, doi: 10.1109/ACCESS.2021.3058052.

[81] G. Singh Chawda, O. Prakash Mahela, N. Gupta, M. Khosravy, and T. Senjyu, "Incremental Conductance Based Particle Swarm Optimization Algorithm for Global Maximum Power Tracking of Solar-PV under Nonuniform Operating Conditions," *Appl. Sci.*, vol. 10, no. 13, p. 4575, Jul. 2020, doi: 10.3390/app10134575.

[82] C. Sun, J. Ling, and J. Wang, "Research on a novel and improved incremental conductance method," *Sci. Rep.*, vol. 12, no. 1, p. 15700, Sep. 2022, doi: 10.1038/s41598-022-20133-7.

[83] S. B. Hamed *et al.*, "A robust MPPT approach based on first-order sliding mode for triple-junction photovoltaic power system supplying electric vehicle," *Energy Reports*, vol. 9, pp. 4275–4297, Dec. 2023, doi: 10.1016/j.egyr.2023.02.086.

[84] Y. Ouberri, H. Yatimi, and E. Aroudam, "Design of a robust sliding mode controller for MPPT based on automation PLC for PV applications," *Int. Trans. Electr. Energy Syst.*, vol. 30, no. 4, Apr. 2020, doi: 10.1002/2050-7038.12296.

[85] B. Deffaf, F. Hamoudi, N. Debdouche, Y. A. Amor, and S. Medjmadj, "Super-twisting Sliding Mode Control for a Multifunctional Double Stage Grid-connected Photovoltaic System," *Adv.*

*Electr. Electron. Eng.*, vol. 20, no. 3, Oct. 2022, doi: 10.15598/aeee.v20i3.4454.

[86] K. Walid, M. Sofiane, H. Benbouhenni, G. Hamza, and T. Es-saadi, "Application of third-order sliding mode controller to improve the maximum power point for the photovoltaic system," *Energy Reports*, vol. 9, pp. 5372–5383, Dec. 2023, doi: 10.1016/j.egyr.2023.04.366.

[87] H. Yatimi and E. Aroudam, "Assessment and control of a photovoltaic energy storage system based on the robust sliding mode MPPT controller," *Sol. Energy*, vol. 139, pp. 557–568, Dec. 2016, doi: 10.1016/j.solener.2016.10.038.

[88] R. Divyasharon, R. Narmatha Banu, and D. Devaraj, "Artificial Neural Network based MPPT with CUK Converter Topology for PV Systems Under Varying Climatic Conditions," in *2019 IEEE International Conference on Intelligent Techniques in Control, Optimization and Signal Processing (INCOS)*, IEEE, Apr. 2019, pp. 1–6. doi: 10.1109/INCOS45849.2019.8951321.

[89] X. Meng, F. Gao, T. Xu, and C. Zhang, "Fast Two-Stage Global Maximum Power Point Tracking for Grid-Tied String PV Inverter Using Characteristics Mapping Principle," *IEEE J. Emerg. Sel. Top. Power Electron.*, vol. 10, no. 1, pp. 564–574, Feb. 2022, doi: 10.1109/JESTPE.2021.3104036.

[90] N. I. Nahin, S. P. Biswas, S. Mondal, M. R. Islam, and S. M. Muyeen, "A Modified PWM Strategy With an Improved ANN Based MPPT Algorithm for Solar PV Fed NPC Inverter Driven Induction Motor Drives," *IEEE Access*, vol. 11, pp. 70960–70976, 2023, doi: 10.1109/ACCESS.2023.3291339.

[91] M. Yilmaz, R. Celikel, and A. Gundogdu, "Enhanced Photovoltaic Systems Performance: Anti-Windup PI Controller in ANN-Based ARV MPPT Method," *IEEE Access*, vol. 11, pp. 90498–90509, 2023, doi: 10.1109/ACCESS.2023.3290316.

[92] R. B. Roy *et al.*, "A Comparative Performance Analysis of ANN Algorithms for MPPT Energy Harvesting in Solar PV System," *IEEE Access*, vol. 9, pp. 102137–102152, 2021, doi: 10.1109/ACCESS.2021.3096864.

[93] S. Allahabadi, H. Iman-Eini, and S. Farhangi, "Fast Artificial Neural Network Based Method for Estimation of the Global Maximum Power Point in Photovoltaic Systems," *IEEE Trans. Ind. Electron.*, vol. 69, no. 6, pp. 5879–5888, Jun. 2022, doi: 10.1109/TIE.2021.3094463.

[94] L. Farah, A. Hussain, A. Kerrouche, C. Ieracitano, J. Ahmad, and M. Mahmud, "A Highly-Efficient Fuzzy-Based Controller With High Reduction Inputs and Membership Functions for a Grid-Connected Photovoltaic System," *IEEE Access*, vol. 8, pp. 163225–163237, 2020, doi: 10.1109/ACCESS.2020.3016981.

[95] A. Srivastava, A. Nagvanshi, A. Chandra, A. Singh, and A. K. Roy, "Grid Integrated Solar PV System with Comparison between Fuzzy Logic Controlled MPPT and P&O MPPT," in *2021 IEEE 2nd International Conference On Electrical Power and Energy Systems (ICEPES)*, IEEE, Dec. 2021, pp. 1–6. doi: 10.1109/ICEPES52894.2021.9699492.

[96] C. Hussaian Basha, V. Bansal, C. Rani, R. M. Brisilla, and S. Odofin, "Development of Cuckoo Search MPPT Algorithm for Partially Shaded Solar PV SEPIC Converter," 2020, pp. 727–736. doi: 10.1007/978-981-15-0035-0_59.

[97] F. M. Oliveira, S. A. Oliveira da Silva, F. R. Durand, L. P. Sampaio, V. D. Bacon, and L. B. G. Campanhol, "Grid-tied photovoltaic system based on PSO MPPT technique with active power line conditioning," *IET Power Electron.*, vol. 9, no. 6, pp. 1180–1191, May 2016, doi: 10.1049/iet-pel.2015.0655.

[98] S. Katoch, S. S. Chauhan, and V. Kumar, "A review on genetic algorithm: past, present, and future," *Multimed. Tools Appl.*, vol. 80, no. 5, pp. 8091–8126, Feb. 2021, doi: 10.1007/s11042-020-10139-6.

[99] S. Hadji, J.-P. Gaubert, and F. Krim, "Real-Time Genetic Algorithms-Based MPPT: Study and Comparison (Theoretical an Experimental) with Conventional Methods," *Energies*, vol. 11, no. 2, p. 459, Feb. 2018, doi: 10.3390/en11020459.

[100] S. Senthilkumar, V. Mohan, S. P. Mangaiyarkarasi, and M. Karthikeyan, "Analysis of Single-Diode PV Model and Optimized MPPT Model for Different Environmental Conditions," *Int. Trans. Electr. Energy Syst.*, vol. 2022, pp. 1–17, Jan. 2022, doi: 10.1155/2022/4980843.

[101] S. Mohanty, B. Subudhi, and P. K. Ray, "A New MPPT Design Using Grey Wolf Optimization Technique for Photovoltaic System Under Partial Shading Conditions," *IEEE Trans. Sustain. Energy*, vol. 7, no. 1, pp. 181–188, Jan. 2016, doi: 10.1109/TSTE.2015.2482120.

[102] D. Suhardi, L. Syafaah, M. Irfan, M. Yusuf, M. Effendy, and I. Pakaya, "Improvement of maximum power point tracking (MPPT) efficiency using grey Wolf optimization (GWO) algorithm in photovoltaic (PV) system," *IOP Conf. Ser. Mater. Sci. Eng.*, vol. 674, no. 1, p. 012038, Nov. 2019, doi: 10.1088/1757-899X/674/1/012038.

[103] S. Kouro, J. I. Leon, D. Vinnikov, and L. G. Franquelo, "Grid-Connected Photovoltaic Systems: An Overview of Recent Research and Emerging PV Converter Technology," *IEEE Ind. Electron. Mag.*, vol. 9, no. 1, pp. 47–61, Mar. 2015, doi: 10.1109/MIE.2014.2376976.

[104] A. Al-Badi, "Performance assessment of 20.4 kW eco-house grid-connected PV plant in Oman," *Int. J. Sustain. Eng.*, vol. 13, no. 3, pp. 230–241, May 2020, doi: 10.1080/19397038.2019.1658824.

[105] M. Drif *et al.*, "Univer Project. A grid connected photovoltaic system of 200kWp at Jaén University. Overview and performance analysis," *Sol. Energy Mater. Sol. Cells*, vol. 91, no. 8, pp. 670–683, May 2007, doi: 10.1016/j.solmat.2006.12.006.

[106] B. R. Kumar, "Case 21: Bhadla Solar Park," in *Project Finance. Management for Professionals*, Springer, Cham, 2022, pp. 205–208. doi: 10.1007/978-3-030-96725-3_25.

[107] M. Y. Ali Khan, H. Liu, Z. Yang, and X. Yuan, "A Comprehensive Review on Grid Connected Photovoltaic Inverters, Their Modulation Techniques, and Control Strategies," *Energies*, vol. 13, no. 16, p. 4185, Aug. 2020, doi: 10.3390/en13164185.

[108] L. B. Bosman and S. B. Darling, "Performance modeling and valuation of snow-covered PV systems: examination of a simplified approach to decrease forecasting error," *Environ. Sci. Pollut. Res.*, vol. 25, no. 16, pp. 15484–15491, Jun. 2018, doi: 10.1007/s11356-018-1748-1.

[109] A. Kumar, N. Gupta, and V. Gupta, "A Comprehensive Review on Grid-TiedSolar Photovoltaic System," *J. Green Eng.*, vol. 7, no. 1, pp. 213–254, 2017, doi: 10.13052/jge1904-4720.71210.

[110] S. R. Pendem and S. Mikkili, "Modelling and performance assessment of PV array topologies under partial shading conditions to mitigate the mismatching power losses," *Sol. Energy*, vol. 160, pp. 303–321, Jan. 2018, doi: 10.1016/j.solener.2017.12.010.

[111] S. Yilmaz and F. Dincer, "Impact of inverter capacity on the performance in large-scale photovoltaic power plants – A case study for Gainesville, Florida," *Renew. Sustain. Energy Rev.*, vol. 79, pp. 15–23, Nov. 2017, doi: 10.1016/j.rser.2017.05.054.

[112] S. Deshpande and N. R. Bhasme, "A review of topologies of inverter for grid connected PV systems," in *2017 Innovations in Power and Advanced Computing Technologies (i-PACT)*, IEEE, Apr. 2017, pp. 1–6. doi: 10.1109/IPACT.2017.8245191.

[113] V. Boddapati and S. A. Daniel, "Performance analysis and investigations of grid-connected Solar Power Park in Kurnool, South India," *Energy Sustain. Dev.*, vol. 55, pp. 161–169, Apr. 2020, doi: 10.1016/j.esd.2020.02.001.

[114] A. Nazer, S. Driss, A. M. Haddadi, and S. Farhangi, "Optimal Photovoltaic Multi-String Inverter Topology Selection Based on Reliability and Cost Analysis," *IEEE Trans. Sustain. Energy*, vol. 12, no. 2, pp. 1186–1195, Apr. 2021, doi: 10.1109/TSTE.2020.3038744.

[115] M. Islam, S. Mekhilef, and M. Hasan, "Single phase transformerless inverter topologies for grid-tied photovoltaic system: A review," *Renew. Sustain. Energy Rev.*, vol. 45, pp. 69–86, May 2015, doi: 10.1016/j.rser.2015.01.009.

[116] H. Keyhani and H. A. Toliyat, "Single-Stage Multistring PV Inverter With an Isolated High-Frequency Link and Soft-Switching Operation," *IEEE Trans. Power Electron.*, vol. 29, no. 8, pp. 3919–3929, Aug. 2014, doi: 10.1109/TPEL.2013.2288361.

[117] M. S. Tariq, S. A. Butt, and H. A. Khan, "Impact of module and inverter failures on the performance of central-, string-, and micro-inverter PV systems," *Microelectron. Reliab.*, vol. 88–90, pp. 1042–1046, Sep. 2018, doi: 10.1016/j.microrel.2018.06.096.

[118] A. M. Noman, K. E. Addoweesh, A. A. Alabduljabbar, and A. I. Alolah, "Cascaded H-Bridge MLI and Three-Phase Cascaded VSI Topologies for Grid-Connected PV Systems with Distributed MPPT," *Int. J. Photoenergy*, vol. 2019, pp. 1–22, Jan. 2019, doi: 10.1155/2019/7642919.

[119] S. Vanti, P. R. Bana, S. D'Arco, and M. Amin, "Single-Stage Grid-Connected PV System With Finite Control Set Model Predictive Control and an Improved Maximum Power Point Tracking," *IEEE Trans. Sustain. Energy*, vol. 13, no. 2, pp. 791–802, Apr. 2022, doi: 10.1109/TSTE.2021.3132057.

[120] S. Albatran, A. R. Al Khalaileh, and A. S. Allabadi, "Minimizing Total Harmonic Distortion of a Two-Level Voltage Source Inverter Using Optimal Third Harmonic Injection," *IEEE Trans. Power Electron.*, vol. 35, no. 3, pp. 3287–3297, Mar. 2020, doi: 10.1109/TPEL.2019.2932139.

[121] N. Soualhi, A. Makouf, N. Nait-Said, and S. Hamada, "Comparison between a Two-Level and Three-Level Inverter fed Induction Motor including Losses and Efficiency," in *Proceedings of the International Conference on Advanced Systems and Emergent Technologies, ICASET 2020*, Hammamet, Tunisia: IEEE, Dec. 2020, pp. 89–94. doi: 10.1109/IC_ASET49463.2020.9318310.

[122] M. Hamdi, M. Hamouda, L. Sbita, and K. Al-Haddad, "FCS-MPC for grid-tied three-phase three-level NPC inverter with experimental validation," in *2017 International Conference on Green Energy Conversion Systems (GECS)*, IEEE, Mar. 2017, pp. 1–6. doi: 10.1109/GECS.2017.8066246.

[123] N. Altin, I. Sefa, H. Komurcugil, and S. Ozdemir, "Three-phase three-level T-type grid-connected inverter with reduced number of switches," in *2018 6th International Istanbul Smart Grids and Cities Congress and Fair (ICSG)*, IEEE, Apr. 2018, pp. 58–62. doi: 10.1109/SGCF.2018.8408942.

[124] Y.-K. Wu, J.-H. Lin, and H.-J. Lin, "Standards and Guidelines for Grid-Connected Photovoltaic Generation Systems: A Review and Comparison," *IEEE Trans. Ind. Appl.*, vol. 53, no. 4, pp. 3205–3216, Jul. 2017, doi: 10.1109/TIA.2017.2680409.

[125] N. Jaalam, N. A. Rahim, A. H. A. Bakar, C. Tan, and A. M. A. Haidar, "A comprehensive review of synchronization methods for grid-connected converters of renewable energy source," *Renew. Sustain. Energy Rev.*, vol. 59, pp. 1471–1481, Jun. 2016, doi: 10.1016/j.rser.2016.01.066.

[126] Y. Han, Y. Feng, P. Yang, L. Xu, Y. Xu, and F. Blaabjerg, "Cause, Classification of Voltage Sag, and Voltage Sag Emulators and Applications: A Comprehensive Overview," *IEEE Access*, vol. 8, pp. 1922–1934, 2020, doi: 10.1109/ACCESS.2019.2958965.

[127] E. A. Nagata, D. D. Ferreira, C. A. Duque, and A. S. Cequeira, "Voltage sag and swell detection and segmentation based on Independent Component Analysis," *Electr. Power Syst. Res.*, vol. 155, pp. 274–280, Feb. 2018, doi: 10.1016/j.epsr.2017.10.029.

[128] N. Minh Khoa and L. Van Dai, "Detection and Classification of Power Quality Disturbances in Power System Using Modified-Combination between the Stockwell Transform and Decision Tree Methods," *Energies*, vol. 13, no. 14, p. 3623, Jul. 2020, doi: 10.3390/en13143623.

[129] J. C. Cebrian, N. Kagan, and J. V. Milanovic, "Probabilistic Estimation of Distribution Network Performance with Respect to Voltage Sags and Interruptions Considering Network Protection Setting-Part I: The Methodology," *IEEE Trans. Power Deliv.*, vol. 33, no. 1, pp. 42–51, Feb. 2018, doi: 10.1109/TPWRD.2016.2633518.

[130] F. Shahnia, R. Majumder, A. Ghosh, G. Ledwich, and F. Zare, "Sensitivity analysis of voltage imbalance in distribution networks with rooftop PVs," in *IEEE PES General Meeting, PES 2010*, Minneapolis, MN, USA: IEEE, Jul. 2010, pp. 1–8. doi: 10.1109/PES.2010.5590149.

[131] A. A. Girgis, J. W. Stephens, and E. B. Makram, "Measurement and prediction of voltage flicker magnitude and frequency," *IEEE Trans. Power Deliv.*, vol. 10, no. 3, pp. 1600–1605, Jul. 1995, doi: 10.1109/61.400945.

[132] A. K. Jindal, A. Ghosh, and A. Joshi, "Voltage regulation using dynamic voltage restorer for large frequency variations," in *IEEE Power Engineering Society General Meeting, 2005*, IEEE, pp. 1780–1786. doi: 10.1109/PES.2005.1489437.

[133] P. Sivaraman and C. Sharmeela, "Power system harmonics," in *Power Quality in Modern Power Systems*, Elsevier, 2021, pp. 61–103. doi: 10.1016/B978-0-12-823346-7.00002-5.

[134] J. C. Das, *Power System Harmonics and Passive Filter Designs*. Wiley, 2015. doi: 10.1002/9781118887059.

[135] A. Arranz-Gimon, A. Zorita-Lamadrid, D. Morinigo-Sotelo, and O. Duque-Perez, "A Review of Total Harmonic Distortion Factors for the Measurement of Harmonic and Interharmonic Pollution in Modern Power Systems," *Energies*, vol. 14, no. 20, p. 6467, Oct. 2021, doi: 10.3390/en14206467.

[136] IEEE, "IEEE Std 519-2014 (Revision of IEEE Std 519-1992), IEEE Recommended Practice and Requirements for Harmonic Control in Electric Power Systems," Mar. 27, 2014, *IEEE, Piscataway, NJ, USA*. doi: 10.1109/IEEESTD.2014.6826459.

[137] S. Mikkili and A. K. Panda, *Power Quality Issues: Current Harmonics*. CRC Press, 2015. doi:

10.1201/9781315222479.

[138] S. R. Das *et al.*, "A Comprehensive Survey on Different Control Strategies and Applications of Active Power Filters for Power Quality Improvement," *Energies*, vol. 14, no. 15, p. 4589, Jul. 2021, doi: 10.3390/en14154589.

[139] L. Morán, J. Dixon, and M. Torres, "Active Power Filters," in *Power Electronics Handbook*, Elsevier, 2018, pp. 1341–1379. doi: 10.1016/B978-0-12-811407-0.00046-5.

[140] M. Bajaj and A. K. Singh, "Grid integrated renewable DG systems: A review of power quality challenges and state-of-the-art mitigation techniques," *Int. J. Energy Res.*, vol. 44, no. 1, pp. 26–69, Jan. 2020, doi: 10.1002/er.4847.

[141] P. S. Sanjan *et al.*, "Enhancement of Power Quality in Domestic Loads Using Harmonic Filters," *IEEE Access*, vol. 8, pp. 197730–197744, 2020, doi: 10.1109/ACCESS.2020.3034734.

[142] S. N. Manias, "Passive and Active Filters," in *Power Electronics and Motor Drive Systems*, Elsevier, 2017, pp. 807–842. doi: 10.1016/B978-0-12-811798-9.00011-1.

[143] S. S. Dheeban and N. B. Muthu Selvan, "ANFIS-based Power Quality Improvement by Photovoltaic Integrated UPQC at Distribution System," *IETE J. Res.*, vol. 69, no. 5, pp. 2353–2371, Jul. 2023, doi: 10.1080/03772063.2021.1888325.

[144] K. Sarita *et al.*, "Power Enhancement With Grid Stabilization of Renewable Energy-Based Generation System Using UPQC-FLC-EVA Technique," *IEEE Access*, vol. 8, pp. 207443–207464, 2020, doi: 10.1109/ACCESS.2020.3038313.

[145] A. Baliyan, M. Jamil, M. Rizwan, I. Alsaidan, and M. Alaraj, "An Intelligent PI Controller-Based Hybrid Series Active Power Filter for Power Quality Improvement," *Math. Probl. Eng.*, vol. 2021, pp. 1–10, Feb. 2021, doi: 10.1155/2021/6565841.

[146] D. Daftary and M. T. Shah, "Design and analysis of hybrid active power filter for current harmonics mitigation," in *2019 IEEE 16th India Council International Conference, INDICON 2019 - Symposium Proceedings*, Rajkot, India, Dec. 2019, pp. 1–4. doi: 10.1109/INDICON47234.2019.9029052.

[147] D. Lumbreras, E. Gálvez, A. Collado, and J. Zaragoza, "Trends in Power Quality, Harmonic Mitigation and Standards for Light and Heavy Industries: A Review," *Energies*, vol. 13, no. 21, p. 5792, Nov. 2020, doi: 10.3390/en13215792.

[148] J. Pederneiras Moraes Rocha, F. Salvadori, L. V. Hartmann, G. Malagoli Buiatti, I. R. Ferreira Moreno Pinheiro da Silva, and C. Seibel Gehrke, "Provision of ancillary services in a grid-connected photovoltaic distributed energy resource," *IET Gener. Transm. Distrib.*, vol. 16, no. 2, pp. 257–266, Jan. 2022, doi: 10.1049/gtd2.12219.

[149] A. N. Abdalla *et al.*, "Integration of energy storage system and renewable energy sources based on artificial intelligence: An overview," *J. Energy Storage*, vol. 40, p. 102811, Aug. 2021, doi: 10.1016/j.est.2021.102811.

[150] R. S. Inomoto, J. R. B. A. Monteiro, and A. J. Sguarezi Filho, "Boost Converter Control of PV System Using Sliding Mode Control With Integrative Sliding Surface," *IEEE J. Emerg. Sel. Top. Power Electron.*, vol. 6777, no. c, pp. 1–1, 2022, doi: 10.1109/JESTPE.2022.3158247.

[151] K. V. G. Raghavendra *et al.*, "A Comprehensive Review of DC–DC Converter Topologies and Modulation Strategies with Recent Advances in Solar Photovoltaic Systems," *Electronics*, vol. 9, no. 1, p. 31, Dec. 2019, doi: 10.3390/electronics9010031.

[152] D. E. O. Mohamed Cherif, A. Chebabhi, and A. Kessal, "An Integral-Backstepping Controller for Interleaved Boost Converter based on Photovoltaic Systems," vol. 71, no. 1, pp. 13–21, 2023, doi: 10.46904/eea.23.71.1.1108002.

[153] I. Kocaarslan, S. Kart, N. Genc, and H. Uzmus, "Design and application of PEM fuel cell-based cascade boost converter," *Electr. Eng.*, vol. 101, no. 4, pp. 1323–1332, Dec. 2019, doi: 10.1007/s00202-019-00871-0.

[154] S. Chakraborty, H.-N. Vu, M. M. Hasan, D.-D. Tran, M. El Baghdadi, and O. Hegazy, "DC-DC Converter Topologies for Electric Vehicles, Plug-in Hybrid Electric Vehicles and Fast Charging Stations: State of the Art and Future Trends," *Energies*, vol. 12, no. 8, p. 1569, Apr. 2019, doi: 10.3390/en12081569.

[155] A. R. Saxena and D. Kumar, "Design and control of a reconfigurable high-gain battery integrated dc-dc boost converter for time-varying loads," *Int. J. Circuit Theory Appl.*, vol. 49, no. 2, pp. 327–347, Feb. 2021, doi: 10.1002/cta.2888.

[156] A. Dali, S. Abdelmalek, and M. Bettayeb, "A Backstepping Controller for Interleaved Boost DC–DC Converter Improving Fuel Cell Voltage Regulation," in *Lecture Notes in Electrical Engineering 682*, 2021, pp. 751–762. doi: 10.1007/978-981-15-6403-1_51.

[157] N. Selvaraju, P. Shanmugham, and S. Somkun, "Two-Phase Interleaved Boost Converter Using Coupled Inductor for Fuel Cell Applications," *Energy Procedia*, vol. 138, pp. 199–204, 2017, doi: 10.1016/j.egypro.2017.10.150.

[158] M. Alaraj, A. Dube, I. Alsaidan, M. Rizwan, and M. Jamil, "Design and development of a proficient converter for solar photovoltaic based sustainable power generating system," *Sustain.*, vol. 13, no. 4, pp. 1–24, 2021, doi: 10.3390/su13042045.

[159] Y. Zhang, H. Liu, J. Li, M. Sumner, and C. Xia, "DC–DC Boost Converter With a Wide Input Range and High Voltage Gain for Fuel Cell Vehicles," *IEEE Trans. Power Electron.*, vol. 34, no. 5, pp. 4100–4111, May 2019, doi: 10.1109/TPEL.2018.2858443.

[160] S. Shibu, E. Babu, S. Neema, and N. Joy, "High gain DC-DC converter with low voltage stress," *Mater. Today Proc.*, vol. 58, pp. 600–606, 2022, doi: 10.1016/j.matpr.2022.04.027.

[161] M. H. Keum, Y. Choi, S. K. Han, and J. Il Kang, "High efficiency voltage-clamped coupled-inductor boost converter," in *IECON Proceedings (Industrial Electronics Conference)*, Vienna, Nov. 2013, pp. 828–833. doi: 10.1109/IECON.2013.6699241.

[162] C. Abdelkhalek, E. B. Said, A. Younes, and A. Hassan, "A Study and Implementation of Interleaved Boost Converter with a Novel MPPT Tactic for PV Systems," *2020 IEEE 2nd Int. Conf. Electron. Control. Optim. Comput. Sci. ICECOCS 2020*, 2020, doi: 10.1109/ICECOCS50124.2020.9314470.

[163] S. Somkun, C. Sirisamphanwong, and S. Sukchai, "A DSP-based interleaved boost DC–DC converter for fuel cell applications," *Int. J. Hydrogen Energy*, vol. 40, no. 19, pp. 6391–6404, May 2015, doi: 10.1016/j.ijhydene.2015.03.069.

[164] G. R. Chandra Mouli, J. H. Schijffelen, P. Bauer, and M. Zeman, "Design and Comparison of a 10-kW Interleaved Boost Converter for PV Application Using Si and SiC Devices," *IEEE J. Emerg. Sel. Top. Power Electron.*, vol. 5, no. 2, pp. 610–623, Jun. 2017, doi: 10.1109/JESTPE.2016.2601165.

[165] L. Callegaro, M. Ciobotaru, J. E. Fletcher, P. A. Rios, and D. J. Pagano, "Design of cascaded control loop for solar power optimizer based on a buck-boost converter," in *2016 IEEE 2nd Annual Southern Power Electronics Conference, SPEC 2016*, Auckland, New Zealand, Dec. 2016, pp. 1–6. doi: 10.1109/SPEC.2016.7846136.

[166] K. Ullah, M. Ishaq, F. Tchier, H. Ahmad, and Z. Ahmad, "Fuzzy-based maximum power point tracking (MPPT) control system for photovoltaic power generation system," *Results Eng.*, vol. 20, p. 101466, Dec. 2023, doi: 10.1016/j.rineng.2023.101466.

[167] S. Chakraverty, D. M. Sahoo, and N. R. Mahato, "Defuzzification," in *Concepts of Soft Computing*, Singapore: Springer Singapore, 2019, pp. 117–127. doi: 10.1007/978-981-13-7430-2_7.

[168] E. Jalalabadi, S. Z. Paylakhi, A. Rahimi-kian, and B. Moshiri, "Integral backstepping Lyapunov redesign control of uncertain nonlinear systems," *IET Control Theory Appl.*, vol. 16, no. 3, pp. 330–339, Feb. 2022, doi: 10.1049/cth2.12229.

[169] H. Gohar Ali, R. Vilanova Arbos, J. Herrera, A. Tobón, and J. Peláez-Restrepo, "Non-Linear Sliding Mode Controller for Photovoltaic Panels with Maximum Power Point Tracking," *Processes*, vol. 8, no. 1, p. 108, Jan. 2020, doi: 10.3390/pr8010108.

[170] H. Komurcugil, S. Biricik, S. Bayhan, and Z. Zhang, "Sliding Mode Control: Overview of Its Applications in Power Converters," *IEEE Ind. Electron. Mag.*, vol. 15, no. 1, pp. 40–49, Mar. 2021, doi: 10.1109/MIE.2020.2986165.

[171] H. Lin *et al.*, "Integral sliding-mode control-based direct power control for three-level NPC converters," *Energies*, vol. 13, no. 1, pp. 1–20, 2020, doi: 10.3390/en13010227.

[172] M. Ali, A. Krama, and S. S. Refaat, "A Robust Grid-Tied PV System based Super-Twisting Integral Sliding Mode Control," in *10th IEEE International Conference on Renewable Energy Research and Applications, ICRERA 2021*, Istanbul, Turkey, Sep. 2021, pp. 402–407. doi: 10.1109/ICRERA52334.2021.9598701.

[173] A. M. Mansour, O. M. Arafa, M. I. Marei, I. Abdelsalam, G. A. A. Aziz, and A. A. Sattar, "Hardware-in-the-Loop Testing of Seamless Interactions of Multi-Purpose Grid-Tied PV

Inverter Based on SFT-PLL Control Strategy," *IEEE Access*, vol. 9, pp. 123465–123483, 2021, doi: 10.1109/ACCESS.2021.3110013.

[174] C. Aouadi, A. Abouloifa, M. Aourir, I. Lachkar, B. Tighazouane, and Y. Boussairi, "Nonlinear Control of Double Stage Three-phase Grid-Connected Photovoltaic Systems," *IFAC-PapersOnLine*, vol. 55, no. 12, pp. 526–531, 2022, doi: 10.1016/j.ifacol.2022.07.365.

[175] A. Ouai, L. Mokrani, M. Machmoum, and A. Houari, "Power Quality Improvement of a Solar Energy Conversion System by a Coordinated Active and LCL Filtering," *Period. Polytech. Electr. Eng. Comput. Sci.*, vol. 65, no. 4, pp. 373–381, Oct. 2021, doi: 10.3311/PPee.17215.

[176] H. Tiwari, A. Ghosh, P. K. Ray, B. Subudhi, G. Putrus, and M. Marzband, "Direct Power Control of a Three-phase AC-DC Converter for Grid-connected Solar Photovoltaic System," in *2021 International Symposium of Asian Control Association on Intelligent Robotics and Industrial Automation, IRIA 2021*, Goa, India, Sep. 2021, pp. 125–130. doi: 10.1109/IRIA53009.2021.9588748.

[177] A. Ouai, L. Mokrani, M. Machmoum, and A. Houari, "Control and energy management of a large scale grid-connected PV system for power quality improvement," *Sol. Energy*, vol. 171, no. June, pp. 893–906, 2018, doi: 10.1016/j.solener.2018.06.106.

[178] S. H. Saidj, S. Boumechta, A. Degla, A. Djoudi, A. H. Arab, and M. Haddadi, "Comparison and Experimental Tests between Conventional and Interleaved DC/DC Boost Converter Topology," in *SIENR 2021 - 6th International Symposium on New and Renewable Energies*, Ghadaia, Algeria: IEEE, Oct. 2021, pp. 1–5. doi: 10.1109/SIENR50924.2021.9631894.

[179] R. A. Soumana, M. J. Saulo, and C. M. Muriithi, "New control strategy for multifunctional grid-connected photovoltaic systems," *Results Eng.*, vol. 14, p. 100422, Jun. 2022, doi: 10.1016/j.rineng.2022.100422.

[180] S. Ouchen, A. Betka, J. P. Gaubert, S. Abdeddaim, and F. Mazouz, "Fuzzy-Direct Power Control of a Grid Connected Photovoltaic System Associate with Shunt Active Power Filter," in *Lecture Notes in Networks and Systems*, vol. 35, 2018, pp. 164–172. doi: 10.1007/978-3-319-73192-6_17.

[181] K. I. Nadine and P. M. Moses, "Grid-connected solar PV with Active Power Filter Services for Power Quality Improvement," in *2022 IEEE PES/IAS PowerAfrica*, Kigali, Rwanda, Aug. 2022, pp. 1–5. doi: 10.1109/PowerAfrica53997.2022.9905276.

[182] M. Boukhalfa, A. Benaissa, M. R. Bengourina, A. Khoudiri, and M. Boudiaf, "Performance Enhancement of the DPC Control Based on a VGPI Controller Applied to a Grid Connected PV System," *Eng. Technol. Appl. Sci. Res.*, vol. 12, no. 2, pp. 8253–8258, Apr. 2022, doi: 10.48084/etasr.4697.

[183] G. Yang, S. Hao, C. Fu, and Z. Chen, "Model Predictive Direct Power Control Based on Improved T-Type Grid-Connected Inverter," *IEEE J. Emerg. Sel. Top. Power Electron.*, vol. 7, no. 1, pp. 252–260, 2019, doi: 10.1109/JESTPE.2018.2871113.

[184] B. Mohamed Rida, M. Rahli, S. Slami, and L. Hassaine, "PSO based Direct Power Control for a Multifunctional Grid Connected Photovoltaic System," *Int. J. Power Electron. Drive Syst.*, vol. 9, no. 2, p. 610, Jun. 2018, doi: 10.11591/ijpeds.v9.i2.pp610-621.

[185] T. Noguchi, H. Tomiki, S. Kondo, and I. Takahashi, "Direct power control of PWM converter without power-source voltage sensors," *IEEE Trans. Ind. Appl.*, vol. 34, no. 3, pp. 473–479, 1998, doi: 10.1109/28.673716.

[186] Tokuo Ohnishi, "Three Phase PWM Converterhverter by means of Instantaneous Active and Reactive Power Control," vol. 1, pp. 819–824, 1991, doi: https://doi.org/10.1109/IECON.1991.239183.

[187] I. Takahashi and T. Noguchi, "A New Quick-Response and High-Efficiency Control Strategy of an Induction Motor," *IEEE Trans. Ind. Appl.*, vol. IA-22, no. 5, pp. 820–827, Sep. 1986, doi: 10.1109/TIA.1986.4504799.

[188] A. Krama, L. Zellouma, B. Rabhi, S. S. Refaat, and M. Bouzidi, "Real-time implementation of high performance control scheme for grid-tied PV system for power quality enhancement based on MPPC-SVM optimized by PSO algorithm," *Energies*, vol. 11, no. 12, 2018, doi: 10.3390/en11123516.

[189] A. Chebabhi and K. Abdelhalim, "Self Tuning Filter and Fuzzy logic Control of Shunt Active Power Filter for Eliminates the Current Harmonics Constraints under Unbalanced Source

Voltages and Loads Conditions," *J. Power Technol.*, vol. 98, no. 1, pp. 1–19, 2018.

[190] S. Biricik, S. Redif, Ö. C. Özerdem, S. K. Khadem, and M. Basu, "Real-time control of shunt active power filter under distorted grid voltage and unbalanced load condition using self-tuning filter," *IET Power Electron.*, vol. 7, no. 7, pp. 1895–1905, Jul. 2014, doi: 10.1049/iet-pel.2013.0924.

[191] T. A. Trivedi, R. Jadeja, and P. Bhatt, "A Review on Direct Power Control for Applications to Grid Connected PWM Converters," *Eng. Technol. Appl. Sci. Res.*, vol. 5, no. 4, pp. 841–849, Aug. 2015, doi: 10.48084/etasr.544.

[192] A. Laib, F. Krim, B. Talbi, A. Kihal, and H. Feroura, "Improved control of three phase dual-stage grid-connected PV system based on a predictive control strategy," *Control Eng. Appl. Informatics*, vol. 20, no. 3, pp. 12–23, 2018.

[193] R.-J. Wai, Y. Yang, and Y.-Q. Wang, "Design of Backstepping Direct Power Control for Three-Phase PWM Rectifier," *IEEE Trans. Ind. Appl.*, vol. 55, no. 3, pp. 3160–3173, May 2019, doi: 10.1109/TIA.2019.2893832.

[194] B. O. Alawode and S. El-Ferik, "Design of Adaptive Backstepping Control for Direct Power Control of Three-Phase PWM Rectifier," pp. 1–6, 2021, [Online]. Available: http://arxiv.org/abs/2107.06343

[195] J.-S. Wang and S.-X. Li, "An Improved Grey Wolf Optimizer Based on Differential Evolution and Elimination Mechanism," *Sci. Rep.*, vol. 9, no. 1, p. 7181, May 2019, doi: 10.1038/s41598-019-43546-3.

[196] H. Özbay, S. Öncü, and M. Kesler, "SMC-DPC based active and reactive power control of grid-tied three phase inverter for PV systems," *Int. J. Hydrogen Energy*, vol. 42, no. 28, pp. 17713–17722, Jul. 2017, doi: 10.1016/j.ijhydene.2017.04.020.

[197] B. E. Youcefa, A. Massoum, S. Barkat, S. Bella, and P. Wira, "DPC Method for Grid Connected Photovoltaic System Acts as a Shunt Active Power Filter Implemented with Processor in the Loop," in *Proceedings of 2018 3rd International Conference on Electrical Sciences and Technologies in Maghreb, CISTEM 2018*, Algiers, Algeria, Oct. 2018, pp. 1–7. doi: 10.1109/CISTEM.2018.8613370.

[198] N. Li, Y. Wang, S. Li, Y. Li, and Z. Wang, "Direct power control strategy used in three-level NPC converters," in *Proceedings of The 7th International Power Electronics and Motion Control Conference*, Harbin, China, Jun. 2012, pp. 1675–1679. doi: 10.1109/IPEMC.2012.6259087.

[199] S. Ouchen, M. Benbouzid, H. Steinhart, A. Betka, F. Blaabjerg, and N. Bekhoucha, "Improved Direct Power Control Applied to Parallel Active Filtering Based on Fuzzy Logic Controller," in *2018 International Conference on Electrical Sciences and Technologies in Maghreb (CISTEM)*, Algiers, Algeria, Oct. 2018, pp. 1–5. doi: 10.1109/CISTEM.2018.8613302.

[200] S. Ouchen, M. Benbouzid, F. Blaabjerg, A. Betka, and H. Steinhart, "Direct Power Control of Shunt Active Power Filter Using Space Vector Modulation Based on Supertwisting Sliding Mode Control," *IEEE J. Emerg. Sel. Top. Power Electron.*, vol. 9, no. 3, pp. 3243–3253, Jun. 2021, doi: 10.1109/JESTPE.2020.3007900.

[201] I. Kanellakopoulos, P. V. Kokotovic, and A. S. Morse, "Systematic design of adaptive controllers for feedback linearizable systems," *IEEE Trans. Automat. Contr.*, vol. 36, no. 11, pp. 1241–1253, Nov. 1991, doi: 10.1109/9.100933.

[202] P.V. Kokotovic, "The joy of feedback: nonlinear and adaptive," *IEEE Control Syst.*, vol. 12, no. 3, pp. 7–17, Jun. 1992, doi: 10.1109/37.165507.

[203] A. Fekik *et al.*, "Direct power control of three-phase PWM-rectifier with backstepping control," in *Backstepping Control of Nonlinear Dynamical Systems*, Elsevier, 2021, pp. 215–234. doi: 10.1016/B978-0-12-817582-8.00017-9.

[204] Y. Bekakra, L. Zellouma, and O. Malik, "Improved predictive direct power control of shunt active power filter using GWO and ALO – Simulation and experimental study," *Ain Shams Eng. J.*, vol. 12, no. 4, pp. 3859–3877, Dec. 2021, doi: 10.1016/j.asej.2021.04.028.

[205] C. Muro, R. Escobedo, L. Spector, and R. P. Coppinger, "Wolf-pack (Canis lupus) hunting strategies emerge from simple rules in computational simulations," *Behav. Processes*, vol. 88, no. 3, pp. 192–197, Nov. 2011, doi: 10.1016/j.beproc.2011.09.006.